

**Design and Characterization of Electrospun Mats with Tailored Morphologies for Enhanced Active Layer Performance in Energy Conversion and Energy Storage Applications**

Scott Joel Forbey

Dissertation submitted to the faculty of the Virginia Polytechnic Institute and State

University in partial fulfillment of the requirements for the degree of

Doctor of Philosophy

In

Chemistry

Robert B. Moore (Chair)

Paul A. Deck

Michael W. Ellis

Harry W. Gibson

James R. Heflin

(March 7<sup>th</sup>, 2014)

(Blacksburg, Va)

Keywords: electrospinning; organic photovoltaic; bulk heterojunction; lithium polymer battery; ionic conductivity; photoinitiator; crosslinking; energy conversion; energy storage

# **Design and Characterization of Electrospun Mats with Tailored Morphologies for Enhanced Active Layer Performance in Energy Conversion and Energy Storage Applications**

Scott Joel Forbey

## **Abstract**

The goal of this research was to utilize the morphological control inherently imparted by the electrospinning process to improve the active layer performance in energy conversion devices as well as to better understand the relationship between morphology and performance in energy storage devices. Discrete control of the active layer morphology can promote exciton dissociation in organic photovoltaic cells (OPVs), whereas developing efficient ion diffusion pathways and beneficial polymer-ion interaction in polymer-gel electrolytes is demonstrated to result in enhanced battery performance.

We demonstrate the ability to develop unique morphologies in Poly(3-hexafluoro propylene) (P3HT) films with energy storage applications using various electrospinning techniques. Electrospinning in a solvent-saturated atmosphere allows for the design of ribbon architectures with polymer domains on the order of 5-10  $\mu\text{m}$ . These ribbon structures form what appear to be bi-continuous films, which could then be filled with an acceptor / fullerene type material to create a bulk heterojunction for OPV devices. Dropping chloroform onto the electrospinning needle during the spinning process results in P3HT fibers with porous surfaces. These fibers have diameters of  $\sim 2 \mu\text{m}$ . Using a coaxial needle to electrospin a P3HT solution in the core, and a  $\text{CHCl}_3$  sheath solution created hybrid ribbon – fiber structures. These structures have even smaller domain sizes than the ribbons created using a solvent

saturated atmosphere. Cospinning P3HT with sacrificial polymers results in P3HT fiber morphologies upon removal of the sacrificial template polymer. Additionally, introducing P3HT into an established fiber matrix results in fibrous P3HT architectures after the template fibers are removed.

Developing hybrid polymer-gel electrolytes using crosslinked PEO electrospun fibers results in membranes with high affinity for liquid electrolyte components. These electrospun PEO fiber mats exhibit excellent ionic conductivities at room temperature (12 mS/cm) exceeding an electrospun PVDF control. Furthermore, the PEO fiber mats can absorb nearly three times as much liquid electrolyte as the PVDF control. PEO has been shown to interact with lithium salts to aid in dissociation and diffusion during battery cycling. Although the ionic conductivity data suggest PEO to be a superior electrolyte, pulsed-field-gradient NMR shows that lithium diffusion is faster in PVDF samples. From coin cell discharge experiments, PEO is believed to interact strongly with  $\text{Li}^+$  ions, inhibiting them from diffusing rapidly during fast charge/discharge rates. However, PEO/PETA fiber electrolytes show nearly 100% theoretical capacity discharge at C/100 and a capacity retention of  $\sim 35\%$  at a C/5 discharge rate in contrast to a glass fiber separator which shows only a capacity that is approximately 85% of the theoretical value.

The unique mechanical properties of PEO/PETA electrospun mats could lead to interesting artificial skin and wound healing applications. Upon crosslinking at elevated temperatures ( $\sim 40^\circ\text{C}$ ), the fiber mats exhibit improved tensile strength and much higher ultimate stress at break. The porous nature of the materials lend to easy oxygen diffusion for wound healing, and the hydrophilicity promotes continued adhesion to existing tissue making these mats possible adhesive – less bandages.

## Acknowledgments

First and foremost I would like to start by thanking my family. Without the love, support, and constant motivation from my mother Tammy and my father Keirsten, I would never have become who I am today. I thank my wonderful fiancé Bonnie for her constant love, affection and support. My entire family has always been there to encourage me to keep going. I would like to thank Mrs. Suzanne Hawthorn my high school biology and physics teacher for planting the seed that would eventually convert my interests from athletics to academia. I would like to thank Mr. Les Sturgeon for first introducing me to chemistry and for believing in me. I thank the instructors at the University of Southern Indiana for fostering an amazing atmosphere in the chemistry department. I would like to thank my committee members Prof. Paul A. Deck, Prof. Michael W. Ellis, Prof. Harry W. Gibson, and Prof. James R. Heflin for constantly challenging and encouraging me throughout my graduate career. I would like to thank the Moore Research Group past and present specifically Dr. Sonya Benson, Dr. Gilles M. Divoux, Amanda Hudson, Mingqiang Zhang, Jeremy Beach, and Orkun Kaymakci. Only because of the family-like atmosphere fostered within this group am I able to accomplish this immense task. I would like to thank David Morris for being the best friend I could ever ask for during my tenure as a graduate student. I thank Bryce E. Kidd and Dr. Louis A. Madsen for their collaboration, the NMR experiments, and for all of the enlightening discussions. Finally, I give enormous thanks to my advisor Prof. Robert B. Moore. I can never express how much his guidance, support and belief in me throughout this experience has helped and how much it means to me.

## Table of Contents

<b>Abstract</b> .....	<b>ii</b>
<b>Acknowledgments</b> .....	<b>iv</b>
<b>Table of Contents</b> .....	<b>v</b>
<b>List of Figures</b> .....	<b>viii</b>
<b>List of Tables</b> .....	<b>xvi</b>
<b>List of Abbreviations</b> .....	<b>xvii</b>
<b>1. Polymeric Materials in Energy Storage and Energy Conversion</b> .....	<b>1</b>
<b>1.1 Introduction</b> .....	<b>1</b>
1.2 Polymers in Organic Photovoltaics (solar cells) .....	1
1.2.1 Organic vs. Inorganic Photovoltaics .....	4
1.2.2 The First Organic Solar Cells .....	6
1.2.3 The Bulk Heterojunction .....	7
1.2.4 Materials .....	8
1.2.5 Polymeric Materials for OPV Electrode Enhancement .....	10
1.3 Polymers in Batteries .....	12
1.3.1 Solid Polymer Electrolytes (SPEs) .....	15
1.3.2 Polymer Separators .....	21
1.3.3 Polymeric-Gel Electrolytes .....	25
1.3.3.1 Polyacrylonitrile Polymeric-Gel Electrolytes .....	26
1.3.3.2 Poly(methyl methacrylate) Polymeric-Gel Electrolytes .....	27
1.3.3.3 Poly(vinyl chloride) Polymeric-Gel Electrolytes .....	28
1.3.3.4 Poly(vinylidene fluoride) Polymeric-Gel Electrolytes .....	28
1.3.3.4 Poly(vinylidene fluoride – co – hexafluoro propylene) Polymeric-Gel Electrolytes .....	29
1.4 References .....	31
<b>2. Electrospinning for Controlled Polymeric Frameworks in Organic Photovoltaic Devices</b> .....	<b>35</b>
2.1 Introduction .....	35
2.2 Electrospinning for Controlled Frameworks .....	36
2.2.1 Electrospun Mats for Tissue Scaffold Engineering .....	37
2.2.2 Separator / Filtration Membranes .....	38
2.2.3 Fuel Cell Membranes .....	39
2.2.4 Energy storage devices .....	39
2.3 Electrospinning in Organic Photovoltaics (OPVs) .....	39
2.4 Electrospinning of Pure P3HT .....	42
2.4.1 Electrospinning in a Saturated Atmosphere .....	44
2.4.2 Chloroform Drop Electrospinning .....	45
2.4.2 Electrospinning from a Coaxial Needle .....	45
2.5 Coaxial Electrospinning PMMA and P3HT .....	47
2.6 Electrospinning Blended Solutions of PCL and P3HT .....	50
2.7 Electrospun Sacrificial Polymer Templates .....	53
2.7.1 Spin-casting onto a PVDF Fiber Containing Substrate .....	53
2.7.2 Electro-Polymerization of Thiophene onto ITO Substrates Containing Sacrificial Fibrous Templates .....	54

2.8 Conclusions .....	65
2.9 References .....	67
<b>3. Electrospun PEO-based Electrolytes for Rechargeable Lithium Polymer Batteries</b> .....	<b>69</b>
3.1 Introduction .....	69
3.2 Electrospinning Crosslinked PEO Mats .....	81
3.3 Experimental .....	82
3.3.1 Materials.....	82
3.3.2 Preparation of Electrospun Mats .....	82
3.3.2.1 Cross-Linking and Characterization of PEO-PETA Mats .....	83
3.3.2.2 Optical Characterization with SEM .....	83
3.3.2.3 Porosity Measurements .....	84
3.3.2.4 Conductivity Measurements .....	84
3.4 Results .....	85
3.4.1 Lithium Loading .....	90
3.4.2 Electrolyte Swelling .....	92
3.4.3 AC Impedance Spectroscopy .....	99
3.4.4 Ionic Conductivity .....	103
3.4.5 Polymer-ion Interactions .....	107
3.4.6 Tortuosity .....	109
3.5 Conclusions .....	114
3.6 References .....	116
<b>4. Characterization of Crosslinked Polyethylene Oxide Electrospun Fibers .....</b>	<b>118</b>
4.1 PEO – PETA Cross-linking Mechanism .....	118
4.2 Effect of Curing Atmosphere .....	122
4.3 Crosslink Density .....	128
4.4 Fiber Melding Due to Photo-curing Temperature .....	129
4.5 Effects of Crosslinking Conditions on Ionic Conductivity .....	131
4.6 Alternative Photoinitiators .....	134
4.7 Addition of Reactive Monomers During the Crosslinking Procedures .....	138
4.8 Temperature Dependence on Ionic Conductivity .....	144
4.9 Conclusions .....	145
4.10 Experimental .....	146
4.10.1 Film Preparation for IR Spectroscopy .....	146
4.10.2 Thermo / Mechanical Characterization .....	146
4.10.3 Conductivity Measurements .....	147
4.10.4 Preparation of Generation 2 PEO/PETA Fiber Mats .....	147
4.11 References .....	148
<b>5. Lithium Transport Within a PEO-based Structured Polymeric-Gel Electrolyte</b> .....	<b>149</b>
5.1 Introduction .....	149
5.2 PGE – Ionic Conductivity .....	154
5.3 Variable Temperature Multi-Nuclear NMR .....	157
5.3.1 Probing Multiple Environments Through Spin-Spin Relaxation .....	158
5.3.2 Morphological Effects on T <sub>2</sub> Relaxation Times .....	163
5.3.3 Liquid Electrolyte Variable Temperature Pulsed-Field Gradient NMR .....	167
5.3.4 Swollen Fiber Mat Variable Temperature Pulsed-Field Gradient NMR .....	169

5.4 Conclusion .....	176
5.5 References .....	180
<b>6. Battery Performance of Electrospun PEO/PETA Electrolytes .....</b>	<b>181</b>
6.1 Introduction .....	181
6.2 PEO/PETA Electrochemical Stability .....	182
6.3 2032 Coin Cell Prototype Batteries .....	183
6.4 Coin Cell Battery Performance .....	185
6.4.1 Initial Coin Cell Properties .....	187
6.4.2 Discharge Properties of Prototype Coin Cells .....	189
6.4.3 Prototype Capacity Retention .....	192
6.5 Conclusions .....	194
6.6 References .....	196
<b>7. Conclusions and Future Work .....</b>	<b>197</b>
7.1 Summary of Results .....	197
7.1.1 Electrospinning Unique Morphologies for Organic Photovoltaics .....	197
7.1.2 Electrospinning Hybrid Polymer-Gel Electrolytes for Lithium Polymer Batteries .....	198
7.2 Future Polymeric-Gel Electrolyte Work .....	204
7.3 Potential Wound Healing / Artificial Skin Application of Gen2 PEO/PETA .....	206

## List of Figures

**Figure 1.1.** General energy level diagram of a photovoltaic device. As photons are absorbed into the device, electrons are excited into the LUMO of the active material. The resulting exciton can separate with the electron traveling to the Al electrode and the hole traveling to the indium tin oxide (ITO) or a similar transparent electrode. (3)

**Figure 1.2.** General energy diagram of a donor/acceptor HJ organic photovoltaic device. These energies are roughly based on the optical band gap energies of poly(3-hexythiophene) (P3HT) and [6,6]-phenylC<sub>61</sub> butyric acid methyl ester (PCBM). (4)

**Figure 1.3.** Device assembly of a heterojunction solar cell. (6)

**Figure 1.4.** Bulk heterojunction photovoltaic device. The active layer consists of two phase-separated materials (polymer donor in blue; fullerene acceptor in gray). (7)

**Figure 1.5.** Several conjugated polymers used in OPV devices. Upper row are hole-conducting materials. Bottom row are electron-conducting materials.<sup>19-21</sup> (8)

**Figure 1.6.** Chemical structures of new conjugated polymers used in OPV cells for enhanced performance.<sup>30, 31</sup> (10)

**Figure 1.7.** Structures of two dopants: left two make up the new TFB:TPDSi<sub>2</sub>; right two make up PEDOT:PSS.<sup>41</sup>(11)

**Figure 1.8.** The schematic of electropolymerizing ordered PEDOT:PSS onto ITO electrodes in OPV devices. Copied with permission from reference 42. (12)

**Figure 1.9.** Schematic of a typical lithium polymer battery. Depicted in the schematic is an electrospun polymeric membrane. The polymeric component may have several different morphologies. (14)

**Figure 1.10.** Schematic of the segmental chain motion involving PEO and lithium ions (green sphere). The dashed lines between the PEO oxygens and the lithium ions represent the coordination from electron density donation. (17)

**Figure 1.11.** The structure of (ethylene oxide)<sub>6</sub>:LiAsF<sub>6</sub>, hydrogen atoms not shown. **a**, View of the PEO<sub>6</sub>:LiAsF<sub>6</sub> structure along *a*, showing rows of Li<sup>+</sup> ions perpendicular to the page. Blue spheres, lithium; white spheres, arsenic; magenta spheres, fluorine; light green, carbon in chain 1; dark green, oxygen in chain 1; pink, carbon in chain 2; red, oxygen in chain 2. **b**, View of the structure showing the relative positions of the chains and their conformations. Thin lines indicate coordination around the Li<sup>+</sup> cation. The lithium-ether oxygen distances (Å) for chain 1 are 2.07(5), 2.26(4), 2.28(4); for chain 2 they are 2.05(5), 2.14(6). (Image copied with permission from reference 50)<sup>50</sup> (19)

**Figure 1.12.** Polymerization product of 1,3-diallylimidazolium bromide and mesitylborane dimethyl sulfide complex after anion exchange.<sup>59</sup> (20)

**Figure 1.13.** Polymeric separator cartoon. Lithium ions diffuse through the polymeric membrane using pores within the film. Not shown in the cartoon are the solvent molecules that interact with lithium salts. **(22)**

**Figure 1.14.** An SEM image of microporous polyethylene produced from the thermal annealing and subsequent stretching technique adopted by Celgard<sup>®</sup>. Image copied with permission from reference 60.<sup>60</sup> **(23)**

**Figure 1.15.** SEM image of a wet process microporous membrane **a.)** bottom of film (in contact with substrate), **b.)** top of film (in contact with air), **c.)** cross-section of film. Image copied with permission from reference 66.<sup>66</sup> **(24)**

**Figure 2.1.** (Top) diagram of electrospinning setup: the syringe contains the polymeric solution and the needle is charged with electrical potential. The polymeric solution moves towards the collector forming first a Taylor cone, then a thin jet. (Bottom) actual images of fiber forming polymer solutions; right is Taylor cone, left is polymer jet/fiber. **(36)**

**Figure 2.2.** Cartoon schematic of an OPV bulk heterojunction device comprised of electrospun P3HT as the donor domain (orange fibers). Fibers must be smaller than 20 nm in diameter to discourage recombination. After electrospinning, the resulting P3HT mat is then filled with a fullerene based acceptor domain (teal). **(42)**

**Figure 2.3.** Electrospun P3HT using 53,000  $M_n$  dissolved in chloroform. The flow rate for each sample was 5 ml/h, the P3HT concentration was 10 wt.% in  $CHCl_3$ , and the applied voltages were A.) 15 kV B.) 20 kV and C.) 25 kV. **(43)**

**Figure 2.4.** Electrospun P3HT in atmospheres saturated with boiling  $CHCl_3$  for A.) 5 minutes B.) 10 minutes C.) 15 minutes of boiling time prior to electrospinning. **(44)**

**Figure 2.5.** SEM images of P3HT using the chloroform drop alternative electrospinning procedure. From left to right the image is simply magnified from 200x to 10,000x. This image is of a representative of samples spun using this technique with various ES parameters. **(45)**

**Figure 2.6.** SEM images of P3HT electrospun from a coaxial needle. Both samples were electrospun from a 14 wt.% P3HT solution in chloroform, at a voltage of 18 kV, an inner flow rate of 5 mL/h and outer flow rates of A.) 7 mL/h and B.) 9 mL/h. **(46)**

**Figure 2.7.** SEM images of pure PMMA electrospun using an applied voltage of 4.5 kV, a collector distance of 15 cm, a polymer concentration of 300 mg/mL and three different flow rates: A.) 0.5 mL/h B.) 1.0 mL/h and C.) 5 mL/h. **(48)**

**Figure 2.8.** Photograph of electrospun samples of pure PMMA (right) and PMMA/P3HT coaxial setup (left). Differences in two PMMA samples: left spun at 8 kV, right spun at 11 kV. Differences for PMMA/P3HT samples are similarly spun at 8 kV (left) and 11 kV (right). **(49)**

**Figure 2.9.** SEM images of PMMA/P3HT coaxially electrospun representative samples. From left to right the samples electrospinning parameters were 4.5 mL/h @ 11 kV, 5 mL/h @ 11 kV, and 5 mL/h @ 9 kV. Each sample was electrospun from a sheath solution containing 300 mg/mL PMMA in chlorobenzene, a P3HT solution of 50 mg/mL in chlorobenzene and with a collector distance of 15 cm. **(50)**

**Figure 2.10.** SEM images of PCL electrospun from chloroform. Additionally, the samples were electrospun from two different polymeric concentrations in  $\text{CHCl}_3$ : Top two rows 25 wt.% solution, bottom two rows 50 wt.% solutions. **(51)**

**Figure 2.11.** Representative SEM images of PCL/P3HT electrospun samples with voltages, flow rates, and concentrations ranging from 10 – 18 kV, 0.7 – 8.0 mL/h, and 20 -50 wt.% respectively. **(52)**

**Figure 2.12.** SEM images of PVDF templating. From right to left: pure PVDF electrospun from DMAc:Acetone 50:50 vol. mixture, PVDF fibers after spin-coating a 13 wt.% P3HT solution in chloroform, SEM image of P3HT structure after removal of PVDF with acetone. **(54)**

**Figure 2.13** Cyclic voltammogram of thiophene in a 0.5 M  $\text{LiClO}_4$  electrolyte solution of acetonitrile using an Ag reference. **(55)**

**Figure 2.14.** Electro-polymerization scheme of thiophene via oxidative dehydrogenation. **(56)**

**Figure 2.15.** Potential profiles for the galvanostatically controlled electro-polymerization of thiophene at various currents vs. silver wire pseudo-reference. **(57)**

**Figure 2.16.** Images of electro-polymerized polythiophene films produced from A.)  $1.0 \text{ mA/cm}^2$ ; B.)  $1.5 \text{ mA/cm}^2$ ; C.)  $2.0 \text{ mA/cm}^2$ ; and D.)  $2.5 \text{ mA/cm}^2$ . **(58)**

**Figure 2.17.** Potential vs. time profile for successive electropolymerizations of a thiophene electrolyte solution using a silver wire reference. **(59)**

**Figure 2.18.** Images of successive electro-polymerized thiophene films obtained from the same electrolyte solution. Samples are presented successively from left to right (top left was polymerized first and the bottom right was polymerized last). **(61)**

**Figure 2.19.** Image of PCL template fibers deposited on an ITO working electrode (left) and SEM images of PCL fibers in ITO slides (right). **(63)**

**Figure 2.21** Photograph of ITO coated glass slides covered in polythiophene film without PCL fibers (left) and with PCL fibers (right) and SEM images of thiophene polymerized onto ITO containing PCL fiber template. **(64)**

**Figure 3.1.** SEM images of PVDF fibers electrospun from various polymer concentrations in DMAc:acetone solutions. Polymer morphologies change from spherical droplets to polymer fibers as the polymer concentration in the electrospinning solution increases. **(70)**

**Figure 3.2.** SEM images of 10 wt.% solutions of PVDF in 50:50 DMAc:acetone with a constant flow rate and varying applied potentials. A.) 8 kV, B.) 12 kV, C.) 16 kV. **(73)**

**Figure 3.3:** Stress-Strain curve of PVDF electrospun fiber mats **a.)** as-spun and **b.)** after thermal annealing at  $160 \text{ }^\circ\text{C}$  for 2 hours.<sup>2</sup> Figure copied with permission from reference 2.<sup>2</sup> **(77)**

**Figure 3.4:** SEM images of PVDF fibers electrospun from two different polymer concentrations. Annealing at  $100 \text{ }^\circ\text{C}$  results in a reduction of beads and a densification of polymer fibers along with possible fiber melding. **(78)**

**Figure 3.5:** Porosity and mean pore size as a function of average fiber diameter. Image copied with permission from reference 9.<sup>9</sup> (79)

**Figure 3.6.** SEM images of PEO with various amounts of PETA after UV exposure: A.) pure PEO, B.) PEO10 C.) PEO20, D.) PEO30. (86)

**Figure 3.7.** SEM images of PEO electrospun fibers containing various wt.% or PETA along with corresponding fiber diameter histograms for A.) PEO10 B.) PEO20 and C.) PEO30. (87)

**Figure 3.8.** SEM images of electrospun PEO/PETA mats following ultrasonic agitation in methanol for A.) PEO10 B.) PEO20 C.) PEO30 and D.) PEO30 as spun (no MeOH wash). (90)

**Figure 3.9.** SEM images of electrospun fibers A.) PEO30 and B.) PVDF after loading with approximately 100 wt.% LiClO<sub>4</sub>. (92)

**Figure 3.10.** Equilibrium uptake swelling of PEO/PETA and PVDF membranes absorbing a 1M LiClO<sub>4</sub> solution of EC:DMC (1:1). (93)

**Figure 3.11** Swelling profile for PEO/PETA electrospun fiber mats. (96)

**Figure 3.12** Electrolyte swelling of PEO/PETA fibrous mats as a function of crosslink density. (97)

**Figure 3.12.** Environmental SEM images of PEO10 samples A.) Swollen with 600 wt.% water and B.) Image acquired during a gradient drying of a fully immersed mat of PEO10 (top right dry region, bottom left wet region). (98)

**Figure 3.13.** Density of two lithium salt liquid electrolytes consisting of EC:DMC (1:1 vol.). Black line represents lithium perchlorate (LiClO<sub>4</sub>). Red line represents lithium triflate (LiCF<sub>3</sub>SO<sub>3</sub>). (99)

**Figure 3.14.** Through-plane AC impedance schematic. The intercept of the impedance spectra with the real axis yields the membrane resistance (at high frequencies). The real resistance of the fixture was determined based on its high frequency impedance, which was subsequently subtracted from the resistive component of the raw data. (100)

**Figure 3.15.** Resistance of PEO/PETA electrospun polymeric-gel electrolytes swollen with 600 wt.% (black) and 800 wt.% (red) electrolyte solution consisting of 1M LiClO<sub>4</sub> in EC:DMC (1:1). The extrapolated resistances corresponding to the cell and the interface are essentially equal (~3 Ω) for both swelling ratios. (101)

**Figure 3.16.** A typical through-plane AC impedance Cole-Cole plot of non-swollen PEO/PETA samples that have been pre-loaded with LiClO<sub>4</sub>. PEO was electrospun and crosslinked with 10 wt.% (red) and 20 wt.% (black) PETA followed by a 1h ultrasonic was in a LiClO<sub>4</sub> solution of methanol. (102)

**Figure 3.17.** Ionic conductivities of various electrospun samples with (red) and without (green) a lithium salt pre-loading treatment. (104)

**Figure 3.18.** Ionic conductivity of liquid electrolyte (red), non-loaded PEO10 (black), PEO with liquid electrolyte (blue), and loaded PEO10 swollen with 1M LiClO<sub>4</sub> (green) as a function of various LiClO<sub>4</sub> concentrations. **(106)**

**Figure 3.19.** Cross sectional schematic of ionic tortuosity through two electrospun polymer gel electrolytes: PVDF mat (top), and PEO mat (bottom). Blue domains represent liquid electrolyte, orange represents polymeric fibers and green represents lithium ions. **(111)**

**Figure 3.20.** Ionic conductivities of PEO/PETA fibers swollen with 400 wt.% of 1 M lithium triflate in EC:DMC. **(113)**

**Figure 3.21.** Ionic conductivities of PEO/PETA samples fully swollen with 1 M lithium triflate in EC:DMC. **(113)**

**Figure 4.1.** Proposed radical mechanism of UV initiated crosslinking of PEO with PETA.<sup>1</sup> **(119)**

**Figure 4.2.** Depiction of possible crosslink pathways occurring in the UV curing of PEO with a PETA photoinitiator. Blue region shows radical reaction of PETA double bonds induced and terminated by a PEO radical. Green region shows combination of PETA radical with PEO radical. Red region shows the combination of two PEO radicals. **(120)**

**Figure 4.3.** IR absorbance spectrum of PEO10 at various UV irradiation times. **(122)**

**Figure 4.4.** Chain scission of a radical containing PEO chain upon exposure to oxygen. **(123)**

**Figure 4.5.** Stress – strain curve for Gen1 (atmospheric crosslinking conditions) for both as-spun fiber mats (no UV exposure – solid lines) and samples after 1 hour of UV exposure (dashed lines). Electrospun PVDF was used as a control. **(124)**

**Figure 4.6.** Stress – strain curves for Gen2 (N<sub>2</sub> purged crosslinking conditions) PEO/PETA electrospun fiber mats. For a control, and electrospun fiber mat of PVDF was subjected to the same tensile experiment. **(125)**

**Figure 4.7.** Young's moduli for electrospun PEO/PETA samples before (solid) and after (lined) UV irradiation. PVDF was electrospun under similar conditions as a control. **(126)**

**Figure 4.8.** Comparison of the Young's modulus observed for PVDF, un-crosslinked Gen1 PEO/PETA, UV cured Gen1 PEO/PETA, and UV cured Gen2 PEO/PETA electrospun mats. **(128)**

**Figure 4.9.** SEM image of a representative PEO10 electrospun sample before UV exposure (top), UV exposure under atmospheric conditions (left), and UV exposure under N<sub>2</sub> purge and at 40 °C (right). The UV exposure time was 30 min for each sample. **(131)**

**Figure 4.10.** Ionic conductivities of Gen1 (blue) and Gen2 (green) PEO/PETA electrospun PGEs swollen with only 400 wt.% of EC:DMC containing 1M LiClO<sub>4</sub>. **(132)**

**Figure 4.11.** Ionic conductivity values for Gen1 and Gen2 samples of electrospun PEO/PETA samples upon immersion swelling in electrolyte solution (1M LiClO<sub>4</sub> in EC:DMC). **(134)**

**Figure 4.12.** Photo of PEO10 sample delamination during a tensile experiment. (138)

**Figure 4.13.** DSC thermograph of Gen1 PEO/PETA electrospun samples with various amounts of PETA including pure PEO (black), 10 wt.% PETA (red), 20 wt.% PETA (blue), and 30 wt.% PETA (green). (139)

**Figure 4.14a.** DSC thermographs of PEO/PETA and PEO/PETA/VPC electrospun fiber mats. The dashed curves correspond to Gen 1 PEO10 (green), PEO20 (red), PEO30 (blue), and the solid line corresponds to a PEO sample containing 5 wt.% PETA and 5 wt.% VPC (black). (141)

**Figure 4.14b.** DSC traces of figure 4.14a with the addition of a PEO/PETA/VPC electrospun sample: the PETA and VPC contents were both 10 wt.%. (142)

**Figure 4.15.** Ionic conductivities for Gen1 PEO samples containing 10 wt.% PETA (blue), 20 wt.% PETA (red), 5 wt.% PETA and 5 wt.% VPC (green), 10 wt.% PETA and 10 wt.% VPC (purple). (143)

**Figure 4.16.** Arrhenius plot of Gen1 and Gen2 PEO10 conductivities. (145)

**Figure 5.1.** Ionic conductivity of Gen1 PEO/PETA electrospun samples upon immersion swelling in EC:DMC containing 1M LiClO<sub>4</sub>. (154)

**Figure 5.2.** Ionic conductivity of Gen1 PEO/PETA samples at various temperatures. Samples include PEO10 (blue), PEO20 (red), and PEO30 (green). (155)

**Figure 5.3.** Arrhenius plot of Gen1 PEO/PETA conductivity values used to determine activation energies. (157)

**Figure 5.4.** <sup>7</sup>Li spin-spin lattice ( $T_2$ ) measurements (at 35 °C) yield two-component decay curves. This is suggestive of lithium within two distinct environments, where the short- $T_2$  may be lithium interacting with PEO, specifically the ether oxygens (i.e., more rigid environment), and the long- $T_2$  may be lithium interacting with the liquid electrolyte (i.e., more mobile environment). Within the figure inset, an increase and decrease in the Li-solvent (15 ms to 48 ms) and Li-polymer (4 ms to 0.8 ms), respectively, is seen as a function of wt. % PETA. Error estimated to be  $\leq 5\%$ . (160)

**Figure 5.6.** <sup>7</sup>Li spin-spin lattice ( $T_2$ ) measurements (at 35 °C) for PEO10 LiClO<sub>4</sub>-loaded (with 1M LiClO<sub>4</sub>), PEO10 LiClO<sub>4</sub>-loaded (without 1M LiClO<sub>4</sub>), and PEO10 (with 1M LiClO<sub>4</sub>), where the previous PEO10 (with 1M LiClO<sub>4</sub>)  $T_2$ -curve is used as a reference, yield two-component decay curves. Error estimated to be  $\leq 5\%$ . (163)

**Figure 5.7.** DSC traces of Gen1 PEO/PETA samples before (solid) and after (dashed) pre-loading with LiClO<sub>4</sub> via ultrasonic agitation in methanol for PEO10 (black), PEO20 (red) and PEO30 (blue). (165)

**Figure 5.8.** Cartoon schematic of electrospun fibers non-loaded (A) and pre-loaded (B) with LiClO<sub>4</sub>. Opaque domains represent fibers, small dark blue lines represent PEO polymer chains, blue bundles represent PEO crystalline regions, light blue regions indicated liquid domains, and small green spheres represent Li<sup>+</sup> ions. (167)

**Figure 5.9.** Arrhenius plots of lithium (<sup>7</sup>Li), perchlorate (<sup>35</sup>Cl), and EC (<sup>1</sup>H) and DMC (<sup>1</sup>H) (with/without LiClO<sub>4</sub>) give insight into pre-diffusion time-scale interactions for the liquid

electrolyte. Carbonate  $D$  and  $E_a$  decrease and increase, respectively, with addition of  $\text{LiClO}_4$ . Lithium  $D$  and  $E_a$  are lower than perchlorate, suggestive of attractive and repulsive ion-dipole interactions between lithium-carbonate and perchlorate-carbonate, respectively. We estimate the error for  $E_a$  values to be  $\leq 1 \text{ kJ mol}^{-1}$ . (168)

**Figure 5.10.** Arrhenius plots of unstructured PEO/EC:DMC gels containing various lithium perchlorate concentrations. Error estimated to be  $\leq 5\%$ . (171)

**Figure 5.11.** Arrhenius plots of PEO/PETA fibrous electrolytes as a function of wt.% PETA allows us to understand how the introduction of a cross-linker influences macro- and microscopic transport properties.  $\text{Li}^+$  diffuses fastest in PEO10 with an  $E_a$  of  $15.5 \text{ kJ mol}^{-1}$ . Error in  $D$  values is estimated to be  $5\%$  and  $E_a$  values to be  $\pm 2 \text{ kJ mol}^{-1}$ . (172)

**Figure 5.12.** Arrhenius plots of lithium ion diffusion as a function of wt.% PETA. Lithium ion diffusion in pure liquid electrolyte is plotted in blue. Black data represent non-loaded PEO10 samples swollen with EC:DMC 1M  $\text{LiClO}_4$ . Red data represent pre-loaded PEO10 swollen with only EC:DMC. Green data represent pre-loaded PEO10 sample swollen with EC:DMC 1M  $\text{LiClO}_4$ . Error estimated to be  $\leq 5\%$ . (174)

**Figure 5.13.** Arrhenius plots of  $\text{Li}^+$  diffusion coefficients in PEO/PETA samples, electrospun PVDF and glass fiber control electrolytes. Error estimated to be  $\leq 5\%$ . (176)

**Figure 5.14.** Cartoon depiction of possible PEO-ion interactions. Charged species traveling through the liquid domains become separated into free (naked) charge carrying species upon interaction with polymeric chains in PEO/PETA fibers. (178)

**Figure 6.1.** Electrochemical stability of electrospun PEO fiber mats: pure PEO (black), 10 wt.% PETA (red), and 10 wt.% PETA + EC:DMC (green). (183)

**Figure 6.2.** Diagram of a 2032 coin cell assembled using a PEO/PETA swollen fiber mat as the electrolyte/separator. Coin cells using a glass fiber separator were also assembled in the same manner. (185)

**Figure 6.3.** SEM images of fibrous electrolytes A.) Electrospun, crosslinked PEO10 fiber mats and B.) glass fiber mats. (186)

**Figure 6.4.** Images of 2032 coin cell batteries assembled with PEO10 (left) and glass fiber (right) electrolytes. Bottom images show both cells ability to light an LED. (187)

**Figure 6.5.** Charging profiles for PEO10 and glass fiber containing coin cells. Cells were charged by holding the potential at 4.2 V until the current dropped below  $2.54 \text{ e}^{-5} \text{ A}$ . (189)

**Figure 6.6.** Discharge profile for PEO10 (black) and GF (red) at a various C rates. (191)

**Figure 6.7.** Specific capacity discharge profiles of PEO10 (black) and GF (red) coin cells at three C rates. (192)

**Figure 6.8.** Capacity retention for PEO10 (black curves) and GF (red curves) at C/30 and C/5 discharge rates. (194)

**Figure 7.1.** Image of electrospun PEO10 crosslinked under Gen2 conditions and swollen with DI water. (207)

**Figure 7.2.** Stress-strain plot of PEO10 Gen2 samples swollen with DI water. (208)

## List of Tables

**Table 3.1:** Average fiber diameters of electrospun PVDF mats spun from solutions with varying polymer concentrations (beads not included in diameter measurements). (71)

**Table 3.2:** Average fiber diameters of electrospun PVDF when spun from a 10 wt.% solution in DMAc:Acetone with various voltages. (75)

**Table 3.3.** Gel fraction and porosity of PEO fiber mats crosslinked with various amounts of PETA after one-hour of methanol ultrasonication. (89)

**Table 3.4.** The number average molecular weights between crosslinks and the crosslink density, as a function of PETA concentration. (95)

**Table 4.1.** Number average molecular weight between crosslinks and crosslink density for Gen1 and Gen2 PEO/PETA samples. (129)

**Table 4.2.** Summary of crosslinking agents used to crosslink PEO electrospun fibers. (135)

## List of Abbreviations

PV	= Photovoltaic
OPV	= Organic Photovoltaic
LPB	= Lithium Polymer Batteries
HJ	= Heterojunction
BHJ	= Bulk Hetero Junction
HOMO	= Highest occupied molecular orbital
LUMO	= Lowest unoccupied molecular orbital
ITO	= Indium tin oxide
P3HT	= poly(3-hexylthiophene)
PCBM	= [6,6]-phenylC <sub>61</sub> butyric acid methyl ester
SPE	= Solid polymer electrolyte
PGE	= Polymer gel electrolyte
PEO	= Polyethylene oxide
PVDF	= Poly(vinylidene oxide)
PAN	= Poly(acrylonitrile)
PMMA	= Poly(methyl methacrylate)
PETA	= Pentaerythritol triacrylate
AC	= Alternating current
PCL	= Polycaprolactone
BP	= Benzophenone
THBP	= 2,2',4,4'- tetrahydroxy benzophenone
BPO	= Biphenyl peroxide
AIBN	= Azobisisobutyronitrile
UV	= Ultraviolet
IR	= Infrared
PE	= Polyethylene
PVC	= Poly(vinyl chloride)
PVDF-HFP	= Poly(vinylidene fluoride – co – hexafluoro propylene)
T <sub>g</sub>	= Glass transition temperature
T <sub>m</sub>	= Melting temperature
DSC	= Differential scanning calorimeter
SEM	= Scanning electron microscope
PVA	= Polyvinyl alcohol
μm	= Micrometer
nm	= Nanometer
s	= Second
S	= Siemen
cm	= Centimeter
T	= Temperature
NMR	= Nuclear magnetic resonance
PFG	= Pulsed field gradient
T <sub>2</sub>	= Spin-spin relaxation
OCV	= Open circuit voltage
V	= Voltage

mA	= milliamperes
h	= Hours
EC	= Ethylene carbonate
DMC	= Dimethyl carbonate
CHCl <sub>3</sub>	= Chloroform
DMac	= Dimethyl acetamide
VPC	= Vinyl propylene carbonate
LiClO <sub>4</sub>	= Lithium perchlorate
PC	= Propylene carbonate
EO	= Ethylene oxide
<i>D</i>	= Diffusion coefficient
<i>E<sub>a</sub></i>	= Activation energy
SEI	= Solid electrolyte interface
LiFePO <sub>4</sub>	= Lithium iron phosphate
Li <sup>+</sup>	= Lithium cation

# Chapter 1

## Polymeric Materials in Energy Conversion and Energy Storage

### *1.1. Introduction*

As the energy needs of consumers around the world increase at alarming rates, the research and development of new and better-performing materials struggle to keep up. With the price of fossil fuel energy soaring, the demand to find cost efficient alternative energy rises.<sup>1-4</sup> Polymeric materials have been investigated for nearly 30 years as potential components in energy storage and conversion devices. Two increasingly promising areas of alternative energy utilizing polymeric materials are organic photovoltaic cells (solar cells, OPVs) and rechargeable lithium polymer batteries (LPB). OPVs offer attractive means of converting abundant solar energy, into usable electrical energy. OPVs not only reduce size and but, the inherently flexible nature of polymeric films allows for the development of flexible solar cells. While OPV devices convert solar power into electrical energy, LPBs function as a promising means of storing that energy. Safe, flexible, lightweight, high energy density and fast charge-discharge properties are only realized by utilizing polymer-based energy storage devices.

### *1.2. Polymers in Organic Photovoltaics (solar cells)*

Organic photovoltaics (OPVs) have gained significant attention over the past 20 years as coal and oil prices soar. The ability to utilize the abundant energy produced from our sun is viewed by many as a necessary step in becoming independent of fossil fuels. In the past three decades, an effort has been made to remodel photovoltaic (PV) devices, devices that convert sunlight into electrical energy, using organic

semiconducting materials. Currently, commercial PVs use inorganic materials (silicon usually) as the photoactive element. Even though these devices have reached record efficiencies of around 21%, they are costly to produce, leading industry to explore alternatives.<sup>5,6</sup> A typical photovoltaic device energy diagram is depicted below in **Figure 1.1**. Although intensive efforts have incorporated semiconducting polymers as the photoactive species recently, the field of organic photovoltaics (OPV) first began with the discovery that organic dyes such as methylene blue exhibited the photovoltaic effect.<sup>1,6</sup> Ensuing incorporation of chlorophylls and carotenes led to single layered “sandwich” devices.<sup>1,7</sup> These single layered OPVs suffer low quantum efficiencies and low power conversions due to the electrode potential differences being insufficient for exciton dissociation. Despite recent improvements and low costs, OPVs have yet to reach the consumer market and compete with the inorganic analogs.<sup>6</sup>

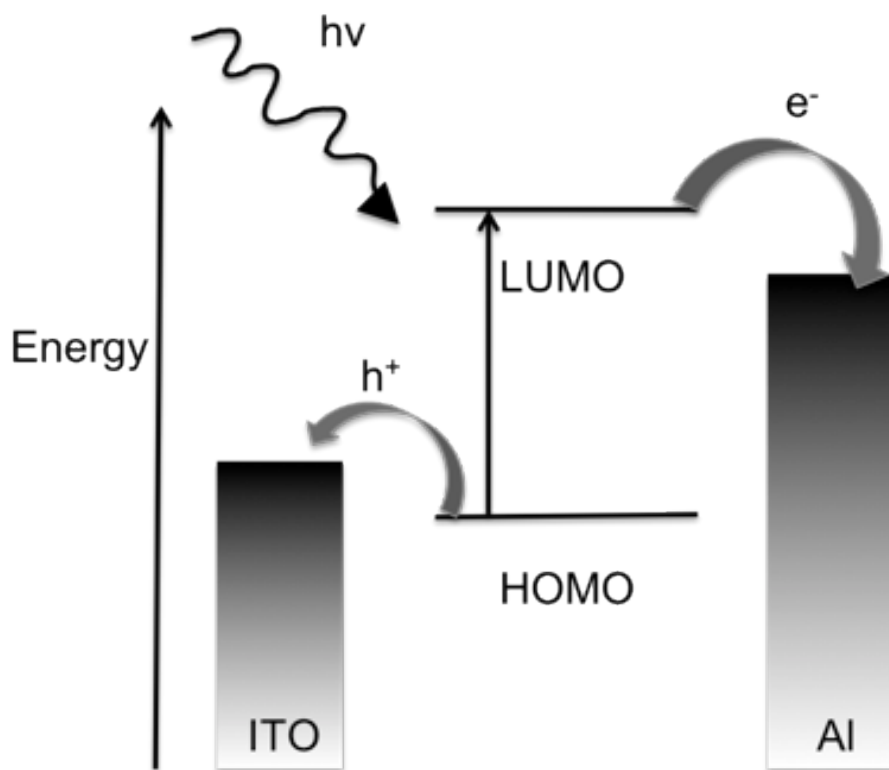


**Figure 1.1.** General energy level diagram of a photovoltaic device. As photons are absorbed into the device, electrons are excited into the LUMO of the active material. The resulting exciton can separate with the electron traveling to the Al electrode and the hole traveling to the indium tin oxide (ITO) or a similar transparent electrode.

The incorporation of  $sp^2$ -hybridized, semiconducting, low molecular weight organic materials led to the first organic photovoltaic devices.<sup>4</sup> These molecules are polarizable due to delocalization of the  $\pi$  electrons allowing for the transport of electric current. Further investigation of higher molecular weight polymers led to even greater efficiencies. However, in 1986 Tang et. al. reported the first heterojunction (two layered) OPV boosting efficiencies to 1%.<sup>8</sup> These bilayer devices were able to overcome exciton separation deficiencies often present in the single layer devices. Building on Tang's

results, research groups have studied the morphology, processing techniques, and post processing treatment, of these heterojunction (HJ's) to further improve efficiencies into the 4-5% range.<sup>9</sup> The concept of donor/acceptor materials arose along with the HJ solar cell. A schematic of a donor/acceptor OPV energy diagram may be seen below in **Figure 1.2**. In most instances, the photoactive polymer is the donor species (p-type); it donates excited electrons and is considered hole-conducting. The accepting species is often a C<sub>60</sub> derivative and is the n-type, electron-conducting member of the heterojunction.

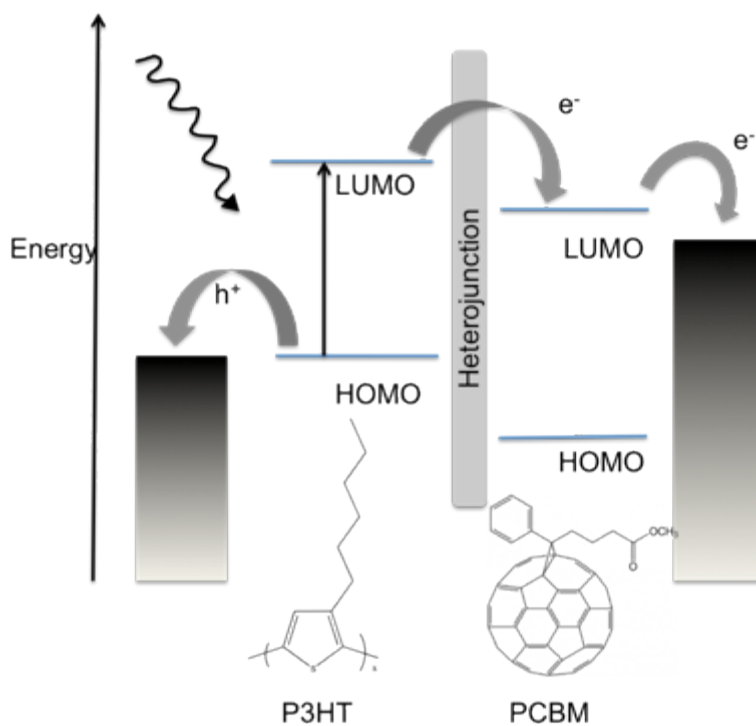


**Figure 1.2.** General energy diagram of a donor/acceptor HJ organic photovoltaic device. These energies are roughly based on the optical band gap energies of poly(3-hexythyophene) (P3HT) and [6,6]-phenylC<sub>61</sub> butyric acid methyl ester (PCBM).

### 1.2.1. Organic vs. Inorganic Photovoltaics

Although the principle of harvesting energy is similar for both inorganic and

organic photovoltaic devices, there are noteworthy differences. One key difference is the mechanism of charge generation. In inorganic PV cells, electron-hole pairs are generated and subsequently dissociated immediately. In contrast, OPV solar cells generate a mobile excited state termed an exciton. The exciton (excited electron and hole pair) in OPV devices experiences a Coulombic attraction greater than inorganic photovoltaics (IPV) devices due to low dielectric constants. Additionally, OPV devices rely on non-covalent electronic interactions to diffuse excitons through the material; this is often referred to as charge hopping. Because of this form of diffusion, the electron and hole are bound tightly to one another, making their separation more difficult (and making recombination easier).<sup>10, 11</sup> The fundamental driving force of OPV devices is the separation of the exciton at the heterointerface. This separation results in a free electron in one phase and a free hole in another phase of the material.<sup>8, 10, 11</sup>

OPV devices also have much lower charge-carrier mobilities than IPV devices. Early OPV's had charge-carrier mobilities around  $10^{-7} \text{ m}^2 \text{ V}^{-1} \text{ s}^{-1}$ . Although the mobilities have increased orders of magnitude since, they are still a main reason of low OPV efficiencies.<sup>12</sup> The excitons must travel through the material to the heterointerface in order to separate, thus the charge-carrier mobility is of great importance for cell efficiency. OPV's have much higher absorption coefficients than silicon counterparts, resulting in less UV penetration. In silicon devices, light is absorbed throughout the entire material, adding to efficiency. However, in organic devices, light absorption is limited by the absorptivities and concentrations of active material leaving only thin film cells viable. Additionally, only the light absorbed in the excitonic layer (layer close enough for the generated excitons to diffuse to the heterointerface) is converted to electrical energy:

silicon cells increase photonic absorption with increasing thickness, but OPV's do not.<sup>13</sup>

### 1.2.2. The First Organic Solar Cells

In a heterojunction device, there is a photoactive material and a semiconductive material, which form two layers between the metal electrodes.<sup>7</sup> A typical heterojunction solar cell assembly is depicted below in **Figure 1.3** which shows the two active layers sandwiched between the metal-oxide and the metal electrodes. Once an electron is excited into the LUMO of the donor species, the electron may transfer from the LUMO of the photoactive species into the LUMO of the acceptor species provided the energies are similar (see **Figure 1.2**). The most commonly used acceptors in the heterojunction device were materials with high electron affinities. Since the efficiency of the device is intrinsically dependent on the separation of the exciton at the heterojunction interface, the interface became an important device parameter for further investigation. Ideally, increasing the interfacial contact area should lead to an increase in efficiency provided the absorbance of photons is unaltered.

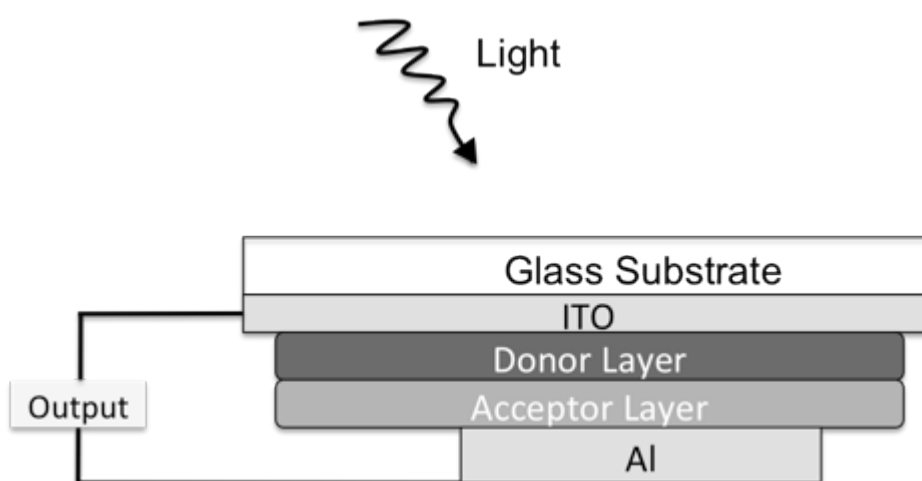


**Figure 1.3.** Device assembly of a heterojunction solar cell.

### 1.2.3. The Bulk Heterojunction

Once it was discovered that  $C_{60}$  effectively quenched any excitons nearby, fullerenes became the standard acceptors for OPVs.<sup>14, 15</sup> The ability for the  $C_{60}$  to separate the excitations is due to its high electron affinity, and because it has a LUMO with a lower band gap than that of the typical polymers used in OPV devices.<sup>6, 16, 17</sup> This quenching only happens at the interface of polymer and fullerene as mentioned previously; this drove researchers to study the interface of the two materials. In 1995, two reports of a new processing technique for the bi-layered heterojunction devices appeared. The techniques involved solution casting a blend of the donor and acceptor into one, phase separated layer (**Figure 1.4**). This phase separated blend was referred to as a bulk heterojunction (BHJ).<sup>15, 18</sup> With the two materials interspersed with one another, a bi-continuous network of donor/acceptor was formed. This network proved to be one of the biggest advancements in OPV's increasing the PCE for P3HT/PCBM devices into the 4% range. The bulk mixing of the donor and acceptor species effectively increases the interfacial area between the polymer donor and the fullerene acceptor species, resulting in more efficient dissociation of the bound electron-hole pair upon excitation.

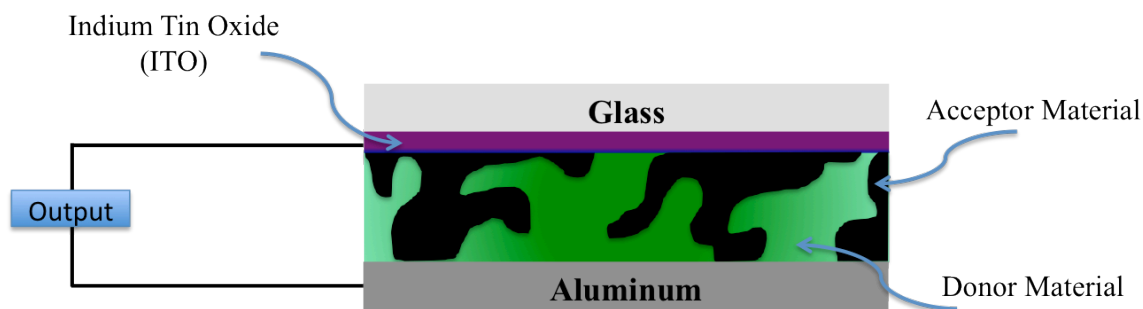


**Figure 1.4.** Bulk heterojunction photovoltaic device. The active layer consists of two phase-separated materials (polymer donor in blue; fullerene acceptor in gray).

### 1.2.4. Materials

Following the incorporation of semiconducting polymers, researchers began to explore the effects of different polymers on device performance. Some common donor/acceptor materials are shown in **Figure 1.5**. The most common hole-conduction polymers are P3HT, PFB (poly(9,9-dioctylfluorene-co-bis-N,N'-(4-butylphenyl)-bis-N,N'-phenyl-1,4-phenylenediamine)), and MDMO-PPV (poly[2-methoxy-5-(3,7-dimethyloctyloxy)]-1,4-phenylenevinylene). Common electron-conducting materials include PCBM, CN-MEH-PPV (poly-[2-methoxy-5-(2'-ethylhexyloxy)-1,4-(1-cyanovinylene)-phenylene]), and F8TB (poly(9,9'-dioctylfluorene-co-benzothiadiazole)).<sup>19-</sup>

21

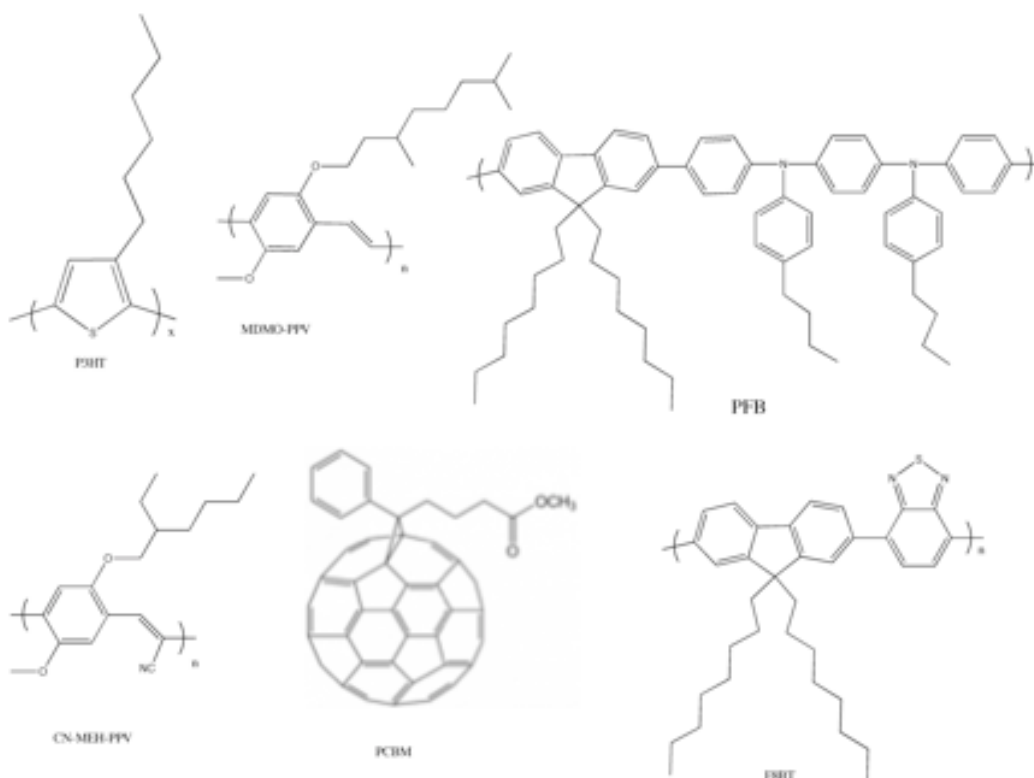


**Figure 1.5.** Several conjugated polymers used in OPV devices. Upper row are hole-conducting materials. Bottom row are electron-conducting materials.<sup>19-21</sup>

Of these materials, P3HT is the most widely used p-type polymer because it has charge mobilities of up to  $0.1 \text{ cm}^2 \text{ V}^{-1} \text{ s}^{-1}$  and because conjugation lengths are relatively long due to self-organization of the regioregular chains.<sup>22-24</sup> However, its inability to absorb photons of wavelength over 650 nm limits this system.<sup>25</sup> As a result, research is beginning to afford new semiconducting polymers with even better mobilities, absorptions and efficiencies. Some of these polymers are shown below in **Figure 1.6**. For the best P3HT device, efficiencies of 5% are recorded.<sup>26, 27</sup> New polymers have raised the PCE up to 6.1% recently. Poly(2-(5'-(5'',6''-bis(octyloxy)-4-(thiophen-2'-yl)benzo[*c*][1,2,5]thiadiazol-7-yl)thiophen-2-yl)-9-octyl-9*H*-carbazole) (**HXS-1**) was found to have hole mobilities of  $\sim 1 \times 10^{-4} \text{ cm}^2 / (\text{V} \cdot \text{sec})$  by Bo et. al. boasting PCE's of 5.4%.<sup>28</sup> This increase in efficiency was attributed to the ability of the HXS-1 polymer to stack together better due to its planar structure: the stacking allowed for more efficient charge hopping, thus reducing recombination and increasing the overall photocurrent. Also, the optical band gap for this polymer was found to be 1.95 eV, which is lower than the typical band gap of P3HT ( $\sim 2 \text{ eV}$ ). Yu et. al. synthesized a conjugated polymer based on alternating thieno-[3,4-*b*]thiophene and benzodithiophene units (**PTB1**) and reported absorption coefficients of  $7.5 \times 10^{-3} \text{ nm}^{-1}$  at 690 nm and optical band gaps of  $\sim 1.62 \text{ eV}$ . The PTB1 polymer exhibited a red-shifted absorption maximum around 690 nm, which is close to the maximum photon flux of the solar spectrum (700 nm).<sup>25</sup> A conjugated polymer consisting of alternating electron-rich bithiophene and electron-deficient thiadiazoloquinoxaline units (**PBTTQ**) was synthesized by Zoombelt et al. recently. The PBTTQ was found to have an even lower band gap than the PTB1 at  $\sim 0.95 \text{ eV}$ . This

polymer has a max absorption around 1165 nm which is well above the solar flux max.<sup>29</sup> Although this material would provide poor efficiency by itself, it could be used in solar cells where various polymer heterojunctions with different absorption maxima are arranged in tandem. This technique has afforded overall PCEs of up to 6.5%.<sup>30, 31</sup>

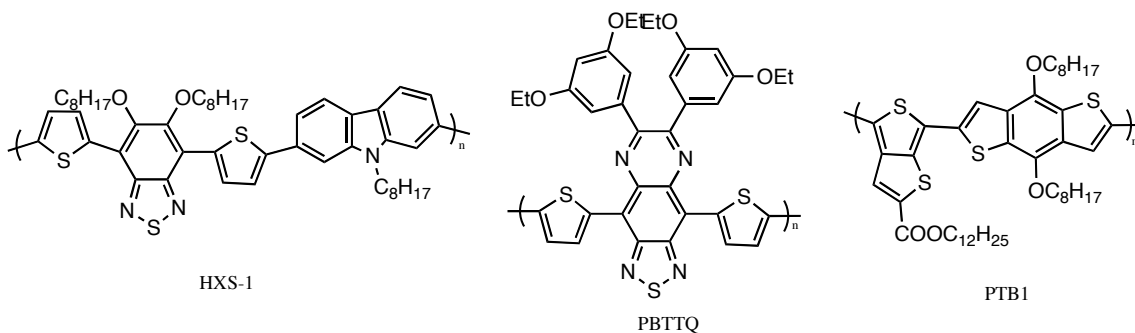


**Figure 1.6.** Chemical structures of new conjugated polymers used in OPV cells for enhanced performance.<sup>30, 31</sup>

### 1.2.5. Polymeric Materials for OPV Electrode Enhancement

The active layer is not the only area of OPV's that has attracted the attention of researchers. Even in BHJ devices the electrodes are an intensely studied area of PV's improved by the addition of dopants: materials that enhance the hole-transfer from polymer to anode.<sup>32</sup> Some of the most common doping agents are drawn below in

**Figure 1.7.** A notable improvement came when poly(3,4-ethylenedioxythiophene):poly(styrenesulfonate) (PEDOT:PSS) was applied to the ITO electrode. The PEDOT:PSS is used to increase open-circuit voltage and enhance hole collection.<sup>33-36</sup> However, PEDOT:PSS is known to corrode ITO at high temperatures because PSS is a strong acid.<sup>37-40</sup> As a result, Hains et al. developed a new anodic interfacial layer using a cross linked blend poly[9,9-dioctylfluorene-*co*-N-[4-(3'-methylpropyl)]-diphenyl-amine] (TFB) + 4,4-bis[*p*-trichlorosilylpropylphenyl]phenylamino]biphenyl (TPDSi<sub>2</sub>)

abbreviated TFB:TPDSi<sub>2</sub>. The TFB:TPDSi<sub>2</sub> forms a better conductive film than PEDOT:PSS because upon cross linking, the film is pinhole free and is homogeneously distributed on the ITO. The mobilities of devices using TFB:TPDSi<sub>2</sub> are approximately  $5 \times 10^{-4} \text{ cm}^2 / \text{V} \cdot \text{sec}$  compared to devices using PEDOT:PSS ( $1.0 \times 10^{-4} \text{ cm}^2 / \text{V} \cdot \text{sec}$ ).<sup>41</sup>

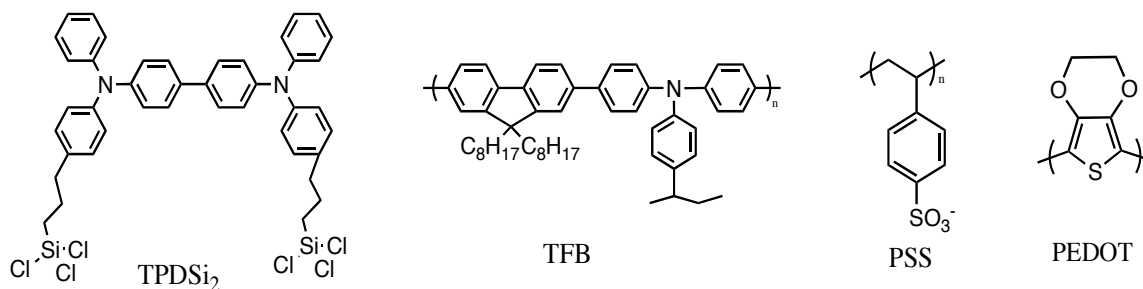


**Figure 1.7.** Structures of two dopants: left two make up the new TFB:TPDSi<sub>2</sub>; right two make up PEDOT:PSS.<sup>41</sup>

Instead of changing the dopant, Brett et al. are studying the effect of aligning the PEDOT:PSS on ITO slides. By allowing vapor phase triethoxy-2-thienylsilane to chemisorb onto hydroxy-functionalized ITO, the group was able to electro-polymerize PEDOT by using the ITO as the working electrode in a classical three-probe electrochemical cell. The result was a thin layer of ordered PEDOT:PSS covalently bound to the ITO electrode (**Figure 1.8**). An increase in PCE (from 1 to 1.5%) was observed for a P3HT:PCBM device.<sup>42</sup>

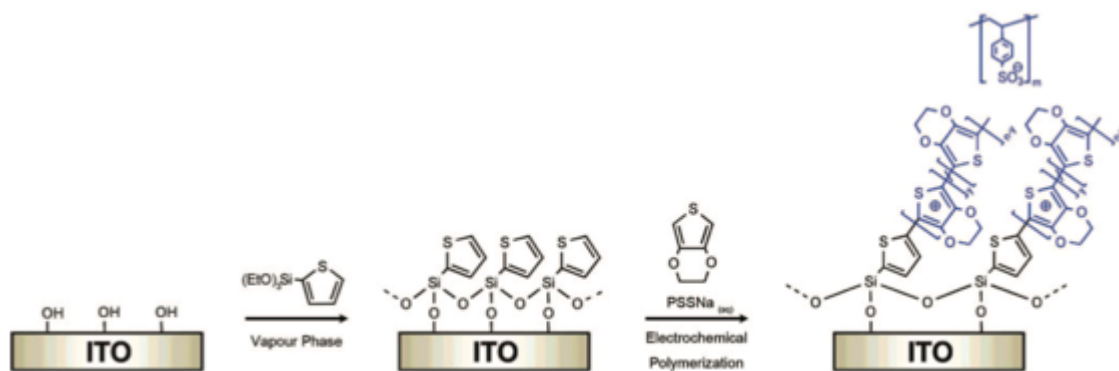


**Figure 1.8.** The schematic of electropolymerizing ordered PEDOT:PSS onto ITO electrodes in OPV devices. Copied with permission from reference 42.

Polymers have begun to show great promise in the enhancement of organic photovoltaic devices. Polymeric components have been incorporated, to some extent, into nearly every aspect of OPV devices in attempts to produce inexpensive, efficient solar cells for next generation energy sources. Only a small discussion of polymeric materials in OPV's has been presented, as the possibilities are vast and the potential of OPV's utilizing polymers is motivating. Although limitless opportunities for polymeric components exist in the overall device architecture of solar cells, for the purposes of this work, the focus was on the improvement of the bulk heterojunction via interface / domain customization.

### ***1.3. Polymers in Batteries***

Polymeric materials have been widely studied for use in energy storage devices. Pressure from industries to create robust, lightweight, and high energy density devices have jumpstarted the lithium polymer battery arena during the last decade. To meet demands, polymeric materials have been incorporated in several ways to improve the

performance and safety of batteries for consumer products: 1.) Polymeric electrolytes are often incorporated to reduce the need for flammable liquid electrolytes, 2.) Polymer separators with safety cutoff mechanisms are incorporated to prevent thermal run away and internal shorting, 3.) And polymeric housings have been developed to reduce the weight of battery packs and to reduce flammability in the event of internal combustion. The work in this discussion will focus only on the first two aforementioned applications. Polymeric separators/electrolytes not only add thermal stability to the device, but allow for flexible devices as well. Since the polymeric membranes are ionically conducting, but electrically insulating, they physically prevent the electrodes from shorting while still allowing for high ionic mobility. This allows for the development of flexible batteries, as no external casing is needed to prevent electrode contact. Additionally, the polymer separator/electrolyte reduces weight, resulting in batteries with high energy densities. A schematic of a typical lithium polymer battery is depicted in **Figure 1.9** below.

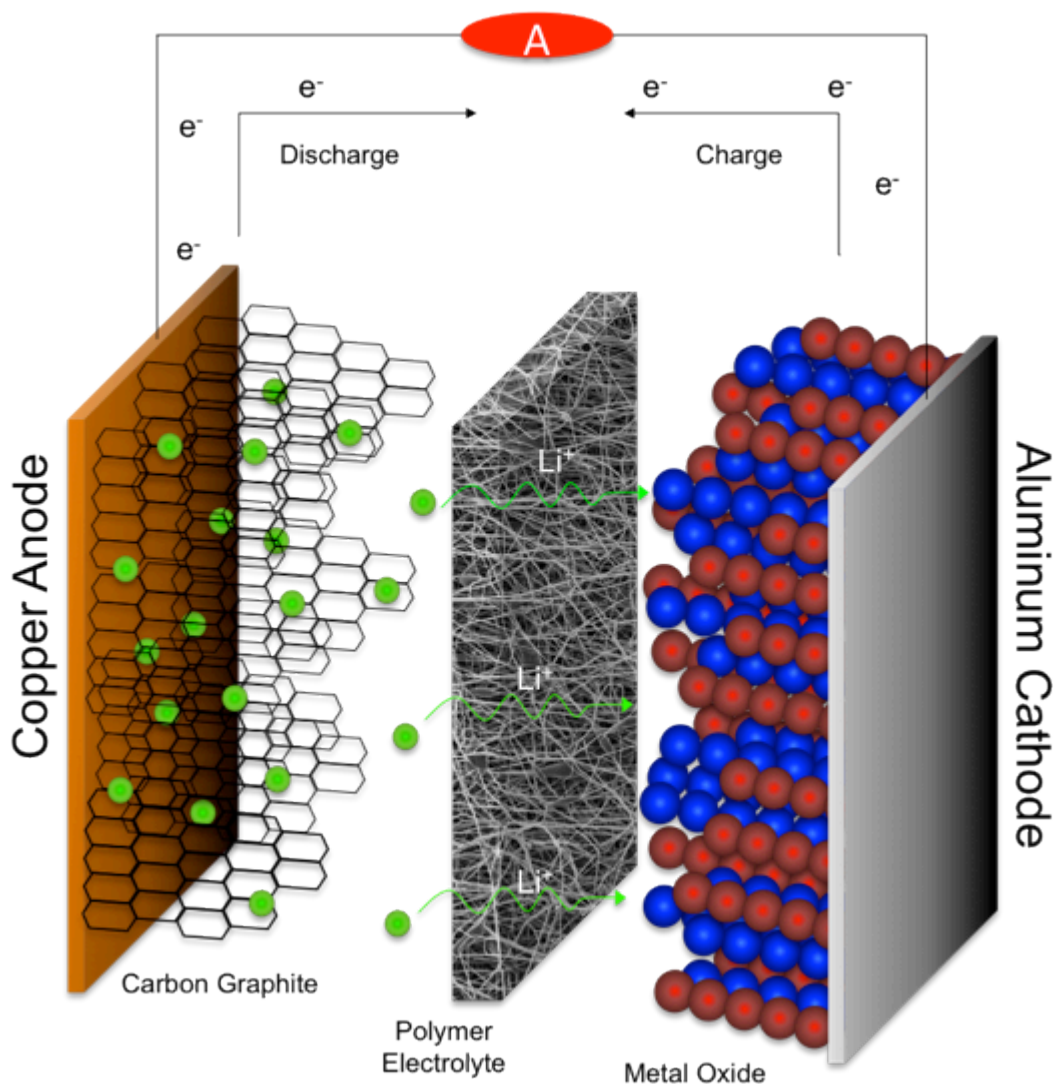


**Figure 1.9.** Schematic of a typical lithium polymer battery. Depicted in the schematic is an electrospun polymeric membrane. The polymeric component may have several different morphologies.

In 2000 Scrosati and Vincent divided polymer electrolytes into five distinct categories:<sup>43</sup> **Class 1:** amorphous macromolecular salt complexes (Usually polyethers), **Class 2:** Plasticized systems, in which small amounts of low molar mass polar liquids are added to class 1 polymer electrolytes, **Class 3:** Gel-electrolytes, formed by incorporating

a nonaqueous electrolyte solution within an inactive structural polymeric matrix, **Class 4:** Polymer-in-salt or rubbery electrolytes, in which high molar mass polymers are dissolved in low temperature molten salt mixtures, **Class 5:** Composites, based on the addition of nanoparticulate ceramics or dual-phase block copolymers. Jacob et. al. further elaborated on this classification in a 2003 publication, grouping polymer electrolytes according to the dominant conduction mechanism.<sup>44</sup> In this paper Jacob groups classes 1 and 2 together as their main conduction mechanism is coupled to the relaxation of the host polymer, while classes 3-5 have conductivities decoupled from the polymer's thermal characteristics. This review will focus on three simplified classifications **1.)** solid polymer electrolytes (containing classes 1 and 5 essentially), **2.)** separator membranes, and **3.)** polymer-gel electrolytes (consisting of Classes 2 and 3). The polymer-in-molten-salt complexes are more akin to lithium ion (liquid like) batteries and therefore will not be included.

### ***1.3.1. Solid Polymer Electrolytes (SPEs)***

SPEs are ionic-conducting single phase systems based on polymer-salt complexes. No liquid components are present, be they additives or solvents. These electrolytes can be prepared from solvent casting, extrusion, lamination, hot pressing, or *in situ* polymerization. Polymeric materials first began to gain attention as potential electrolytes for energy storage when Fenton, Parker, and Wright first reported salt complexation of PEO and sodium / potassium salts in 1973.<sup>45</sup> In the years following Wright's findings, significant research was conducted to investigate these materials. Because the electrolytes typically consisted of a lithium salt dissolved into a solid polymeric matrix,

they were referred to as solid polymer electrolytes (SPE). A major advantage of SPEs is that they serve two principle roles in batteries. SPEs act as traditional electrolytes in that they are the medium for ionic transport; however, they also function as a separator, electrically insulating the anode from the cathode. Following Wright, early work with SPEs mainly focused on polyesters, [poly(ethylene oxide) and poly(propylene oxide)] due to the electron donating capabilities of the oxygen units along the polymer backbone. PEO is a semi-crystalline polymer with a glass transition temperature ( $T_g$ ) and a melting point ( $T_m$ ) around  $-60\text{ }^\circ\text{C}$  and  $65\text{ }^\circ\text{C}$  respectively. Due to its high dielectric constant and the electron donating ether oxygens, PEO is able to dissolve lithium salts within the amorphous regions. The ionic conduction is generally believed to be based on an oxygen-assisted hopping mechanism within the amorphous region above the  $T_g$ , where long-range segmental motion of the polymer chains is allowed (**Figure 1.10**). The conductivity is relatively low at room temperature due to the semi-crystalline nature of polyethers below  $T_m$ . Thus, the vast majority of research involving these systems focuses on reducing the crystallinity and on enhancing segmental chain motion within the amorphous domains. Unfortunately, reduction of the crystalline phase (and subsequent increase in amorphous phase) often has the undesirable consequence of deteriorating the mechanical properties. Furthermore, the amorphous phases are metastable and undergo crystallization over time, resulting in a reduction in conductivity.<sup>46</sup>

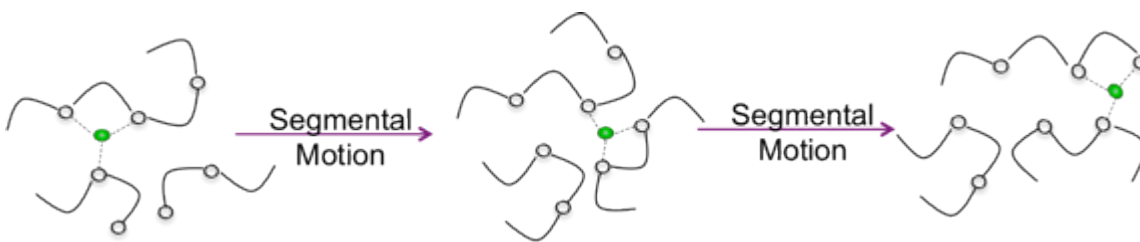


**Figure 1.10.** Schematic of the segmental chain motion involving PEO and lithium ions (green sphere). The dashed lines between the PEO oxygens and the lithium ions represent the coordination from electron density donation.

Interestingly, the belief that  $\text{Li}^+$  transport occurs most efficiently in the amorphous domains of PEO in solid polymer electrolytes is being challenged. Early work with polyether SPEs has demonstrated that multiple crystalline domains exist in PEO:LiX films (where X=  $\text{ClO}_4$ ,  $\text{PF}_6$ , TFSI and others).<sup>47, 48</sup> The three most notable, and most prevalent, crystalline structures are  $\text{EO}_6$ :LiX,  $\text{EO}_3$ :LiX and pure PEO crystallites. X-ray powder diffraction and *ab initio* calculations suggest that the  $\text{PEO}_6$ :LiX structure exists as a pair of PEO chains in cylindrical tunnels in which  $\text{Li}^+$  ions are coordinated with the ether oxygens on the inside of the tunnel while the anion remains on the outside of the tunnel (**Figure 1.11**). Multiple cylinders then align together with columns of anions in between.<sup>49-55</sup> Bruce et al. show that by selecting specific molecular weights of PEO and controlling the lithium salt concentration during film casting,  $\text{EO}_6$ :LiSbF<sub>6</sub> can be attained free from contamination by amorphous material. They observed that the ionic conductivity of the  $\text{PEO}_6$ :LiSbF<sub>6</sub> crystalline material is higher than the amorphous film.<sup>52</sup> Although no evidence exists to suggest that there is  $\text{Li}^+$  transport through pure PEO crystalline domains, the  $\text{EO}_3$ :LiX crystalline domain shows ionic diffusion as well. Unlike the  $\text{PEO}_6$ :LiX that has two PEO chains in a cylinder, the  $\text{EO}_3$ :LiX adopts a single

chain helical structure with  $\text{Li}^+$  ions residing within each turn of the PEO chain, coordinated with 3 ether oxygens.<sup>55</sup> Similar to the 6:1 samples, the  $\text{PEO}_3:\text{LiX}$  samples exhibit increased ionic conductivity within a limited temperature range.<sup>56</sup> Although the ionic conductivity may be improved with PEO:LiX crystalline structures in very limited temperature ranges, overall, the major contribution to ionic diffusion seems to be primarily in the amorphous domains when considering typical operating temperature ranges.

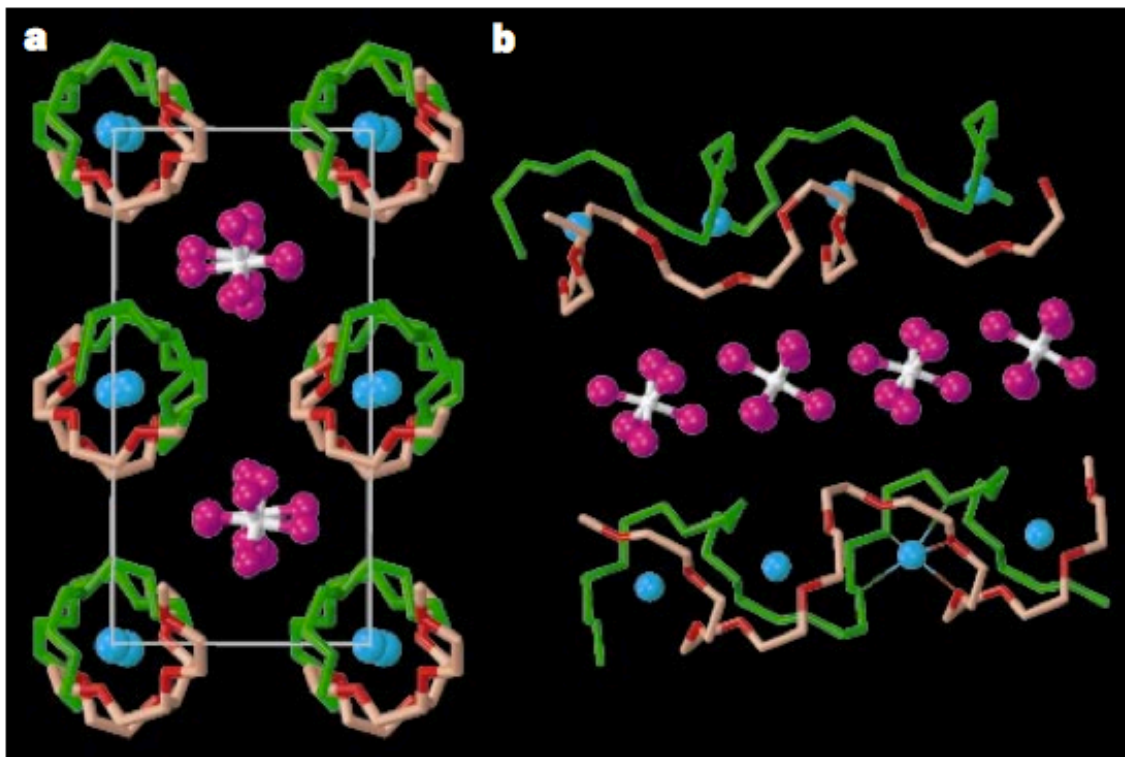


**Figure 1.11.** The structure of  $(\text{ethylene oxide})_6:\text{LiAsF}_6$ , hydrogen atoms not shown. **a**, View of the  $\text{PEO}_6:\text{LiAsF}_6$  structure along  $a$ , showing rows of  $\text{Li}^+$  ions perpendicular to the page. Blue spheres, lithium; white spheres, arsenic; magenta spheres, fluorine; light green, carbon in chain 1; dark green, oxygen in chain 1; pink, carbon in chain 2; red, oxygen in chain 2. **b**, View of the structure showing the relative positions of the chains and their conformations. Thin lines indicate coordination around the  $\text{Li}^+$  cation. The lithium-ether oxygen distances ( $\text{\AA}$ ) for chain 1 are 2.07(5), 2.26(4), 2.28(4); for chain 2 they are 2.05(5), 2.14(6). (Image copied with permission from reference 50)<sup>50</sup>

Other polyethers have been employed as SPE membranes for lithium batteries including poly(ethylene oxide-methylether) methacrylate (PEOMA), and poly(ethylene

glycol) alkylacrylate, all showing conductivities similar to those of the PEO-salt complexes.<sup>57</sup>

Polymeric electrolytes based on polymerized ionic liquids has recently been proposed.<sup>58</sup> Ohno and coworkers were able to synthesize an ionic liquid polymer with an organoboron unit (**Figure 1.12**). This polymer was able to anion exchange with LiTFSI up to 90%. The resulting electrolyte exhibited ionic conductivities of up to  $3.74 \times 10^{-5}$  S/cm but more importantly, the transference number (ratio of anionic diffusion to cationic diffusion) was determined to be up to 0.87. A transference number of 1 indicates equal diffusion (or mobilities) of both anionic and cationic species. As the transference number increases past 1, the cationic species travels faster through the given medium and the reverse is true as the transference number decreases from unity. This high transference number suggests anion trapping which could have a huge impact on battery performance and will be mentioned in the concluding section of this discussion.<sup>59</sup>

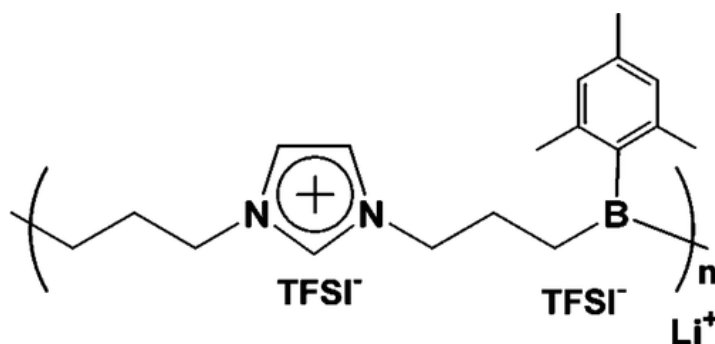


**Figure 1.12.** Polymerization product of 1,3-diallylimidazolium bromide and mesitylborane dimethyl sulfide complex after anion exchange.<sup>59</sup>

The biggest disadvantage of the SPE is the inherently low room temperature ionic conductivity, which effectively translates to low ionic mobility. An SPE has an ionic

conductivity around 1/100th the conductivity of a typical lithium solution electrolyte. As a result of their low ionic conductivity, the charge and discharge capabilities of SPEs is often too low for consumer products at ambient temperatures. Consequently, research shifted quickly to using porous polymeric membranes as separators housing an ionically conducting liquid electrolyte.

### ***1.3.2. Polymeric Separators***

In contrast to SPEs, polymeric separators have little or no contribution to ionic conductivity. Insoluble polymeric membranes are supplemented with a liquid, lithium containing electrolyte and subsequently sandwiched between an anode and cathode. As a result of having a highly mobile liquid electrolyte phase, the conductivities of devices prepared with swollen separator membranes are much higher than the SPE counterparts. Separator membranes must have a precisely controlled structural architecture in order to ensure efficient diffusion pathways for the liquid electrolyte and charge carriers. Since the polymer separator does not significantly interact with charge carriers in electrolyte solutions, diffusion pathways throughout the membrane represent the only means of translation for the charge carriers (**Figure 1.13**).

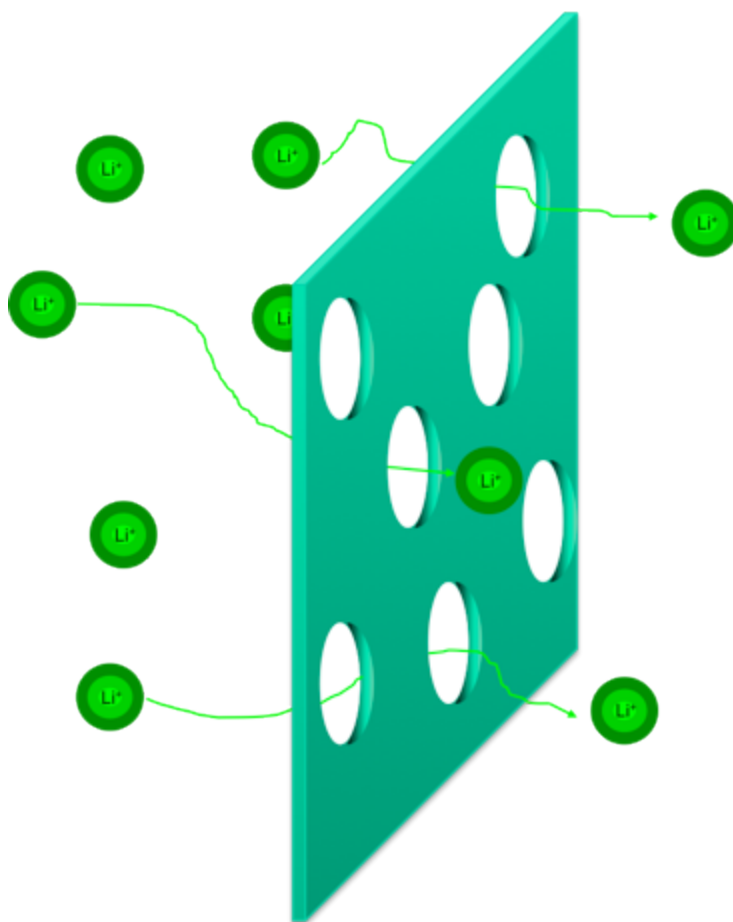


**Figure 1.13.** Polymeric separator cartoon. Lithium ions diffuse through the polymeric membrane using pores within the film. Not shown in the cartoon are the solvent molecules that interact with lithium salts.

These pathways are often incorporated as pores through processing techniques including melt stretching, phase-inversion, electrospinning and salt leaching. The vast majority of polymeric separator membranes in the literature (and in the marketplace) focus on polyolefins, mainly polyethylene (PE) and polypropylene (PP). Other polymers that have been suggested include nylon, poly(tetrafluoroethylene) (PTFE), poly(vinyl chloride) (PVC), and even naturally occurring substances including rubber and wood.<sup>60</sup>

Essentially there are two techniques used to produce porous polyolefin films. The dry process involves melting a polyolefin resin, extruding it into a film, thermally treating the film to increase the size and number of crystalline lamella and then precisely stretching it to form tightly ordered micropores.<sup>61-64</sup> Although the discrete mechanisms for this phenomenon are beyond the scope of this discussion, briefly, rows of lamellae generated during the initial extrusion and annealing step are oriented such that upon stretching they form “shish kabob” - type structures resulting in pores (**Figure 1.14**).

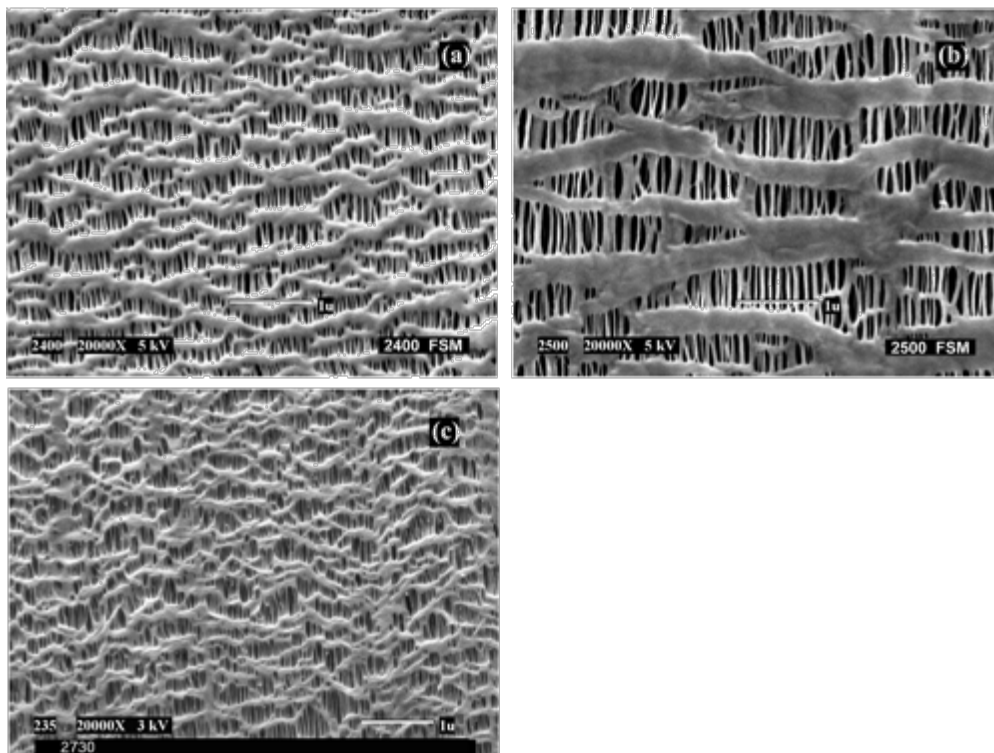


**Figure 1.14.** An SEM image of microporous polyethylene produced from the thermal annealing and subsequent stretching technique adopted by Celgard<sup>®</sup>. Image copied with permission from reference 60.<sup>60</sup>

The wet process consists of three steps **1.**) mixing of the polymer, a paraffin oil, additives, and antioxidants into a homogenous solution, **2.**) extrusion of that solution into

a gel-like film, and 3.) extraction of the paraffin oil and any other additives using a volatile solvent. Unlike the dry process, the wet processed films have similar mechanical properties in all directions due to lack of alignment from stretching.<sup>65</sup> This process is less reliable, however, as the pores created are often heterogeneously distributed throughout the film. **Figure 1.15** below is an SEM image of a microporous membrane produced from a wet process.<sup>66</sup> This inhomogeneity has severe consequences on ionic mobility and thus battery performance.

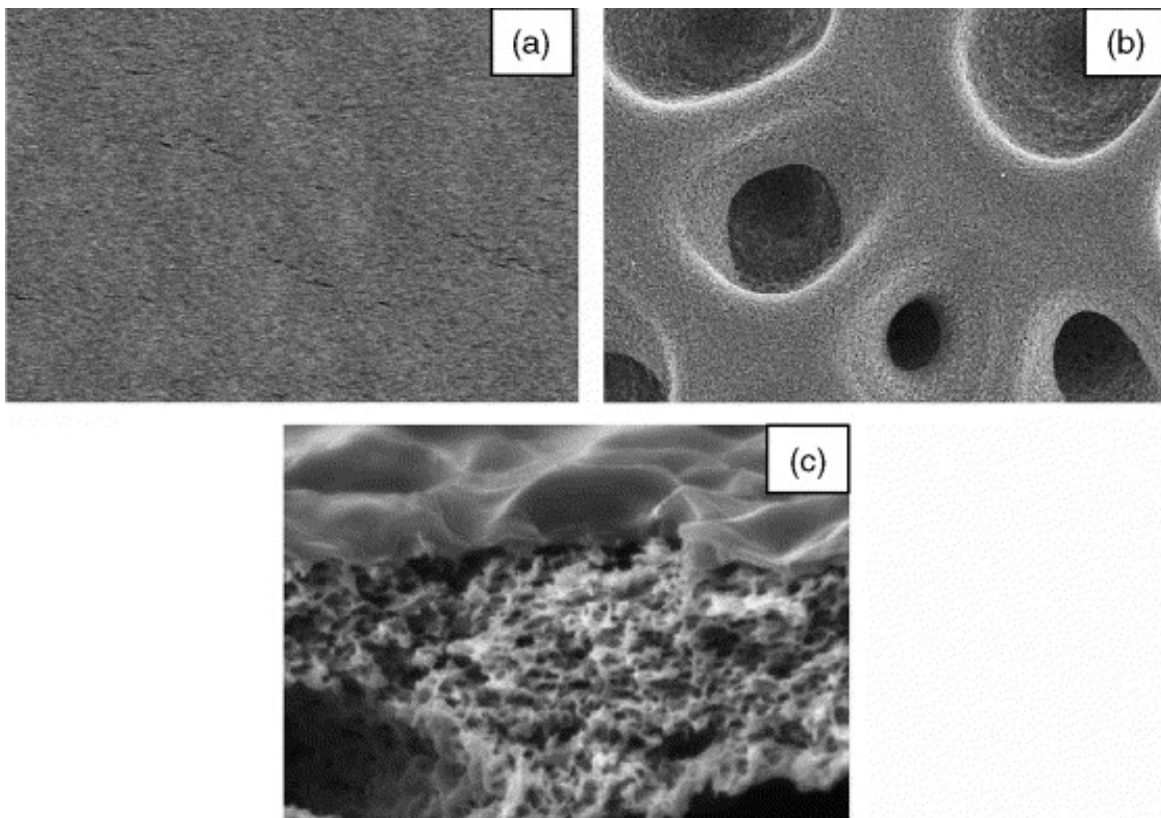


**Figure 1.15.** SEM image of a wet process microporous membrane **a.)** bottom of film (in contact with substrate), **b.)** top of film (in contact with air), **c.)** cross-section of film. Image copied with permission from reference 66.<sup>66</sup>

Major disadvantages of polymeric separators include the need for vast amounts of flammable liquid electrolytes, difficulty in absorbing aforementioned liquid electrolytes, and non-continuous pore structure hindering ionic mobility. The low ionic mobility prohibits lithium batteries with polymeric separators as viable energy devices for applications with high power demands. Although batteries assembled with polymeric separators often have slightly lower performance than pure liquid batteries, physically separating the electrodes with a flexible, lightweight polymeric membrane increases device safety, while maintaining and even increasing energy density by reducing the overall mass of the device. Due to the advantages polymeric separators have over pure liquid systems, they have gained monumental traction in portable and small-scale consumer technology and clearly the safety of these materials outweighs the reduced power output. In an effort to overcome the poor liquid electrolyte uptake and thus low ionic mobility of polymer separator membranes, research has shifted to polymeric-gel electrolytes (PGEs).

### ***1.3.3. Polymeric-Gel Electrolytes***

In a polymeric-gel electrolyte, a polymeric membrane is swollen with a liquid electrolyte and a lithium salt similar to that of a separator membrane. A major difference here however, is that after swelling with the liquid electrolyte, the polymeric component in a PGE becomes a gel with weak mechanical properties. Due to this lack of mechanical stability, PGE's have difficulty behaving as a separator to prevent internal shorting in the event of compression. Stand-alone PGE's are unattractive and they are usually coupled with a separator or employed in devices with structural rigidity designed into the device

housing. Unlike SPEs, the polymeric component in a PGE has little interaction with the charge carrying species. Thus the polymeric component acts as an inert cage to house the liquid electrolyte, rendering the device safer in the event of a puncture by reducing leakage and formation of an aerosol of the liquid electrolyte. The relatively non-interacting nature of the polymeric component forces the charge carrying species (lithium ions) to travel through the liquid domains; thus the conductivity is dependent on the amount of liquid component available, similar to that of a separator membrane. Typically, PGEs have the ability to house up to 300 wt.% of a liquid electrolyte resulting in room temperature conductivities in the 1 mS/cm range. Several polymers have been investigated for use as PGEs in lithium batteries including poly(acrylonitrile), poly(methyl methacrylate), poly(vinyl chloride), poly(vinylidene fluoride), poly(vinylidene fluoride-hexafluoro propylene) and others.<sup>67</sup>

#### ***1.3.3.1 Polyacrylonitrile Polymeric-Gel Electrolytes***

PAN – based PGEs have shown interesting and promising properties in earlier work. In fully amorphous gels of PAN and LiClO<sub>4</sub>, a room temperature conductivity on the order of  $1 \times 10^{-3}$  S/cm at ambient temperature was observed.<sup>68</sup> In early research, Wanatanbe et al. suggested that the PAN host was inactive in the ionic transport mechanism. Their work shows that the high ionic mobility is related to the regions in the film with relatively low microscopic viscosities – likely due to molecularly dispersed plasticizers, chiefly ethylene carbonate. Additionally, the ionic conductivity increased with increasing EC content up to a molar ratio of 2. At molar ratios under 2, the plasticizing material has a significant effect on the conductivity. This effect is likely due

to the plasticizer's ability to influence the local viscosities of the PGE.<sup>69, 70</sup> The polar nitrile group on PAN has been suggested to interact with Li<sup>+</sup> ions, thus facilitating salt dissolution / dissociation, similar to PEO solid polymer electrolytes. Raman and IR spectroscopy has shown that the C≡N functional groups of PAN interact with Li<sup>+</sup>.<sup>71</sup> Unlike PEO, however, since PAN has no oxygen atoms, the polymer-ion interactions are weak, resulting in transference numbers of up to 0.7 when large anions are used (Bis(trifluoromethane)sulfonimide (TFSI) and Bis(trifluoromethylsulfonyl)methyl (TFSM)).<sup>67</sup> Although PAN films have several advantageous properties, including high room temperature ionic conductivity, electrochemical stability, and a high transference number, poor compatibility with lithium metal electrodes has eliminated PAN based electrolytes from Li<sup>+</sup> battery applications.<sup>67</sup>

### ***1.3.3.2 Poly(methyl methacrylate) Polymeric-Gel Electrolytes***

PMMA initially received attention due to its relatively large temperature stability window ranging from -110 to 240 °C.<sup>72</sup> Appetecchi and coworkers indicated that the electrochemical stability of PMMA gel electrolyte systems was dependent on the polymeric host and lithium salt composition. Additionally, a significant fraction of lithium is lost during cycling through degradative reactions with PMMA. This loss of lithium results in the need for a large excess of lithium in order to obtain batteries with sufficient lifetimes.<sup>73</sup> In 1993, Bohnke suggested that the ester substituents on PMMA are able to interact with metal cations and solvate them, similar to PAN and PEO. Investigation of conductivity and chain dynamics as a function of temperature further

supported this claim.<sup>74</sup> Homogeneous gels containing 15 wt.% PMMA have reached conductivities up to  $10^{-3}$  S/cm.<sup>73, 74</sup>

#### ***1.3.3.3. Poly(vinyl chloride) Polymeric-Gel Electrolytes***

PVC based polymeric-gel electrolytes have been investigated as it is commercially available, chemically stable, and has poor combustion properties. Despite these favorable characteristics and recent results suggesting Cl-Li<sup>+</sup> interactions, poor ionic conductivity limits its applicability in batteries.<sup>75, 76</sup> Blended films of PVC and PMMA have shown encouraging results with conductivities approaching the mS/cm range. Increasing the PMMA content resulted in an increase in the overall ionic conductivity.<sup>77-79</sup> Eventually, capacity fading from LiCl formation on the anode surface moved research to PVC's fluorinated counterpart.

#### ***1.3.3.4. Poly(vinylidene fluoride) Polymeric-Gel Electrolytes***

PVDF based electrolytes are perhaps the most widely studied gel type electrolytes for several reasons. With a dielectric constant of approximately 8.4, which aids in ionic dissociation, and the highly electronegative, electron withdrawing fluorine groups resulting in strong anodic stability, PVDF has emerged as the chosen polymer for PGE based lithium batteries.<sup>67</sup> Homogeneous gels of low PVDF composition and large amounts of liquid lithium containing electrolytes initially reached conductivities of up to  $1 \times 10^{-3}$  S/cm. A major advance in PVDF electrolyte performance was realized upon the migration from classical gels towards more structured polymer architecture. The idea was to form highly porous membranes of PVDF, then swell them with large amounts of

liquid electrolyte. Since it is generally believed that the ionic transport is mainly occurring in liquid rich domains, providing pathways (similar to separator membranes) would result in an increase in the overall conductivity.<sup>80, 81</sup> Further investigation into the solution behavior within PVDF membranes elucidated interesting results. Initially, the electrolyte solution becomes trapped within the pores of the membrane. However, the solution penetrates the polymer matrix, swelling the polymer chains. Over time, a continuous exchange of liquid between the pores and the polymeric domains results in a gelatinous equilibrium state. In PVDF membranes with heterogeneously dispersed pores, the ionic conductivity increases until an equilibrium is reached in a homogeneous gel state.<sup>82, 83</sup> However, in membranes with controlled or continuous porous pathways through the film, the opposite effect is observed.<sup>82, 83</sup>

### ***1.3.3.5 Poly(vinylidene fluoride - co - hexafluoropropylene) Polymeric-Gel Electrolytes***

Incorporation of hexafluoropropylene (HFP) in a copolymer with PVDF results in a lower degree of crystallinity and greater absorption of liquid electrolyte. Typical PVDF-HFP copolymers with between 12 and 19 mol% HFP are sold commercially (Kynar Flex, Solef, F-26) and exhibit  $T_m \sim 130-140$  °C, and  $T_g$  from -40 to -35 °C. Higher HFP content (Fluorel, Vitron A, SKF-26) results in completely amorphous materials with  $T_g$  in the range of -22 to -29 °C.<sup>84</sup> Room temperature conductivities of up to  $7.94 \cdot 10^{-3}$  S/cm have been achieved using a PDVF-HFP copolymer and PVA dissolved into DMF, cast over a glass support and then washed with water to remove the PVA. This process results in a microporous structure consisting of up to 85% porosity, and ~90 % electrolyte uptake. When swollen with a 1M LiClO<sub>4</sub> solution of EC-DEC (1:1 vol.

ratio), these membranes exhibit some of the highest ionic conductivities reported for these systems.<sup>85</sup>

With the exception of the PAN system, the polymers used in PGE's have little influence on the diffusion / transport / dissociation properties of the charge carrying species of interest ( $\text{Li}^+$ ). Instead, the morphology of the polymeric component along with the liquid electrolyte characteristics dominate the ionic conductivity properties of PGE's. The work detailed in the following sections involving polymer electrolytes for lithium batteries focuses on designing a system in which the polymeric component influences the ionic diffusion characteristics in the hopes of creating high performance electrolytes for fast charge / discharge applications.

#### 1.4. References

1. A. Goetzberger, C. Hebling and H.-W. Schock, *Materials Science and Engineering: R: Reports*, 2003, **40**, 1-46.
2. G. A. Chamberlain, *Solar Cells*, 1983, **8**, 47-83.
3. C. J. Brabec, N. S. Sariciftci and J. C. Hummelen, *Advanced Functional Materials*, 2001, **11**, 15-26.
4. P. Peumans, A. Yakimov and S. R. Forrest, *Journal of Applied Physics*, 2003, **93**, 3693-3723.
5. M. A. Green, K. Emery, Y. Hishikawa and W. Warta, *Progress in Photovoltaics: Research and Applications*, 2008, **16**, 61-67.
6. H. Spanggaard and F. C. Krebs, *Solar Energy Materials and Solar Cells*, 2004, **83**, 125-146.
7. C. W. Tang and A. C. Albrecht, *The Journal of Chemical Physics*, 1975, **62**, 2139-2149.
8. C. W. Tang, *Applied Physics Letters*, 1986, **48**, 183-185.
9. J. K. Lee, W. L. Ma, C. J. Brabec, J. Yuen, J. S. Moon, J. Y. Kim, K. Lee, G. C. Bazan and A. J. Heeger, *Journal of the American Chemical Society*, 2008, **130**, 3619-3623.
10. B. A. Gregg and M. C. Hanna, *Journal of Applied Physics*, 2003, **93**, 3605-3614.
11. B. A. Gregg, *Chemical Physics Letters*, 1996, **258**, 376-380.
12. H. Nakamura, M. Saito, T. Kusumoto, T. Yasuda and T. Tsutsui, *Applied Physics Express*, **1**, 021802.
13. M. M. Mandoc, L. J. A. Koster and P. W. M. Blom, *Applied Physics Letters*, 2007, **90**, 133504.
14. J. Nelson, *Current Opinion in Solid State and Materials Science*, 2002, **6**, 87-95.
15. G. Yu, J. Gao, J. C. Hummelen, F. Wudl and A. J. Heeger, *Science*, 1995, **270**, 1789-1791.
16. N. S. Sariciftci, L. Smilowitz, A. J. Heeger and F. Wudl, *Synthetic Metals*, 1993, **59**, 333-352.
17. R. H. Friend, G. J. Denton, J. J. M. Halls, N. T. Harrison, A. B. Holmes, A. Köhler, A. Lux, S. C. Moratti, K. Pichler, N. Tessler and K. Towns, *Synthetic Metals*, 1997, **84**, 463-470.
18. J. J. M. Halls, C. A. Walsh and N. Greenham, *Nature*, 1995, **376**, 498-500.
19. H. Hoppe and N. S. Sariciftci, *Journal of Materials Research*, 2004, **19**, 1924-1945.
20. J. H. Burroughes, D. D. C. Bradley, A. R. Brown, R. N. Marks, K. Mackay, R. H. Friend, P. L. Burns and A. B. Holmes, *Nature*, 1990, **347**, 539-541.
21. H. J. Snaith, A. C. Arias, A. C. Morteani, C. Silva and R. H. Friend, *Nano Letters*, 2002, **2**, 1353-1357.
22. P. J. Brown, H. Sirringhaus and R. H. Friend, *Synthetic Metals*, 1999, **101**, 557-560.
23. H. Sirringhaus, N. Tessler and R. H. Friend, *Science*, 1998, **280**, 1741-1744.
24. X. Yang, J. Loos, S. C. Veenstra, W. J. H. Verhees, M. M. Wienk, J. M. Kroon, M. A. J. Michels and R. A. J. Janssen, *Nano Letters*, 2005, **5**, 579-583.

25. Y. Liang, Y. Wu, D. Feng, S.-T. Tsai, H.-J. Son, G. Li and L. Yu, *Journal of the American Chemical Society*, 2008, **131**, 56-57.
26. C. H. Woo, B. C. Thompson, B. J. Kim, M. F. Toney and J. M. J. Fréchet, *Journal of the American Chemical Society*, 2008, **130**, 16324-16329.
27. B. C. Thompson and J. M. J. Fréchet, *Angewandte Chemie International Edition*, 2008, **47**, 58-77.
28. R. Qin, W. Li, C. Li, C. Du, C. Veit, H.-F. Schleiermacher, M. Andersson, Z. Bo, Z. Liu, O. Inganäs, U. Wuerfel and F. Zhang, *Journal of the American Chemical Society*, 2009.
29. A. P. Zoombelt, M. Fonrodona, M. M. Wienk, A. B. Sieval, J. C. Hummelen and R. A. J. Janssen, *Organic Letters*, 2009, **11**, 903-906.
30. G. Dennler, M. C. Scharber, T. Ameri, P. Denk, K. Forberich, C. Waldauf and C. J. Brabec, *Advanced Materials*, 2008, **20**, 579-583.
31. G. Dennler, H.-J. Prall, R. Koeppel, M. Egginger, R. Autengruber and N. S. Sariciftci, *Applied Physics Letters*, 2006, **89**, 073502.
32. D. S. Germack, C. K. Chan, B. H. Hamadani, L. J. Richter, D. A. Fischer, D. J. Gundlach and D. M. DeLongchamp, *Applied Physics Letters*, 2009, **94**, 233303.
33. L. S. Roman, W. Mammo, L. A. A. Pettersson, M. R. Andersson and O. Inganäs, *Advanced Materials*, 1998, **10**, 774-777.
34. M. Granstrom, K. Petritsch, A. C. Arias, A. Lux, M. R. Andersson and R. H. Friend, *Nature*, 1998, **395**, 257-260.
35. P. Peumans and S. R. Forrest, *Applied Physics Letters*, 2001, **79**, 126-128.
36. J. C. Scott, S. A. Carter, S. Karg and M. Angelopoulos, *Synthetic Metals*, 1997, **85**, 1197-1200.
37. S. H. Kwon, S. Y. Paik and J. S. Yoo, *Synthetic Metals*, 2002, **130**, 55-60.
38. C. Piliago, M. Mazzeo, B. Cortese, R. Cingolani and G. Gigli, *Organic Electronics*, 2008, **9**, 401-406.
39. S. Sapp, S. Luebben, Y. B. Losovyj, P. Jeppson, D. L. Schulz and A. N. Caruso, *Applied Physics Letters*, 2006, **88**, 152107.
40. C. Tao, S. Ruan, X. Zhang, G. Xie, L. Shen, X. Kong, W. Dong, C. Liu and W. Chen, *Applied Physics Letters*, 2008, **93**, 193307.
41. A. W. Hains and T. J. Marks, *Applied Physics Letters*, 2008, **92**, 023504.
42. D. A. Rider, K. D. Harris, D. Wang, J. Bruce, M. D. Fleischauer, R. T. Tucker, M. J. Brett and J. M. Buriak, *ACS Applied Materials & Interfaces*, 2008, **1**, 279-288.
43. B. Scrosati and C. A. Vincent, *MRS Bulletin*, 2000, **25**, 28-30.
44. M. M. E. Jacob, E. Hackett and E. P. Giannelis, *Journal of Materials Chemistry*, 2003, **13**, 1-5.
45. D. E. Fenton, J. M. Parker and P. V. Wright, *Polymer*, 1973, **14**, 589.
46. E. Quartarone and P. Mustarelli, *Chemical Society Reviews*, 2011, **40**, 2525-2540.
47. C. D. Robitaille and D. Fauteux, *Journal of The Electrochemical Society*, 1986, **133**, 315-325.
48. S. K. Fullerton-Shirey and J. K. Maranas, *Macromolecules*, 2009, **42**, 2142-2156.
49. Y. G. Andreev and P. G. Bruce, *Journal of Physics: Condensed Matter*, 2001, **13**, 8245.

50. S. G. MacGlashan, Y. G. Andreev and P. G. Bruce, *Nature* 1999, **398**, 2.
51. Z. Gadjourova, D. Martín y Marero, K. H. Andersen, Y. G. Andreev and P. G. Bruce, *Chemistry of Materials*, 2001, **13**, 1282-1285.
52. Z. Gadjourova, Y. G. Andreev, T. P. D. and P. G. Bruce, *Nature*, 2001, **412**, 3.
53. O. Borodin and G. D. Smith, *Macromolecules*, 2006, **39**, 1620-1629.
54. E. Staunton, Y. G. Andreev and P. G. Bruce, *Faraday Discussions*, 2007, **134**, 143-156.
55. Y. G. Andreev, P. Lightfoot and P. G. Bruce, *Chemical Communications*, 1996, 2169-2170.
56. M. Marzantowicz, J. R. Dygas, F. Krok, Z. Florjańczyk and E. Zygadło-Monikowska, *Electrochimica Acta*, 2007, **53**, 1518-1526.
57. J. W. Fergus, *Journal of Power Sources*, 2010, **195**, 4554-4569.
58. H. Ohno, *Electrochimica Acta*, 2001, **46**, 1407-1411.
59. N. Matsumi, K. Sugai, M. Miyake and H. Ohno, *Macromolecules*, 2006, **39**, 6924-6927.
60. P. Arora and Z. Zhang, *Chem Rev*, 2004, 4419-4462.
61. T. H. Yu, Virginia Polytechnic Institute and State University 1996.
62. M. B. Johnson and G. L. Wilkes, *Journal of Applied Polymer Science*, 2001, **81**, 2944-2963.
63. M. B. Johnson and G. L. Wilkes, *Journal of Applied Polymer Science*, 2002, **84**, 1762-1780.
64. M. B. Johnson and G. L. Wilkes, *Journal of Applied Polymer Science*, 2002, **83**, 2095-2113.
65. D. Ihm, J. Noh and J. Y. Kim, *Journal of Power Sources*, 2001, **109**, 5.
66. S. S. Zhang, *Journal of Power Sources*, 2007, **164**, 351-364.
67. M. S. A, *European Polymer Journal*, 2006, **42**, 21-42.
68. K. M. Abraham and M. Alamgir, *Journal of The Electrochemical Society*, 1990, **137**, 1657-1658.
69. M. Watanabe, M. Kanba, K. Nagaoka and I. Shinohara, *Journal of Polymer Science: Polymer Physics Edition*, 1983, **21**, 939-948.
70. M. Watanabe, M. Kanba, K. Nagaoka and I. Shinohara, *Journal of Applied Polymer Science*, 1982, **27**, 4191-4198.
71. Z. Wang, B. Huang, H. Huang, L. Chen, R. Xue and F. Wang, *Electrochimica Acta*, 1996, **41**, 3.
72. O. Bohnke, C. Rousselot, P. A. Gillet and C. Truche, *Journal of The Electrochemical Society*, 1992, **139**, 1862-1865.
73. G. B. Appetecchi, F. Croce and B. Scrosati, *Electrochimica Acta*, 1995, **40**, 991-997.
74. O. Bohnke, G. Frand, M. Rezrazi, C. Rousselot and C. Truche, *Solid State Ionics*, 1993, **66**, 105-112.
75. M. Alamgir and K. M. Abraham, *Journal of The Electrochemical Society*, 1993, **140**, L96-L97.
76. S. Ramesh and A. K. Arof, *Materials Science and Engineering: B*, 2001, **85**, 11-15.
77. N.-S. Choi and J.-K. Park, *Electrochimica Acta*, 2001, **46**, 1453-1459.

78. S. Ramesh, K. H. Leen, K. Kumutha and A. K. Arof, *Spectrochimica Acta Part A: Molecular and Biomolecular Spectroscopy*, 2007, **66**, 1237-1242.
79. A. Manuel Stephan, Y. Saito, N. Muniyandi, N. G. Renganathan, S. Kalyanasundaram and R. Nimma Elizabeth, *Solid State Ionics*, 2002, **148**, 467-473.
80. A. Bottino, G. Camera-Roda, G. Capannelli and S. Munari, *Journal of Membrane Science*, 1991, **57**, 1-20.
81. Y. Saito, H. Kataoka, C. Capiglia and H. Yamamoto, *The Journal of Physical Chemistry B*, 2000, **104**, 2189-2192.
82. H. Kataoka, Y. Saito, T. Sakai, E. Quartarone and P. Mustarelli, *The Journal of Physical Chemistry B*, 2000, **104**, 11460-11464.
83. Y. Saito, H. Kataoka and A. M. Stephan, *Macromolecules*, 2001, **34**, 6955-6958.
84. Y. V. Baskakova, O. V. Yarmolenko and O. N. Efimov, *Russian Chemical Reviews*, 2012, **81**, 367 - 380.
85. N. T. K. Sundaram and A. Subramania, *Journal of Membrane Science*, 2007, **289**, 1-6.

## Chapter 2

### Electrospinning for Controlled Polymeric Frameworks in Organic

#### Photovoltaic Devices

##### *2.1. Introduction*

Electrospinning (ES) is a process utilizing charge separation to form fibers with high aspect ratios (nanofibers). For a typical electrospinning setup (**Figure 2.1**), a polymeric solution is extruded through a needle/capillary that has been charged with a high potential: on the order of kV. The charges forming on the surface of the polymer solution as it leaves the needle tip repel each other. This charge forces the solution to spread out, thus reducing the coulombic repulsion.<sup>1</sup> This only happens if the surface charge is greater than the surface tension and thus requires kV potentials.<sup>2-4</sup> Once the charge on the solution surface overcomes the surface tension of the droplet, a tear drop/cone shaped configuration is adopted directly on the needle tip/capillary. This cone is referred to as the Taylor cone.<sup>5,6</sup> Immediately following the Taylor cone, the charged polymeric solution enters an instability region forcing the newly formed polymer jet to whip back and forth as the charges attempt to repel each other further. The polymer jet gains speed as the whipping motion becomes larger and larger and as the polymer jet accelerates toward the grounded counter electrode, the solvent evaporates and a solid polymer fiber is deposited on the substrate. There are many aspects of electrospinning that affect fiber size, and because we are interested in controlling the domain sizes of the active layer in OPV devices, the size of the fibers are of great importance. Parameters such as applied potential, potential bias (positive or negative), solution concentration,

flow rate, molecular weight, and distance of collecting substrate all play vital roles in the size and formation of fibers.<sup>7-9</sup>

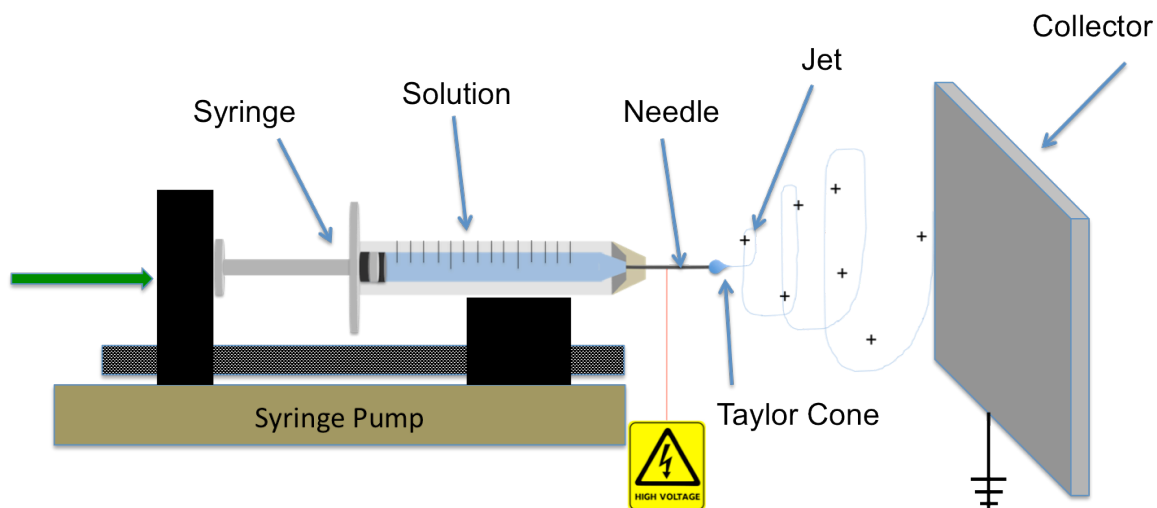


**Figure 2.1.** (Top) diagram of electrospinning setup: the syringe contains the polymeric solution and the needle is charged with electrical potential. The polymeric solution moves towards the collector forming first a Taylor cone, then a thin jet. (Bottom) actual images of fiber forming polymer solutions; right is Taylor cone, left is polymer jet/fiber.

## ***2.2. Electrospinning for Controlled Frameworks***

Electrospinning has gained the attention of researchers in a myriad of fields as it offers a unique, easy, reliable way to produce polymeric structures with tailored architecture. Tuning the various processing parameters can precisely control the properties of electrospun mats. The tunable properties of electrospun fiber mats include fiber diameter, fiber density, porosity, and average pore size to name a few. Additionally, the control does not stop on the macro-scale. The properties of the fibers

themselves are also easily controllable. Fiber composition, and fiber morphology (inner construction and surface construction) can be controlled by tuning processing parameters, allowing for a wide variety of architectures for many different applications. In the last decade, various polymers have been electrospun to create three-dimensional structures with controlled frameworks for tissue scaffolding, separator membrane technology, fuel cell membranes and electrode and electrolyte materials for energy storage devices. Each application utilizes the unique characteristics of fibrous membranes that electrospinning offers to optimize the properties of applied mats.

### ***2.2.1. Electrospun Mats for Tissue Scaffold Engineering***

Electrospun mats consisting of biocompatible polymers such as poly(ethylene oxide) (PEO), poly(caprolactone) (PCL) and poly(L-lactic acid) have been produced for tissue scaffolding applications. Tissue engineering has been recognized as an alternative to autografts or allografts for tissue repair / reconstruction.<sup>10, 11</sup> During tissue repair, the electrospun mats provide a unique structure offering a scaffold for new tissue to grow on while allowing nutrients and vascularization during the repair process due to the intrinsically porous structure of electrospun membranes.<sup>12</sup> Optimizing the diffusion of nutrients by controlling the porosity and pore size of the electrospun mats greatly improves the repairing process and reduces healing time. Additionally, as the compositions of electrospun membranes are easily controlled by controlling the compositions of the polymeric solution, spinning tissue scaffolds which contain vital therapeutic components also reduces healing time, reduces local swelling, and aids in more complete repair. Lastly, due to the ability to significantly alter the mechanical

properties of electrospun fiber mats by orientation, additives, or crosslinking, electrospun scaffolds can be tailored to simulate a variety of biological systems to allow for even more efficient tissue repair. It is easy to imagine a tissue scaffold that needs to be very flexible for the repair of a biological system such as muscle repair, and just as easy to imagine a system that requires a significantly more durable scaffold such as bone repair.<sup>13</sup>

### **2.2.2. Separator / Filtration Membranes**

Separator membranes have been developed from structured frameworks using electrospinning in the last few decades. Essentially, two key attributes can be used to describe the effectiveness of a separator / filter membrane: *Selectivity* – governed by surface properties of the membrane, and *Flux* – how fast solutes traverse the membrane. Electrospun membranes offer unique advantages in filtration and purification applications as they can be spun from polymers with affinities towards various contaminants, have tunable pore sizes, contain interconnected open pore structures, and have high gas permeability, thus the selectivity and flux may be tuned to nearly any specification by simple modification in the electrospinning procedure.<sup>14</sup> A three-tier composite structure incorporating poly(vinyl alcohol) showed up to 99.8% total organic solute rejection after crosslinking with glutaraldehyde.<sup>15</sup> Electrospun PAN membranes were demonstrated to be >99.9% selective for oily wastewater, while simultaneously boosting the flux to 1.3 L/m<sup>2</sup>h at 1psi.<sup>16</sup> Cellulose acetate electrospun nanofibrous membranes showed capture capacities of 13mg/g upon activation with Cibacron Blue F3GA.<sup>17</sup> Additionally, sterilization and sanitation additives can easily be incorporated into the electrospinning solution to further improve the quality of the filtrate.<sup>18</sup>

### ***2.2.3. Fuel Cell Membranes***

For the last three decades, significant attention has been focused on proton exchange membranes (PEMs) as alternative energy sources for transportation. Similar to energy storage devices, a charged species ( $H^+$ ) must diffuse through a solid membrane upon operation. As the pathway for that charged species improves, so to does the overall performance of the device. Uniaxial aligned electrospun sulfonated polyimide nanofibers have been reported to exhibit significantly higher proton conductivity in the parallel direction of the fibers. Additionally, the oxidative and hydrolytic stability were both enhanced due to fiber orientation.<sup>19</sup> An electrospun mat of partially sulfonated poly(ether sulfone), when impregnated with Nafion<sup>®</sup> showed proton conductivities nearly twice that of a pure Nafion<sup>®</sup> film.<sup>20</sup> Sulfonated poly(arylene ether sulfone) electrospun mats were also reported to have proton conductivities similar to neat Nafion 117 samples but proved to have lower oxygen permeability.<sup>21</sup>

### ***2.2.4. Energy storage devices***

As mentioned previously in the introduction, polymers have found application in many areas of energy storage. Electrospinning has recently resulted in polymeric components with even further enhanced characteristics for battery applications. Polymers such as PVDF and PVDF-HFP along with PAN and PMMA have been electrospun and investigated as potential electrolytes for lithium batteries. These systems will be discussed further in chapter 3.

## ***2.3. Electrospinning in Organic Photovoltaics (OPVs)***

One of the major issues with flexible solar energy harvesting systems (OPVs) stems from the inefficiency of the devices. Although OPVs have several advantages over classical silicon based PV devices – flexibility, reduced cost, reduced weight – these advantages simply do not overcome the efficiency short falls of OPVs when compared to the efficiency of traditional devices. Unlike silicon based solar cells where the electron and the hole both travel through the same media (silicon), in OPV devices, the excited electron and the Columbicly bound hole must travel together until they reach the donor/acceptor interface. Following dissociation, the electrons travel through a p-type, electron-accepting domain, while the holes travel through the n-type, electron-donating domain. As such, a limiting factor in an OPV device's efficiency involves the diffusion of the exciton to the heterojunction and subsequent dissociation of the exciton at the n/p or donor/acceptor interface.

In OPV devices, since the donor domain is chemically different from the acceptor domain, the interface (referred to as the bulk heterojunction – BHJ) is extremely important in the efficiency of the devices. As such, the morphology of the BHJ has been widely studied and is a major focus for improving OPV device performance. Quickly, it became very clear that not only is the donor/acceptor interface important, but that the morphology of each domain was of extreme importance for device performance. Several processing techniques have been employed over the years to tailor/optimize the morphologies of the discrete domains within a bulk heterojunction. Of several promising techniques, electrospinning has emerged as an effective way to produce active layers in the BHJ with unique and reproducible morphologies. Additionally, the morphologies of

BHJ domains can be altered easily by adjusting processing parameters quickly and effectively.

Our work in this area focuses on utilizing electrospinning to develop a completely bi-continuous BHJ that has very small polymer (donor) and C<sub>60</sub> (acceptor) domains. Ideally, if the polymeric domains consisted of fibers that existed with diameters that were similar to the average diffusion length of an exciton, then the likelihood of an exciton reaching the donor/acceptor interface would increase dramatically. If each exciton created could reach the interface, then exciton recombination would be stymied and the overall efficiency would be greatly enhanced. Thus our goal was to electrospin P3HT into a non-woven fibrous mat consisting of fibers with an average diameter on the order of 10-20 nanometers. The electrospun mat would then be imbibed with a PCMB acceptor component and result in an OPV with improved efficiency (**Figure 2.2**).

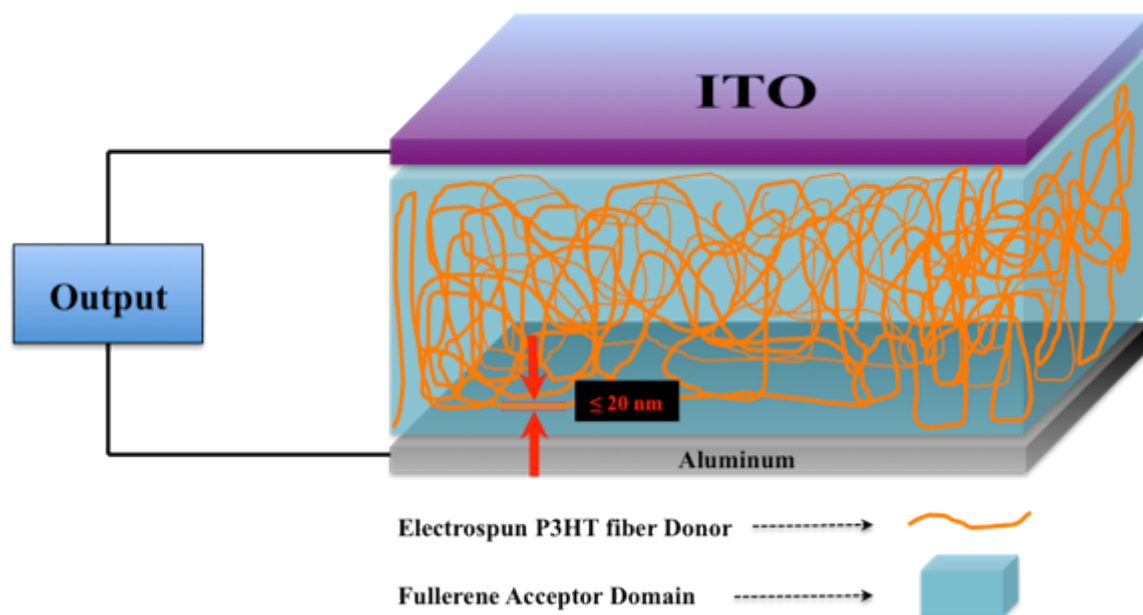


**Figure 2.2.** Cartoon schematic of an OPV bulk heterojunction device comprised of electrospun P3HT as the donor domain (orange fibers). Fibers must be smaller than 20 nm in diameter to discourage recombination. After electrospinning, the resulting P3HT mat is then filled with a fullerene based acceptor domain (teal).

#### ***2.4. Electrospinning of Pure P3HT***

In order for P3HT to be effective in OPV devices, the regioregularity is of extreme importance. Perfect head-to-tail polymerization is necessary to ensure long-range conjugation, which allows for the transport of electrons. If any head-to-head, or tail-to-head connections exist, then the polymer chains experience torsional strain, which disrupts the conjugation.<sup>22</sup> Initially, electrospinning pure, regioregular P3HT proved to be difficult (see **Figure 2.3**). Due to the necessity of the P3HT to be regio-regular (perfect head-to-tail polymerization), high molecular weight P3HT was impractical to obtain. Low molecular weight polymers suffer from limited chain entanglements. Chain entanglements are one of the fundamental driving forces for producing continuous

polymer fibers throughout the electrospinning process. Additionally, the solubility of P3HT severely limited the solvent systems available further increasing the difficulty to electrospin this polymer.

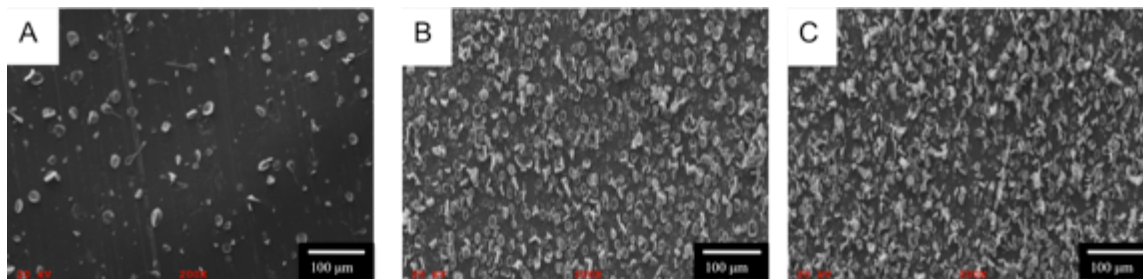


**Figure 2.3.** Electrospun P3HT using 53,000  $M_n$  dissolved in chloroform. The flow rate for each sample was 5 ml/h, the P3HT concentration was 10 wt.% in  $\text{CHCl}_3$ , and the applied voltages were A.) 15 kV B.) 20 kV and C.) 25 kV.

As indicated in **Figure 2.3** above, the product of electrospun regioregular P3HT from  $\text{CHCl}_3$  was not a non-woven mat of fibers. Rather, this procedure resulted in electro spraying to produce a film of P3HT droplets. Along with the low degree of chain entanglements, the high volatility of the chloroform solvent proved to be a hindrance during the spinning process. As mentioned in the introduction section of this chapter, once the polymer droplet forms, a liquid polymer jet must then whip back and forth, elongating on its way to the collector. The solvent is present (although steadily evaporating) throughout the instability (whipping) region and only completely evaporates after the jet travels away from the Taylor cone.<sup>1</sup> Since  $\text{CHCl}_3$  has such a low boiling point, it was postulated that premature evaporation might be contributing to the lack of continuous fiber formation.

### 2.4.1. Electrospinning in a Saturated Atmosphere

In order to overcome the high evaporation rate of  $\text{CHCl}_3$ , the atmosphere of the electrospinning box was saturated with  $\text{CHCl}_3$ . This was accomplished by boiling reagent grade chloroform inside the ES chamber during electrospinning. **Figure 2.4** shows the ESM images of electrospun P3HT membranes using a  $\text{CHCl}_3$  saturated atmosphere.

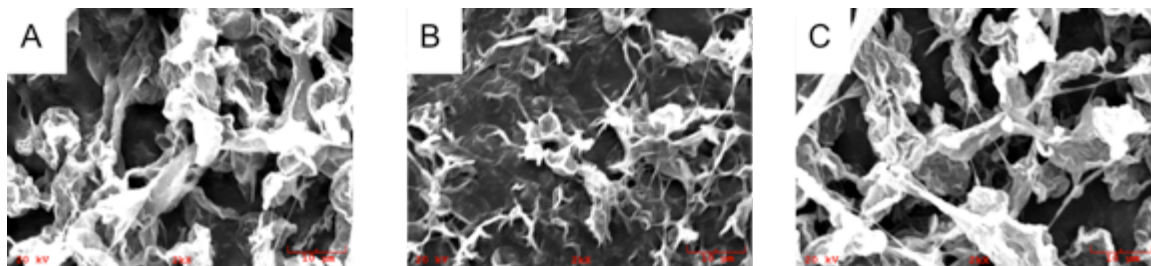


**Figure 2.4.** Electrospun P3HT in atmospheres saturated with boiling  $\text{CHCl}_3$  for A.) 5 minutes B.) 10 minutes C.) 15 minutes of boiling time prior to electrospinning.

**Figure 2.4** clearly shows that saturating the electrospinning atmosphere with chloroform prevents the “electrospraying” process. When the atmosphere is saturated with chloroform, the electrospun P3HT forms ribbon like structures. As the  $\text{CHCl}_3$  saturation time increases, the resulting P3HT adopts some fiber formation along with the ribbons that are formed. Prolonged saturation after 15 minutes yielded no significant improvements on fiber formation. Regardless of the lack of fiber formation, these results were initially promising. The morphology of the resulting polymer component is unimportant; rather it is the domain sizes that would dictate the performance. Thus, even if only ribbon type structures could be produced, as long as they had diameters (widths) of close to 10 nm then the dissociation of excitons will likely still be promoted. After

several attempts at adjusting the polymer composition of the electrospinning solution, the applied voltage and the distance to the collector, the resulting ribbons showed no significant deviation from those depicted in **Figure 2.4**.

#### ***2.4.2. Chloroform Drop Electrospinning***

Additional attempts at electrospinning pure P3HT including purging with chloroform rich N<sub>2</sub> gas, dropping chloroform onto the Taylor cone, and using a co-axial needle (with P3HT/CHCl<sub>3</sub> in the inner capillary and pure CHCl<sub>3</sub> in the outer capillary) resulted in some minor fiber formation. However, none of the aforementioned procedures proved to be a reliable method for producing continuous P3HT fibers on the nanometer length scale. **Figure 2.5** shows some SEM images of P3HT fibers resulting from dropping CHCl<sub>3</sub> onto the Taylor cone during electrospinning attempts.

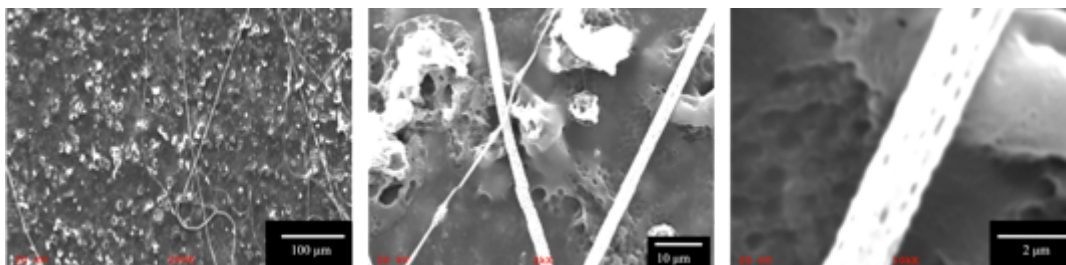


**Figure 2.5.** SEM images of P3HT using the chloroform drop alternative electrospinning procedure. From left to right the image is simply magnified from 200x to 10,000x. This image is of a representative of samples spun using this technique with various ES parameters.

#### ***2.4.3. Electrospinning from a Coaxial Needle***

Building on the modest success of the CHCl<sub>3</sub> dropping technique, a coaxial needle was developed. Recent reports in the literature describe using this method to protect

against  $\text{CHCl}_3$  evaporation.<sup>23</sup> Electrospinning using a coaxial needle presents challenges, as the flow rates of the inner and outer solutions need to be controlled independently. Thus, two syringe pumps were used. One pump controlled the P3HT solution and was connected directly to the inner capillary. The second syringe pump was connected to the outer capillary via flexible tubing with an inner diameter of approximately 1 mm. Although several ES parameters and flow rates were investigated, an inner flow rate of 5 mL/h and two outer flow rates of 7 and 9 mL/h produced the best results. **Figure 2.6** shows SEM images of the two samples. These results indicate that the coaxial needle produced a ribbon like configuration similar to the results obtained from electrospinning in an atmosphere saturated in  $\text{CHCl}_3$ . Although the coaxial samples do appear to be more fibrous in character, domain sizes smaller than those depicted in **Figure 2.6** were not achieved using this procedure.

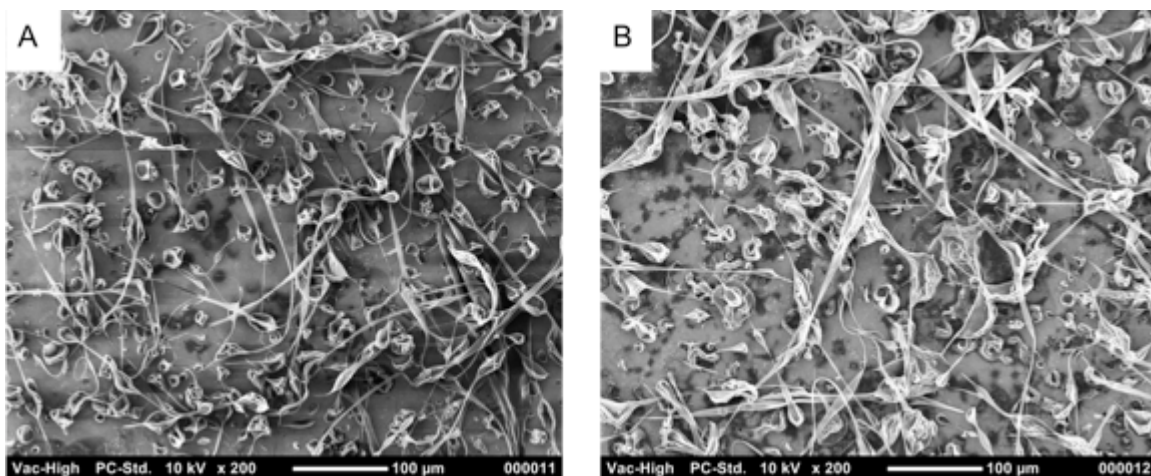


**Figure 2.6.** SEM images of P3HT electrospun from a coaxial needle. Both samples were electrospun from a 14 wt.% P3HT solution in chloroform, at a voltage of 18 kV, an inner flow rate of 5 mL/h and outer flow rates of A.) 7 mL/h and B.) 9 mL/h.

Out of the three procedures attempted, dropping chloroform onto the Taylor cone during the electrospinning process resulted in the best fiber formation. From **Figure 2.5**, it appears that the majority of the electrospun P3HT exists as a film with very few fibers on the surface. Additionally, the fibers appear to be porous. Porous fibers could be advantageous for OPVs provided that the resulting acceptor material ( $C_{60}$  derivative) can penetrate into the fibers. If porous or hollow fibers are produced, then the need to keep the fiber diameter below 2x the excitation diffusion length would be unnecessary. Although fibers were formed using this method, no parameter composition (including flow rate of polymeric solution, flow rate of additional chloroform, applied voltage, and collector distance) consistently resulted in continuous fiber formation. Ultimately, due to P3HT's limited solubility and relatively low molecular weight, electrospinning pure, regioregular P3HT proved unfeasible.

### ***2.5. Coaxial Electrospinning PMMA and P3HT***

As an alternative to electrospinning pure P3HT, in 2009 two groups reported the electrospinning of P3HT by using template polymers. Two main polymers have been reported as the best candidates for the template (sacrificial) component due to their ease of electrospinning, their solubility in chloroform, and because they are easily removed from the fiber mat immediately following electrospinning. Kuo and coworkers devised a coaxial system in which core/sheath polymer fibers were produced. Using poly(methyl methacrylate) (PMMA), they were able to produce fibers that contained PMMA in the core while consisting of P3HT on the sheath. These electrospun fibers were reported to have diameters of 700-800 nm.<sup>24</sup> Although this work originally developed these

core/sheath fibers for oxygen sensors, we envisioned applying a similar procedure, removing the PMMA component in hopes of creating small pure P3HT fiber mats. Another difference we envisioned was using PMMA as the sheath and P3HT as the core. This orientation was chosen for two reasons. Firstly, removal of PMMA on the surface of the fibers will likely be easier than if the PMMA were in the core. Secondly, if the P3HT domains were on the surface, then subsequent washing would result in large diameter fibers, which would defeat the original domain size goal. Before a blend solution was attempted, it was important that we could control the diameter of pure PMMA. Since PMMA is our template/sacrificial polymer, it will be used to control the fiber characteristics. **Figure 2.7** below contains SEM images for three electrospun PMMA samples using different flow rates. The average fiber diameters of PMMA samples electrospun from 0.5 mL/h, 1.0 mL/h and 5.0 mL/h were determined to be approximately 400 nm, 650 nm and 2.5  $\mu\text{m}$  respectively with an error of 50 nm.

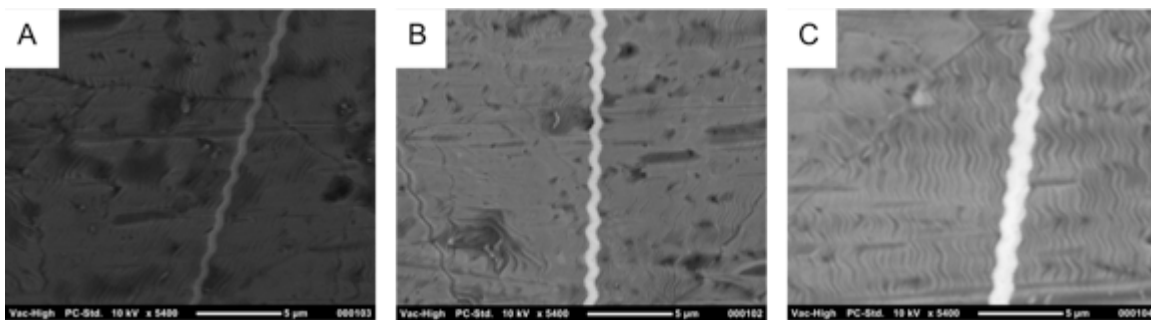


**Figure 2.7.** SEM images of pure PMMA electrospun using an applied voltage of 4.5 kV, a collector distance of 15 cm, a polymer concentration of 300 mg/mL and three different flow rates: A.) 0.5 mL/h B.) 1.0 mL/h and C.) 5 mL/h.

Since control of the fiber diameter was possible by simply changing the flow rate, the coaxial needle was set up with PMMA on the sheath and P3HT in the core. The

concentrations of each ES solution was chosen to match those reported by Kuo with the PMMA concentration being 300 mg/mL and the P3HT concentration being 50 mg/mL.<sup>24</sup>

**Figure 2.8** is a photograph of electrospun samples of pure PMMA and the coaxial PMMA/P3HT. Pure PMMA produced white opaque fiber mats whereas the product of the coaxial system was an orange/red tint due to the absorbance characteristics of P3HT.

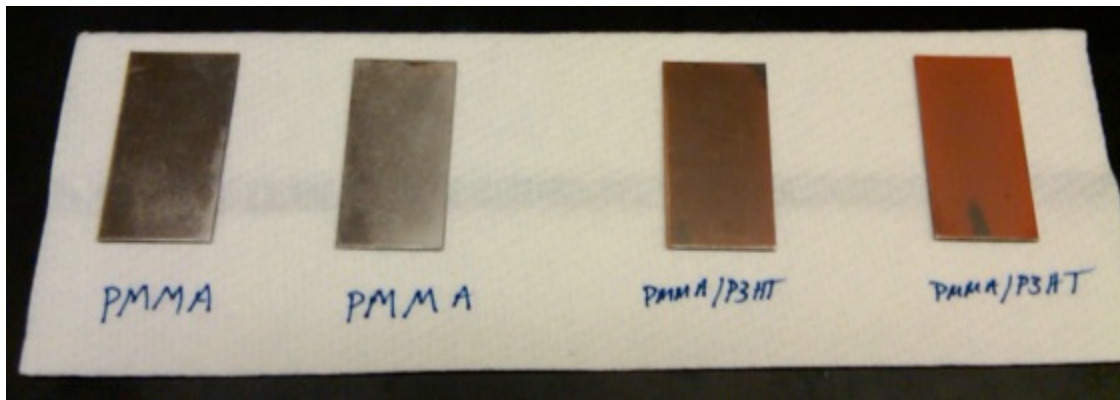


**Figure 2.8.** Photograph of electrospun samples of pure PMMA (right) and PMMA/P3HT coaxial setup (left). Differences in two PMMA samples: left spun at 8 kV, right spun at 11 kV. Differences for PMMA/P3HT samples are similarly spun at 8 kV (left) and 11 kV (right).

Although PMMA has been successfully electrospun into bead-less fibers from solutions of dimethylformamide (DMF),<sup>25</sup> ethyl acetate,<sup>26</sup> tetrahydrofuran (THF) and chloroform,<sup>27</sup> upon addition of P3HT our research was only able to produce beaded, “necklace” type fibers. **Figure 2.9** contains SEM images representing the fibers obtained from coaxially electrospinning PMMA/P3HT solutions in chloroform and chlorobenzene.

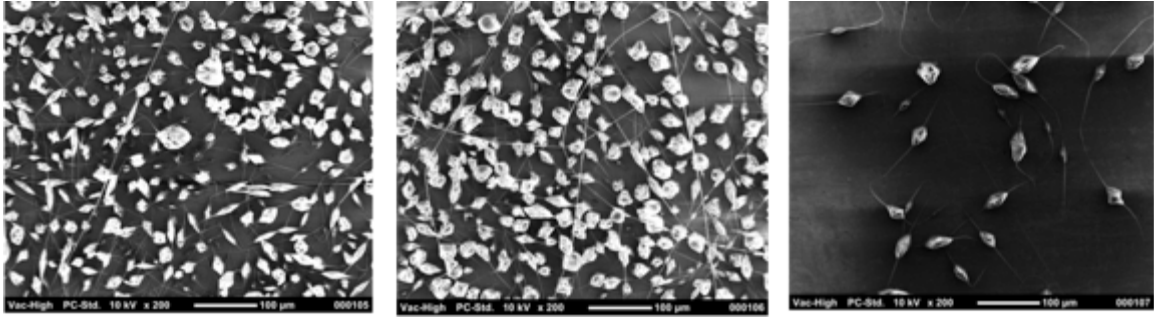


**Figure 2.9.** SEM images of PMMA/P3HT coaxially electrospun representative samples. From left to right the samples electrospinning parameters were 4.5 mL/h @ 11 kV, 5 mL/h @ 11 kV, and 5 mL/h @ 9 kV. Each sample was electrospun from a sheath solution containing 300 mg/mL PMMA in chlorobenzene, a P3HT solution of 50 mg/mL in chlorobenzene and with a collector distance of 15 cm.

## ***2.6. Electrospinning Blended Solutions of PCL and P3HT***

Since electrospinning a coaxial setup of PMMA/P3HT was unsuccessful in producing non-beaded fibers with diameters on the scale of tens of nanometers, research moved to blend solutions of P3HT with poly( $\epsilon$ -caprolactone) (PCL) as described in previous work.<sup>23</sup> **Figure 2.10** contains SEM images of pure PCL electrospun with various parameters. As indicated in **Figure 2.10**, the best parameters to electrospin pure PCL is in a voltage range of 11 – 15 kV and a flow rate of 3 mL/h. Samples were electrospun from two different polymeric concentrations in chloroform: 25 and 50 wt.%.

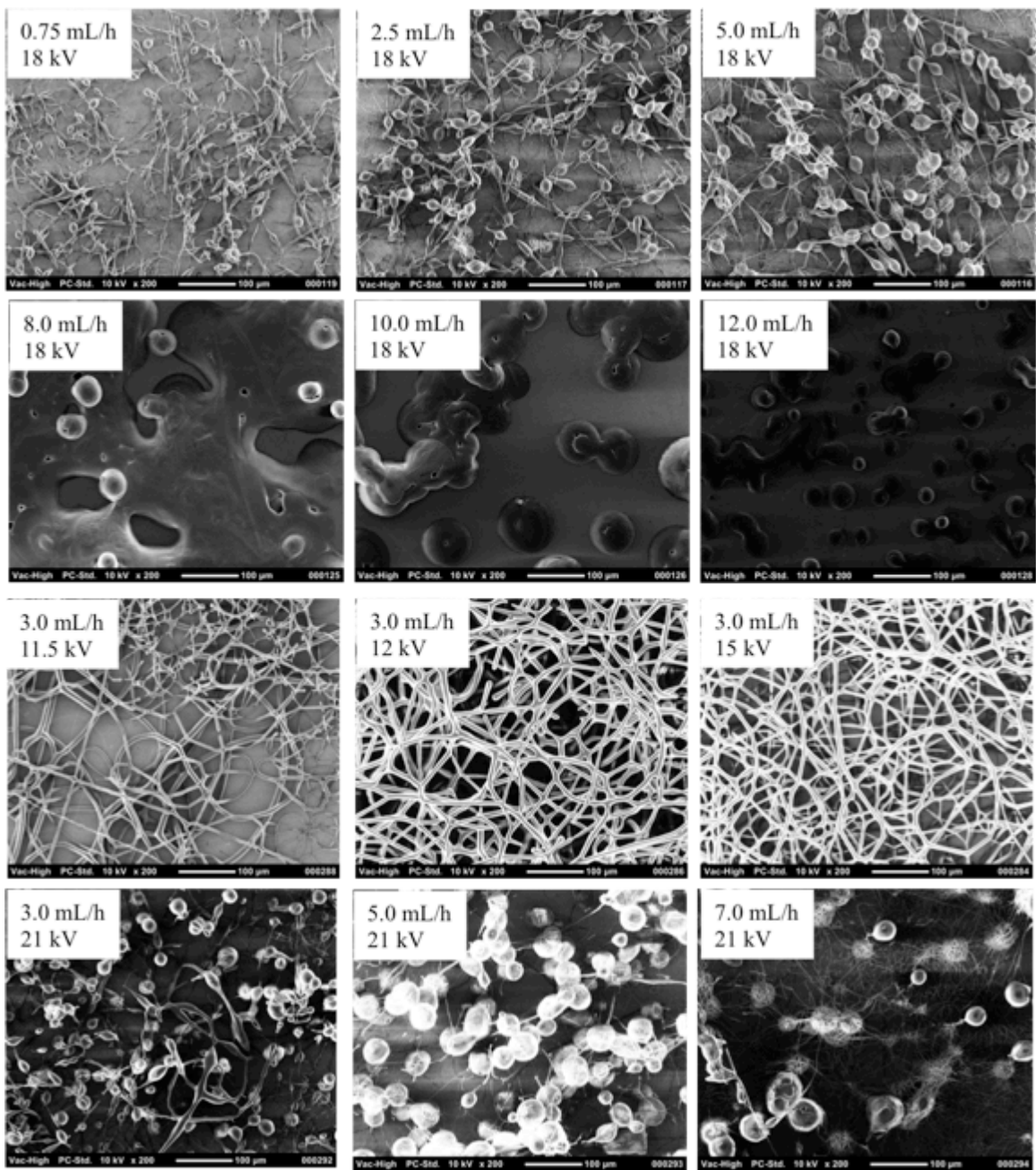


**Figure 2.10.** SEM images of PCL electrospun from chloroform. Additionally, the samples were electrospun from two different polymeric concentrations in  $\text{CHCl}_3$ : Top two rows 25 wt.% solution, bottom two rows 50 wt.% solutions.

Unlike the coaxial procedure, P3HT and PLC were both dissolved in chloroform and electrospun from a single capillary. Following the procedure described by Lee *et al.*, a 90:10 w/w solution of PCL/P3HT in chloroform was prepared. The PCL/P3HT solution was electrospun using flow rates ranging from 0.7 – 8.0 mL/h and a voltage potentials ranging from 11 – 18 kV. Although the ideal electrospinning parameters for pure PCL included a flow rate of 3 mL/h, an applied voltage of ~12 kV, and a concentration of 50 wt.%, the addition of P3HT significantly affects polymer chain dynamics within the electrospinning solution. Reported in **Figure 2.11**, the results from electrospinning a blended solution of PCL/P3HT in chloroform showed very little fiber formation. The SEM images in **Figure 2.11** are representative of nearly every parameter combination. Nearly every sample consisted mainly of non-structured, non-fibrous films with large fibrils present in a very limited quantity.

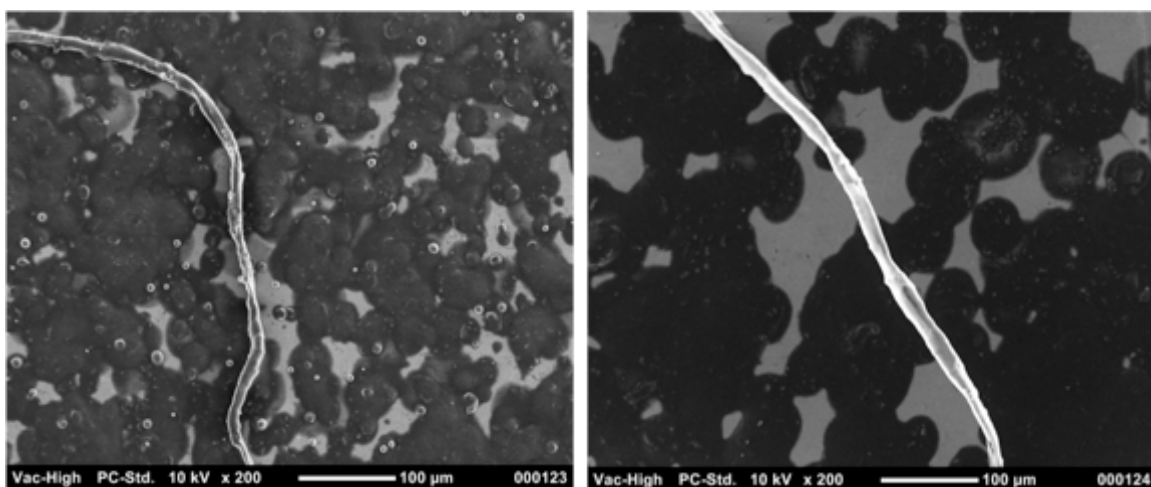


**Figure 2.11.** Representative SEM images of PCL/P3HT electrospun samples with voltages, flow rates, and concentrations ranging from 10 – 18 kV, 0.7 – 8.0 mL/h, and 20 -50 wt.% respectively.

## ***2.7. Electrospun Sacrificial Polymer Templates***

Other techniques were used in this work to achieve controllable P3HT domain sizes. These techniques included PVDF templating (electrospinning PVDF onto a substrate, filling in the voids with P3HT then removing the PVDF with acetone), and electrochemically-polymerizing thiophene onto substrates containing electrospun fibers (ideally the polymerization would occur in the void spaces leaving a porous network upon removal of the electrospun component).

### ***2.7.1 Spin-casting onto a PVDF Fiber Containing Substrate***

PVDF was electrospun from a 50:50 vol. mixture of DMAC:acetone containing approximately 20 wt./vol. % of PVDF. This solution was electrospun at a flow rate of 3 mL/h to a grounded collector positioned 25 cm away. The collector was an ITO coated glass slide, which would ultimately act as the transparent electrode in the OPV device. A CHCl<sub>3</sub> solution containing 13 wt. % P3HT was then spin-coated onto the PVDF fiber mat supporting ITO slide at ~2500 RPM. Once the PVDF fibers were coated in P3HT, the sample was submerged in acetone to remove the PVDF component. **Figure 2.12** shows SEM images of the electrospun PVDF, the P3HT coated PVDF fibers and the resulting P3HT structure following PVDF removal in acetone. Using this technique, small domains of what is believed to be P3HT were achieved after removal of the PVDF fiber template. The domain sizes are on the order of a 1  $\mu\text{m}$ . Tuning the electrospinning parameters of PVDF will allow for smaller PVDF template fibers, which will translate to smaller P3HT domains. Unfortunately, the P3HT component, although not soluble in acetone, delaminates from the ITO surface during the acetone wash. Delamination of the

P3HT domains is a major drawback as it causes discontinuity in the resulting film. Because the P3HT only adheres to the ITO via weak intermolecular interactions, the delamination decreases the reproducibility of producing defect-free bi-continuous polymer domains.

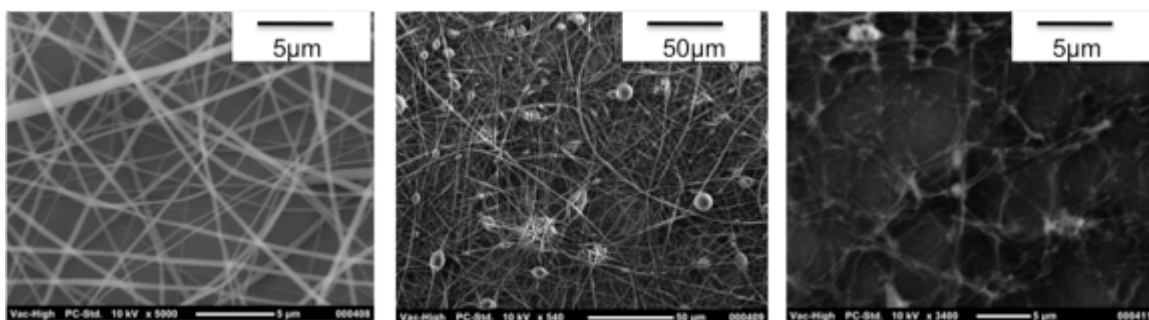


**Figure 2.12.** SEM images of PVDF templating. From right to left: pure PVDF electrospun from DMAC:Acetone 50:50 vol. mixture, PVDF fibers after spin-coating a 13 wt.% P3HT solution in chloroform, SEM image of P3HT structure after removal of PVDF with acetone.

### ***2.7.2 Electro-Polymerization of Thiophene onto ITO Substrates Containing Sacrificial Fibrous Templates***

Electrochemical polymerization of P3HT was investigated as an alternative to spin-coating since the weak interactions between P3HT and the ITO electrode resulting from spin-coated samples are insufficient to prevent delamination during PDVF removal. Since polymerization to regioregular P3HT requires sophisticated catalysts systems, thiophene was used as a model system for proof of concept. In accordance with a publication in 1992 by Ritter and Nofle,<sup>28</sup> The electrochemical polymerization of thiophene was accomplished by constructing an electrochemical cell comprised of an ITO coated glass slide as the working electrode, a platinum counter electrode, a silver wire pseudo-reference electrode, and an electrolyte solution of thiophene in acetonitrile

containing 0.5 M LiClO<sub>4</sub>. LiClO<sub>4</sub> was dried in a vacuum oven at 110 °C for 24 hours and stored in a desiccator. Thiophene (Aldrich) was purified by distillation at 80 °C and added to the electrolyte solution at 0.2M. Electrolyte solutions were degassed prior to each experiment by ultrasonic agitation for 20 minutes. Cyclic voltammetry was conducted on the electrolyte solution to evaluate the oxidative and reductive characteristics of thiophene at a scan rate of 100 mV/s. **Figure 2.13** indicates that thiophene has an oxidative peak at ~ 1.4 V and a redox peak at ~ 0.7 V. Further analysis of the CV supports the findings of Tanaka, suggesting that the electrochemical polymerization of thiophene likely occurs via cationic means following the oxidation of thiophene monomer at the working electrode.<sup>29</sup>

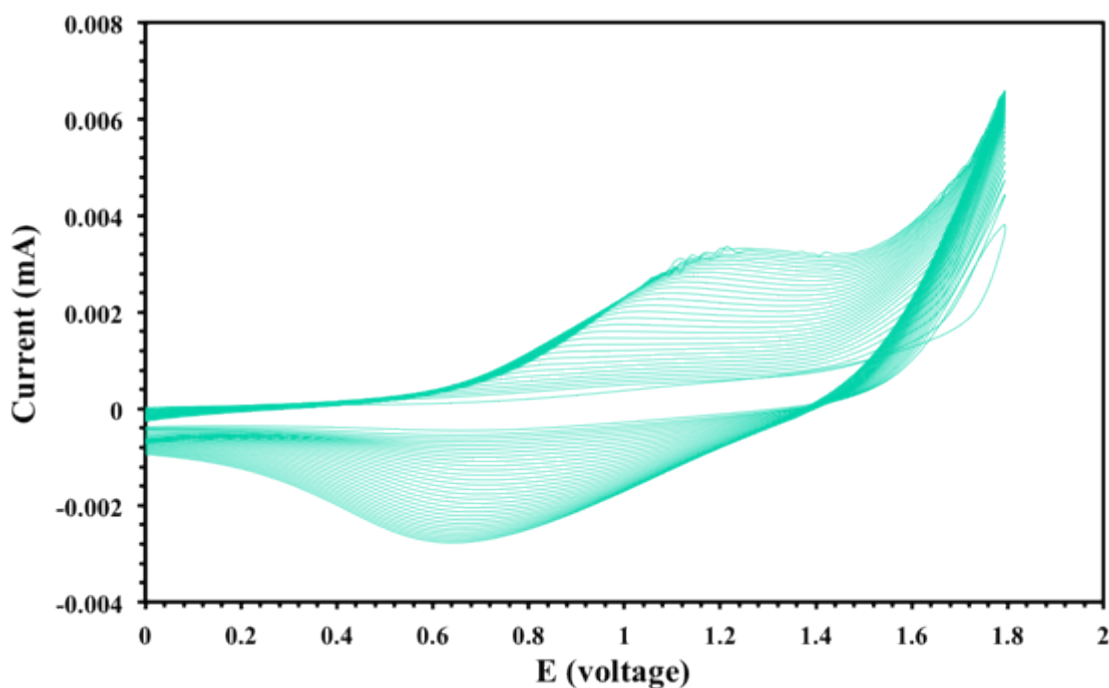


**Figure 2.13** Cyclic voltammogram of thiophene in a 0.5 M LiClO<sub>4</sub> electrolyte solution of acetonitrile using an Ag reference.

As **Figure 2.13** suggests by the redox peak being nearly equal to the oxidation peak in the CV, the polymerization of thiophene on the ITO surface is reversible. Thus polymerization via cyclic voltammetry is inefficient. The polymerization is believed to occur by the oxidation of thiophene on the ITO electrode thus the polymerizations were carried out galvanostatically at a positive current. **Figure 2.14** is the suggested reaction mechanism for the cationic polymerization of thiophene resulting from oxidation on the ITO electrode.

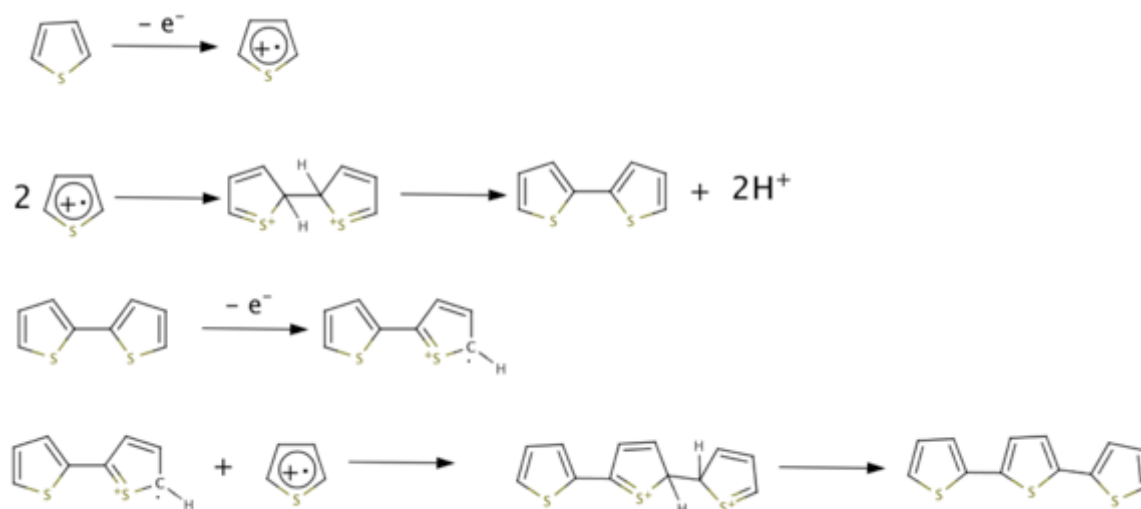


**Figure 2.14.** Electro-polymerization scheme of thiophene via oxidative dehydrogenation.

Thiophene was polymerized galvanostatically by holding a constant current across the electrochemical cell. The samples were held at different currents for 10 minutes and evaluated for film development. **Figure 2.15** shows the voltage for each sample vs. time at 5 different currents. With the exception of the sample held at 1 mA/cm<sup>2</sup>, the voltages for all samples were nearly constant at 1.7 volts, which is attributed to the oxidation of thiophene as shown in the CV (**Figure 2.13**). Photographs of the resulting polythiophene films (**Figure 2.16**) indicate incomplete coverage of the ITO

coated working electrode. As the polymerization current increased, the coverage of the ITO working electrode also increased.

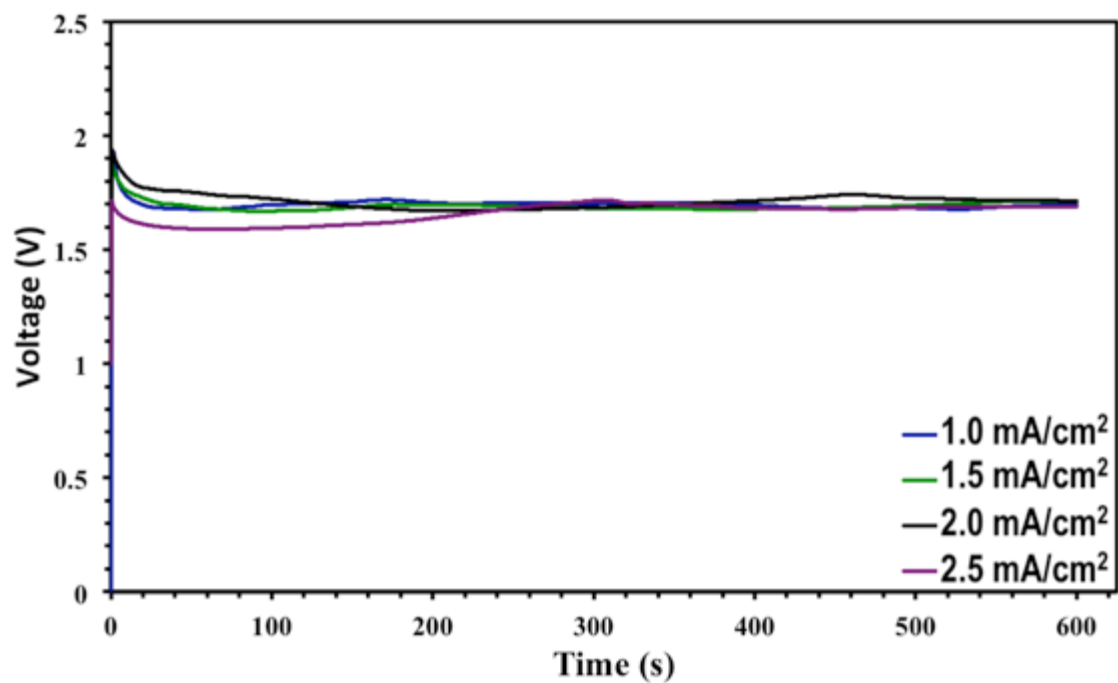


**Figure 2.15.** Potential profiles for the galvanostatically controlled electro-polymerization of thiophene at various currents vs. silver wire pseudo-reference.

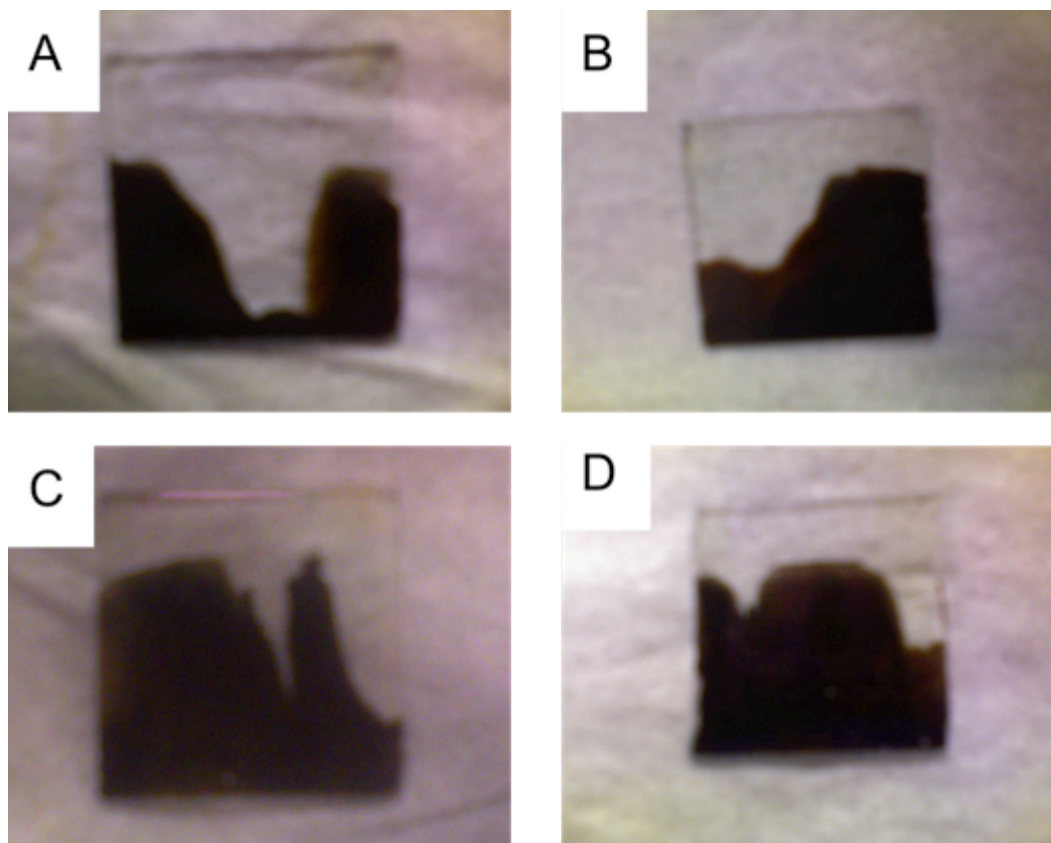


**Figure 2.16.** Images of electro-polymerized polythiophene films produced from A.)  $1.0 \text{ mA/cm}^2$ ; B.)  $1.5 \text{ mA/cm}^2$ ; C.)  $2.0 \text{ mA/cm}^2$ ; and D.)  $2.5 \text{ mA/cm}^2$ .

During the course of optimizing the monomer, salt, and current effects on the electro-polymerized polythiophene films, it was observed that the solutions after each experiment turned from colorless to light yellow. There has been much debate on whether the presence of low molecular weight oligomers enhance the electro-polymerization of heterocyclic monomers or not.<sup>30</sup> To investigate this phenomenon, one electrolyte solution consisting of  $0.1 \text{ M}$  thiophene and  $0.5 \text{ M}$   $\text{LiClO}_4$  in acetonitrile was electro-polymerized on several ITO working electrodes at two different currents. The

voltage profiles for these samples look similar to each other at a voltage of  $\sim 2.5\text{V}$  (Figure 2.17).

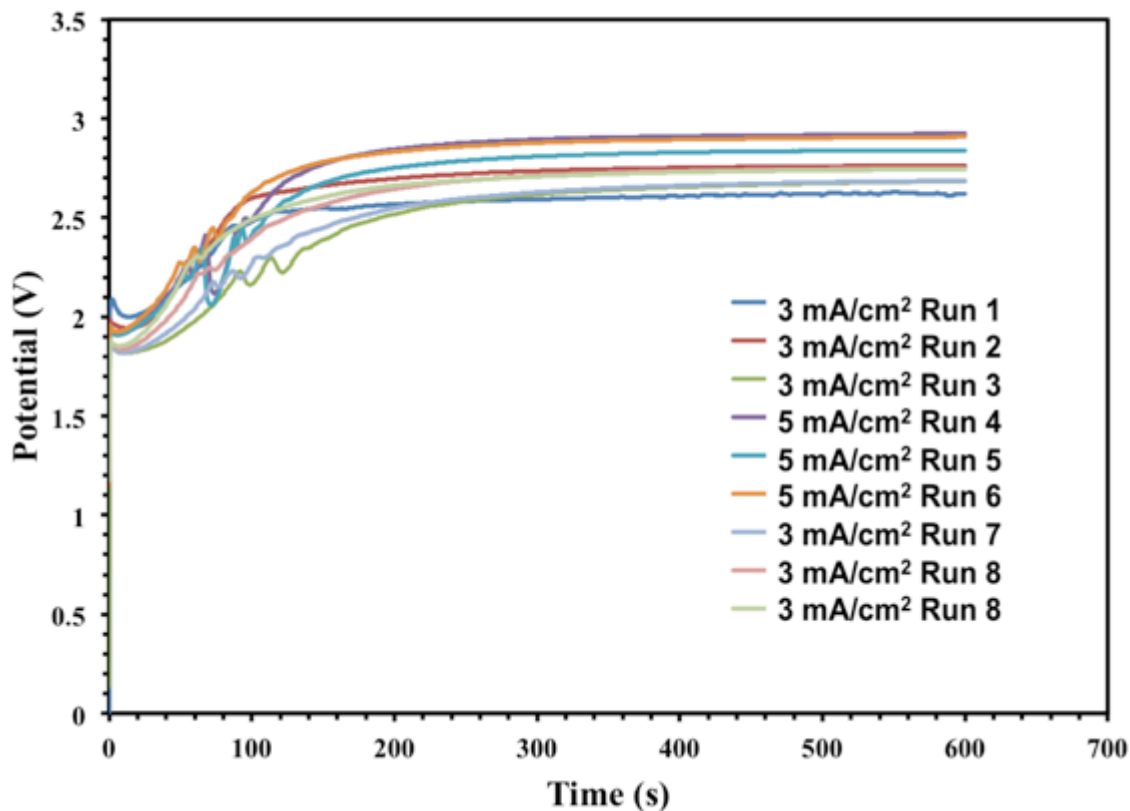


**Figure 2.17.** Potential vs. time profile for successive electropolymerizations of a thiophene electrolyte solution using a silver wire reference.

Photographs of the resulting films offer more information than the voltage profiles. As seen in **Figure 2.18**, the top row of photographs represent three electropolymerizations of thiophene each at  $3\text{ mA/cm}^2$ . Successive polymerizations from the same electrolyte solution (from left to right) result in better film formation. The presence of thiophene oligomers, suggested by yellow coloration of the electrolyte solution, appears to enhance the film deposition and coverage. If the current is increased from 3 to  $5\text{ mA/cm}^2$  the coverage is thicker as indicated by the inability to see the blue reference

star under the glass electrode for the middle row images. Finally, reducing the current back to  $3 \text{ mA/cm}^2$  after the previous 6 polymerizations resulted in three uniform films with a thickness close to the third sample (top right). These results indicate that “charging” the solution with thiophene oligomers from the first two or three polymerization attempts, results in more uniform films regardless of the experimental current. Once the electrolyte is charged, the current only serves to alter the thickness of the resulting film.

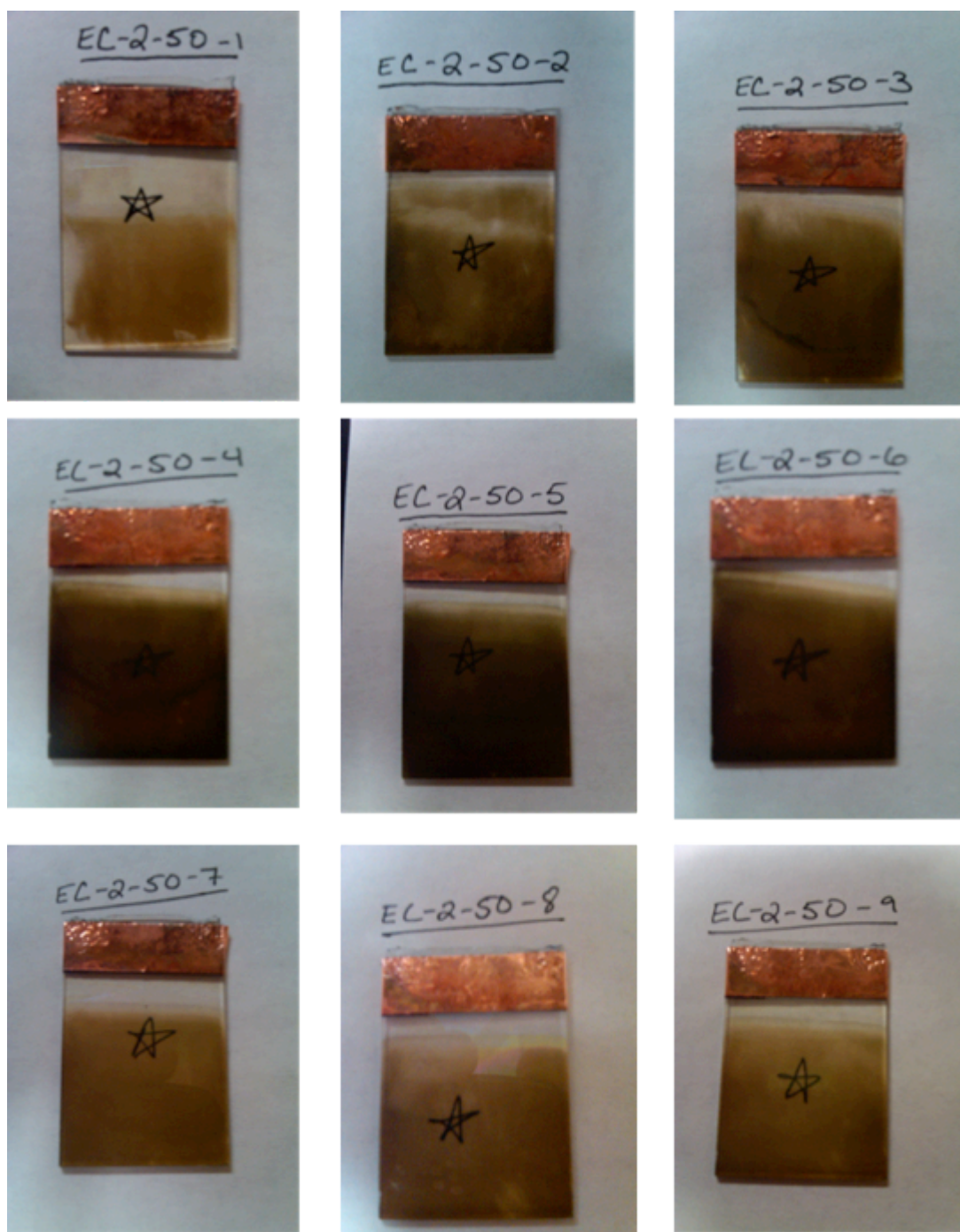


**Figure 2.18.** Images of successive electro-polymerized thiophene films obtained from the same electrolyte solution. Samples are presented successively from left to right (top left was polymerized first and the bottom right was polymerized last).

Once the optimal electrolyte solution and conditions for the electropolymerization of thiophene were determined to be between 3 and 5 mA/cm<sup>2</sup> with an oligomer charged solution, thiophene was electro-polymerized onto ITO substrates containing electrospun poly(caprolactone) (PCL). The electrospun PCL fibers act as a template, allowing for the polymerization of thiophene in PCL poor regions of the ITO surface. Ideally, the thiophene would polymerize in the bi-continuous network formed between the PCL fibers. Then, subsequent removal of the PCL with water would result in fibrous voids into which a C<sub>60</sub> derivative could be introduced. Thus with this technique, unlike either electrospinning P3HT or spin-casting onto the PVDF template fibers, the fullerene acceptor domain would be the fibrous domain. **Figure 2.19** shows the ITO working electrode coated in electrospun PCL fibers.

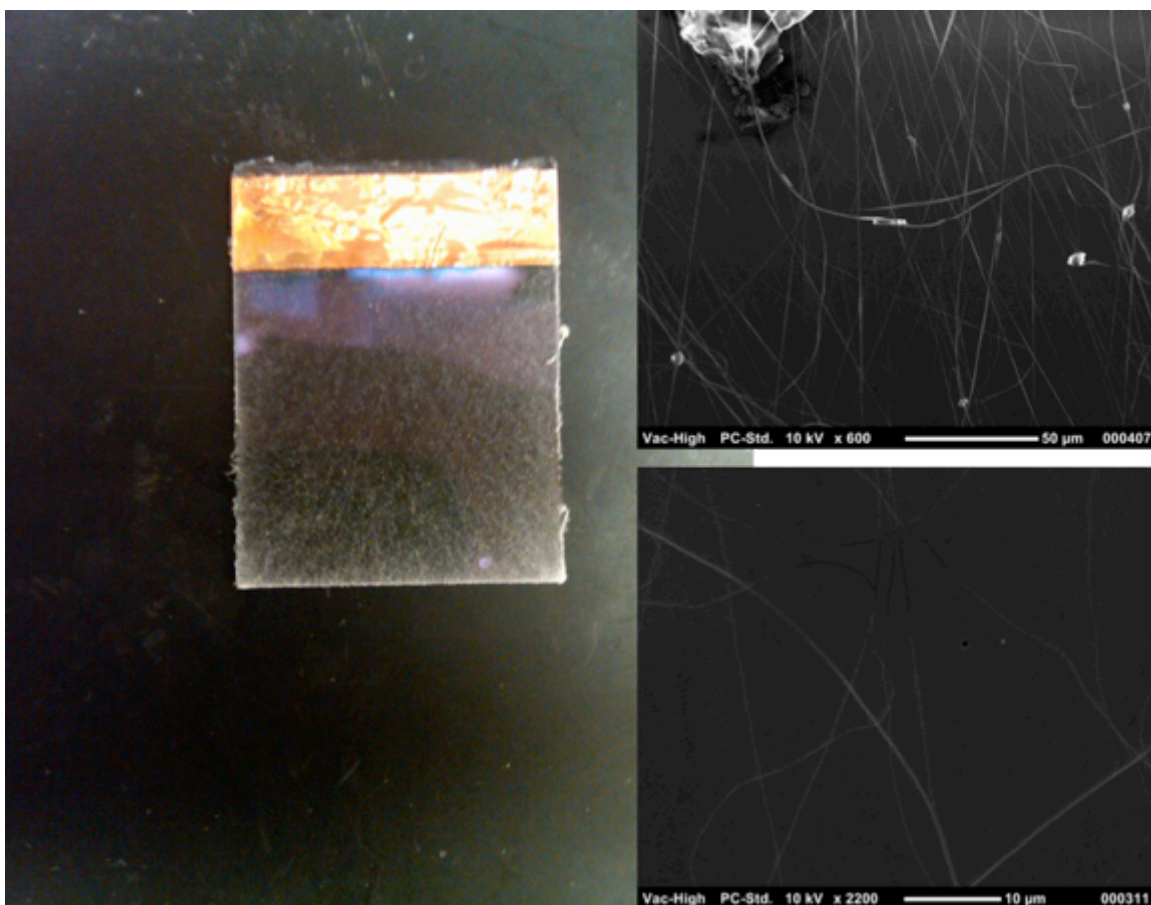


**Figure 2.19.** Image of PCL template fibers deposited on an ITO working electrode (left) and SEM images of PCL fibers in ITO slides (right).

Prior to using the PCL template ITO, the electrolyte solution was charged by performing two electro-polymerizations on neat ITO slides (**Figure 2.20**). Following the charging procedure, the ITO working electrodes containing PCL fibers were submerged in a charged electrolyte solution containing 0.1 M thiophene and 0.5 M LiClO<sub>4</sub>. Using a current of 5 mA/cm<sup>2</sup>, thiophene was polymerized onto the PCL template ITO slides. **Figure 2.21** shows a photograph of the film resulting from the last (third) charging cycle along side of the electro-polymerized thiophene film on the PCL template electrode. The figure also shows SEM images of the resulting thiophene films and the PCL fibers. The

SEM image in **Figure 2.21 B** shows fibers that appear to be underneath the thiophene film with one large fiber situated half underneath and half on top of the thiophene film. SEM image **Figure 2.21 C** also shows fibers that appear to be underneath the thiophene film (lighter fibers) and fibers sitting on top of the polythiophene film (darker fibers). Image **Figure 2.21 D** only shows fibers existing under the electro-polymerized thiophene film.

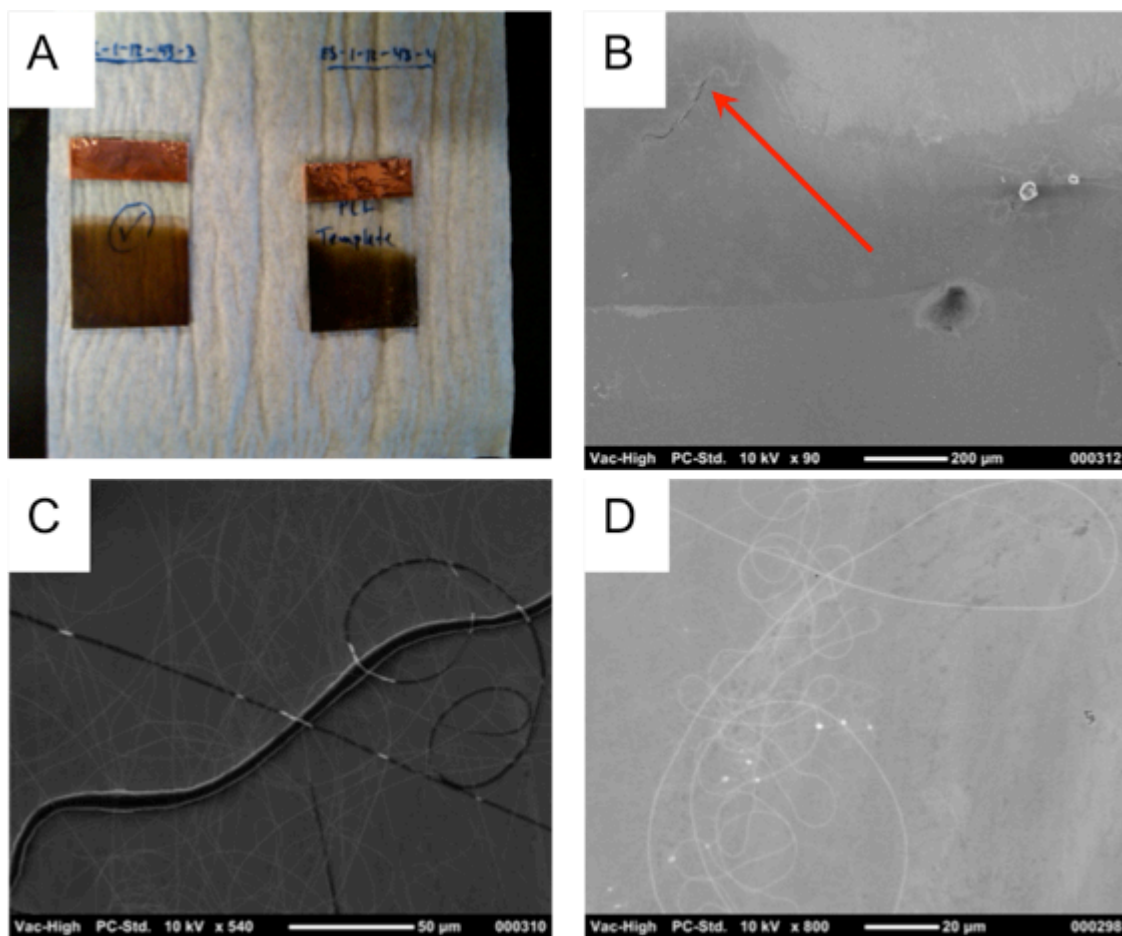


**Figure 2.21** Photograph of ITO coated glass slides covered in polythiophene film without PCL fibers (left) and with PCL fibers (right) and SEM images of thiophene polymerized onto ITO containing PCL fiber template.

## **2.8. Conclusions**

This work demonstrates that electrospinning can be used to obtain a vast array of conductive polymer morphologies. The electrospinning of pure P3HT in chloroform results in polymer films consisting of platelet type morphologies with diameters on the order of 10  $\mu\text{m}$ . Electrospinning of P3HT in chloroform in a  $\text{CHCl}_3$  saturated atmosphere results in very unique “ribbon” type morphologies. These ribbon type films contain P3HT domains on the order of 5 $\mu\text{m}$  and appear to be bi-continuous which would promote charge transfer in both the donor and acceptor domains. Dropping pure chloroform onto the needle tip during electrospinning resulted in P3HT fibers with porous morphologies and fiber diameters of approximately 2  $\mu\text{m}$ . These fibrous morphologies could prove to be very beneficial to exciton dissociation as the acceptor material could potentially fill the polymer fiber pores thus promoting dissociation. Electrospinning P3HT from a coaxial needle where a pure  $\text{CHCl}_3$  solution is the sheath produced the most promising results. The coaxial technique resulted in a hybrid between ribbon and fiber type morphologies with diameters / domain sizes in the range of 5-20  $\mu\text{m}$ .

Using sacrificial polymers as either electrospinning supports or as fibrous templates resulted in the formation of unique morphologies, including necklace type fibers (P3HT & PMMA) and blended solid fibers (P3HT & PCL blends). Spin-casting P3HT solutions onto substrates containing electrospun fiber templates resulted in interesting fibrillar type structures upon removal of the PVDF domain. Electropolymerization results suggest the possibility of polymerizing a network of conductive material around a fibrous template. Although the successful electrospinning of pure P3HT and various blends of P3HT with template / sacrificial polymers has been

previously reported in the literature, we were unable to get continuous fiber formation free of beads or ribbon defects. Unfortunately, none of the techniques used in this research resulted in the production of P3HT films with domain sizes on the order of 10-20 nm. Although unsuitable for P3HT based OPV's, the results of this work gave way to design concepts that might be applied to other polymeric donor types. Additionally, the results from the OPV work could be applied to producing novel polymer gel electrolytes via electrospinning for development of lithium polymer batteries with high energy densities and superior charge-discharge properties.

## 2.9. References

1. Z.-M. Huang, Y. Z. Zhang, M. Kotaki and S. Ramakrishna, *Composites Science and Technology*, 2003, **63**, 2223-2253.
2. J. Doshi and H. D. Reneker, *Journal of Electrostatics*, 1995, **35**, 151-160.
3. H. D. Reneker and C. Iksoo, *Nanotechnology*, 1996, **7**, 216-223.
4. A. Greiner and J. H. Wendorff, *Angewandte Chemie International Edition*, 2007, **46**, 5670-5703.
5. A. L. Yarin, S. Koombhongse and D. H. Reneker, *Journal of Applied Physics*, 2001, **90**, 4836-4846.
6. G. Taylor, *Proceedings of the Royal Society of London. A. Mathematical and Physical Sciences*, 1969, **313**, 453-475.
7. J. M. Deitzel, J. Kleinmeyer, D. Harris and N. C. Beck Tan, *Polymer*, 2001, **42**, 261-272.
8. A. Koski, K. Yim and S. Shivkumar, *Materials Letters*, 2004, **58**, 493-497.
9. C. J. Thompson, G. G. Chase, A. L. Yarin and D. H. Reneker, *Polymer*, 2007, **48**, 6913-6922.
10. A. Martins, R. L. Reis and N. M. Neves, *International Materials Reviews*, 2008, **53**, 18.
11. J. A. Burdick and R. L. Mauck, *Biomaterials for Tissue Engineering Applications: A Review of the Past and Future Trends*, Springer-Verlag/Wien, New York, 2011.
12. X. Liu and P. X. Ma, *Annals of biomedical engineering*, 2004, **32**, 477-486.
13. M. Shin, H. Yoshimoto and J. P. Vacanti, *Tissue engineering*, 2004, **10**, 33-41.
14. R. Gopal, S. Kaur, Z. Ma, C. Chan, S. Ramakrishna and T. Matsuura, *Journal of Membrane Science*, 2006, **281**, 581-586.
15. X. Wang, X. Chen, K. Yoon, D. Fang, B. S. Hsiao and B. Chu, *Environmental Science & Technology*, 2005, **39**, 7684-7691.
16. K. Yoon, K. Kim, X. Wang, D. Fang, B. S. Hsiao and B. Chu, *Polymer*, 2006, **47**, 2434-2441.
17. Z. Ma, M. Kotaki and S. Ramakrishna, *Journal of Membrane Science*, 2005, **265**, 115-123.
18. D. T. Schoen, A. P. Schoen, L. Hu, H. S. Kim, S. C. Heilshorn and Y. Cui, *Nano Letters*, 2010, **10**, 3628-3632.
19. T. Tamura and H. Kawakami, *Nano Letters*, 2010, **10**, 1324-1328.
20. I. Shabani, M. M. Hasani-Sadrabadi, V. Haddadi-Asl and M. Soleimani, *Journal of Membrane Science*, 2011, **368**, 233-240.
21. J. Choi, K. M. Lee, R. Wycisk, P. N. Pintauro and P. T. Mather, *Macromolecules*, 2008, **41**, 4569-4572.
22. R. D. McCullough, S. Tristram-Nagle, S. P. Williams, R. D. Lowe and M. Jayaraman, *Journal of the American Chemical Society*, 1993, **115**, 4910-4911.
23. S. Lee, G. D. Moon and U. Jeong, *Journal of Materials Chemistry*, 2009, **19**, 743-748.
24. C.-C. Kuo, C.-T. Wang and W.-C. Chen, *Macromolecular Symposia*, 2009, **279**, 41-47.

25. H. Wang, Q. Liu, Q. Yang, Y. Li, W. Wang, L. Sun, C. Zhang and Y. Li, *J Mater Sci*, 2010, **45**, 1032-1038.
26. L. R. Li Lu, Li U. Lingna, F. Tao, *CIESC Journal*, 2013, 1869-1875.
27. Y. Liu, Y. Ji, K. Ghosh, R. A. F. Clark, L. Huang and M. H. Rafailovich, *Journal of Biomedical Materials Research Part A*, 2009, **90A**, 1092-1106.
28. S. K. Ritter and R. E. Nofle, *Chemistry of Materials*, 1992, **4**, 872-879.
29. K. Tanaka, T. Shichiri, S. Wang and T. Yamabe, *Synthetic Metals*, 1988, **24**, 203-215.
30. J. Roncali, *Chemical Reviews*, 1992, **92**, 711-738.

## Chapter 3

# Electrospun PEO-based Electrolytes for Rechargeable Lithium Polymer Batteries

### 3.1. Introduction

Polymeric-gel electrolytes (PGEs) are becoming attractive because they exhibit much higher room temperature conductivities than their solid polymer electrolyte (SPE) counterparts while affording safer alternatives to liquid type electrolyte cells.<sup>1-3</sup> PGEs are typically polymer membranes swollen with liquid organic electrolytes (usually a mixture of polar aprotic carbonates and cyclic carbonates) and lithium salts. To enhance the ion migration through PGEs, pores are often incorporated into the polymer membranes.<sup>4</sup> Pores create pathways of liquid domains to enhance ionic mobility, in addition to facilitating high amounts of electrolyte swelling. Among other methods (phase inversion and salt leaching for example), electrospinning has become an advantageous means to efficiently and reproducibly introduce porosity into polymer membranes by creating a fibrous mat morphology.<sup>2, 5-7</sup> Furthermore, tuning the processing parameters allows for control of physical characteristics such as average fiber size, fiber density, average pore size, and membrane porosity.<sup>8</sup> Several polymeric components have been electrospun for incorporation as an electrolyte (or electrolyte components) for lithium battery devices.

Perhaps the most notable polymer in the early stages of electrospun polymer electrolytes was poly(vinylidene fluoride) (PVDF) and its derivatives. PVDF was appealing due to its relative inexpensiveness, high mechanical strength, and inertness to the components and electrochemical processes typically found in lithium-based batteries. Additionally, it became apparent that the electrospinning process was highly tunable,

which results in highly customizable polymeric frameworks for polymeric-gel electrolytes. Research in our lab shows that PVDF fibers can be tailored by slight alterations in the electrospinning parameters. **Figure 3.1** shows SEM images of PVDF fibers electrospun from various polymer concentrations in a 50:50 volume mixture of dimethylacetamide (DMAc):acetone.

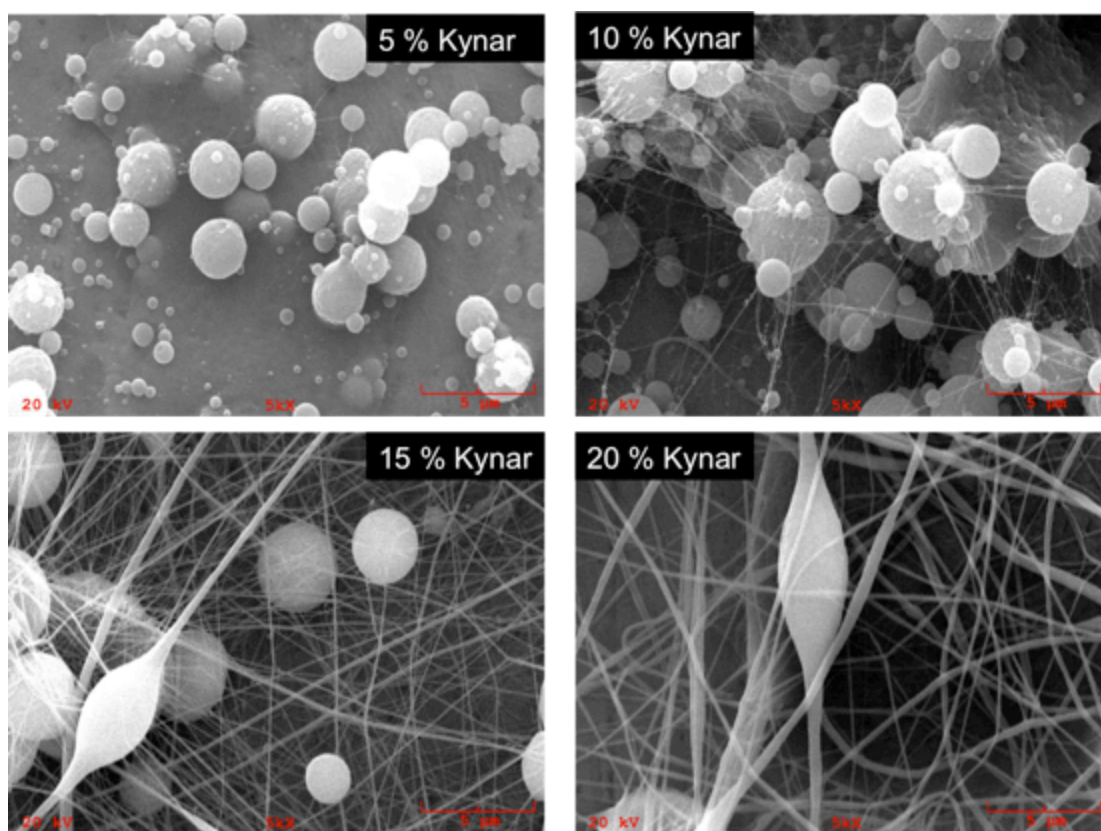


**Figure 3.1.** SEM images of PVDF fibers electrospun from various polymer concentrations in DMAc:acetone solutions. Polymer morphologies change from spherical droplets to polymer fibers as the polymer concentration in the electrospinning solution increases.

**Figure 3.1** shows that at low polymer concentrations in PVDF solutions, the electrospinning process behaves more like an *electrospraying* process, in which polymer droplets are deposited on the grounded collector. Upon close inspection of the resulting film, one can see that the PVDF droplets are connected by several very small polymer fibers. As the polymer concentration of the spinning solution increases, the presence of the small connecting fibers becomes increasingly clear, and an increase in the average diameter of the connecting fibers is observed. At 15 wt.% PVDF, the resulting membrane is represented largely by non-woven fibers of PVDF and the presence of beads diminishes drastically. Finally, at 20 wt.%, the electrospinning process results in a fiber mat consisting mostly of fibrous PVDF with very few beads present. Increasing the polymer concentration (while leaving all other parameters constant i.e., voltage, flow rate, and collector distance) resulted in a reduction of beads, an increase in fiber density and an increase in the average fiber diameter. The average fiber diameter of each electrospun sample is recorded in **Table 3.1**.

**Table 3.1:** Average fiber diameters of electrospun PVDF mats spun from solutions with varying polymer concentrations (beads not included in diameter measurements).

Solution Concentration (wt.%)	Average Diameter of Fibers (nm)
5	55 ± 15
10	80 ± 20
15	170 ± 40
20	285 ± 50

The concentration of the electrospinning solution is only one of many processing parameters that can affect the morphology of the resulting fiber mats. The voltage is another extremely important parameter affecting fiber diameter. **Figure 3.2** shows SEM images of PVDF samples electrospun from a 10 wt.% solution from our lab at three different potentials.

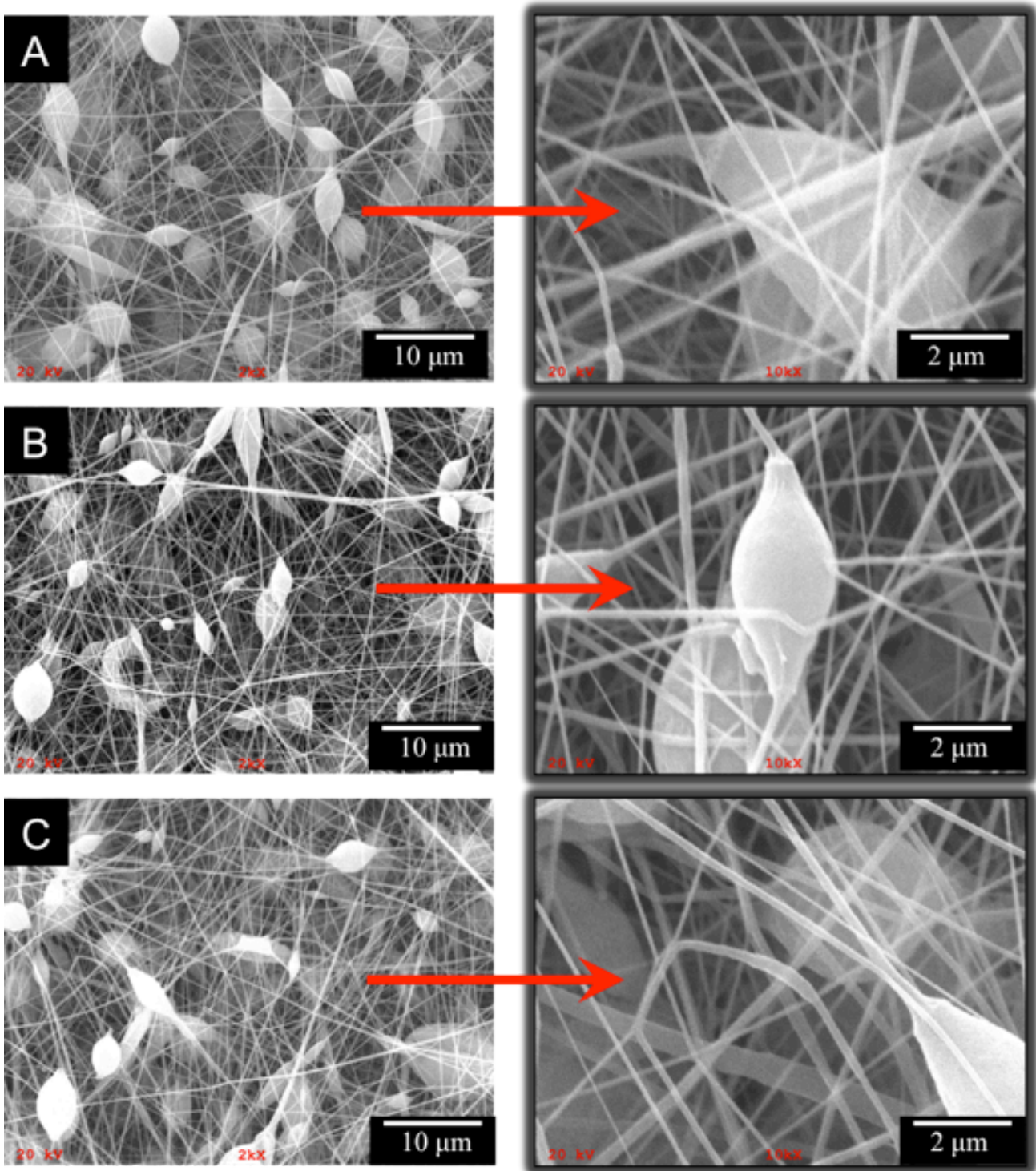


**Figure 3.2.** SEM images of 10 wt.% solutions of PVDF in 50:50 DMAc:acetone with a constant flow rate and varying applied potentials. A.) 8 kV, B.) 12 kV, C.) 16 kV.

The average fiber diameters for fiber mats spun with varying voltages were determined via analysis of SEM images and are tabulated in **Table 3.2** below. One can see that as the potential increases from 8 to 12 kV, the average fiber diameter decreases (within this voltage range for PVDF in DMAc:acetone). This is most likely due to the fact that as the polymer becomes more and more charged, the velocity of the polymer jet increases. This increase in the velocity subsequently causes the polymer fiber to elongate faster during the instability region, resulting in smaller fiber diameters. However, the data in **Table 3.2** indicates that increasing the applied potential from 12kV to 16 kV resulted in an increase in the fiber diameter (back to the diameter of the 8 kV fibers). This increase in fiber diameter was unexpected, but it may be due to the increased velocity carrying the polymer jet (and subsequent fiber) to the collector too rapidly to elongate as effectively as the 12 kV samples. The fast moving fibers do not have the time necessary to elongate and thin during the instability region because they are speeding towards the collector too quickly. This suggests that there may be a balance between the surface charge of the polymer jet and the electric field produced from the applied potential. In order to produce very small fibers, the applied potential must be optimized for each polymer system. Analysis of the fiber diameters also showed that for the 16 kV electrospun PVDF mats, the fiber diameters followed a bimodal distribution. In this distribution, a little over half of the fibers had an average diameter of close to 80 nm while the rest displayed a diameter averaging close to 200 nm. This bimodal distribution may be the result of a phenomenon known as splaying. If the polymer jet elongating from the droplet becomes overcharged, then the elongating fiber could split (or splay) into several smaller fibers. This behavior is not maintained throughout the

electrospinning process and occurs many times for each sample. This reoccurring, brief event could be what causes fibers of two different average diameters to collect on the target. Because of this high degree of structural control, electrospinning PVDF has emerged as the production method of choice for PGEs.

**Table 3.2:** Average fiber diameters of PVDF electrospun from a 10 wt.% solution in DMAc:acetone with various voltages.

Applied Potential	Average Diameter of Fibers
8	160 ± 30
12	120 ± 30
16	160 ± 60

In 2003, a paper detailed the electrospinning of PVDF for potential use as a polymeric-gel electrolyte. The microporous polymeric matrix was swollen with a 1 M LiPF<sub>6</sub>-EC/DMC (1:1, wt./wt.) solution where EC is ethylene carbonate and DMC is dimethyl carbonate. It was suggested that, due to the 3-dimensional network structure of the electrospun mat, the liquid electrolyte could be easily incorporated and held in the pores between fibers resulting in good electrochemical and mechanical properties.<sup>5</sup> Upon swelling with a liquid electrolyte, these mats were reported to exist as three component systems: a solid polymer phase with partially swollen PVDF fibers (responsible for the mechanical strength), a gel phase formed on the fiber surface by swelling (responsible for holding the liquid tightly within the mat), and a liquid phase of pores filled with the electrolyte solution (responsible for the majority of the ionic conductivity). The resulting

freestanding polymeric-gel electrolyte displayed high ionic conductivity at room temperature ( $\sim 2$  mS/cm), electrochemical stability up to 4.5V, and a stable interface with the electrodes of a prototype cell.<sup>5</sup>

Several publications involving electrospinning PVDF and PVDF derivatives have subsequently been submitted, focusing on the various aspects that the electrospun fiber mats have to offer. According to one publication, annealing can enhance the mechanical strength of an electrospun mat of PVDF. Electrospun mats of PVDF following a thermal treatment of 160 °C for 2h displayed a higher modulus, a higher tensile strength, and a larger elongation at break as compared to as-spun samples. This enhancement in mechanical properties was attributed to increased crystallinity and interfiber bonding (melding) as a result of the thermal treatment.<sup>2</sup> **Figure 3.3** shows the stress-strain curves of the as-spun and the annealed PVDF electrospun fiber mats.

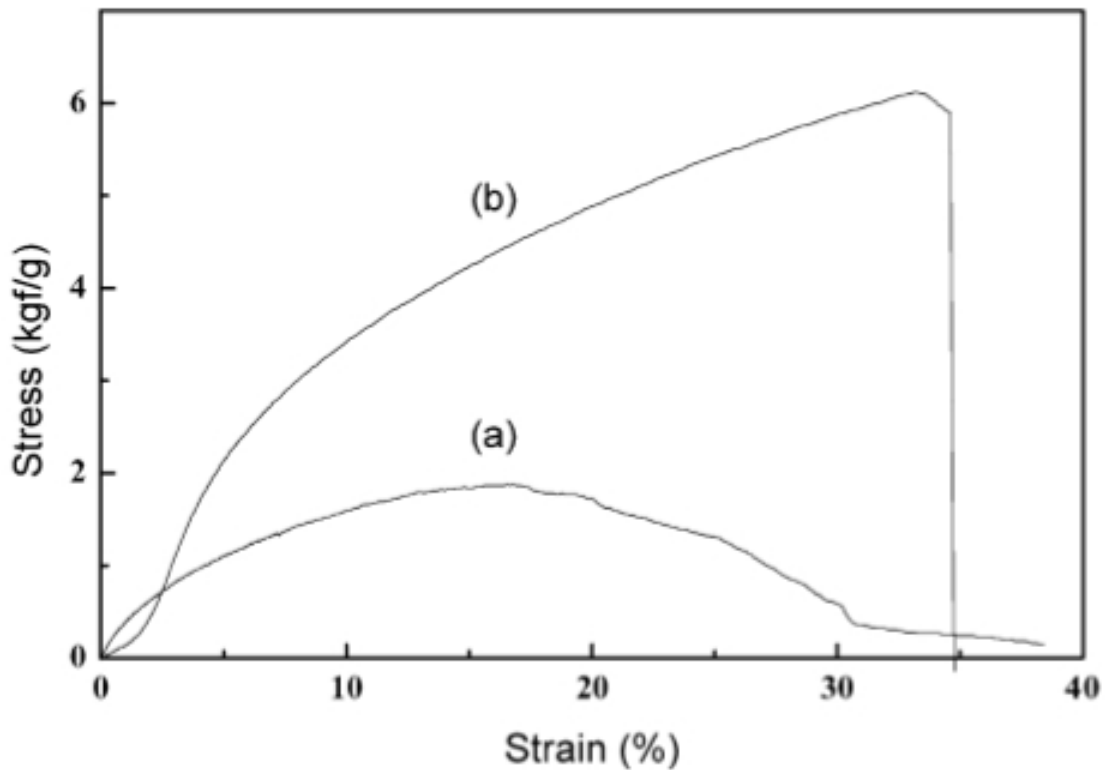


**Figure 3.3:** Stress-Strain curve of PVDF electrospun fiber mats **a.)** as-spun and **b.)** after thermal annealing at 160 °C for 2 hours.<sup>2</sup> Figure copied with permission from reference 2.<sup>2</sup>

Our work on annealing PVDF electrospun fiber mats confirms findings reported by Choi *et al.* revealing that annealing at 100 °C (150 °C for Choi) increases the average fiber diameter.<sup>2</sup> SEM images from our work (**Figure 3.4**) show that the morphology of the fiber mats changes also. Prior to annealing, the fiber mats have a large population of beads. After annealing at 100 °C for 20 h, the number of beads decreases, and evidence of fiber melding is present, as the average diameter appears to increase. The loss of beads unifies the polymer fibers and the melding could presumably lead to the enhanced mechanical properties reported by Choi and coworkers.

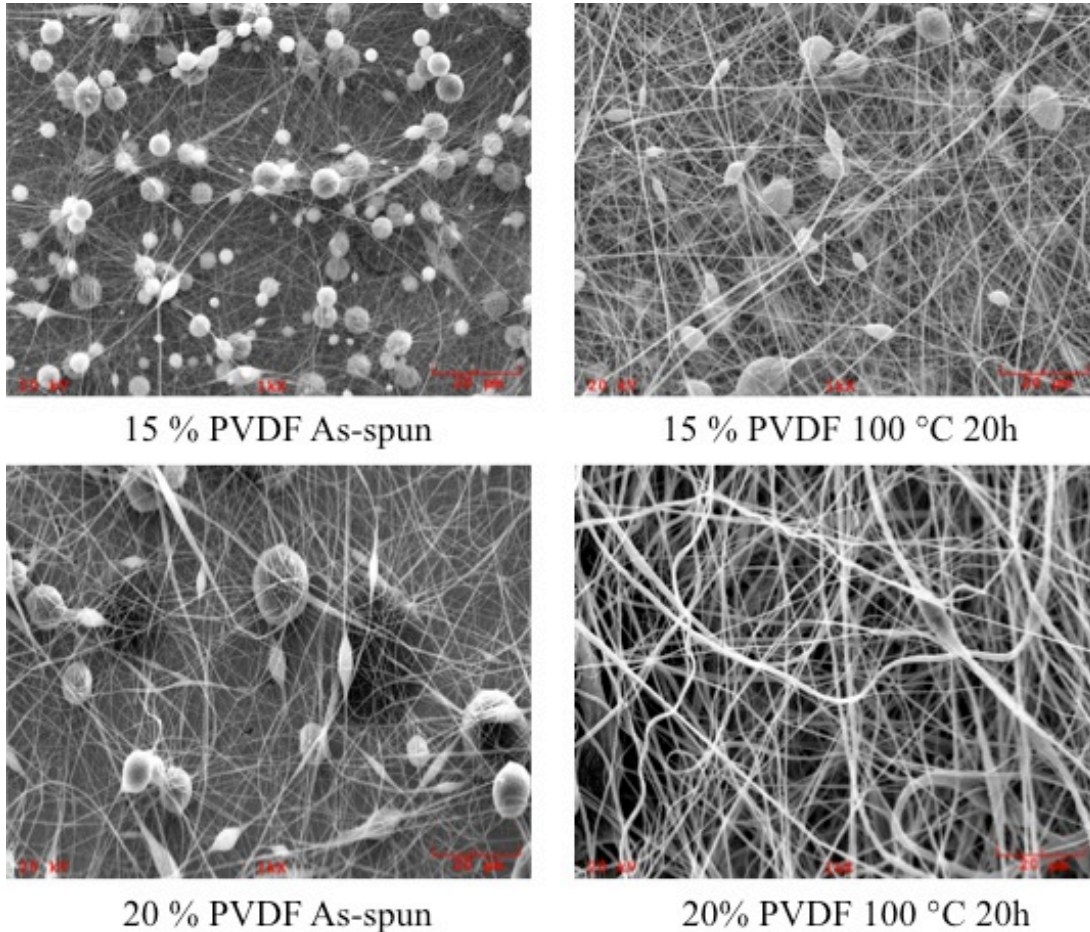


**Figure 3.4:** SEM images of PVDF fibers electrospun from two different polymer concentrations. Annealing at 100 °C results in a reduction of beads and a densification of polymer fibers along with possible fiber melding.

Other workers have investigated the importance of porosity and pore size in electrospun PVDF polymer-gel electrolytes.<sup>9</sup> According to Kim *et al.*, the ionic conductivity of electrospun PVDF fiber mats increased as the average fiber diameter decreased. **Figure 3.5** shows Kim’s findings, displaying the relationship between the average fiber diameter and the average pore size. The average porosity was found to be approximately 88% (determined from a ratio of the membrane density to the polymer

density) when the average fiber size was 0.45  $\mu\text{m}$ . As the average fiber diameter increased (up to 1.38  $\mu\text{m}$ ), the average porosity decreased to 80%. Thinner fibers are able to stack closer together, ultimately increasing the overall density of the fiber mats. The ability to stack closer results in smaller interstitial spacing, thus reducing the overall pore sizes. Conversely, as the diameter of the fibers increased, the mean pore size also increased. Thicker fibers result in loose packing, increasing the interstitial spaces between fibers. Additionally, Kim's results showed that due to the large surface area and the higher porosities, the electrospun mats of PVDF with smaller fiber diameters absorbed more liquid electrolyte. The ability to absorb larger amounts of liquid electrolyte ultimately led to a higher ionic conductivity.

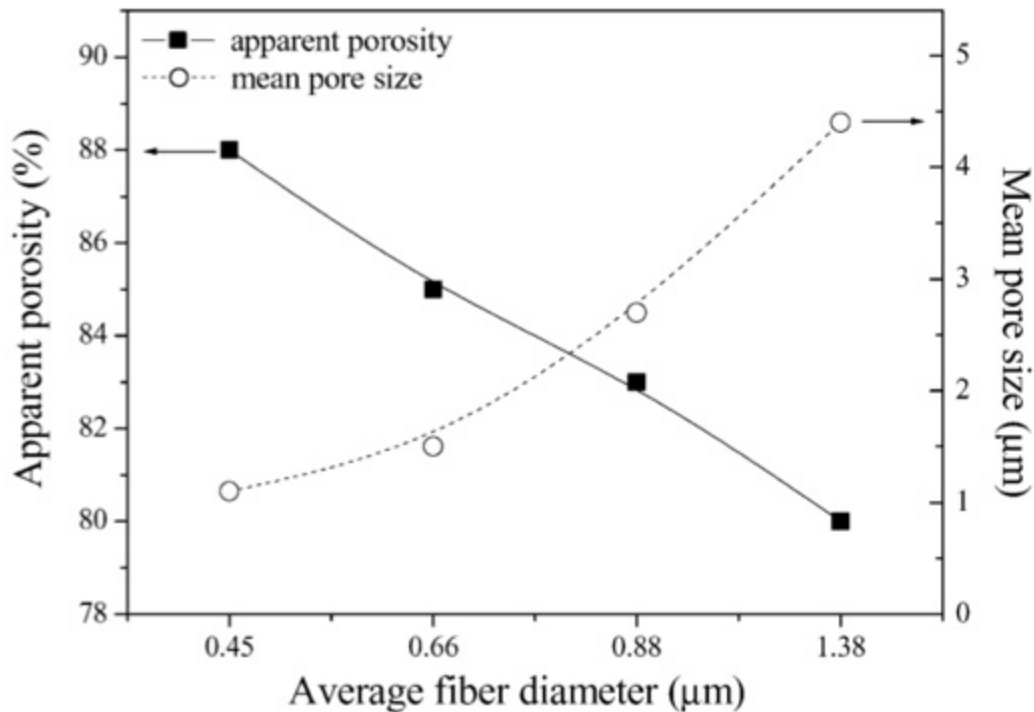


**Figure 3.5:** Porosity and mean pore size as a function of average fiber diameter. Image copied with permission from reference 9.<sup>9</sup>

To further improve the performance of PVDF-based electrospun electrolytes, copolymers with hexafluoropropylene (HFP), and blends with other polymers including polyacrylonitrile (PAN) and poly(methyl methacrylate) (PMMA) have been developed and characterized. The copolymer of PVDF-HFP exhibited a higher ionic conductivity, which was attributed to the reduction of crystallinity afforded by the HFP regions.<sup>10, 11</sup> Electrospun blends of PVDF and PAN resulted in polymer-gel electrolytes with very high room temperature conductivities (~8 mS/cm) and the addition of PAN also lowers the interfacial resistance between the electrolyte and the electrodes.<sup>12</sup> Electrospun blends of PVDF-HFP and PMMA showed even higher electrolyte uptakes than the PVDF or PVDF/PAN microporous membranes. These mats exhibited good room temperature conductivity, less leakage and better mechanical properties than pristine PVDF-HFP electrospun polymer-gel electrolytes.<sup>10</sup>

Although PVDF and its derivatives are the most widely studied electrospun, polymeric-gel electrolytes, other polymers have been electrospun and investigated for potential application as electrolytes for lithium batteries. Poly(acrylonitrile) has been previously electrospun and evaluated for incorporation as a PGE in lithium batteries.<sup>13</sup> PAN has received much attention in the PGE arena due to its suggested interactions with Li<sup>+</sup> ions. Raman spectroscopy has shown that the C≡N stretch adopts a shoulder as the lithium salt concentration increases, suggesting an interaction between the nitrile group and the Li<sup>+</sup> cation.<sup>14, 15</sup> PAN electrospun into fiber mats and swollen with a solution of EC:DMC:DEC (where DEC is diethyl carbonate) containing 1M LiPF<sub>6</sub> exhibited remarkably high liquid electrolyte uptake (upwards of 1100 %). These mats had porosities greater than 80% (compared to commercial polypropylene membranes that

have porosities around 35%) and displayed ionic conductivities of  $1.7 \times 10^{-5}$  S/cm at 20 °C.<sup>13</sup> Although these PAN fibers displayed low conductivities, the charge-discharge capacities out-performed that of a commercial polypropylene separator. The authors attributed the enhanced performance to the PAN mat's ability to absorb more liquid electrolyte; however, the interactions between the lone pair of electrons on the nitrogen and the Li<sup>+</sup> ions were likely substantial in dictating the electrochemical properties of these PGEs.

To date, polymers conventionally used in electrospun electrolyte applications (e.g., PVDF) have limited affinity toward lithium ions (with the PAN exception), do not swell appreciably in electrolyte solvents, and thus are essentially inert cages to encapsulate the electrolyte with little, if any, contribution to ionic conductivity.<sup>3</sup> Recent reports of electrospun electrolyte systems demonstrated room temperature conductivities in the range of  $(5.3-7.8) \times 10^{-3}$  S/cm with electrolyte loadings limited to a maximum of about 400 wt% (based on the mass of the dry mat).<sup>12, 16, 17</sup>

### ***3.2. Electrospinning Crosslinked PEO Mats***

Although PEO is the benchmark material for SPEs due to its inherent affinity towards Li<sup>+</sup> ions and desirable chain/transport dynamics, it has yet to be utilized as a polymeric-gel electrolyte material due to its high solubility in common electrolyte solvents. To overcome this undesirable solubility of PEO, photoinitiated reactions may be utilized to crosslink the polymer.<sup>18</sup> In 2001, Doytcheva<sup>19</sup> demonstrated that PEO films and powders may be crosslinked using pentaerythritol triacrylate (PETA) to greatly reduce solubility in polar solvents. Recently, Zhou<sup>20</sup> used this UV-initiated approach to

crosslink electrospun PEO/cellulose nanocrystal composites for tissue scaffolds used in aqueous media. To greatly improve the performance of polymer-based electrolytes, we report here the application of crosslinked (insoluble) PEO electrospun fiber mats as structured electrolyte frameworks for Li<sup>+</sup> battery applications. With this approach, we envision a hybrid electrolyte that encompasses the advantages of both electrospun fibrous frameworks (operative on micron length scales) and conventional PGEs (operative on molecular length scales).

### ***3.3. Experimental***

#### ***3.3.1 Materials***

Poly(ethylene oxide) (PEO,  $M_n = 300,000$ , Aldrich Chemical Co.), pentaerythritol triacrylate (PETA, Aldrich Chemical Co.), poly(vinylidene fluoride) (Kynar<sup>®</sup>), methanol (MeOH, Aldrich Chemical Co.), dimethylacetamide (DMAc, Aldrich Chemical Co.), acetone (Aldrich Chemical Co.), ethylene carbonate and dimethyl carbonate (Aldrich Chemical Co.), and anhydrous acetonitrile (Aldrich Chemical Co.) were used as received. Lithium perchlorate (LiClO<sub>4</sub>, Aldrich Chemical Co.) was dried under vacuum at 100 °C for 24 h and stored in a desiccator before use.

#### ***3.3.2 Preparation of Electrospun Mats***

Nonwoven PEO mats were prepared by electrospinning at room temperature using a Spellman high voltage source (Berton 205B) and a KDscientific 100 syringe pump. Solutions of PEO and PETA were prepared in acetonitrile at a composition of 5% wt./vol. PEO and variable compositions of PETA. These polymer solutions were

extruded from a 3-mL syringe through a non-bevelled stainless steel needle tip having an inner diameter of approximately 0.8 mm, at a flow rate of 4 mL/hr. The voltage applied to the needle tip ranged from 8 - 12 kV (negative biased) and the distance from needle tip to collector was 25 cm. The electrospun fibers were collected on a 1 cm diameter aluminium cylinder rotating at approximately 200 RPM. The resulting fiber mats contained 10% wt. PETA (**PEO10**), 20% wt. PETA (**PEO20**), and 30% wt. PETA (**PEO30**), based on the mass of PEO. As a control, PVDF mats were electrospun from 20% wt./vol. solutions in 1:1 DMAc:acetone to yield comparable mat architectures (i.e., fiber diameter and porosity).

### ***3.3.2.1 Cross-Linking and Characterization of PEO-PETA Mats***

The electrospun mats were removed from the collector, placed on stainless steel plates, and positioned under a 459 watt mercury vapour UV lamp at a distance 25 cm. The mats were exposed to the UV light for 30 minutes on each side for a total exposure time of 60 minutes. To determine the gel fractions, the resulting cross-linked mats were weighed, ultrasonicated in methanol for one hour, dried in a vacuum oven at 25 °C overnight, and then re-weighed. Based on the mass before and after MeOH exposure, a standard gravimetric method was used to calculate the gel fraction.

### ***3.3.2.2 Optical Characterization with SEM***

Scanning electron microscopy (SEM) was used to image the resulting fiber mats. Prior to SEM analysis, the mats were gold sputter coated using a Denton Vacuum Desk V sputter coater. A Joel Neoscope JCM 5000 SEM with an electron acceleration of 15kV was used to image all samples. An FEI Quanta 600 FEG environmental scanning electron

microscopy (ESEM) equipped with a Bruker EDX silicon drift detector was used to image fiber mats exposed to liquid water.

### 3.3.3. Porosity Measurements

Porosity measurements were obtained using the *n*-butanol uptake method.<sup>4</sup> Prior to porosity measurements, the samples were exposed to methanol (same treatment as gel fraction procedure) to remove the soluble fraction of PEO in the mats. Subsequently, each MeOH washed sample was submerged in a solution of *n*-butanol for 24h (note that *n*-butanol is a non-solvent for PEO). Afterward, each sample was blotted to remove excess surface liquid and weighed to determine the mass of *n*-butanol absorbed. Using the following equation, the porosities,  $P(\%)$ , for each mat were calculated as,

$$P(\%) = \frac{M_{BuOH}/\rho_{BuOH}}{M_{BuOH}/\rho_{BuOH} + M_{mat}/\rho_{PEO}} \quad (1)$$

where  $M_{BuOH}$  is the mass of the butanol taken up by the fiber mat,  $\rho_{BuOH}$  is the density of butanol,  $M_{mat}$  is the mass of the fiber mat used, and  $\rho_{PEO}$  is the density of the polymer.

### 3.3.4. Conductivity Measurements

To facilitate the uptake of  $Li^+$  ions into the PEO framework, the mats were ultrasonicated in a 1M lithium perchlorate ( $LiClO_4$ ) solution in methanol for 1 hour. The pre-loaded mats were then quickly rinsed with pure MeOH and dried in a vacuum oven at 25 °C overnight. After drying, each sample was weighed and the average  $LiClO_4$  uptake was found to be approximately 100 wt.% of the original fiber mat mass. For control experiments, without pre-loaded  $LiClO_4$ , the mats were ultrasonicated in pure methanol, followed by drying in a vacuum oven at 25 °C overnight. The samples were then swollen

with an electrolyte solution containing 1M LiClO<sub>4</sub> in a 1:1 mixture, by volume, of ethylene carbonate (EC) and dimethyl carbonate (DMC). Electrolyte swollen samples containing 400 wt % electrolyte were sandwiched between two gold plated stainless steel electrodes of a Solartron 12960 sample holder containing a built in micrometer. For AC impedance spectroscopy, a Solartron SI 1260 impedance analyzer was used along with the Scribner Z-Plot software to obtain standard Nyquist plots in the frequency range of 1.7 MHz to 0.1 Hz. The high frequency intercept of the real impedance,  $Z'$ , of the materials was considered to be the electrolyte resistance,  $R$ , following accepted protocol.<sup>4, 7, 21</sup> Using the equation below,

$$\sigma = \frac{d}{R \times S} \quad (2)$$

conductivities,  $\sigma$ , of the electrolyte swollen mats of surface area,  $S$ , and thickness,  $d$ , were calculated.<sup>4</sup> Mat thickness values were determined using the built-in micrometer during impedance measurements.

### **3.4. Results**

After electrospinning, the fibrous mats were imaged and fiber diameter histograms were plotted. **Figure 3.6** shows a representative SEM image immediately following the electrospinning and UV irradiation process. As indicated in the histograms (**Figure 3.7**), the average fiber diameter was found to be  $1 \pm 0.3 \mu\text{m}$ . The SEM images also show that the fibers are isotropically distributed within the mat with little or no preferential orientation.

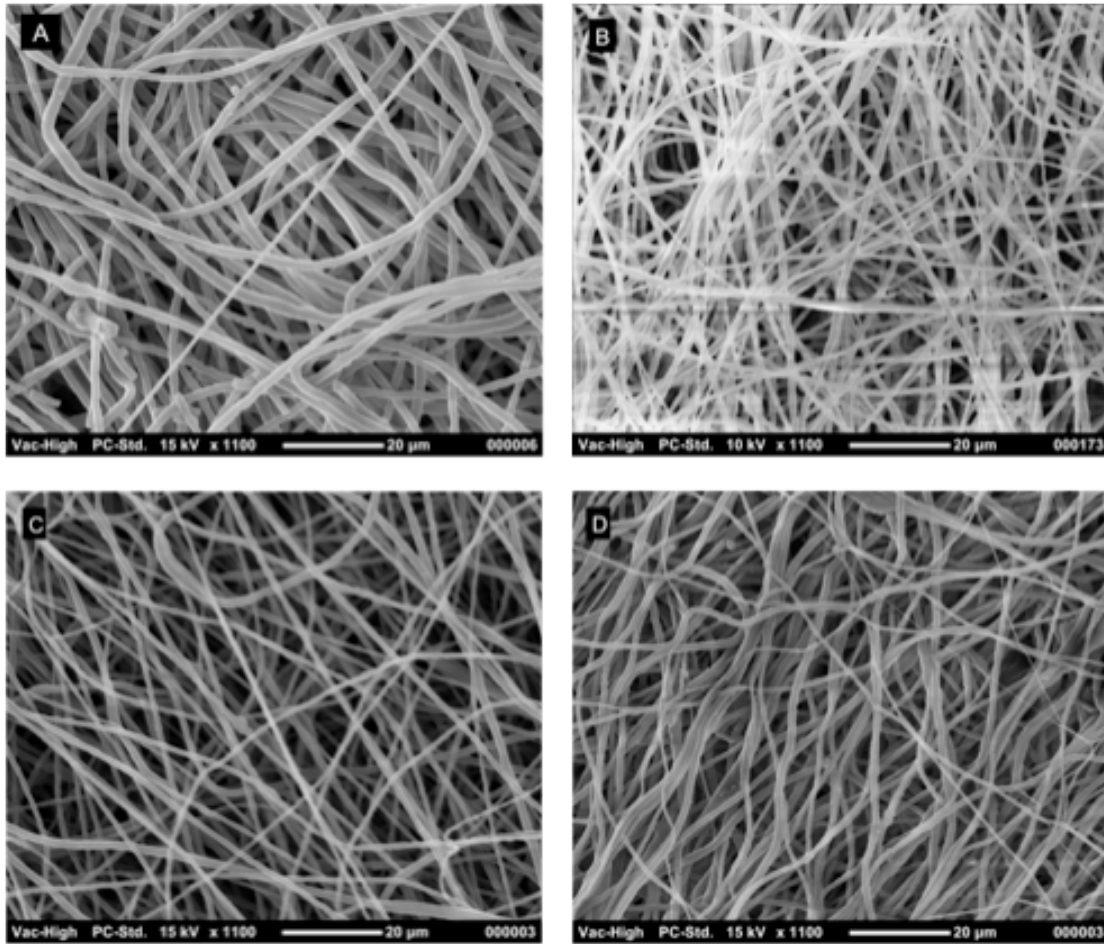


**Figure 3.6.** SEM images of PEO with various amounts of PETA after UV exposure: **A.)** pure PEO, **B.)** PEO10 **C.)** PEO20, **D.)** PEO30.

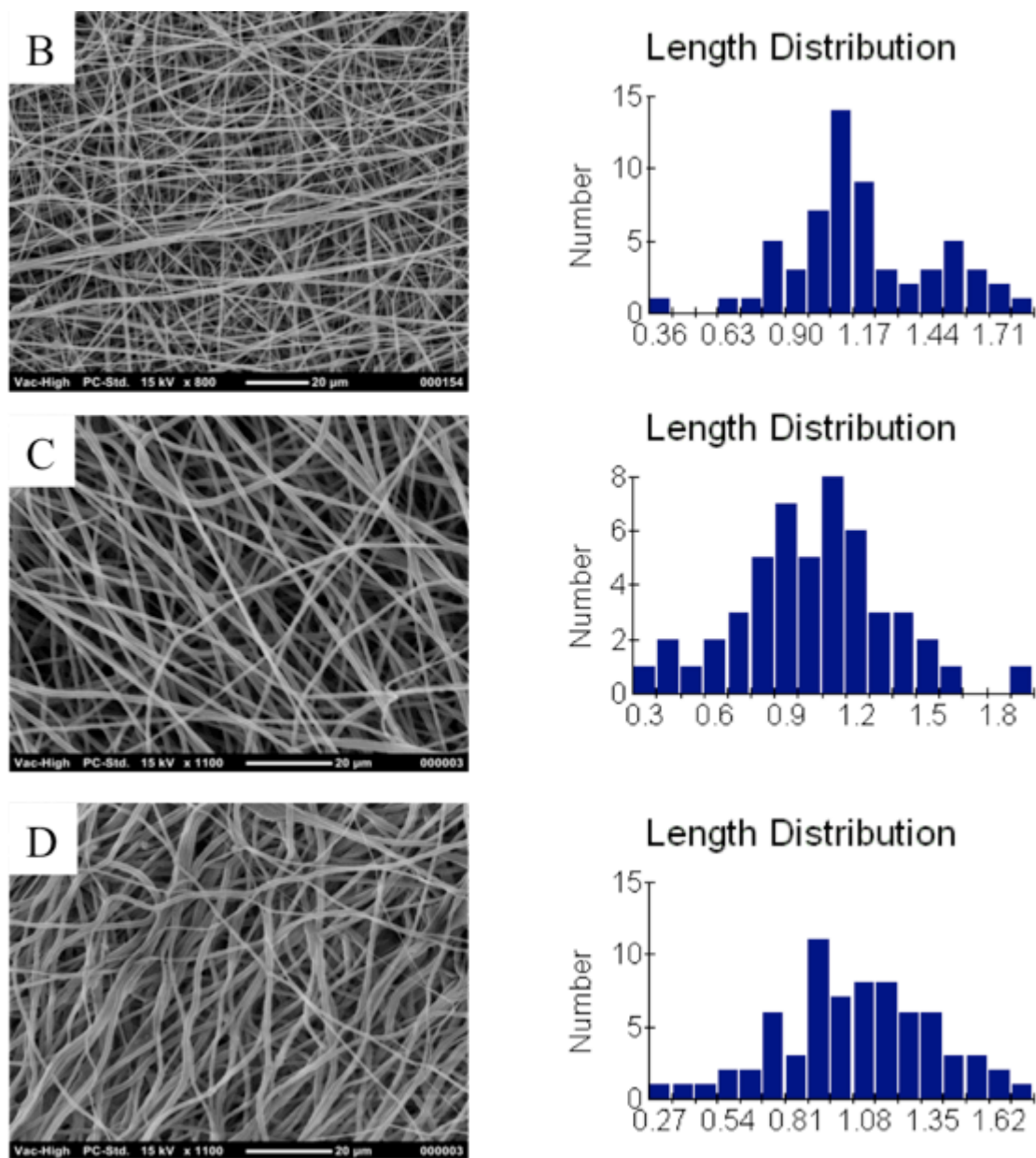


**Figure 3.7.** SEM images of PEO electrospun fibers containing various wt.% or PETA along with corresponding fiber diameter histograms for A.) PEO10 B.) PEO20 and C.) PEO30.

Following UV irradiation, gel fractions were determined gravimetrically after exposing the fiber mats to methanol under ultrasonic agitation for 1 hour. The original mass of each sample was compared to the mass after the ultrasonic methanol wash and the results are listed in **Table 3.3**. Each PEO/PETA fiber mat retained 80 – 90% of its

original mass. Since linear PEO is completely soluble in methanol, the pure PEO mats (without PETA) exposed to UV irradiation completely dissolved in methanol. However, the resulting insolubility of the UV irradiated PEO/PETA mats confirms that PETA is an efficient crosslinking agent for PEO. As reported in previous works,<sup>19,20</sup> PETA acts not only as the photo-initiator but also as the crosslinking agent.

The gel fraction data (insoluble fraction) in **Table 3.3** indicates that increasing the amount of crosslinking agent results in a small increase in the fraction of insoluble PEO. Since PEO is soluble in many polar organic solvents common to PGEs, it is imperative for the mats to be highly crosslinked so as not to dissolve upon solvent exposure. The high gel fraction and observed insolubility (including exposure to various alkyl carbonate solvents) supports the feasibility for these crosslinked fiber mats to be utilized as structured electrolytes in PGE-based Li-ion batteries.

In conventional PGEs, the ionic conductivity is often dependent on the porosity and tortuosity through pores within the polymer membrane.<sup>4, 22</sup> Using the *n*-butanol uptake method,<sup>4</sup> the porosities of each of the structured electrolyte samples were determined and are listed in **Table 3.3**. While the SEM images of the as-spun, UV irradiated mats in **Figure 3.7** would imply similar porosities for all PETA compositions, it is surprising to note that the porosity data in **Table 3.3** show that an increase in the PETA composition results in an increase in the porosity. For the PEO10 sample, the porosity was found to be significantly lower than that of the mats containing higher PETA contents. This unexpected observation may be explained by analysis of the mat morphology following the solvent exposure processes used to determine the gel fraction and porosity values.

**Table 3.3.** Gel fraction and porosity of PEO fiber mats crosslinked with various amounts of PETA after one-hour methanol ultrasonication.

PETA % wt.	Gel Fraction (wt.%)	Porosity (vol.%)
10	82 ± 0.5	65 ± 5
20	84 ± 1.4	83 ± 1
30	86 ± 1.5	85 ± 1
PVDF	NA	80 ± 1

SEM images of the fiber mats after solvent exposure (ultrasonic agitation in methanol) are shown in **Figure 3.8**. For the PEO10 sample, the discrete fiber morphology observed in the as-spun state (**Figure 3.8B**) becomes noticeably perturbed following solvent exposure (**Figure 3.8A**). The PEO10 mat appears to have densified by partial fusing of the fibrous framework. This solvent induced densification behaviour effectively decreases the porosity of the mat. Given that the PEO10 mat exhibited the lowest gel fraction, the densification may be attributed to a low crosslink density and consequently greater polymer chain mobility as a result of using a relatively lower amount of crosslinking agent. However, as the amount of PETA increases, it is likely that the crosslink density increases such that the PEO fibers retain more of their original discrete fibrous morphology. Clearly fiber fusion diminishes as the PETA content increases to 20 and 30 wt.% (**Figures 3.8B and 3.8C**), which is consistent with the observed higher porosities (**Table 3.3**).

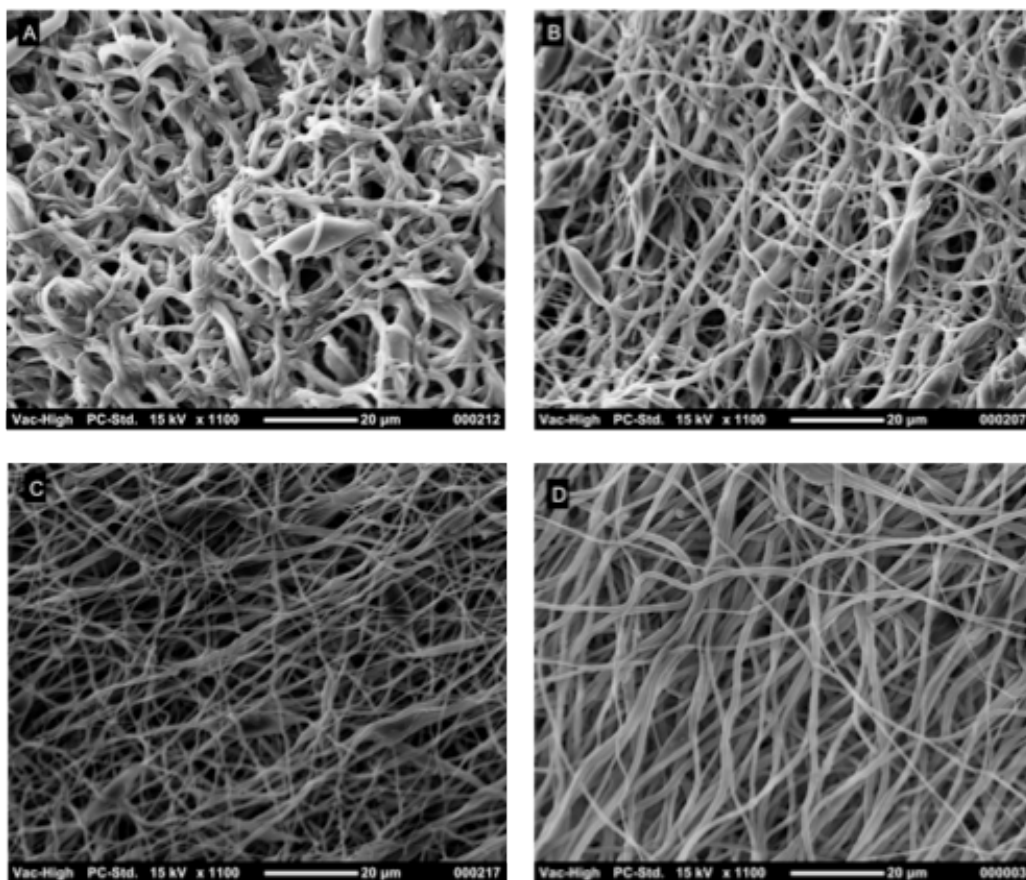


**Figure 3.8.** SEM images of electrospun PEO/PETA mats following ultrasonic agitation in methanol for A.) PEO10 B.) PEO20 C.) PEO30 and D.) PEO30 as spun (no MeOH wash).

### ***3.4.1. Lithium Loading***

The differentiating aspects of these polymer-based electrolytes, in comparison to conventional PGEs, are that the structured PEO framework remains intact upon exposure to the liquid electrolyte component (due to cross-linking), and that the supporting polymer structure is capable of actively participating in  $\text{Li}^+$  ion complexation and transport. In order to ensure that the PEO polymer chains within the fibrous framework are capable of participating in  $\text{Li}^+$  ion transport,  $\text{Li}^+$  ions must be introduced into the polymer fibers. Introducing  $\text{Li}^+$  ions into polymeric fibers can be accomplished, to a limited

extent, by swelling the mats with a liquid electrolyte containing lithium salts. Alternatively, we have found that  $\text{Li}^+$  ions may be easily introduced into the fibers (before electrolyte swelling) by exposing the crosslinked mats to a solution of lithium perchlorate in methanol with ultrasonic agitation. This pre-loading process insures that the ions are intimately associated with the PEO chains within the fibers, and effectively increases the number of charge carriers for maximum involvement in conductivity. Using this pre-loading process, the average amount of lithium salt loaded into the electrospun mats was determined gravimetrically to be approximately 100 wt. %, based on the dry mass of the mat. As a control, PVDF electrospun samples were also subjected to the same pre-loading process. SEM images immediately following the pre-loading procedure (**Figure 3.9**) clearly show that PEO and PVDF fiber mats absorb the lithium salt very differently. In the PEO mat sample (**Figure 3.9A**), the fibers appears to be uniformly swollen with no visual evidence of excess lithium perchlorate crystals external to the fibers, indicating that the salt is easily accommodated within the cross-linked polymer fibers. In contrast, the PVDF mat sample (**Figure 3.9B**) contains coarse salt aggregates (crystals) dispersed between the fibers, demonstrating that the pre-loaded salt is not appreciably incorporated within the PVDF fibers.

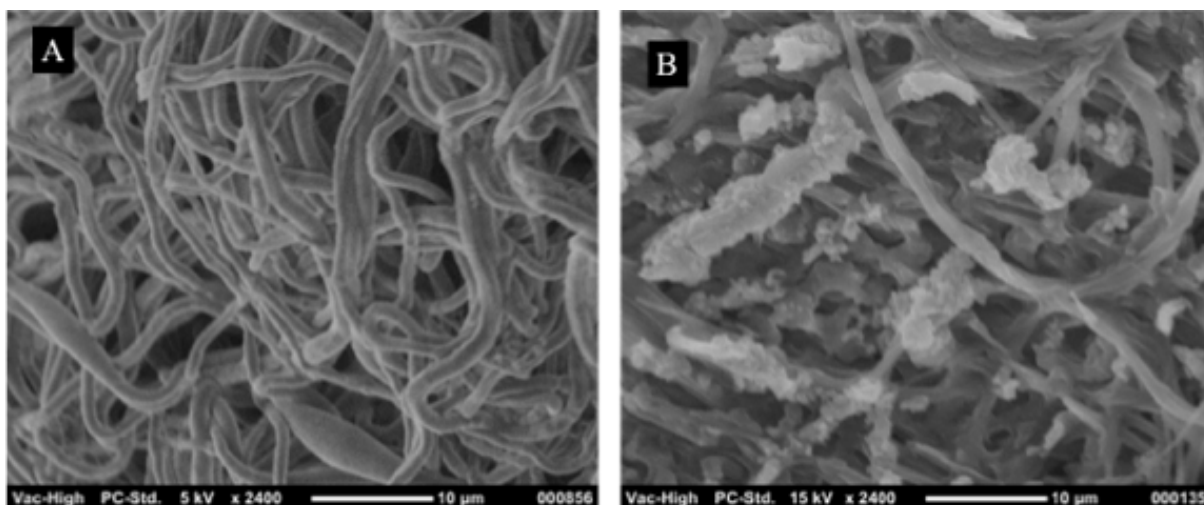


**Figure 3.9.** SEM images of electrospun fibers A.) PEO30 and B.) PVDF after loading with approximately 100 wt.% LiClO<sub>4</sub>.

### 3.4.2. Electrolyte Swelling

To act as a structured PGE, the cross-linked PEO fiber mats must be swollen with liquid electrolyte in a manner that preserves the fibrous framework architecture. Equilibrium swelling data (**Figure 3.10**) show that these PEO-based mats have a remarkably high affinity for the liquid electrolyte. In contrast to conventional PVDF-based PGEs, which have been shown to have equilibrium electrolyte swelling of only 300% to 400%,<sup>9, 12</sup> these PEO mats are effectively super-absorbent and capable of accommodating 2 to 3 times more electrolyte, depending on the degree of crosslinking. With increasing PETA content, the equilibrium swelling in the electrolyte decreases from 1200 wt.% (PEO10) to approximately 800 wt.% (PEO30). Additionally, the electrospun PEO10 fiber mat swells much more than the cast PEO10 sample. This further demonstrates the advantages of using electrospun mats over non-structured membranes. In agreement with the Flory-Rehner equilibrium swelling theory,<sup>23</sup> this decrease in

electrolyte uptake can be attributed to an increase in crosslink density with increasing PETA content.

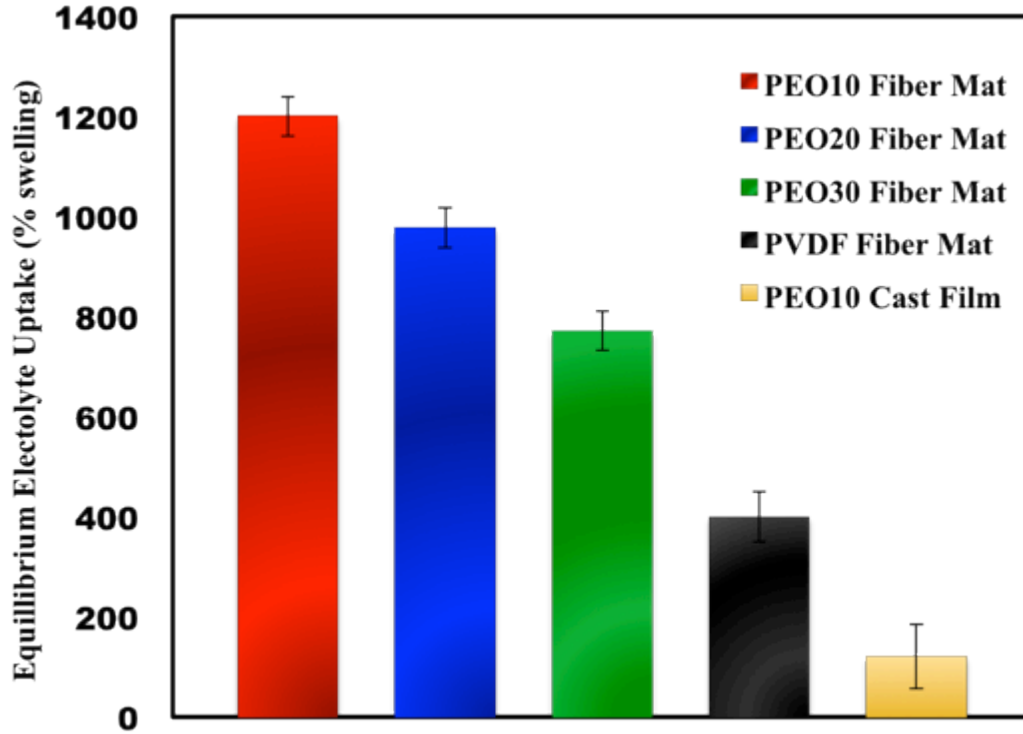


**Figure 3.10.** Equilibrium uptake swelling of PEO/PETA and PVDF membranes absorbing a 1M LiClO<sub>4</sub> solution of EC:DMC (1:1).

According to Flory and Rehner, the molecular weight between crosslinks ( $M_c$ ) can be determined by the following equation:

$$M_c = \frac{V_1 \rho_1 \left( V_{2m}^{1/3} - \frac{V_{2m}}{2} \right)}{-[\ln(1 - V_{2m}) + V_{2m} + \chi V_{2m}^2]} \quad (3)$$

Where  $V_1$  is the molar density of the swelling solvent,  $\rho_1$  is the initial density of the polymer,  $V_{2m}$  is the equilibrium volume fraction of the polymer, and  $\chi$  is the solvent-

polymer interaction parameter.<sup>23, 24</sup>  $V_{2m}$  may be calculated by weighing the polymer sample before ( $\omega_0$ ) and after ( $\omega_s$ ) swelling using the following equations:

$$V_{eq} = \frac{\omega_0}{\rho_2} + \frac{\omega_s + \omega_0}{\rho_1} \quad (4)$$

$$V_{2m} = \frac{\omega_0}{V_{eq} \times \rho_2} \quad (5)$$

Where  $\rho_1$  is the solvent density, and  $\rho_2$  is the polymer density. Once the  $V_{2m}$  was calculated, the number average molecular weight between crosslinks could be determined as well as the crosslink density ( $1/2M_c$ ). As one can see from **Equation 3**, the  $\chi$  interaction parameter plays an important role in determining the  $M_c$ . Using the Bristow and Watson semi-empirical equation, the interaction parameter for crosslinked PEO swollen with ethanol was calculated.

$$\chi = \beta_1 + \left(\frac{V_s}{RT}\right) (\delta_s - \delta_p)^2 \quad (6)$$

Where  $\beta_1$  is the lattice constant (usually 0.34),  $V_s$  is the molar volume of the solvent,  $R$  is the universal gas constant,  $T$  is the absolute temperature, and  $\delta$  is the solubility parameter of the solvent ( $\delta_s = 12.92 \text{ cal/cm}^3$ ) and the polymer ( $\delta_p = 12.0 \text{ cal/cm}^3$ ).<sup>24-26</sup> Using **Equation 6**, the interaction parameter for PEO and ethanol was calculated to be 0.43. Using **Equation 3**, the number average molecular weights between crosslinks for various PEO/PETA electrospun samples were calculated and are presented in **Table 3.4**.

**Table 3.4.** The number average molecular weights between crosslinks and the crosslink density, as a function of PETA concentration.

Electrospun Sample	Number Average Molecular Weight Between Crosslinks ( $M_c$ )	Crosslink Density
PEO10	25 kg/mol	$2.1 \times 10^{-5}$
PEO20	15 kg/mol	$3.5 \times 10^{-5}$
PEO30	9.5 kg/mol	$5.3 \times 10^{-5}$

It is important to note that the crosslink densities and the  $M_c$  calculated for this system are estimates. As mentioned previously, the  $\chi$  interaction parameter can vastly change the outcome of the  $M_c$  calculated from **Equation 3**. For instance, if a  $\chi$  of 0.3 is used instead of 0.43 then the PEO10  $M_c$  would be roughly 10 kg/mol. That is a two-fold difference resulting from a very small change in the interaction parameter. Thus it is important to realize that the interaction parameter used here (0.43) was calculated assuming there are essentially no interactions of either the PEO or the ethanol with the crosslinking agent PETA. Additionally, the solubility parameter for PEO was selected to be  $12.0 \text{ cal/cm}^3$  from the findings of Allen and Barton, suggesting that the solubility parameter of PEO changes according to the polarity of the solvent and the ability to hydrogen bond. Since a range of 9.2 – 14.5 was suggested for strongly hydrogen-bonded solvents, the average (12.0) was used in the above calculations.<sup>26</sup> Interestingly, the PEO samples exhibited absorbance characteristic that were significantly faster than PVDF analogs. Ethanol swelling versus time is shown in **Figure 3.11**. Additionally, the electrolyte swelling properties of PEO/PETA electrospun membranes show a linear relationship as a function of crosslink density (**Figure 3.12**).

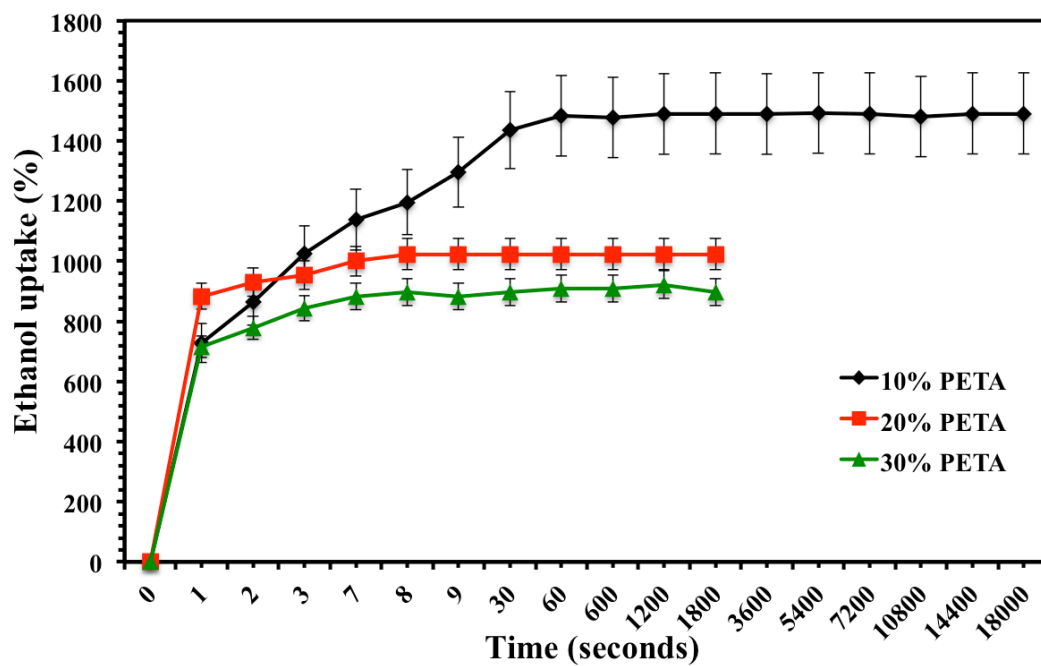
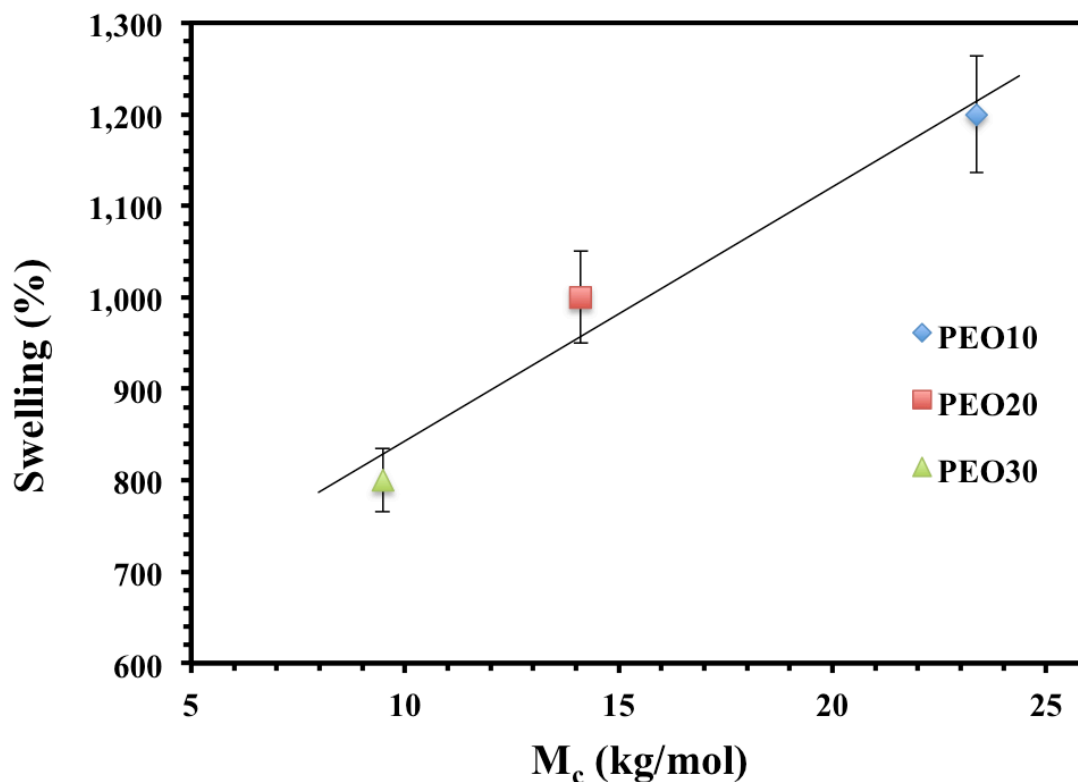


Figure 3.11 Swelling profile for PEO/PETA electrospun fiber mats.



**Figure 3.12** Electrolyte swelling of PEO/PETA fibrous mats as a function of crosslink density.

Although the cross-linked PEO mats are capable of swelling to many times their original mass upon exposure to liquid electrolyte, it is important to note that the chemical cross-linking of the PEO chains within the electrospun fibers preserves the fibrous framework within the solvent swollen PGE. **Figure 3.12A** shows an ESEM micrograph of a PEO10 mat containing 600 wt.% water. Even in this highly swollen state, it is clear that the gel maintains a network structure originating from the fibrous framework of the nonwoven electrospun mat. Upon removal of the swelling solvent (**Figure 3.12B**), little, if any, change is observed in the original structure of the fibrous framework (**Figure 3.8A**). As such, it is reasonable to envision potential conductive pathways for  $\text{Li}^+$  ions within the electrolyte-swollen mats to allow transport through liquid-like domains

between the cross-linked fibers and transport through PEO gel domains within the solvent-swollen cross-linked fibers. We will discuss this potential structural contribution to the  $\text{Li}^+$  ion conductivity of these unique PGEs in more detail below.

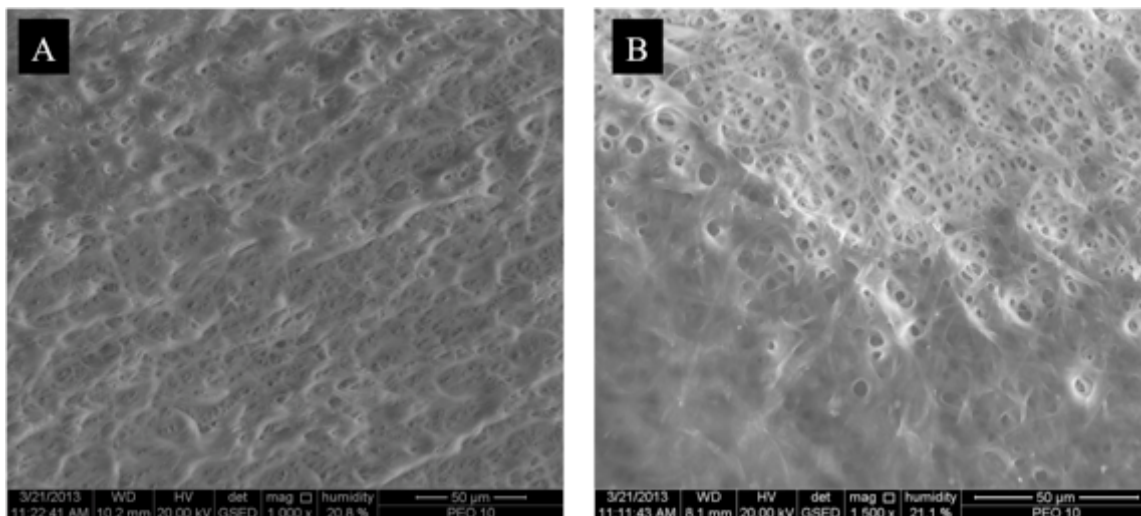


**Figure 3.12.** Environmental SEM images of PEO10 samples A.) Swollen with 600 wt.% water and B.) Image acquired during a gradient drying of a fully immersed mat of PEO10 (top right dry region, bottom left wet region).

To evaluate the PGE performance of the PEO fibrous frameworks and the impact of cross-linker content and pre-loading process on  $\text{Li}^+$  ion transport, ionic conductivities of the electrolyte-swollen mats were compared to the conductivity of a control PVDF mat (having the same physical structure, including fiber diameter and porosity). Since the electrospun PVDF mats were only capable of accommodating 400 wt. % of electrolyte, all conductivity measurements were conducted with a set electrolyte content of 400 wt. % (i.e., only 30% of the maximum electrolyte capacity for the PEO10 mat sample). This was accomplished by evaluating the densities of  $\text{Li}^+$  salt samples and by using a micropipette. **Figure 3.13** below shows the density determination of a 1 M  $\text{LiClO}_4$

sample in ED:DMC (1:1).

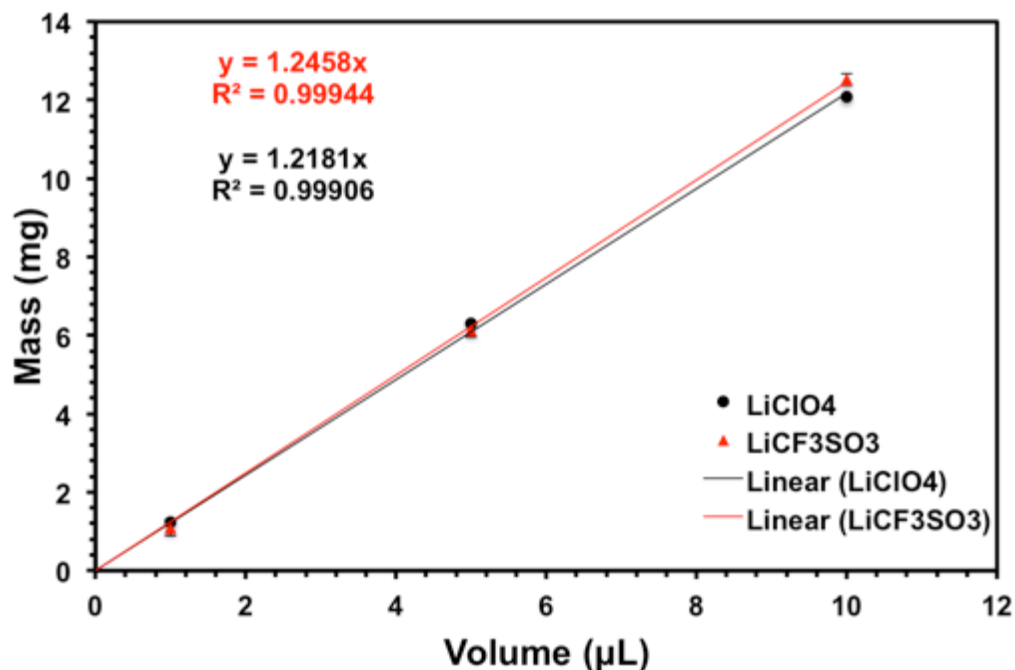


**Figure 3.13.** Density of two lithium salt liquid electrolytes consisting of EC:DMC (1:1 vol.). Black line represents lithium perchlorate ( $\text{LiClO}_4$ ). Red line represents lithium triflate ( $\text{LiCF}_3\text{SO}_3$ ).

### 3.4.3. AC Impedance Spectroscopy

To investigate the potential application of new electrolytes for lithium batteries, AC impedance is a standard test utilized to evaluate ionic conductivity. Equivalent circuit modelling of polymer-gel electrolyte systems using AC impedance has been extensively investigated in the literature and is beyond the scope of this document.<sup>21, 27-30</sup> Briefly, in through-plane AC impedance spectroscopy, an electrolyte is sandwiched between two blocking type electrodes and an alternating current is passed between them in a range of frequencies. An electrochemical analyser monitors the impedance of the sample as the current passes back and forth between the electrodes. As the impedance is

composed of imaginary components ( $Z''$ ) and real components ( $Z'$ ), a plot of  $Z''$  vs  $Z'$  (also known as a Cole-Cole plot) may be used to determine the resistance of the electrolyte. **Figure 3.14** is a schematic explanation of through-plane AC impedance spectroscopy used to determine ionic conductivity.

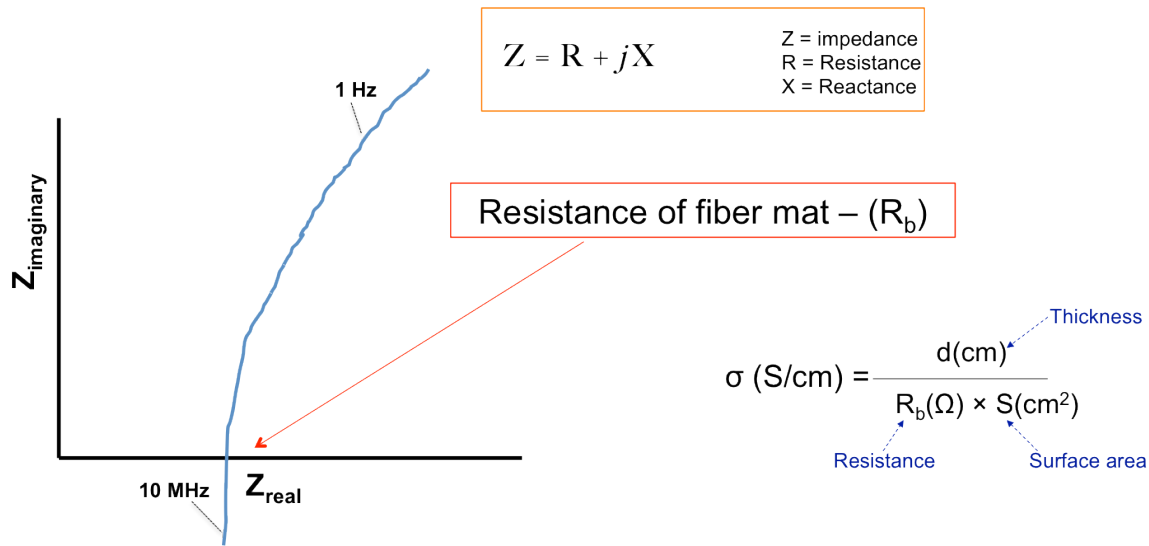


**Figure 3.14.** Through-plane AC impedance schematic. The intercept of the impedance spectra with the real axis yields the membrane resistance (at high frequencies). The real resistance of the fixture was determined based on its high frequency impedance, which was subsequently subtracted from the resistive component of the raw data.

The first thru-plane cell developed in our group consisted of two polished copper electrodes with varying diameters fixed into Teflon<sup>®</sup> sheaths. Copper leads were soldered to the disk electrodes and subsequently attached to the impedance analyser. In order to determine the membrane resistance free of any internal resistance (within the analyser and the fabricated thru-plane cell) and interfacial resistance between the copper electrodes and the PGE, the resistance contributions of each were determined. A series of PEO10 polymeric-gel electrolytes with varying thicknesses was produced and the

resistance as a function of thickness was plotted. As the resistance of the membrane should have a linear relationship to the thickness, extrapolating to zero thickness will yield the internal and interfacial resistance of the system. This value was then subtracted from all impedance values to obtain the true membrane resistance. **Figure 3.15** shows the graph of resistance versus thickness for the homemade through-plane impedance cell.

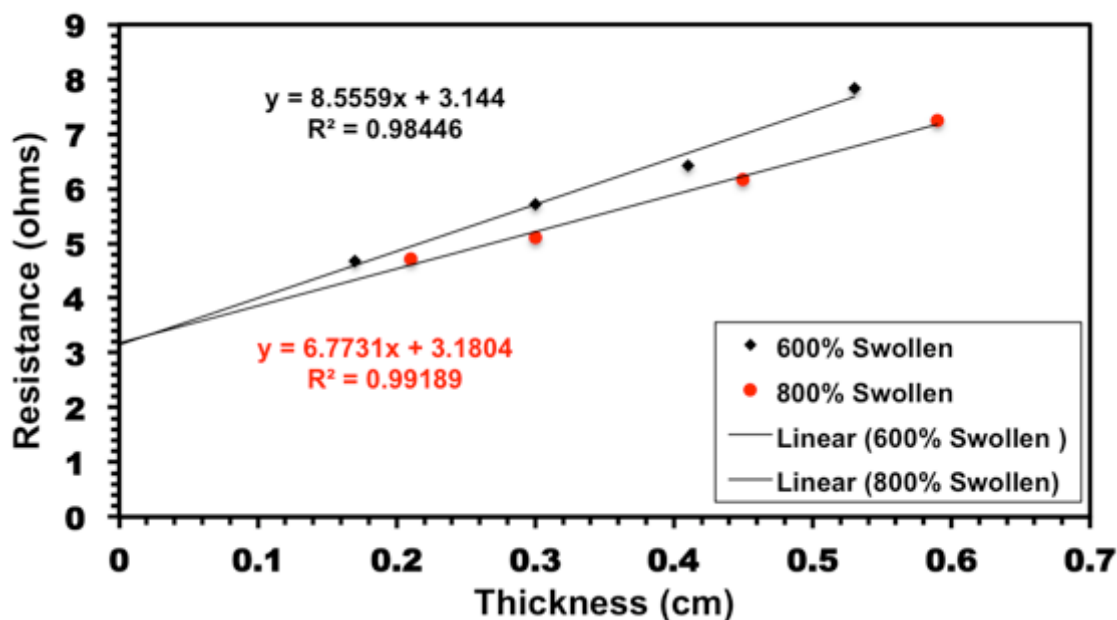


**Figure 3.15.** Resistance of PEO/PETA electrospun polymeric-gel electrolytes swollen with 600 wt.% (black) and 800 wt.% (red) electrolyte solution consisting of 1M LiClO<sub>4</sub> in EC:DMC (1:1). The extrapolated resistances corresponding to the cell and the interface are essentially equal (~3 Ω) for both swelling ratios.

Since the internal and interfacial resistances were determined to be approximately 3 Ω, every impedance measurement was reported after a 3 Ω subtraction. With the purchase of a commercially available through-plane cell made by Solatron<sup>®</sup> (see experimental), the internal and interfacial resistance of the new cell was determined to be

only  $0.6 \Omega$ . Thus, for the majority of the conductivity values described in this work, only  $0.6 \Omega$  was subtracted from the original measured resistance obtained from the Cole-Cole impedance plots. Initially, the impedances of PEO10 and PEO20 samples were investigated to determine the solid-state impedance. The as-spun fiber mats (containing no lithium salt) were essentially insulating with resistance values too high to measure. However, after pre-loading with  $\text{LiClO}_4$ , the PEO10 and PEO20 samples displayed a  $Z'$  intercept at  $2.5 \times 10^4$  and  $4.0 \times 10^4 \Omega$  respectively. Typical impedance spectra of the solid PEO/PETA samples may be seen in **Figure 3.16** below. The high frequency intercept (the intercept connecting the semi-circular region associated with the electrochemical response of the sample – and the linear region associated with Warburg diffusion) was used as the membrane resistance in **Equation 2** to calculate the ionic conductivity of each sample.

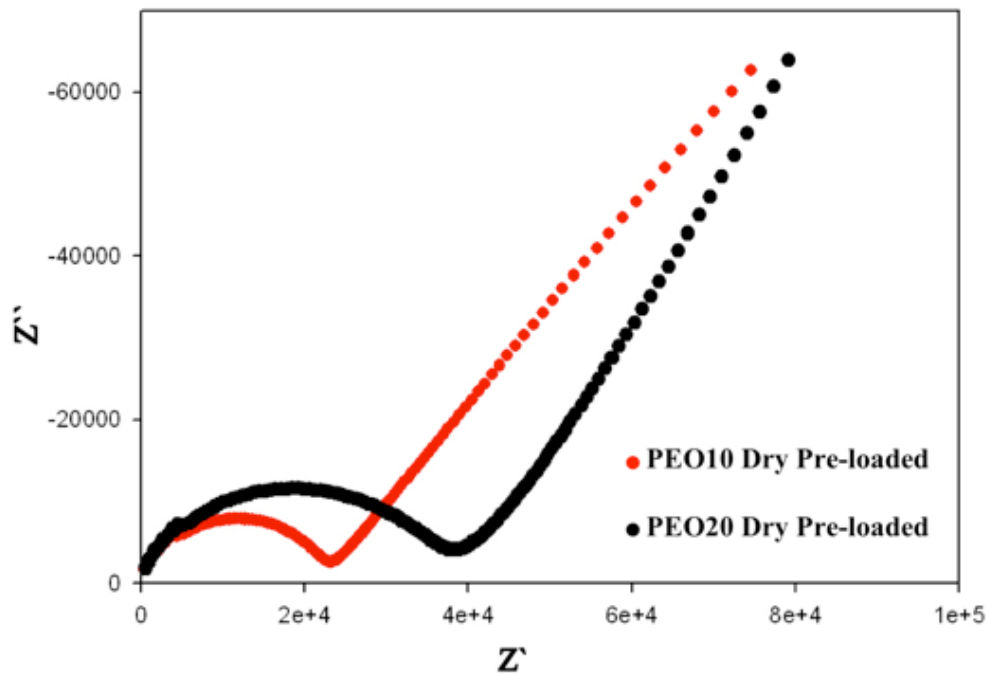


**Figure 3.16.** A typical through-plane AC impedance Cole-Cole plot of non-swollen PEO/PETA

samples that have been pre-loaded with LiClO<sub>4</sub>. PEO was electrospun and crosslinked with 10 wt.% (red) and 20 wt.% (black) PETA followed by a 1h ultrasonic was in a LiClO<sub>4</sub> solution of methanol.

#### **3.4.4. Ionic Conductivity**

**Figure 3.17** compares the ionic conductivities of electrolyte-swollen PEO mats prepared with varying PETA concentrations. The conductivity obtained for the PVDF control was approximately  $4.5 \times 10^{-3}$  S/cm at room temperature. This result is consistent with results for similar systems reported in the literature.<sup>2, 6, 9</sup> In contrast, the conductivity of the pre-loaded PEO10 mat shows a remarkably high room temperature conductivity of  $1.2 \times 10^{-2}$  S/cm, which is well over twice that of the PVDF control. To the best of our knowledge, this is the highest conductivity reported to date for electrospun PGEs.

For all of the PEO mats, the conductivities were found to decrease with increasing cross-linker composition. Since PEO strongly interacts with Li<sup>+</sup> ions and the polymer chains have been found to be active in the ion transport process, previous studies of SPEs<sup>23</sup> have shown that a high degree of polymer chain mobility is necessary to achieve optimal conductivity.<sup>31-33</sup> Moreover, structural factors such as increasing crystallinity in SPEs and crosslink density in GPEs<sup>34, 35</sup> have been shown to adversely affect chain mobility and thus restrict ion transport. Within the crosslinked PEO fibers of the electrolyte-swollen mats, it is reasonable to expect that an increase in crosslink density will effectively reduce the segmental chain motions, which are coupled to ionic mobility. Therefore the reduction in ionic conductivity with increasing PETA content (**Figure 3.17**) may be attributed to restricted segmental chain motions resulting from an increase

in the crosslink density.

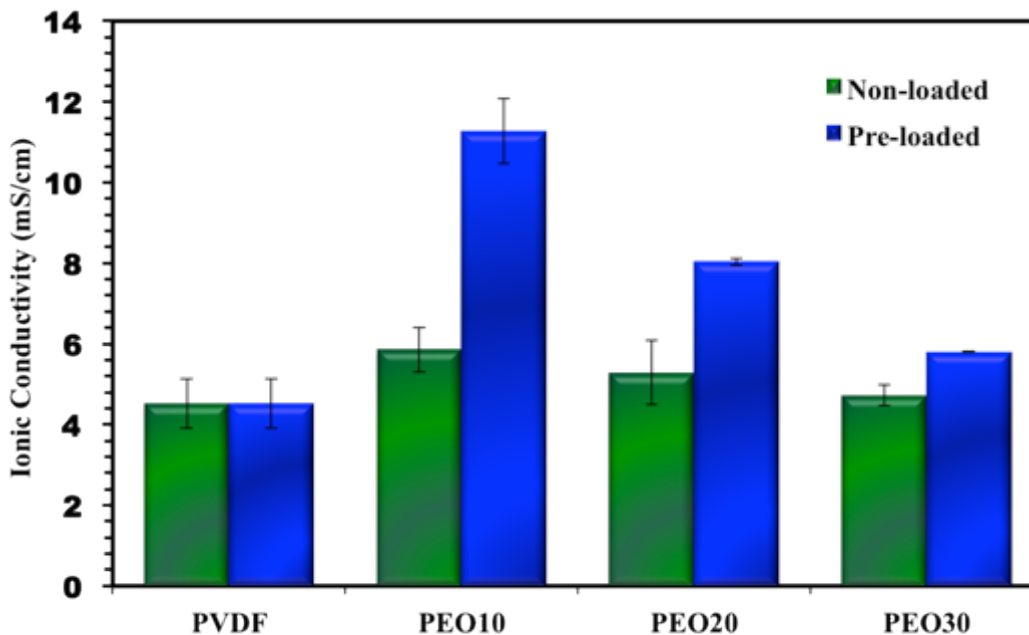


**Figure 3.17.** Ionic conductivities of various electrospun samples with (red) and without (green) a lithium salt pre-loading treatment.

Regardless of cross-linker content, each PEO sample showed a significantly higher ionic conductivity in the pre-loaded state. Surprisingly, however, the PVDF control did not show an increase in conductivity following the pre-loading treatment, even though the concentration of ionic species was consequently increased. This behavior suggests that an increase in salt concentration (beyond 1M LiClO<sub>4</sub>) does not effectively increase the ionic conductivity in the PVDF-based PGE. Since pre-loading of the PVDF mats does not appear to facilitate absorption of ions into the PVDF fibers (**Figure 3.9**), this process essentially just increases the LiClO<sub>4</sub> concentration in the liquid electrolyte surrounding the fibers. Thus, in these control mats, the PVDF fibers appear to act as a relatively non-interactive, inert support for the liquid electrolyte. As such, the

PVDF fibers in the control mats are not expected to significantly participate in the conduction of  $\text{Li}^+$  ions or in the dissociation of lithium salts. In contrast, the pre-loading process has a profound impact on the performance of the highly interactive PEO-based PGEs. Furthermore, the conductivity results in **Figure 3.17** indicate that the  $\text{LiClO}_4$  pre-loading process is necessary in order to obtain the highest conductivities of the electrolyte-swollen PEO mats (swollen with 400 wt.%). To further probe the effect of salt pre-loading on the ionic conductivity of the fibrous framework PGEs, PEO10 samples were exposed to 400 wt.% of EC:DMC electrolytes of varying  $\text{LiClO}_4$  concentrations. The conductivity of typical electrolyte systems can be described by the following equation:

$$\sigma = F \sum_i |z_i| \mu_i C_i \quad (7)$$

where  $\sigma$  is the ionic conductivity,  $F$  is Faraday's constant,  $C_i$  is the concentration of the ionic charge carriers (e.g., dissociated lithium ions),  $z$  is the charge of ionic species  $i$ , and  $\mu$  is the ionic mobility.

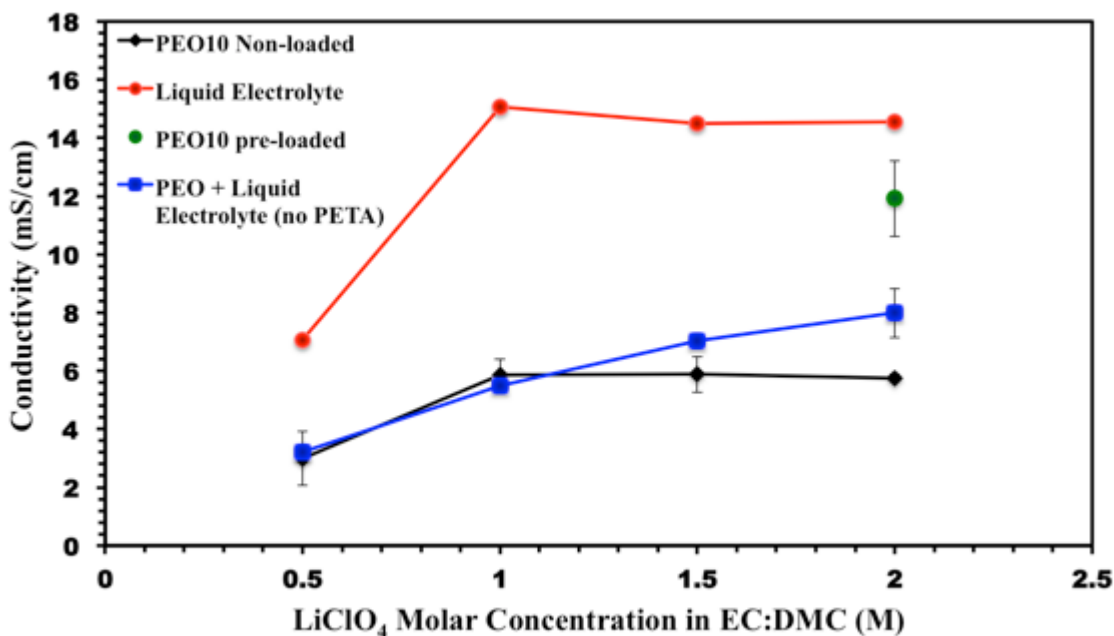


**Figure 3.18.** Ionic conductivity of liquid electrolyte (red), non-loaded PEO10 (black), PEO with liquid electrolyte (blue), and loaded PEO10 swollen with 1M LiClO<sub>4</sub> (green) as a function of various LiClO<sub>4</sub> concentrations.

**Figure 3.18** compares the ionic conductivity of the PEO fibrous framework PGEs to pure liquid electrolyte and electrolytes containing dissolved PEO chains. For the pure liquid electrolyte, the conductivity increases with [LiClO<sub>4</sub>] up to a concentration of 1M; beyond this concentration, the conductivity levels off at a value of ~15 mS/cm. According to previous work,<sup>36</sup> this phenomenon is most likely due to the solubility characteristics of lithium salts in polar aprotic organic solvents. Up to 1M, the lithium perchlorate salt effectively dissociates resulting in an increase in free ions. However, above a concentration of 1M, LiClO<sub>4</sub> can exist in the electrolyte as free ions, as well as a number of other species including contact ion pairs, solvent associated ion pairs, and higher aggregates that do not significantly contribute to ionic conduction. Consequently,

the fraction of free ions contributing to the electrolyte conductivity effectively becomes solubility limited with increasing LiClO<sub>4</sub> concentration. Therefore, in agreement with the findings of Chen et al.,<sup>36</sup> only the free ions are effective charge carriers (**Equation 3.7**), such that further addition of LiClO<sub>4</sub> beyond 1M has little effect on conductivity.

#### ***3.4.5. Polymer-ion Interactions***

As a control, un-crosslinked PEO was dissolved into a 50:50 vol. EC:DMC at a constant composition identical to that of the fibrous framework PGEs (i.e., 400 wt.% EC:DMC). In contrast to the fibrous framework PGEs, the conductivity of the unstructured PEO/EC:DMC mixtures (prepared without PETA or UV irradiation) continues to increase up to ~8 mS/cm beyond 1 M lithium salt concentration. This increase in conductivity may be attributed to PEO/Li<sup>+</sup> interactions, which facilitate an increase in the number of free lithium ion charge carriers. PEO has basic ether groups along the backbone, which have been shown to coordinate/interact with Li<sup>+</sup> ions.<sup>34, 37, 38</sup> As a result, the presence of PEO chains dispersed in the electrolyte aid in the dissociation of lithium salts, yielding a higher concentration of free Li<sup>+</sup> ion charge carriers, and consequently an increase in the ionic conductivity.<sup>39</sup>

In contrast to the homogeneous (un-crosslinked) PEO gel controls, structuring of the PEO component by electrospinning and UV crosslinking lends a number of advantageous characteristics to the electrolyte. For non-loaded PEO fibrous framework PGEs, it is interesting to note that the ionic conductivity vs. [LiClO<sub>4</sub>] behaviour resembles that of the pure liquid electrolyte, although the maximum conductivity is limited to ~6 mS/cm. However, when the PEO fibrous framework PGEs are pre-loaded

with lithium salt, and subsequently swollen with a 1 M LiClO<sub>4</sub> solution (50:50 EC:DMC), the room temperature ionic conductivity increases twofold up to ~12 mS/cm. Note that the pre-loaded PEO10 sample used for the data point in **Figure 3.19** (green) was swollen with 1 M LiClO<sub>4</sub> EC:DMC solution, and also contained an additional amount of LiClO<sub>4</sub> from the pre-loading treatment. Thus, the overall [LiClO<sub>4</sub>] in the pre-loaded samples was effectively 2 M.

By exposing the electrospun PEO mats to a LiClO<sub>4</sub> solution in a highly swelling solvent such as methanol, the pre-loading process facilitates exposure of PEO chains (within the fibers) to lithium ions. This treatment consequently enhances PEO/Li<sup>+</sup> interactions in the fibrous framework. With these strong PEO/Li<sup>+</sup> interactions, it is likely that an increase in the concentration of dissociated Li<sup>+</sup> ions.<sup>39</sup> Therefore, since ionic conductivity is a function of charge carrier concentration in a given matrix (**Equation 7**), pre-loading effectively increases conductivity as a result of increasing the free Li<sup>+</sup> ion concentration within the swollen PEO fibers. Surprisingly, however, the conductivity of the pre-loaded PEO10 fibrous framework PGEs is significantly higher than that of the dissolved PEO gel control at 2 M [LiClO<sub>4</sub>]. Even though both the PEO fibrous framework PGE and the gel control electrolytes contain an equivalent mass fraction of PEO, this behaviour may be attributed to the heterogeneous structure of the fibrous framework.

In the PEO10 fibrous framework PGE, it is important to note that within the solvent swollen fibers, the crosslinked PEO chains form a network constituting a conventional crosslinked gel. In these structured microgels, it is reasonable to expect that the local dynamics of the EC:DMC solvent molecules (and conceivably the Li<sup>+</sup> ions) are

coupled to the PEO segmental chain dynamics. In addition, the PEO fibrous framework PGEs contain a significant amount of free liquid electrolyte in the open pores of the electrospun mat (**Figure 3.12B**). Therefore, within these inter-fibrillar domains, it is likely that the mobility of the solvent molecules and ionic species is similar to that of the pure liquid electrolyte.

#### **3.4.6. Tortuosity**

While the profound difference in conductivity between the electrolyte-swollen PEO mats and the control PVDF mats may be rationalized based on the tendency of PEO to enhance the concentration of free  $\text{Li}^+$  ions, it is also necessary to consider tortuosity as an additional parameter impacting the observed conductivity of these electrolyte swollen PGEs.<sup>40</sup> Tortuosity may be considered as the mean path-length through the electrolyte relative to the electrolyte layer thickness. If the electrolyte contains insulating structures or domains, then ions are forced to migrate around the insulating components, which increases the mean path-length, resulting in high tortuosity and a relatively low effective conductivity. For the PVDF control PGE in this study, the PVDF fibers are effectively inert and relatively insulating compared to the liquid electrolyte. Consequently, these control PGEs constitute a tortuous electrolyte and exhibit relatively low conductivities (analogous to that observed for conventional electrolyte swollen separator membranes).<sup>40</sup> In contrast, for the PEO-based fibrous framework PGEs (having an identical fiber density, fiber size, and porosity), the effective tortuosity may be related to conductivity within the fibrous framework. **Figure 3.19** is an illustration of the mean diffusion path-lengths through a cross-section of an electrospun PVDF fiber mat (top) and a PEO

electrospun fiber mat (bottom) upon swelling with a liquid electrolyte. In this illustration, the  $\text{Li}^+$  ions inherently migrate along the path of least resistance. Within the PVDF mat, any ions that enter the PVDF fibers are limited in mobility and thus, the ions traveling throughout the tortuous liquid electrolyte domains surrounding the fibers dominate the effective conductivity of the PGE. For the preloaded PEO mats, however, highly mobile  $\text{Li}^+$  ions exist within both the PEO fibers and the liquid electrolyte surrounding the fibers. If the ionic conductivity of the PEO/electrolyte gel fibers is similar to that of the liquid electrolyte surrounding the fibers, and the interfacial resistance for transport of ions between the fibers and electrolyte is low, then this structured gel effectively constitutes a “Phantom-like” fibrous framework with respect to ion transport. Consequently, the free  $\text{Li}^+$  ions can traverse the electrolyte layer with a negligible diffusive barrier from the PEO fibers. Under these conditions, tortuosity is minimized and the effective conductivity of the electrolyte approaches that of the pure liquid electrolyte (as shown in **Figure 3.18**).

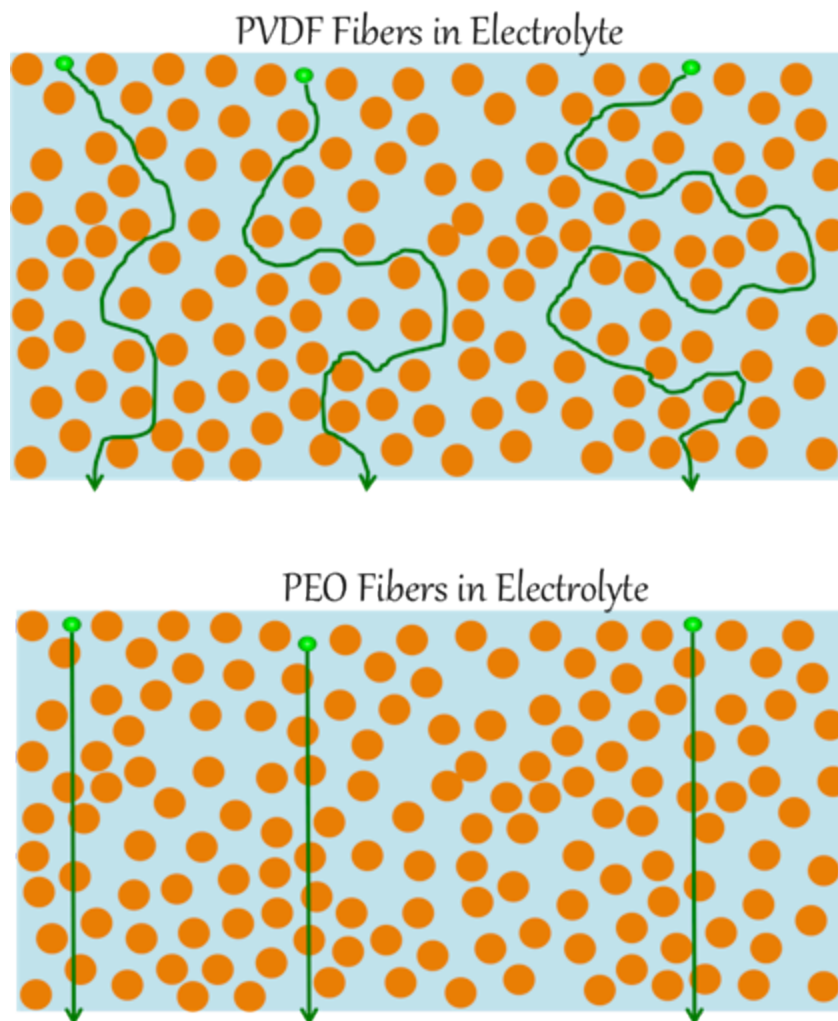


**Figure 3.19.** Cross sectional schematic of ionic tortuosity through two electrospun polymer gel electrolytes: PVDF mat (top), and PEO mat (bottom). Blue domains represent liquid electrolyte, orange represents polymeric fibers and green represents lithium ions.

The tortuosity consideration is also applicable to the data in **Figure 3.17**, which shows a decrease in conductivity with increasing cross-linker content. With an increase in the cross-link density, the reduction in ionic mobility decreases the conductivity within the PEO fibers (**Equation 7**) relative to the liquid electrolyte. As the difference in

conductivity between the cross-linked PEO gel fibers and the liquid electrolyte increases, the  $\text{Li}^+$  ions become biased toward a path of least resistance within the liquid electrolyte. This more favored transport within the liquid electrolyte re-establishes a significant tortuosity contribution and thus lowers the effective conductivity with increasing cross-link density.

To ensure that this PEO/PETA system is not dependent on a particular lithium salt system, conductivity experiments performed on Li-triflate ( $\text{LiCF}_3\text{SO}_3$ ) for both 400 wt.% and fully immersed samples. Due to lack of availability of Li-triflate, only non-loaded samples were prepared and investigated. **Figures 3.20** and **3.21** show the 400 wt.% and immersed PEO/PETA samples along with the PVDF control respectively. We see that the lithium triflate exhibits lower ionic conductivities than the perchlorate counterpart when swollen into PEO/PETA mats. This is likely due to the large polar anion of the triflate salt. Since the anionic diffusion is the major contributor to ionic conductivity (due to transference numbers being less than 1) if the anion mobility decreases but the cation mobility stays the same, then the overall conductivity will decrease.

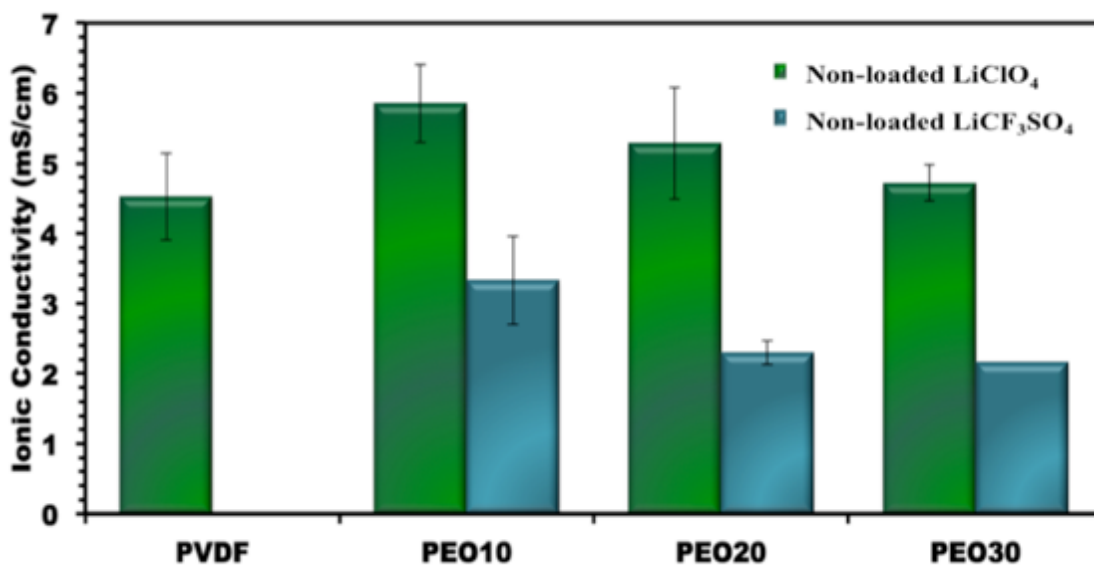


Figure 3.20. Ionic conductivities of PEO/PETA fibers swollen with 400 wt.% of 1 M lithium triflate in EC:DMC.

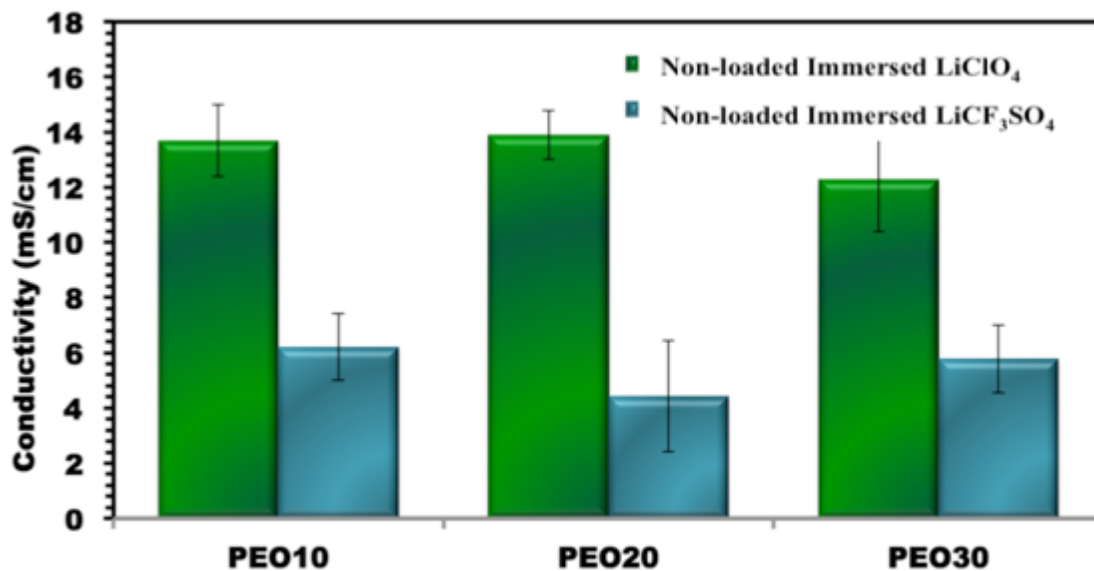


Figure 3.21. Ionic conductivities of PEO/PETA samples fully swollen with 1 M lithium triflate in EC:DMC.

### ***3.5. Conclusions***

Electrospun poly(ethylene oxide) fiber mats have been crosslinked by UV curing with pentaerythritol triacrylate and utilized as insoluble, mechanically robust polymer-gel electrolytes. SEM images indicate that the electrospinning process is an efficient method for obtaining reproducible fibrous framework structures over a range of solution compositions. Gel fraction and porosity data indicate that PETA is an effective crosslinking agent for the PEO mats, yielding gel fractions in excess of 80%.

Upon exposure to liquid electrolyte, the fibrous framework originating from the non-woven structure of the as-spun mats persists. Solvent uptake experiments show that the PEO mats are capable of absorbing large amounts of liquid electrolyte, in excess of 1000 wt.%. Equilibrium uptake swelling experiments indicate that an increase in the PETA composition results in a decrease in the amount of liquid electrolyte absorbed. As the degree to which a cross-linked network swells is inversely proportional to the cross-link density, it may be deduced from the electrolyte uptake experiments that increasing the concentration of PETA also increased the cross-link density ultimately restricting chain mobility.

AC impedance measurements of electrolyte swollen fiber mats show the PEO samples to have higher ionic conductivities than the PVDF control at all PETA concentrations. The conductivities of PEO fiber mats decrease with increasing PETA content due to limited chain mobility upon increasing cross-link density. The PEO fibers appear to be effective at enhancing the overall fraction of free lithium ions, leading to improved conductivity. Furthermore, to the best of our knowledge, the room temperature conductivities for the PEO10 sample are the highest reported for electrospun PGEs.

Since the PEO fibrous frameworks appear to exhibit ionic mobilities similar to the liquid electrolyte components, the PEO structured gel exist as a phantom-like network with respect to ion diffusion allowing ionic transport with little or no diffusive barrier from the PEO fibers. An increase in PETA content corresponds to an increase in the amount of crosslinks and ultimately in a restriction in the polymer chain mobility, which results in a reduction of ionic mobility. If the mobile polymer chains are essential to ion diffusion, then restricting chain mobility would result in a loss of conductivity. Furthermore, because restricted polymeric chain mobility limits ionic diffusion,  $\text{Li}^+$  ions will become biased towards diffusion through the liquid components, resulting in increased diffusion length and an overall reduction in conductivity. The preferential diffusion of  $\text{Li}^+$  ions through the liquid component re-establishes a significant tortuosity contribution approaching that of the PVDF control with respect to PETA content.

It is reasonable to expect that prolonged exposure to the liquid electrolyte solution containing a lithium salt will result in an exchange equilibrium of  $\text{Li}^+$  ions between the liquid domains and the fibrous polymeric domains. This exchange is likely only expedited by the pre-loading procedure. Additionally, the crosslinking reaction is subject to atmospheric purity and thus optimization of the crosslinking procedure should lead to even better mechanical performance of the PEO-based PGE's.

### 3.6. References

1. D. Saikia, H.-Y. Wu, Y.-C. Pan, C.-P. Lin, K.-P. Huang, K.-N. Chen, G. T. K. Fey and H.-M. Kao, *Journal of Power Sources*, 2011, **196**, 2826-2834.
2. S.-S. Choi, Y. S. Lee, C. W. Joo, S. G. Lee, J. K. Park and K.-S. Han, *Electrochimica Acta*, 2004, **50**, 339-343.
3. E. Quartarone and P. Mustarelli, *Chemical Society Reviews*, 2011, **40**, 2525-2540.
4. Q. Shi, M. Yu, X. Zhou, Y. Yan and C. Wan, *Journal of Power Sources*, 2002, **103**, 286-292.
5. S. W. Choi, S. M. Jo, W. S. Lee and Y. R. Kim, *Advanced Materials*, 2003, **15**, 2027-2032.
6. F. Boudin, X. Andrieu, C. Jehoulet and I. I. Olsen, *Journal of Power Sources*, 1999, **81-82**, 804-807.
7. A. Du Pasquier, P. C. Warren, D. Culver, A. S. Gozdz, G. G. Amatucci and J. M. Tarascon, *Solid State Ionics*, 2000, **135**, 249-257.
8. D. Li and Y. Xia, *Advanced Materials*, 2004, **16**, 1151-1170.
9. J. R. Kim, S. W. Choi, S. M. Jo, W. S. Lee and B. C. Kim, *Electrochimica Acta*, 2004, **50**, 69-75.
10. Y. Ding, P. Zhang, Z. Long, Y. Jiang, F. Xu and W. Di, *Journal of Membrane Science*, 2009, **329**, 56-59.
11. S. W. Lee, S. W. Choi, S. M. Jo, B. D. Chin, D. Y. Kim and K. Y. Lee, *Journal of Power Sources*, 2006, **163**, 41-46.
12. A. I. Gopalan, P. Santhosh, K. M. Manesh, J. H. Nho, S. H. Kim, C.-G. Hwang and K.-P. Lee, *Journal of Membrane Science*, 2008, **325**, 683-690.
13. P. Carol, P. Ramakrishnan, B. John and G. Cheruvally, *Journal of Power Sources*, 2011, **196**, 10156-10162.
14. B. Huang, Z. Wang, G. Li, H. Huang, R. Xue, L. Chen and F. Wang, *Solid State Ionics*, 1996, **85**, 79-84.
15. Z. Wang, B. Huang, H. Huang, L. Chen, R. Xue and F. Wang, *Electrochimica Acta*, 1996, **41**, 1443-1446.
16. N. Chand, N. Rai, T. S. Natarajan and S. L. Agrawal, *Fibers Polym*, 2011, **12**, 438-443.
17. H.-R. Jung and W.-J. Lee, *Electrochimica Acta*, 2011, **58**, 674-680.
18. M. Doytcheva, D. Dotcheva, R. Stamenova, A. Orahovats, C. Tsvetanov and J. Leder, *Journal of Applied Polymer Science*, 1997, **64**, 2299-2307.
19. M. Doytcheva, D. Dotcheva, R. Stamenova and C. Tsvetanov, *Macromolecular Materials and Engineering*, 2001, **286**, 30-33.
20. C. Zhou, Q. Wang and Q. Wu, *Carbohydrate Polymers*, 2012, **87**, 1779-1786.
21. P. Ravn Sørensen and T. Jacobsen, *Electrochimica Acta*, 1982, **27**, 1671-1675.
22. Y. Saito, H. Kataoka, E. Quartarone and P. Mustarelli, *The Journal of Physical Chemistry B*, 2002, **106**, 7200-7204.
23. P. J. Flory and J. J. Rehner, *The Journal of Chemical Physics*, 1943, **11**, 521-526.
24. M. Barlkanl and C. Hepburn, *Iranian Journal of Polymer Science and Technology*, 1992, **vol. 1**, 5.

25. G. M. Bristow and W. F. Watson, *Transactions of the Faraday Society*, 1958, **54**, 1731-1741.
26. A. F. M. Barton, *Chemical Reviews*, 1975, **75**, 731-753.
27. R. Ian D, *Solid State Ionics*, 1986, **18-19, Part 1**, 40-49.
28. W. J.C, *Electrochimica Acta*, 1993, **38**, 2111-2114.
29. L. Coury, *Current Separations*, 1999, **18:3**, 6.
30. T. Soboleva, Z. Xie, Z. Shi, E. Tsang, T. Navessin and S. Holdcroft, *Journal of Electroanalytical Chemistry*, 2008, **622**, 145-152.
31. J. Shi and C. A. Vincent, *Solid State Ionics*, 1993, **60**, 11-17.
32. E. Quartarone, P. Mustarelli and A. Magistris, *Solid State Ionics*, 1998, **110**, 1-14.
33. C. Berthier, W. Gorecki, M. Minier, M. B. Armand, J. M. Chabagno and P. Rigaud, *Solid State Ionics*, 1983, **11**, 91-95.
34. W. H. Meyer, *Advanced Materials*, 1998, **10**, 439-448.
35. K. Murata, S. Izuchi and Y. Yoshihisa, *Electrochimica Acta*, 2000, **45**, 1501-1508.
36. H. P. Chen, J. W. Fergus and B. Z. Jang, *Journal of The Electrochemical Society*, 2000, **147**, 399-406.
37. M. B. Armand, J. M. Chanbango and M. J. Duclot, *Fast Ion Transport in Solids*, Eds. North-Holland, Amsterdam, 1979.
38. P. G. Bruce and C. A. Vincent, *Journal of the Chemical Society, Faraday Transactions*, 1993, **89**.
39. Y. Saito, M. Okano, K. Kubota, T. Sakai, J. Fujioka and T. Kawakami, *The Journal of Physical Chemistry B*, 2012, **116**, 10089-10097.
40. P. Arora and Z. Zhang, *Chem Rev*, 2004, 4419-4462.

## Chapter 4

### Characterization of Crosslinked Polyethylene Oxide Electrospun Fibers

#### 4.1. PEO – PETA Cross-linking Mechanism

Due to its inherent solubility in polar solvents, PEO must be crosslinked in order to produce freestanding, mechanically robust membranes upon addition of the liquid electrolyte component. Understanding the crosslink mechanics is useful for optimizing membrane production. Not only is the concentration of the initiator important, but also the temperature, atmosphere, curing time, and mobility of reacting species all play a crucial role in the efficiency and consistency of crosslinking agents. As mentioned in chapter 3, Doycheva *et al.* reported the successful UV initiated crosslinking of PEO using PETA. Although the actual crosslinking mechanism was not studied, it was suggested to proceed through a radical intermediate.<sup>1</sup> The suggested mechanism may be seen in **Figure 4.1**. A photon is absorbed by PETA causing a carbonyl group to become excited. If a PEO chain is available, then PETA will abstract a hydrogen by cleaving the C-H bond. Hydrogen abstraction leads to the formation of a hydroxyl group on PETA as well as a carbon radical in the PEO chain.



polymerization mechanism plays a large role in the overall curing of the electrospun samples.

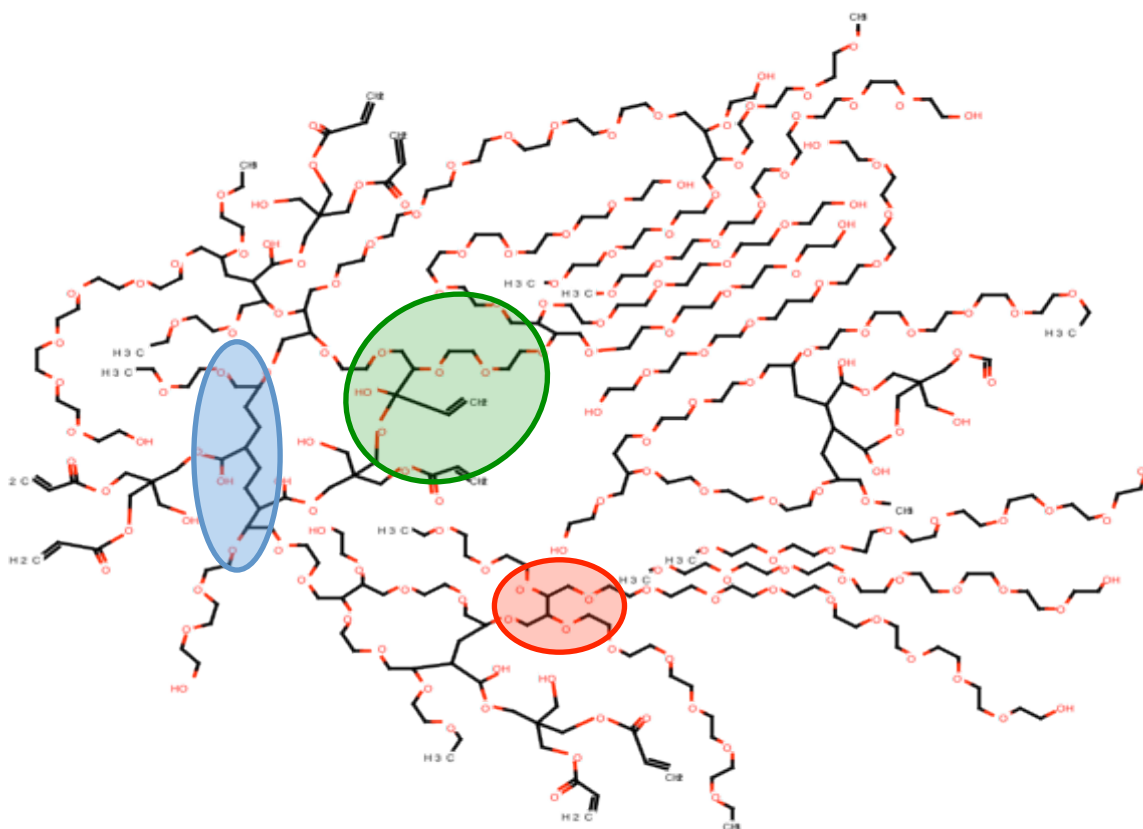


**Figure 4.2.** Depiction of possible crosslink pathways occurring in the UV curing of PEO with a PETA photoinitiator. Blue region shows radical reaction of PETA double bonds induced and terminated by a PEO radical. Green region shows combination of PETA radical with PEO radical. Red region shows the combination of two PEO radicals.

The mechanism associated with the UV photo curing of PEO with PETA was briefly investigated using IR spectroscopy. Samples of PEO cast with 10 wt.% PETA were subjected UV irradiation for varying amounts of time. The IR absorbance as a

function of irradiation time was collected (**Figure 4.3**). As indicated in the figure, the characteristic carbonyl absorbance peak associated with the PETA C=O (1730) decreases as a function of time from 10 to 20 min. The peak changes only slightly from 20 to 30 minutes suggesting that after 20 minutes, nearly all of photoinitiated PETA has reacted with PEO to abstract the hydrogen and form the polymeric and PETA radicals.<sup>2</sup> An absorbance peak associated with the C=C double bond (1625) also decreases as a function of time, which suggests that a radical reaction involving the C=C does occur during the crosslinking mechanism and is affected by curing time. Whether PETA reacts radically to form short PETA chains before being quenched or if the PETA radical is immediately quenched by a neighboring PEO radical is unclear. Other reactions that could prevent crosslinking might also occur, including degradation by reacting with atmospheric oxygen. It is well known that oxygen inhibits the free-radical polymerization of acrylates.<sup>3-5</sup> However, unlike the carbonyl absorbance peak, the C=C peak continues to decrease up to 30 minutes of UV exposure indicating that this reaction occurs slower than the initiation reaction. Additionally, a peak at 1400 wavenumbers, associated with the C-H bending of an sp<sup>2</sup> – hybridized carbon, decreases as a function of curing time. Reduction of the 1400 peak further supports the involvement of a radical reaction with PETA C=C at some point in the mechanism pathway. Recently, Wu and coworkers reported IR results supporting this conclusion. Wu suggested that the reduction in the C=O peak with irradiation time indicated that PETA was a photoinitiator. Furthermore, reduction of the 1630 peak suggested that radical polymerization occurs with the PETA.<sup>6</sup>

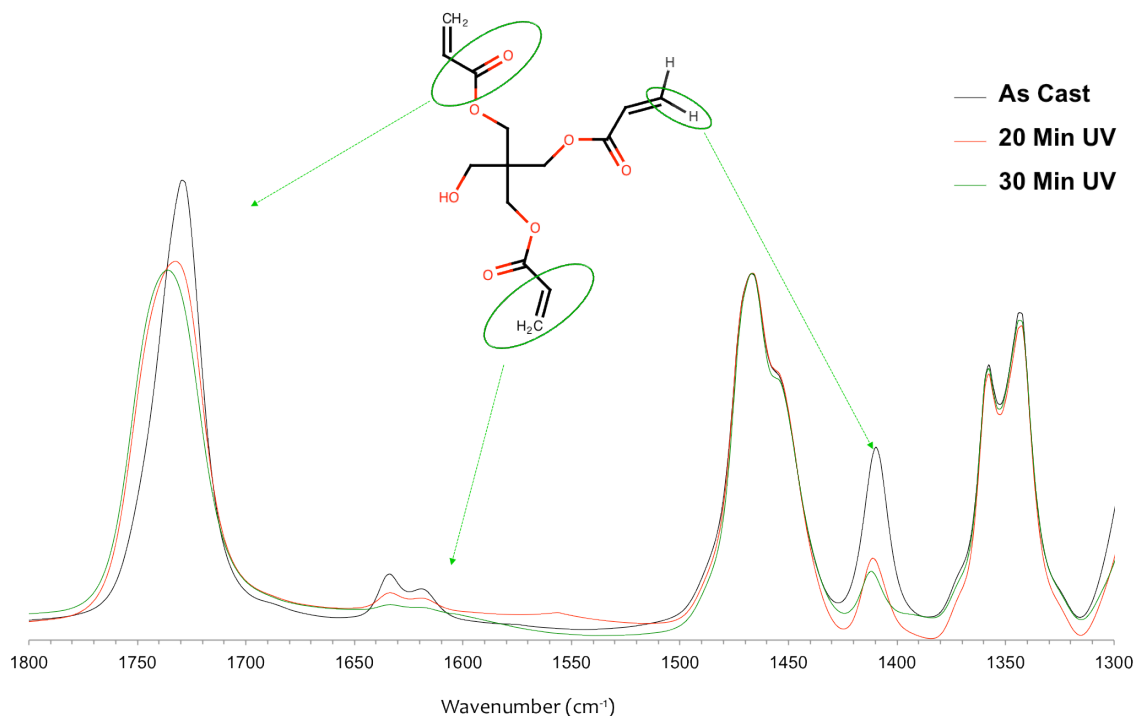


**Figure 4.3.** IR absorbance spectrum of PEO10 at various UV irradiation times.

#### 4.2. Effect of Curing Atmosphere

During the crosslinking process, the PEO and PETA radicals are very reactive and may easily terminate through degradative or undesirable reactions. PEO degradation through random chain scission involving C-O and C-C bonds is well established.<sup>7-9</sup> Perhaps more relevant to this work, a detailed study of potential radical degradation processes of PEO was published in 2009.<sup>10</sup> In this publication, several mechanisms involving PEO radicals are coupled to oxidative degradation. **Figure 4.4** shows a potential mechanism that could lead to chain scission of polyether radicals in the presence of atmospheric O<sub>2</sub>.

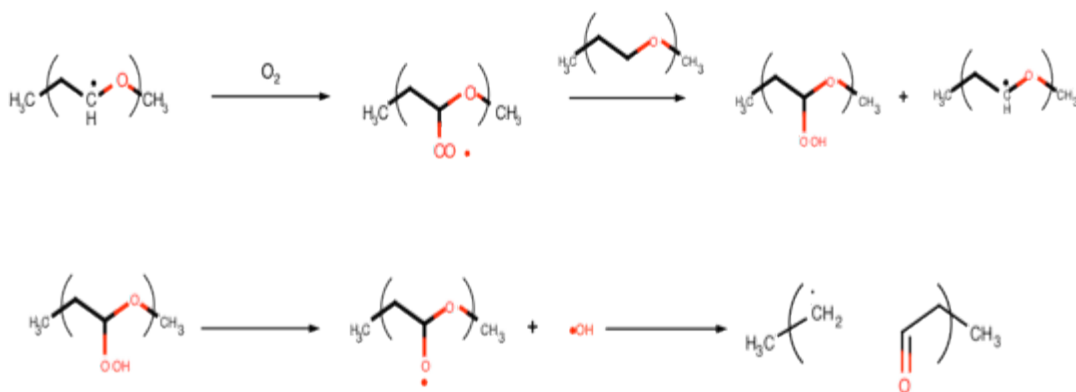


**Figure 4.4.** Chain scission of a radical containing PEO chain upon exposure to oxygen.

This mechanism is of particular interest as the PETA photoinitiator presumably produces a PEO radical. Additionally, this reaction was initially performed under atmospheric conditions where  $O_2$  likely reduced the overall crosslinking reaction. Fortunately, the adverse effects of  $O_2$  radical quenching appear to be largely overcome in the PEO/PETA fiber mats as high gel fractions indicate effective crosslinking. In an attempt to limit the amount of radical quenching by oxygen, a new generation (Gen2) of PEO/PETA electrospun fiber mats was prepared and crosslinked in an oven and under a nitrogen purge. The temperature of the crosslinking oven was kept below  $40\text{ }^\circ\text{C}$ , the  $N_2$  purge was accomplished by flowing the gas into the bottom of the oven and exiting via a small hole in the ceiling, and the UV source was kept the same distance as generation 1 (Gen1) samples (25 cm). Although the gel fractions of Gen2 samples were indistinguishable from the Gen1 (PEO/PETA crosslinked under atmospheric conditions), the tensile properties were significantly different. **Figures 4.5** and **4.6** show the tensile properties for PEO samples crosslinked under two different conditions.

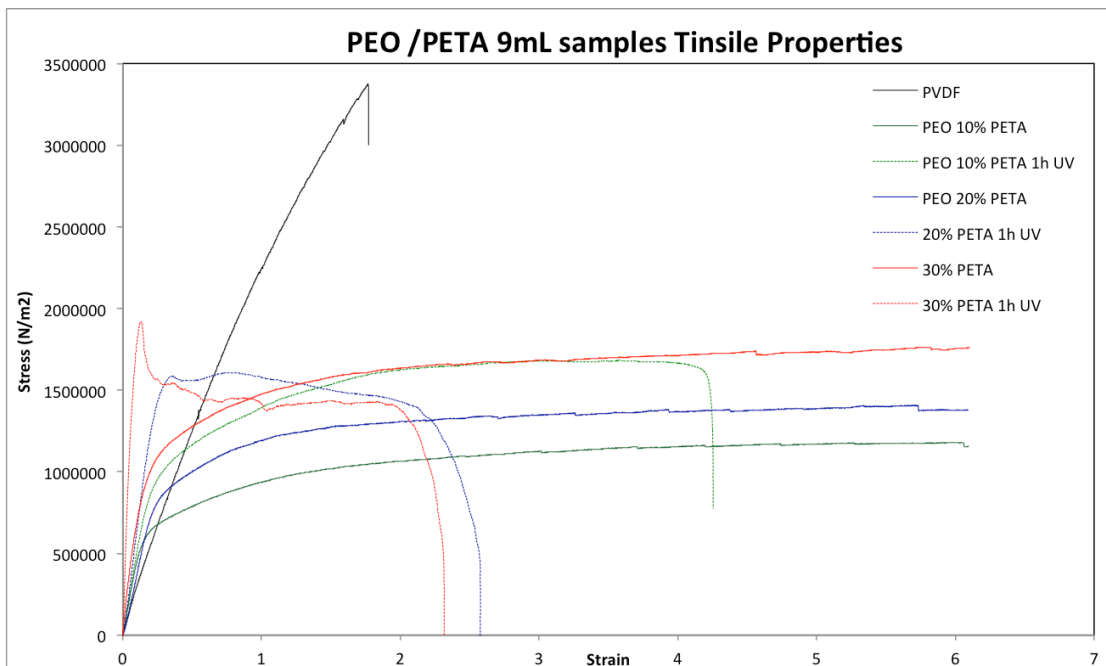


**Figure 4.5.** Stress – strain curve for Gen1 (atmospheric crosslinking conditions) for both as-spun fiber mats (no UV exposure – solid lines) and samples after 1 hour of UV exposure (dashed lines). Electrospun PVDF was used as a control.

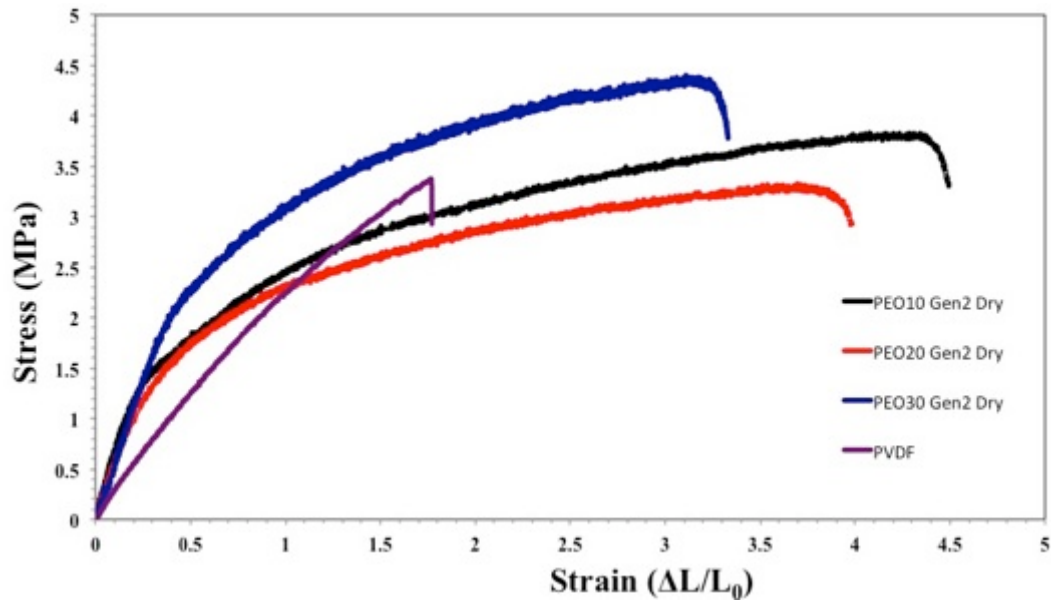


**Figure 4.6.** Stress – strain curves for Gen2 ( $N_2$  purged crosslinking conditions) PEO/PETA electrospun fiber mats. For a control, and electrospun fiber mat of PVDF was subjected to the same tensile experiment.

Gen1 PEO/PETA mats (**Figure 4.5**) show an increase in the overall tensile strength as the concentration of PETA increases even before UV exposure. Strong dipolar and hydrogen bonding interactions between the PEO chains and the carbonyl/hydroxyl groups in PETA are likely responsible for this direct correlation between tensile strength and PETA concentration.<sup>11, 12</sup> As one example, the introduction of cellulose nanocrystals (CN) has been widely investigated in several polymer systems including PEO,<sup>6, 13</sup> poly(acrylic acid),<sup>14</sup> and poly( $\epsilon$ -caprolactone).<sup>15</sup> These Gen1 PEO/PETA samples appear highly ductile with large elongations before break (no break was observed in these experiments). Although the Young's modulus (see **Figure 4.7**) for each PEOs sample was greater than the PVDF control, the tensile strength of PEO samples was significantly than PVDF. In contrast to the un-crosslinked samples, the

Gen1 PEO/PETA mats that were exposed to UV irradiation broke during the tensile test. When the PEO/PETA samples were exposed to UV irradiation, their Young's moduli increased, along with the tensile strength. Similar to the trend with the as-spun samples, the tensile strength and the Young's modulus both increase with increasing PETA content. In agreement with the equilibrium swelling data reported in chapter 3, increasing the concentration of PETA increases the crosslink density. More crosslink density typically translates to a higher elastic modulus as polymer chains are prevented from sliding past one another due to chemical crosslinks. The increases in tensile strength along with increasing Young's moduli and overall loss in elongation until break are indicative of chemical crosslinking.

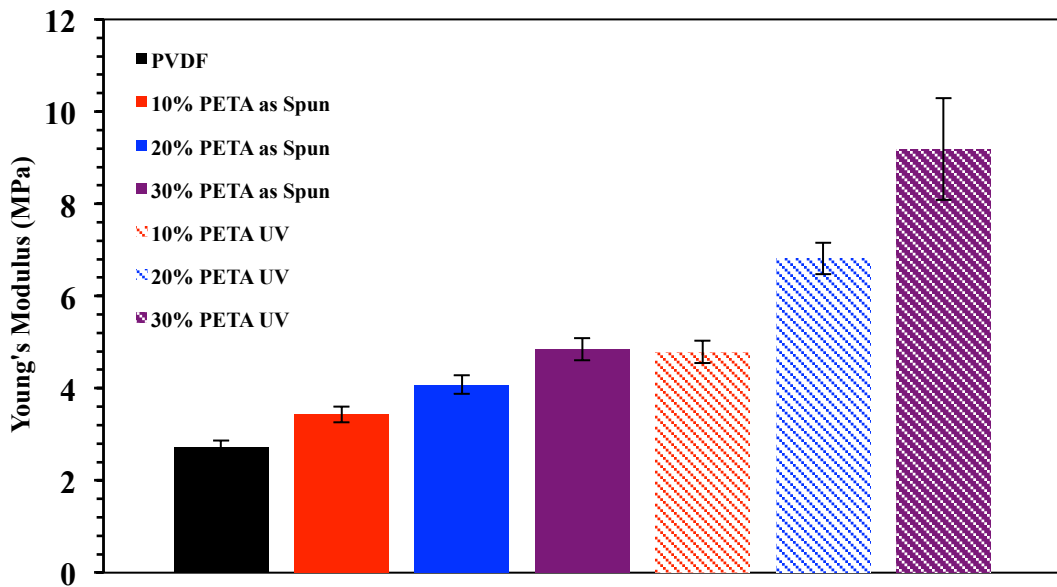


**Figure 4.7.** Young's moduli for electrospun PEO/PETA samples before (solid) and after (lined) UV irradiation. PVDF was electrospun under similar conditions as a control.

The Gen2 PEO/PETA samples exhibited much improved mechanical properties over the previous generation crosslinked fibers. From the results reported in **Figure 4.6**,

crosslinking under a nitrogen purge and at 40 °C results in cured mats with nearly a two fold increase in the overall tensile strength as well as an increase in the Young's modulus. Not only do the tensile properties of Gen2 PEO/PETA mats out-perform Gen1, but they are also tougher than the PVDF electrospun control. For the PEO10, the tensile strength approaches 3 MPa, which is very close to the PVDF tensile strength of 3.2 MPa. The PEO20 and PEO30 samples cured under N<sub>2</sub> at 40 °C both show tensile strengths above PVDF at ~ 3.5 and 4.2 MPa respectively. In addition to the elastic modulus and the tensile strength being either equal to (PEO10) or greater (PEO20 + PEO30) than the PVDF control, the overall strain at break is nearly twice that of the PVDF electrospun mat. The mechanical integrity of the PEO/PETA hybrid polymer-gel electrolyte is crucial to preventing thermal runaway due to shorting. If these crosslinked mats are to act as potential electrolyte/separator membranes, then they must be able to prevent electrode shorting. **Figure 4.8** compares the Young's modulus of PVDF, Gen1 and Gen2 electrospun samples (note: then un-crosslinked Gen2 samples exhibited similar tensile profiles as the un-crosslinked Gen1 samples). The Young's Moduli for the Gen2 samples are very similar. Unexpectedly, Gen2 samples exhibit a weaker elastic modulus than the Gen1 samples following UV curing, although still higher than the PVDF control.

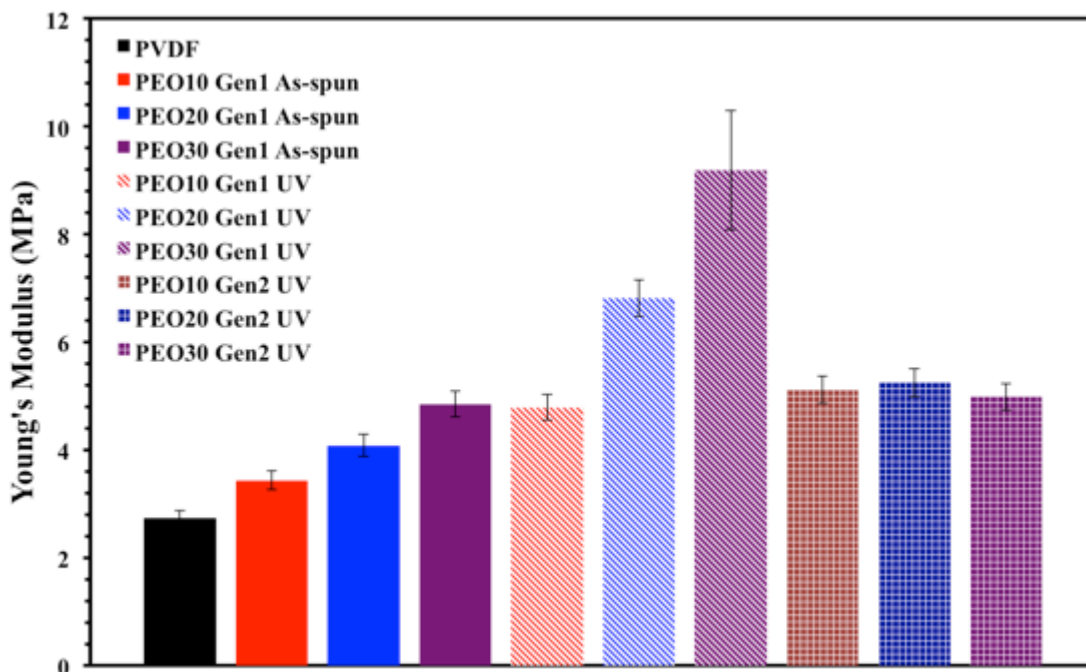


**Figure 4.8.** Comparison of the Young's modulus observed for PVDF, un-crosslinked Gen1 PEO/PETA, UV cured Gen1 PEO/PETA, and UV cured Gen2 PEO/PETA electrospun mats.

### 4.3. Crosslink Density

Since the Gen2 samples displayed much higher stresses at break than the Gen1 samples and since the Young's moduli for the Gen2 samples were slightly lower than the Gen1 samples, it is clear that the conditions affect the curing process. The increase in the tensile strength is likely due to a higher degree of crosslinking. Thus the degree of crosslinking must be different between the two samples. **Table 4.1** shows the approximate molecular weight between crosslinks ( $M_c$ ) for the Gen1 and Gen 2 samples. The  $M_c$  for Gen2 samples was calculated according to the procedure outlined in chapter 3. The same assumptions were made regarding the interaction parameter.

**Table 4.1.** Number average molecular weight between crosslinks and crosslink density for Gen1 and Gen2 PEO/PETA samples.

<b>Electrospun Sample</b>	<b>Number Average Molecular Weight Between Crosslinks (<math>M_c</math>)</b>	<b>Crosslink Density</b>
<b>PEO10 Gen1</b>	25 kg/mol	$2.1 \times 10^{-5}$
<b>PEO20 Gen1</b>	15 kg/mol	$3.5 \times 10^{-5}$
<b>PEO30 Gen1</b>	9.5 kg/mol	$5.3 \times 10^{-5}$
<b>PEO10 Gen2</b>	10 kg/mol	$5.1 \times 10^{-5}$
<b>PEO20 Gen2</b>	8 kg/mol	$5.5 \times 10^{-5}$
<b>PEO30 Gen2</b>	7 kg/mol	$5.6 \times 10^{-5}$

Crosslink density and  $M_c$  show only a slight increase and decrease respectively for the Gen2 samples as the PETA concentration increases. The largest improvement was with the PEO10 samples. The molecular weight between crosslinks was reduced from 25 kg/mol (Gen1) to only 10 kg/mol (Gen2). PEO20 and PEO30 showed only slight reductions in  $M_c$  along with slight increases in the crosslink density. Thus the improved tensile performance for the PEO10 samples may be attributable to the higher degree of crosslinking. However, since the PEO20 and PEO30 samples show almost negligible differences in crosslinking density and  $M_c$ , it is possible that the enhanced tensile properties may be attributed to another effect of the Gen2 procedure.

#### ***4.4. Fiber Melding Due to Photo-curing Temperature***

Other than reducing the  $O_2$  quenching of PEO radicals via the nitrogen purge, the temperature for the Gen2 samples may have an effect on the overall morphology. Up to this point, it was assumed that only *intra*-fiber crosslinking was occurring during the UV

curing process; that is, nearly all of the crosslinking was happening between PETA and PEO chains within each individual fiber and little if any crosslinking between fibers was occurring. It was believed that the small contact area resulting from fiber stacking effectively prevented any significant *inter*-fiber crosslinking. However, curing at an elevated temperature, leads to fiber melding. Fiber melding during the crosslinking procedure may have a significant effect on the overall mechanical performance of electrospun mats. It is reasonable to expect that fiber melding during the curing process would foster *inter*-fiber crosslinking along with the *intra*-fiber crosslinking observed in Gen1 samples. Chemically crosslinking fibers together within the non-woven mat would have a profound impact on the mechanical properties. SEM images comparing Gen1 and Gen2 samples of PEO10 show fiber melding for Gen2 and no fiber melding for Gen1 (**Figure 4.9**).

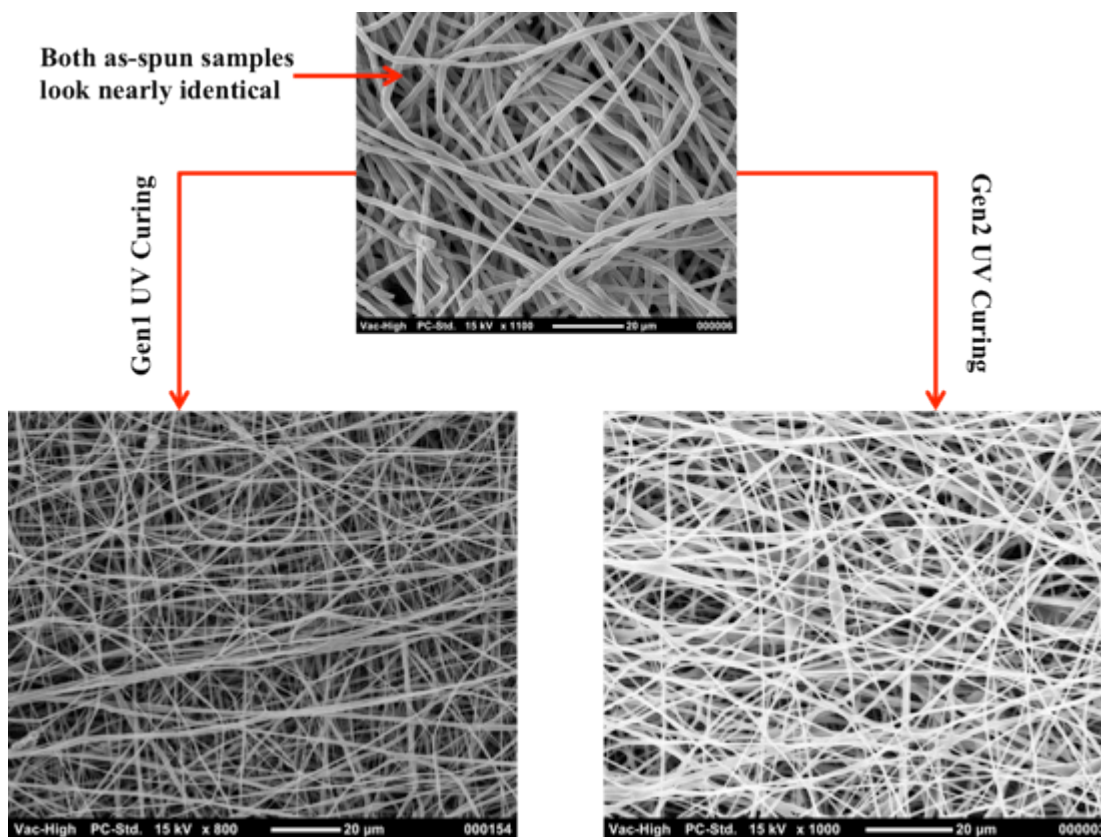


**Figure 4.9.** SEM image of a representative PEO10 electrospun sample before UV exposure (top), UV exposure under atmospheric conditions (left), and UV exposure under N<sub>2</sub> purge and at 40 °C (right). The UV exposure time was 30 min for each sample.

#### ***4.5. Effects of Crosslinking Conditions on Ionic Conductivity***

The ionic conductivities of pre-loaded Gen1 and Gen2 samples swollen with only 400 wt.% of liquid electrolyte are very similar, but the Gen2 mats appear to have slightly better performance. This result is surprising, as one would expect the reduced mobility imparted by the higher crosslink density would limit polymer-ion interactions. Thus the concentration of free Li<sup>+</sup> ions would be reduced along with the polymer mobility. This could indicate that polymer assisted Li<sup>+</sup> diffusion via chain reptation (**Figure 1.10**) may only result in a minor increase in performance and that polymer-ion interactions resulting

in more free charge carriers may be the major factor affecting ionic conductivity. Similar to the Gen1 samples, a decrease in ionic conductivity with increasing PETA concentration is observed. The chain mobility is coupled to polymer-ion interactions not only affecting polymer-assisted diffusion, but also charge dissociations. The more PETA crosslinks PEO reducing the  $M_c$ , the more difficult polymer-ion interactions become. If PEO chains cannot coordinate with and facilitate lithium dissociation, then the overall concentration of charge carriers decreases, thus causing the ionic conductivity to decrease. This rational does not explain why Gen2 PEO10 samples are so similar to Gen1 PEO10 samples. One would expect that the significant decrease in  $M_c$  between the two samples ( $\sim 15$  kg/mol) would prevent Gen2 samples from forming the necessary coordinations with  $\text{Li}^+$ s. However, it is important to keep in mind that the Gen2 samples experience fiber melding. It is currently unclear what effect the fiber melding has on 400 wt.% swollen samples.

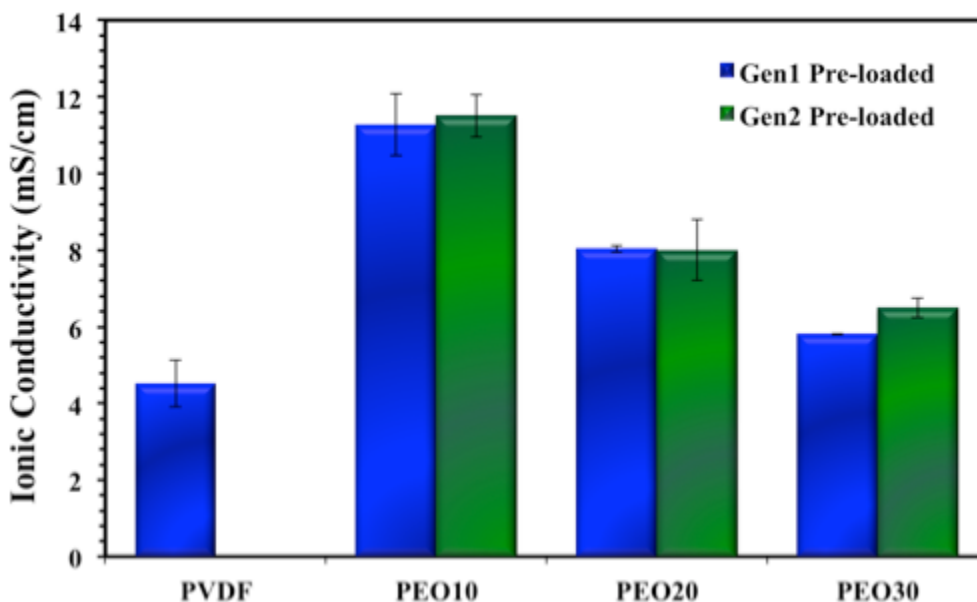


**Figure 4.10.** Ionic conductivities of Gen1 (blue) and Gen2 (green) PEO/PETA electrospun PGES swollen with only 400 wt.% of EC:DMC containing 1M  $\text{LiClO}_4$ .

The conductivity differences between fully swollen Gen1 and Gen2 samples are small if any. The values indicate that crosslinking under an N<sub>2</sub> atmosphere and at 40 °C results in only a slight increase in the conductivities of the PEO10 samples when the fiber mats are immersed in an EC:DMC solution containing 1M LiClO<sub>4</sub>. For the PEO20 and PEO 30 samples, only negligible changes in the ionic conductivity were observed when fully immersed. **Figure 4.11** shows the ionic conductivity data for immersion-swollen samples calculated from AC impedance measurements. Although the mean conductivity for Gen2 PEO10 samples was above the mean of the Gen1 samples, the two values are within error of each other, suggesting that the N<sub>2</sub> atmosphere and the higher curing temperature has no appreciable benefit to ionic conductivity when the samples are fully immersed at room temperature. Discussed in greater detail later, the ionic conductivity is believed to be mainly associated with the liquid domains in the immersion-swollen samples. Polymer-ion contributions may play a role in individual species mobilities but for the most part, the conductivity properties appear to be dominated by the liquid domain characteristics.

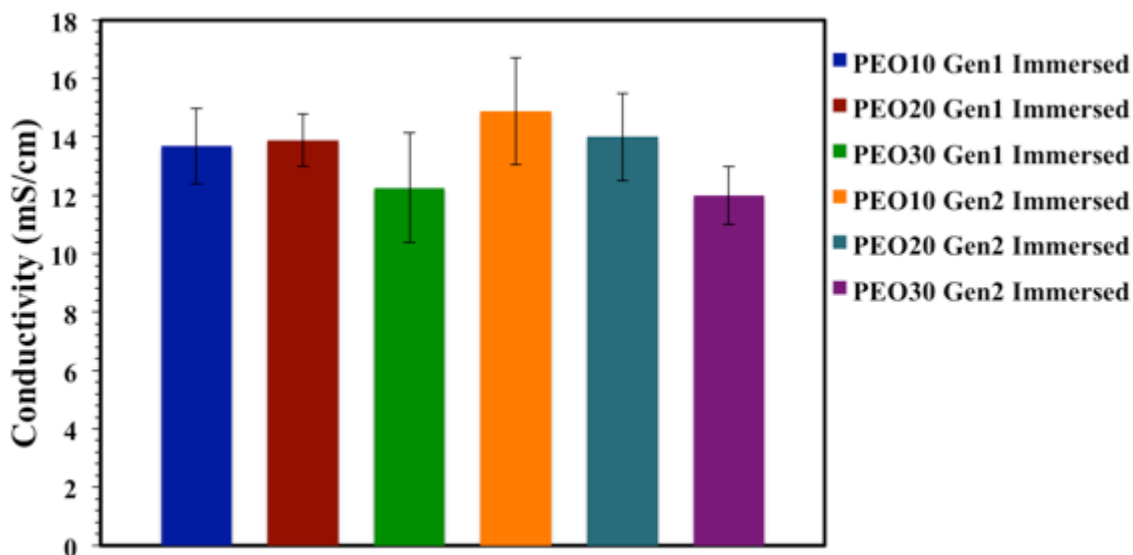


**Figure 4.11.** Ionic conductivity values for Gen1 and Gen2 samples of electrospun PEO/PETA samples upon immersion swelling in electrolyte solution (1M LiClO<sub>4</sub> in EC:DMC).

#### **4.6. Alternative Photoinitiators**

Although PETA has proven to be a suitable photoinitiator for the hydrogen abstraction from PEO chains, the necessity for large amounts of PETA (> 10 wt. %), insolubility in environmentally safe solvents (water, ethanol), and reactive hydroxyl hydrogens make it slightly unattractive for commercial use. As a result, several efforts at crosslinking PEO electrospun fibers were attempted using various thermally and photolytically active initiators. **Table 4.2** summarizes the crosslinking studies. PEO and the crosslinking agents were dissolved into one homogeneous electrospinning solution and the resulting PEO/x-linker fiber mat was exposed to its respective initiation conditions. Following the crosslinking procedure, each sample was submerged in DI water and ultrasonicated to evaluate the resulting fiber mat's solubility. Samples resulting in insoluble gel fractions were considered successful (marked with a **yes**),

whereas samples that completely dissolved were considered unsuccessful (marked with a **no**).

**Table 4.2.** Summary of crosslinking agents used to crosslink PEO electrospun fibers.

<b>Crosslinking Agent</b>	<b>Crosslinking Conditions</b>	<b>Successful Crosslinking</b>
<b>*Pentaerythritol Triacrylate (PETA)</b>	UV irradiation 1 h	Yes
<b>*Benzophenone (BP)</b>	UV irradiation 1 h	No
<b>*2,2',4,4'-Tetrahydroxy Benzophenone (THBP)</b>	UV irradiation 1 h	No
<b>**Benzoyl Peroxide (BPO)</b>	Thermally annealed at (50-60 °C)	No
<b>**Azobisisobutyronitrile (AIBN)</b>	Thermally annealed (50-70 °C)	No

\* Photoinitiators – initiate by hydrogen abstraction upon UV irradiation

\*\* Thermal initiators –initiate by free radicals at elevated temperatures

Benzophenone (BP) has been reported in the literature as an effective means of abstracting hydrogens from PEO chains in thin film and polymer solutions upon exposure to UV irradiation.<sup>16, 17</sup> Since, BP has shown promise in solid film and solution chemistry, crosslinking electrospun PEO fibers with BP was attractive. BP was specifically attractive, as its tetrahydroxyl (THBP) derivative is water-soluble. In addition to water solubility, THBP could be used in its lithiated salt form by exposure to LiOH. As indicated in **Table 4.2**, neither BP nor THBP were effective in crosslinking PEO fiber samples. These results contradict the thin film and solution results reported in the literature.<sup>16, 17</sup> Differences in the crosslinking mechanism may account for why BP does not effectively crosslink PEO fibers whereas PETA does. Mentioned previously, using PETA allows for at least three possible crosslinking mechanisms. The mechanism

involving polymerization of PETA vinyl groups (supported by IR spectroscopy), in particular, could be a deciding factor. Unlike PETA, benzophenone based crosslinkers have only one major crosslinking pathway / mechanism. Immediately following the hydrogen abstraction (similar to PETA mechanism), only the combination of two PEO chain radicals will result in crosslinking. Each benzophenone has only has the ability to abstract one hydrogen resulting in a BP molecule with only one radical. If a BP radical combines with a PEO radical, no crosslinking can occur. Additionally, it would be difficult for a PEO radical to combine with BP due to steric hindrance even if BP had the ability to H-abtract more than once. Also, with benzophenone based crosslinking agents, successful crosslinking depends on PEO chain radicals being either close enough, or mobile enough to combine. In film samples, the bulk polymer chains have access to many neighboring chains, and solution mobility makes PEO radical combination effective. However, since electrospun fibers are essentially isolated from each other, have high aspect ratios with very little “bulk” type domains, a PEO radical is likely too far from another PEO radical to combine before some other reaction occurs, preventing crosslinking. It is reasonable to expect that PEO radicals are longer lived by reacting with PETA, since PETA has reactive vinyl substituents. Additionally, since the PEO radicals formed from BP hydrogen abstraction were isolated, they eventually reacted in unconstructive means often resulting in UV treated films that are very brittle and difficult to handle.

A major drawback of using crosslinking agents such as PETA and BP is that they rely on UV irradiation to become excited to abstract a PEO hydrogen thereby creating radicals. UV penetration into polymer films is weak especially if the film has

components with large UV absorptivity coefficients as is the case with PETA. As such, only thin fiber mats are useful for consistent homogeneous crosslinking. Fortunately, the PEO/PETA mats also contain a high concentration of light diffracting morphologies (crystallinity, fibers), which allow for the UV incident rays to penetrate the film. During the tensile experiments, it was discovered that crosslinking samples thicker than 70  $\mu\text{m}$  resulted in a “delamination” of the outer, crosslinked shell from the inner un-crosslinked core. Solubility tests confirmed that the delaminated shells were crosslinked and that the core was completely soluble in DI water. The thickness of each delaminated shell was approximately 35  $\mu\text{m}$ , suggesting that the UV penetration is on the order of 35  $\mu\text{m}$  for PEO/PETA samples containing 10 – 30 wt.% PETA. Since the crosslinking procedure involves exposing both sides of the fiber mat to UV irradiation, fiber mats up to a maximum thickness of  $\sim 70$   $\mu\text{m}$  could be completely crosslinked. **Figure 4.12** shows an image of a crosslinked PEO10 fiber mat after delamination during a tensile experiment. Using thermally initiated crosslinking agents would be an easy way to produce insoluble PEO fiber mats without the need to limit the mat thickness. Free radical initiators such as BPO and AIBN however proved unsuccessful in crosslinking PEO. Although BPO and AIBN produce free radicals upon thermal degradation, neither initiator reacted with PEO to form an insoluble network. Failure to cure the fibrous networks could be either a result of insufficient H – abstraction, or for similar reasons as BP. Since neither BPO nor AIBN contain radical reactive substituents, if any PEO radicals are formed, they might be degrading before they get a chance to combine with each other.

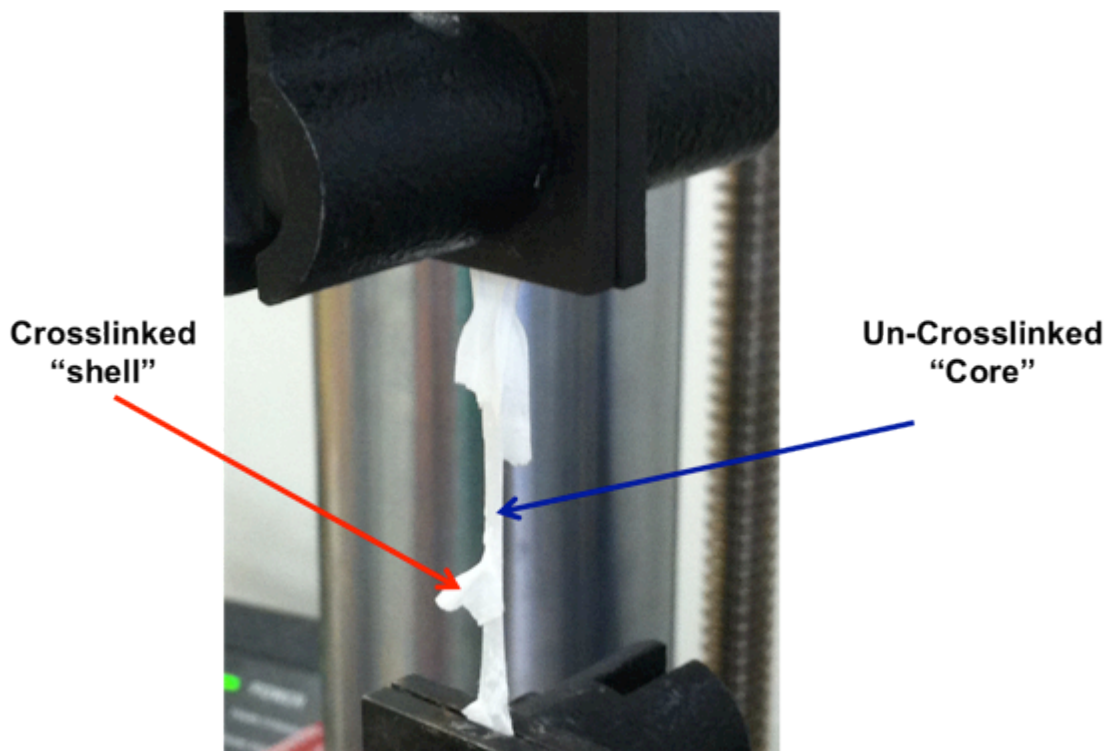


**Figure 4.12.** Photo of PEO10 sample delamination during a tensile experiment.

#### ***4.7. Addition of Reactive Monomers During the Crosslinking Procedures***

Knowing that the crosslinking reaction of PEO/PETA likely involves a free radical reaction with the vinyl substituents on PETA, additional reactive vinyl monomers could be incorporated into the crosslinked network. Propylene carbonate (PC) is a highly efficient polar solvent for lithium electrolytes. Solutions of PC exhibit ionic conductivities similar to EC:DMC mixtures typically. However, the reactivity of PC on the electrodes of rechargeable lithium batteries has prevented it from becoming a viable electrolyte for the consumer market.<sup>18, 19</sup> Much like EC and DMC, propylene carbonate can coordinate with  $\text{Li}^+$  cations, promoting dissociation due to its high dielectric constant. Polymer films of poly(propylene carbonate) have been reported to reach conductivities in the mS/cm range.<sup>20</sup> Addition of PC into the PEO crosslinked network would likely result

in additional coordination sites, further coupling the polymer electrolyte to device performance. Upon addition of vinylpropylene carbonate (VPC) into the electrospinning solution, fibrous non-woven mats of PEO/PETA/VPC were produced. The thermal properties and ionic conductivities of PEO/PETA mats electrospun with VPC were compared to Gen1 PEO/PETA mats. **Figure 4.13** shows the DSC traces of Gen1 PEO10, PEO20 and PEO30.

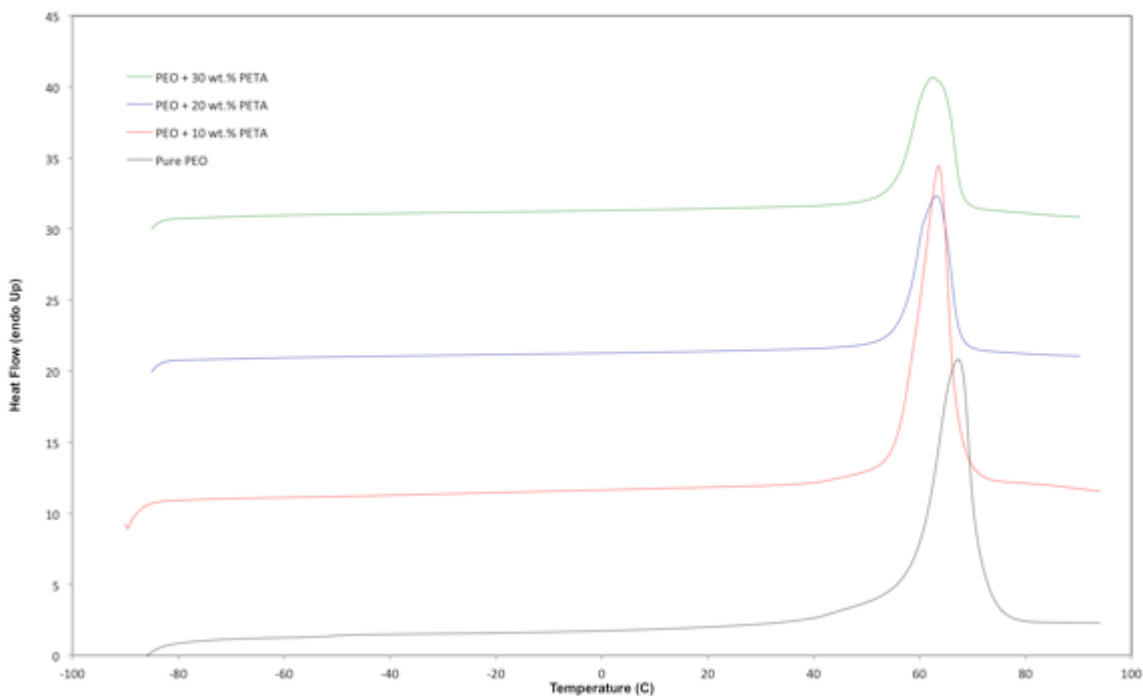


**Figure 4.13.** DSC thermograph of Gen1 PEO/PETA electrospun samples with various amounts of PETA including pure PEO (black), 10 wt.% PETA (red), 20 wt.% PETA (blue), and 30 wt.% PETA (green).

An endotherm associated with the melting of PEO crystallites may be observed at approximately 65 °C. The addition of PETA reduces the melting point maximum indicating that PETA weakens the PEO crystal structures. Additionally, increasing the amount of PETA reduces the area under the melting endotherm. This reduction suggests

that PETA not only acts as a photoinitiator, but it also disrupts PEO crystallinity. Disrupting crystallinity allows for greater chain mobility and  $\text{Li}^+$ -PEO interactions. We note that increasing the percentage of PETA has the added effect of reducing the overall amount of crystallizable PEO. However, when corrected for PETA content, the energies associated with the melting of PEO crystallites were reduced from 234 J/g for pure PEO to 275 J/g, 270 J/g, and 260 J/g for PEO10, PEO20 and PEO30 respectively. Comparing the crystallinity of PEO/PETA/VPC samples to Gen1 PEO/PETA samples, **Figure 4.14a** shows that samples with VPC have significantly lower melting endotherms. When comparing the Gen1 PEO10 sample with a PEO/PETA/VPC sample containing 5 wt.% PETA and 5 wt.% VPC (denoted as PEO5/5), the sample with VPC exhibits a smaller melting endotherm indicating that VPC disrupts PEO crystallinity even more than PETA. A PEO sample containing 10 wt.% of both PETA and VPC (PEO10/10) behaved in a similar manner. When compared to a Gen1 PEO20 sample, the PEO10/10 mat showed a reduction in the energy associated with the melting endotherm of PEO crystallites (**Figure 4.14b**).

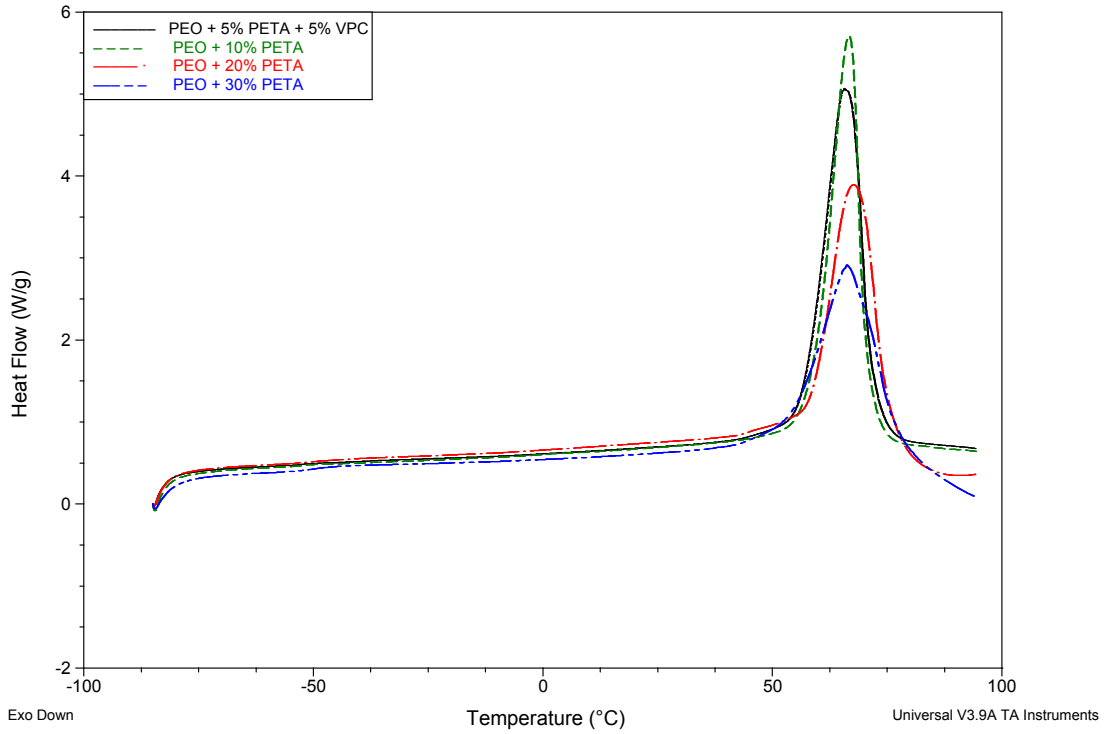


**Figure 4.14a.** DSC thermographs of PEO/PETA and PEO/PETA/VPC electrospun fiber mats. The dashed curves correspond to Gen 1 PEO10 (green), PEO20 (red), PEO30 (blue), and the solid line corresponds to a PEO sample containing 5 wt.% PETA and 5 wt.% VPC (black).

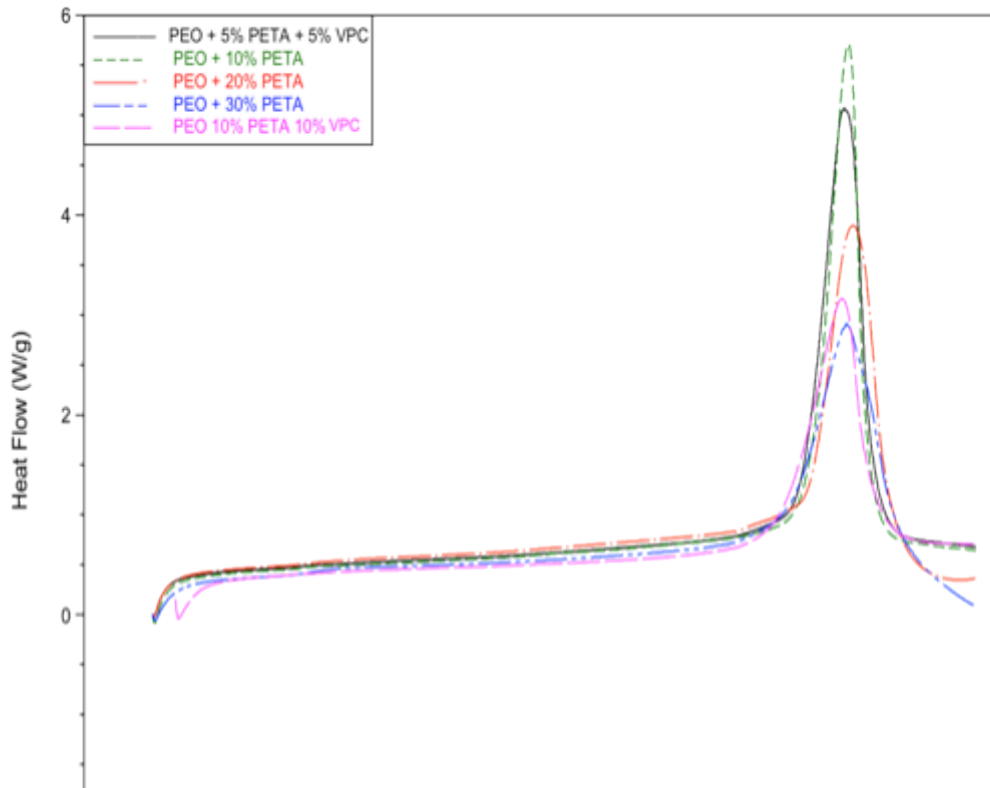


**Figure 4.14b.** DSC traces of figure 4.14a with the addition of a PEO/PETA/VPC electrospun sample: the PETA and VPC contents were both 10 wt.%.

The ionic conductivities of samples including VPC (**Figure 4.15**) were calculated using AC impedance spectroscopy as described in chapter 3. The PEO/PETA/VPC fiber mats were electrospun, crosslinked by exposing to UV irradiation for 30 minutes on both sides, swollen with various amounts of liquid electrolyte (EC:DMC with 1M LiClO<sub>4</sub>), and then measured for impedance. The conductivity of the PEO5/5 sample was observed to be higher than the PEO10 sample at all electrolyte loadings. Similarly, the PEO10/10 samples containing 10 wt.% VPC exhibited ionic conductivities higher still. Unlike the PEO20 sample, which has a lower ionic conductivity than PEO10, the PEO10/10 sample has an opposite trend when compared to the PEO5/5 sample. Our reasoning for why PEO20 loses conductivity involved polymer chain mobility. Increasing the amount of

PETA increased the crosslink density, thus reducing long chain mobility. This reduction in chain mobility adversely affects the PEO chain's ability to coordinate with  $\text{Li}^+$  ions. Since the polymer chains are more restricted as the crosslink density increases, coordination sites become less accessible, lithium salt dissociation is not promoted as much and thus the overall conductivity suffers. However, with the PEO/PETA/VPC samples, the VPC appears to counteract the chain mobility effect. Unfortunately, PEO with only 5 wt.% PETA does not result in a free-standing membrane; thus we can only speculate that going from 5 wt.% PETA to 10 wt.% PETA would follow the same trend as going from 10 wt.% to 20 wt.% PETA. Likely, the reduction in crystallinity caused by VPC allows for significant PEO- $\text{Li}^+$  interactions, which untimely lead to improved ionic conductivities as the concentration of VPC is increased.

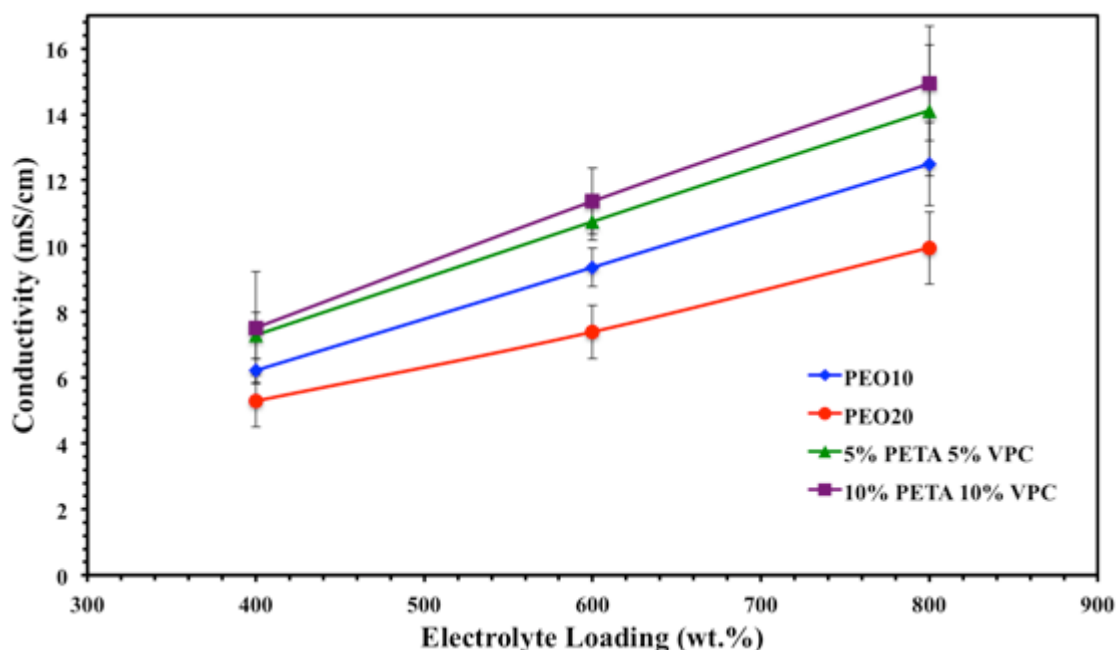


**Figure 4.15.** Ionic conductivities for Gen1 PEO samples containing 10 wt.% PETA (blue), 20 wt.% PETA (red), 5 wt.% PETA and 5 wt.% VPC (green), 10 wt.% PETA and 10 wt.% VPC (purple).

#### ***4.8 Temperature Dependence on Ionic Conductivity***

While PEO/PETA fiber mats displayed superior ionic conductivity performance when compared to other polymer-gel electrolytes, one rational suggested in chapter 3 involved the diffusion of  $\text{Li}^+$  ions facilitated by segmental chain motion of PEO. For the fully immersed samples, the  $\text{Li}^+$  diffusion is believed to be predominantly in the liquid domains as they account for well over 75% of the active material. Thus for the fully swollen membranes, the PEO contributions are primarily in increasing the charge carriers and possibly by reducing the tortuosity of the diffusing species. However, for the 400 wt.% swollen samples, the PEO chains could be involved in lithium transport through PEO- $\text{Li}^+$  coordination and subsequent reptation of the PEO chains (**Figure 1.10**). If we treat the 400 wt.% loaded samples like a solid polymer electrolyte plasticized with the liquid electrolyte, then there are two dominant conduction mechanisms: Vogel-Tammann-Fulcher (VTF) behavior and Arrhenius type behavior.<sup>21</sup> From the Arrhenius plots of conductivity for both Gen1 and Gen2 samples we see that the conductivity increases with temperature consistent with Arrhenius type behavior (**Figure 4.16**).

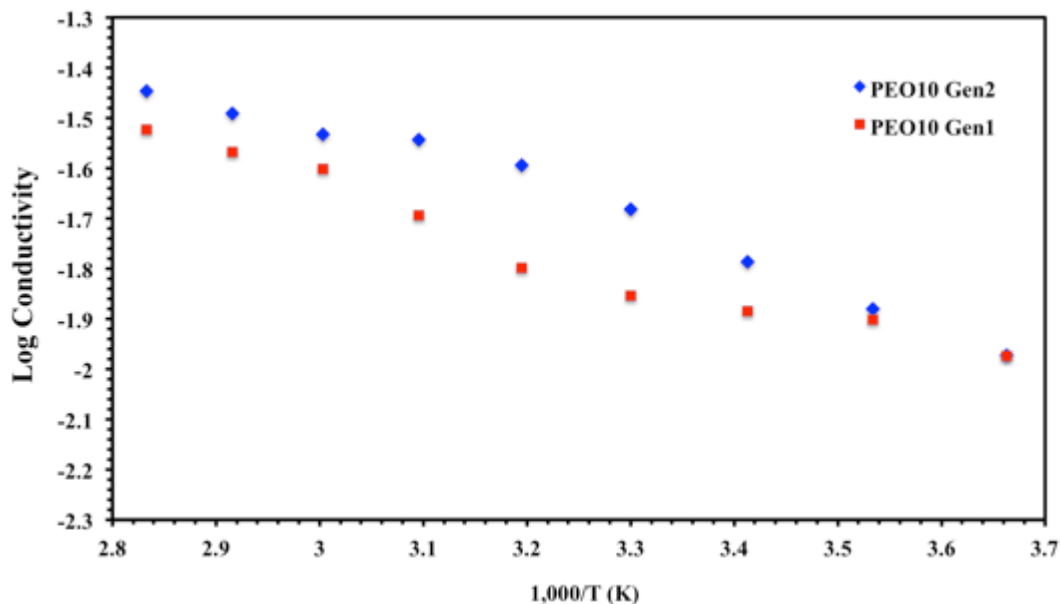


**Figure 4.16.** Arrhenius plot of Gen1 and Gen2 PEO10 conductivities.

#### **4.9. Conclusions**

The ultraviolet light initiated crosslinking of electrospun PEO fiber mats is possible with the use of a pentaerythritol triacrylate. Other photo- and thermoinitiators proved to be unsuccessful at producing insoluble mats. IR spectroscopy suggests that the reactivity of vinyl substituents on PETA likely provides a non-degrading means of coupling PEO radicals to form a crosslinked, insoluble network. Furthermore, reactive vinyl monomers such as vinylpropylene carbonate may be introduced into the network during UV curing. It is currently unclear whether or not VPC polymerizes after reacting with PEO radicals. However, a free-standing fibrous mat of PEO using 5 wt.% PETA is only produced in the presence of VPC, indicating that VPC might be involved in the crosslinking mechanism. Additionally, PEO fiber mats electrospun and crosslinked in the presence of VPC exhibited smaller melting endotherms than Gen1 PEO/PETA

samples, indicating a reduction in crystallinity. These PEO/PETA/VPC mats also demonstrated higher ionic conductivities than their PEO/PETA counterparts. Unlike Gen1 PEO/PETA, the ionic conductivities of the PEO/PETA/VPC mats increased when going from PEO5/5 to PEO10/10. This increase in conductivity means that VPC somehow overcomes the loss of chain mobility imparted by additional crosslink density. It is unclear whether the reduction in crystallinity or the increase in coordination sites is responsible for the increasing direct relationship between conductivity and VPC content.

#### ***4.10. Experimental***

##### ***4.10.1. Film Preparation for IR Spectroscopy***

Films of PEO10 were prepared by dissolving PEO and PETA into acetonitrile to yield a 5 wt. / vol. % solution. The polymeric solution was cast onto glass slides to produce films with a uniform thickness of 75  $\mu\text{m}$  upon drying under atmospheric conditions. Cast films were exposed to UV irradiation identical to the procedure outlined in chapter 3 for various amounts of time. The absorbance spectra of cast films of PEO10 were obtained via transmission experiments using a Varian 640-FT-IR spectrometer.

##### ***4.10.2. Thermo / Mechanical Characterization***

The Young's Moduli of electrospun fibers were assessed by tensile experiments. A 4 cm x 1 cm rectangle of each electrospun mat was prepared using a dog-bone punch. The fiber strips were clamped into an Instron Model 5564 Table Mounted Materials Testing System. The stress associated with an elongation rate of 0.5 mm/min was measured and used to develop the stress-strain plots.

Differential scanning calorimeter was performed on non- and pre-loaded PEO/PETA electrospun fiber mats using a TA-Q2000 DSC. Small 0.5 cm disks of PEO/PETA mats were punched out and placed into DSC pans to the approximate mass of 10 mg. The scanning profile began at -80 °C and was raised to a maximum of 95 °C at a rate of 5 °C / min.

#### ***4.10.3. Conductivity Measurements***

The conductivity data was collected similar to the procedure described in chapter 3. Samples were swollen with liquid electrolyte by either starve feeding or immersion and subsequently sandwiched between two gold electrodes. A Solartron Thru-plane impedance cell was used for all samples. The conductivity versus temperature data for Arrhenius plots were obtained by placing the impedance cell into an Espec SH-241 temperature / humidity chamber at the desired temperatures.

#### ***4.10.4. Preparation of Generation 2 PEO/PETA Fiber Mats***

The electrospinning of Gen 2 samples was identical to the Gen 1 procedure outlined in chapter 3. However, Gen 2 samples were crosslinked in a chamber with a nitrogen purge entering through the bottom and exiting through a small hole in the top of the chamber. During the 1 h curing process, the temperature of the chambers reached 40 °C.

#### 4.11. References

1. M. Doytcheva, D. Dotcheva, R. Stamenova and C. Tsvetanov, *Macromolecular Materials and Engineering*, 2001, **286**, 30-33.
2. M. B. Mellott, K. Searcy and M. V. Pishko, *Biomaterials*, 2001, **22**, 929-941.
3. C. Nason, T. Roper, C. Hoyle and J. A. Pojman, *Macromolecules*, 2005, **38**, 5506-5512.
4. C. G. Roffey, *Photogeneration of reactive species for UV curing*, Wiley Chichester, 1997.
5. A. F. Jacobine, *Radiation Curing in Polymer Science and Technology*, 1993, **3**, 219-268.
6. C. Zhou, Q. Wang and Q. Wu, *Carbohydrate Polymers*, 2012, **87**, 1779-1786.
7. S. L. Madorsicy and S. Straus, *Journal of Polymer Science*, 1959, **36**, 183-194.
8. K. J. Voorhees, S. F. Baugh and D. N. Stevenson, *Journal of Analytical and Applied Pyrolysis*, 1994, **30**, 47-57.
9. N. Grassie and G. A. Perdomo Mendoza, *Polymer Degradation and Stability*, 1984, **9**, 155-165.
10. P. de Sainte Claire, *Macromolecules*, 2009, **42**, 3469-3482.
11. L. Chen, Y. Qin, X. Wang, X. Zhao and F. Wang, *Polymer*, 2011, **52**, 4873-4880.
12. M. S. Peresin, Y. Habibi, A.-H. Vesterinen, O. J. Rojas, J. J. Pawlak and J. V. Seppälä, *Biomacromolecules*, 2010, **11**, 2471-2477.
13. W.-I. Park, M. Kang, H.-S. Kim and H.-J. Jin, *Macromolecular Symposia*, 2007, **249-250**, 289-294.
14. P. Lu and Y.-L. Hsieh, *Nanotechnology*, 2009, **20**, 415604.
15. J. O. Zoppe, M. S. Peresin, Y. Habibi, R. A. Venditti and O. J. Rojas, *ACS Applied Materials & Interfaces*, 2009, **1**, 1996-2004.
16. M. Doytcheva, D. Dotcheva, R. Stamenova, A. Orahovats, C. Tsvetanov and J. Leder, *Journal of Applied Polymer Science*, 1997, **64**, 2299-2307.
17. M. A. Tasdelen, N. Moszner and Y. Yagci, *Polym. Bull.*, 2009, **63**, 173-183.
18. K. Xu, *Chemical Reviews*, 2004, **104**, 4303-4418.
19. H. Zhao, S.-J. Park, F. Shi, Y. Fu, V. Battaglia, P. N. Ross and G. Liu, *Journal of The Electrochemical Society*, 2014, **161**, A194-A200.
20. D. Zhou, R. Zhou, C. Chen, W.-A. Yee, J. Kong, G. Ding and X. Lu, *The Journal of Physical Chemistry B*, 2013, **117**, 7783-7789.
21. R. C. Agrawal and G. P. Pandey, *Journal of Physics D: Applied Physics*, 2008, **41**, 223001.

## Chapter 5

# Lithium Transport Within a PEO-based Structured Polymer-Gel Electrolyte

### 5.1. Introduction

A key component to the success of PGEs is the liquid electrolyte. Thus in order to understand how polymer-ion interactions affect conductivity, lithium diffusion, and ultimately, battery performance, it is necessary to understand fundamental issues associated with the liquid component. From the Nernst-Einstein equation (**Equation 1**),

$$\sigma = \frac{(D_+ C_+ + D_- C_-) q^2}{kT}, \quad (1)$$

where  $\sigma$  is ionic conductivity,  $D_{+/-}$  are diffusion coefficients for cation (+) and anion (-),  $c_{+/-}$  are the concentrations of each charge carrier,  $q$  is the unit charge of the carrier, and  $kT$  is the average thermal energy ( $k$  is Boltzmann's constant and  $T$  is temperature), we see that the ionic conductivity has a strong dependence on the diffusion and concentration of both cation and anion. A main issue with solvent-mediated charge transport is overcoming electrostatic interactions, such as ion-dipole and ion-ion, which can influence ion transport properties, thus impacting conduction. Based on Coulomb's law (**Equation 2**),

$$F = \frac{q_1 q_2}{4\pi\epsilon r^2}, \quad (2)$$

where  $F$  is the magnitude of the Coulombic force,  $q_1$  and  $q_2$  are point charges of oppositely charged species,  $4\pi r^2$  is the surface area of a sphere ( $r$  is the distance between

the oppositely charged species), and  $\epsilon$  is the dielectric constant of the medium, the dielectric constant is a measurement of a medium's ability to shield Coulombic attractions. Specifically, electrostatic interactions between oppositely charged ions. Short time-scale interactions<sup>1</sup> between cations and anions can result in the formation of ion pairs (dipoles), triples, quadrupoles, and higher order aggregated charged species lowering diffusion coefficients, which reduce the bulk ionic conductivity (discussed below).<sup>2</sup> Cyclic polar solvents EC and PC have  $\epsilon$  values of 89.6 and 64.4, respectively, as a result of large dipole moments. Linear polar solvents, such as DMC and DEC, have  $\epsilon$  values of 3.11 and 2.88, respectively, as a result of small dipole moments.<sup>3</sup> Thus, a solvent with a high dielectric constant yields a medium in which electrostatic attractions between oppositely charged ions are minimized, often resulting in a high ionic conductivity. However, as described by the Stokes-Einstein relation (**Equation 3**),

$$D = \frac{kT}{6\pi\eta r_H}, \quad (3)$$

where  $D$  is the diffusion coefficient,  $kT$  is the average thermal energy,  $6\pi$  is a constant that is dependent on the diffusing species geometry,  $\eta$  is the viscosity, and  $r_H$  is the hydrodynamic radius, viscosity is inversely proportional to diffusion. EC and PC have  $\eta$  values of 1.86 and 2.53 cP, respectively, and DMC and DEC have  $\eta$  values of 0.59 and 0.75 cP, respectively.<sup>4</sup> Thus, delicate tailoring of the liquid electrolyte can provide a medium that shields lithium-anion interactions, minimizes viscosity, and maximizes ionic conductivity.

New insights into how the composition of the liquid electrolyte influences ionic conductivity must be made. While ionic conductivity measurements can provide information on the conductive nature of systems, it is a bulk measurement and lacks the

ability to quantify separate cation and anion contributions to the experimentally measured  $\sigma$  value. Thus, a technique that allows distinct characterization of all species must be used. Nuclear magnetic resonance (NMR) is a powerful technique with many advantages over other techniques, including nuclear specificity, non-destructiveness, and the ability to study dynamics on multiple time-scales. Relying on differences in local magnetic fields (i.e., magnetic field inhomogeneity), spin-spin relaxation ( $T_2$ ) measurements can probe chemical species that may reside within multiple environments. Thus, for PGEs where interactions between polymer, lithium, and solvent are present, multiple  $T_2$  times may be present and allow a better understanding of how morphological changes influence ion transport. In conjunction with  $T_2$  measurements, pulsed-field gradient (PFG) NMR allows for the direct measurement of small ion and small molecule transport properties, such as diffusion ( $D$ ), activation energy ( $E_a$ ), and the pre-exponential factor ( $D_0$ ), which is often described as the diffusion at infinite temperature, thus providing a deeper and more comprehensive understanding of how such properties correspond to bulk conductivity measurements within PGEs. For the scope of this work, the diffusion of charge carriers within PEO/PETA hybrid polymer-gel electrolytes will be discussed.

Previous reports in the literature have investigated the polymer-ion interactions between PGEs and charge carriers. For instance, Adebahr and coworkers reported a PGE based on methacrylates that were grafted with ethylene oxide (EO).<sup>5</sup> They observed two distinct  $T_2$  relaxations, which suggested  $\text{Li}^+$  ions existing in two distinctly different environments. The environments suggested consisted of  $\text{Li}^+$ -solvent interactions (longer  $T_2$  values) and  $\text{Li}^+$ -polymer interactions (shorter  $T_2$  values) with the caveat that each environment likely had contributions from both solvent- and polymer-ion interactions.

Thus the longer  $T_2$  is likely for  $\text{Li}^+$  only coordinated with 1 – 2 EO oxygens and 3 – 4 solvent molecules, whereas the environment represented by the shorter  $T_2$  is likely the opposite with more  $\text{Li}^+$ -polymer interactions and few  $\text{Li}^+$ -solvent interactions. This rationale was supported by the decrease in relaxation times as the number of EO units increased. Since both  $T_2$  relaxation times decrease with increasing polymer content, polymer-ion interactions are prevalent in both environments. As the chain length increases, the polymer chain mobility decreases, resulting in a more ridged environment thus causing a faster spin-spin relaxation in both environments.<sup>5</sup> It is possible that the polymer chain length simply affects the viscosity of the longer  $T_2$  environment, which would also account for the reduction in spin-spin relaxation, as the environment would be considerably less mobile as the viscosity increases.

PFG-NMR was used to investigate the diffusion coefficients of  $\text{Li}^+$  and  $\text{N}(\text{CF}_3\text{SO}_2)_2^-$  ions in PGEs based on PVDF-HFP. In films cast from THF, using a liquid electrolyte of the aforementioned salt and EC:DMC, the diffusion of the anions was reported to be faster than the cations and both diffusion coefficients increased with EC:DMC content.<sup>6</sup> Furthermore, Arrhenius plots of the ionic conductivity for these PGEs shows VTF-like behavior at low polymer compositions. This suggests that the polymeric component is not involved in the diffusion of charge carriers and is indicated by a linear relationship of the diffusion coefficients when plotted in an Arrhenius plot.<sup>7, 8</sup>

PFG-NMR experiments on polymer-gel electrolytes obtained by the polymerization of oligo(ethylene glycol)<sub>23</sub> – dimethacrylate and acrylonitrile swollen with dimethyl ether and lithium triflate also show that anionic diffusion is faster than cationic diffusion.<sup>9</sup> In agreement with subsequent work, these results suggest strong

interactions existing between PEO ether oxygens and  $\text{Li}^+$  cations.<sup>5</sup> The polymer- $\text{Li}^+$  interactions inhibit lithium diffusion while simultaneously boosting (or at least not hindering) the counter ion diffusion. Further supporting this claim is the transference number dependence on temperature. The lithium transference number is reported to increase with temperature up until the melting temperature of PEO ( $\sim 60\text{ }^\circ\text{C}$ ).<sup>9</sup> As the polymer chains become more mobile, the PEO assisted  $\text{Li}^+$  diffusion increases, thus resulting in higher transference numbers. Since the PEO does not interact with the counter ion, there is no temperature dependence on anionic diffusion associated with the polymer chains.

In collaboration with Bryce E. Kidd from Dr. Louis A. Madsen's research group we were able to observe two-component  $^7\text{Li}$  spin-spin relaxation ( $T_2$ ) values; the short- $T_2$  (4 ms to 0.8 ms) and long- $T_2$  (15 ms to 48 ms) are attributed to lithium-polymer and lithium-solvent interactions in our PEO/PETA electrospun mats when swollen with EC:DMC containing Li salts. Interestingly, these  $T_2$  relaxations appear to be independent of high cross-link density when fully swollen with liquid electrolyte. Using variable temperature  $^7\text{Li}$  pulsed-field gradient (PFG) nuclear magnetic resonance (NMR), we were able to elucidate fundamental lithium transport properties on the diffusion ( $t = 25 - 50$  ms) and pre-diffusion time-scale ( $t = \tau_c$ ), affording diffusion coefficients  $D$  and translational activation energies  $E_a$ . Consistent with ionic conductivity results, lithium  $D$  ( $10^{-10}\text{ m}^2\text{ s}^{-1}$ ) and  $E_a$  ( $16\text{ kJ mol}^{-1}$ ) are also independent of high cross-link density when fully swollen with liquid electrolyte. Interestingly, pre-loading lithium into the fiber-mat affects  $T_2$ ,  $D$ , and  $E_a$ .

## 5.2. PGE – Ionic Conductivity

In this study, Gen1 PEO/PETA electrospun fiber mats were used. The electrospinning conditions are described in chapter 3. Electrospun PEO/PETA fiber were submerged in a 50:50 vol. mixture of EC:DMC containing 1 M LiClO<sub>4</sub>. AC impedance was used to calculate the ionic conductivity also described in a previous section. Unlike the PEO/PETA samples in chapter 3, which are swollen with only 400 wt.% liquid electrolyte, **Figure 5.1** shows that for the fully swollen Gen1 PEO/PETA samples, the conductivity is nearly independent of crosslink density.

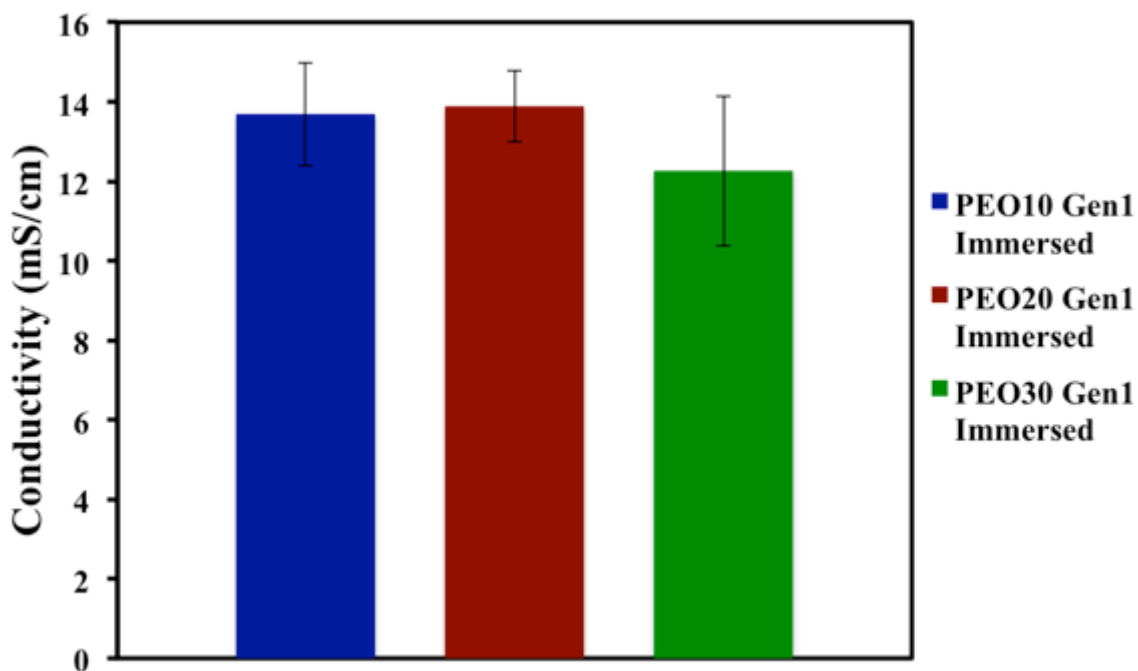


**Figure 5.1.** Ionic conductivity of Gen1 PEO/PETA electrospun samples upon immersion swelling in EC:DMC containing 1M LiClO<sub>4</sub>.

Ionic conductivity profiles for Gen1 PEO/PETA samples show that for all temperatures below 20 °C, the PEO10 conductivity was higher than PEO20, which was

in turn higher than PEO30. At room temperature, PEO10 and PEO20 were nearly identical; however, PEO30 had slightly lower average ionic conductivity. At temperatures above 20 °C, the ionic conductivity values became nearly indistinguishable. **Figure 5.2** shows the conductivity-temperature profiles for Gen1 electrospun PEO/PETA samples. Although **Figure 5.2** shows that at lower temperatures PEO10 appears to exhibit higher ionic conductivities, and PEO30 show the lowest values, the results are within error. Similar conductivity values suggest that there is no significant ionic conductivity dependence for fully immersion swollen PEO/PETA samples.

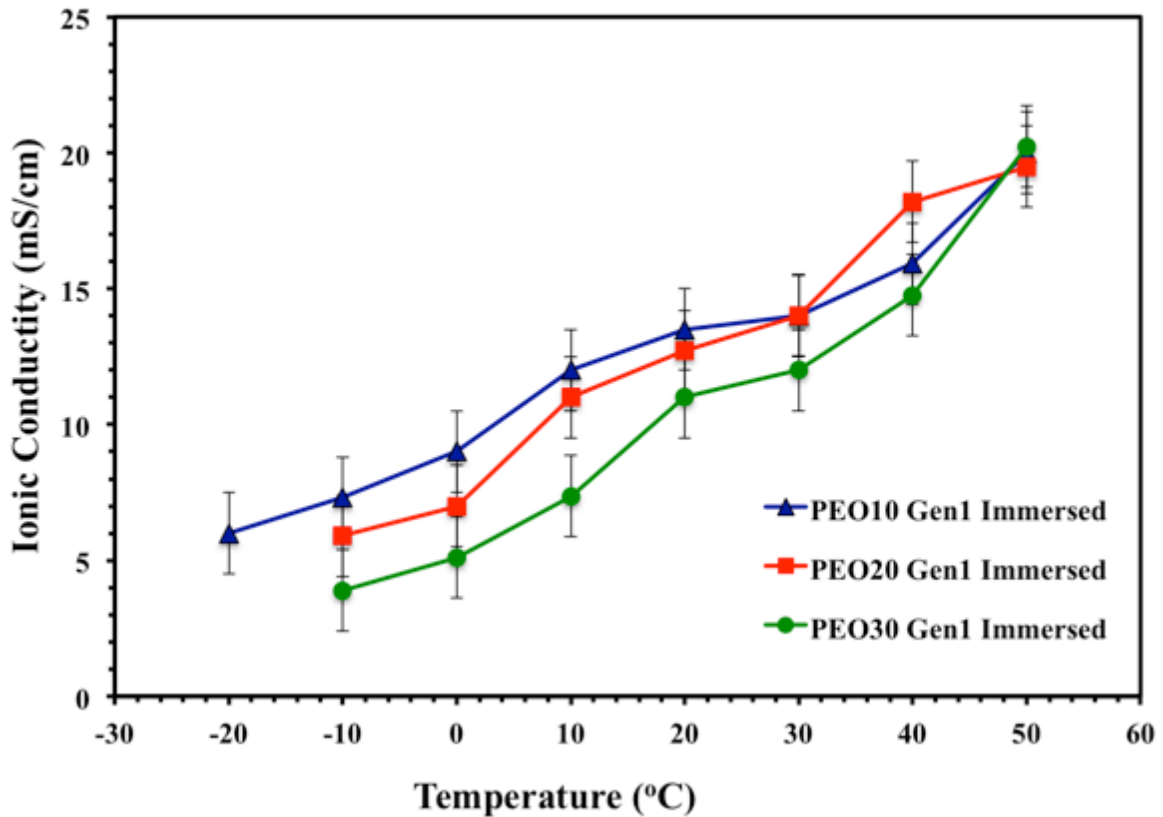


**Figure 5.2.** Ionic conductivity of Gen1 PEO/PETA samples at various temperatures. Samples include PEO10 (blue), PEO20 (red), and PEO30 (green).

Similar to PFG-NMR, translational activation energies can be obtained from ionic conductivity measurements. The activation energies obtained through ionic conductivity includes ion-ion interaction energy and ion-polymer interaction energies.<sup>10, 11</sup> One important difference between  $E_a$  derived from ionic conductivity is that the activation energies have contributions from both the cationic and anionic species. Unlike PFG-NMR, which can distinguish  $E_a$  values for each diffusing species independently, AC impedance spectroscopy lacks that ability. From an Arrhenius plot of the Gen1 PEO/PETA ionic conductivities (**Figure 5.3**), the activation energies were determined to be 9.8 kJ/mol, 17.7 kJ/mol, and 18.3 kJ/mol for PEO10, PEO20 and PEO30 respectively. We see that the conductivity derived  $E_a$  values increase as function of PETA content. This would suggest that increasing PETA either increases the ion-ion interactions or somehow disturbs the ion-polymer interactions.

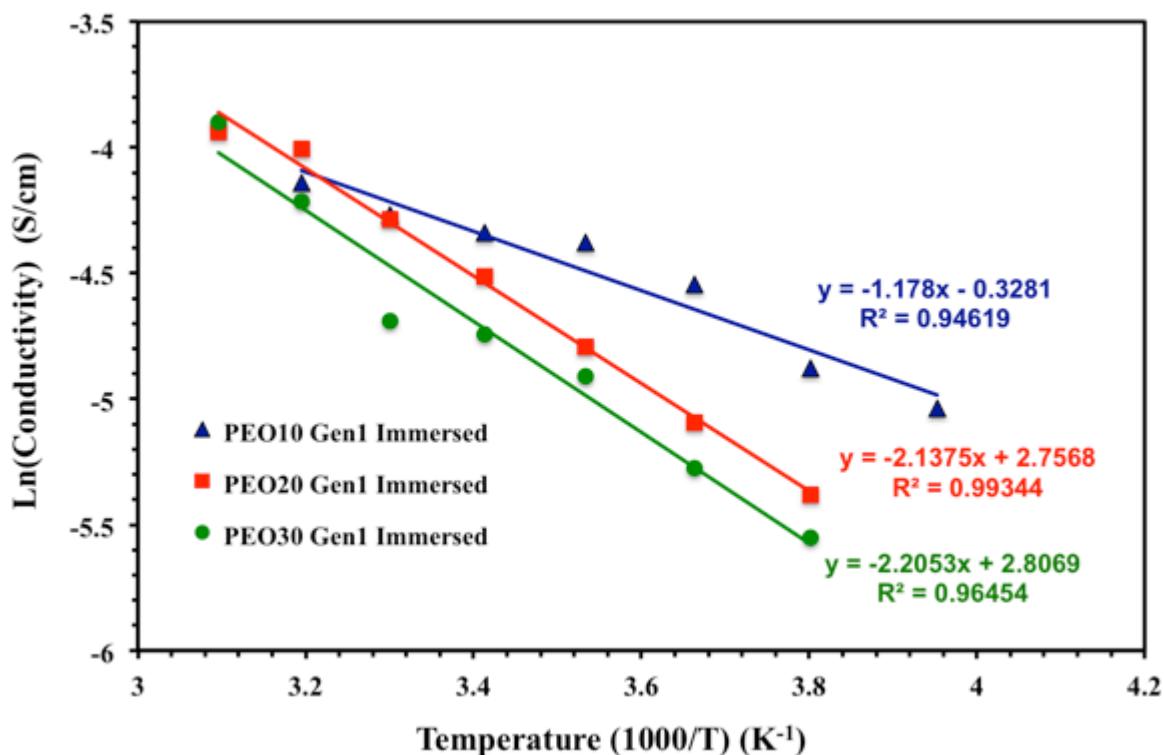


**Figure 5.3.** Arrhenius plot of Gen1 PEO/PETA conductivity values used to determine activation energies.

### 5.3. Variable Temperature Multi-Nuclear NMR

Due to the volatile and hygroscopic nature of the liquid electrolyte, samples were sealed in 5 mm NMR tubes containing 4 axial capillaries of 0.8 mm I.D. and 1.0 mm O.D. (Fisher Scientific). The use of capillaries was to prevent the contribution of convective flow to the measured diffusion coefficients. Electrospun cross-linked PEO fiber mats, electrospun PVDF (control), and glass fibers (control) were cut into 2 mm x 10 mm strips and threaded into 3 mm I.D. / 4 mm O.D. hollow glass tubes. The samples were vacuum dried at ambient temperature for 24 hrs to remove any water and then allowed to soak in a hermetically sealed vial with the liquid electrolyte for three days.

Residual liquid electrolyte was blotted off and the sample-loaded glass tubes were then loaded into a 5 mm NMR tube and sealed.

### 5.3.1. Probing Multiple Environments Through Spin-Spin Relaxation

All spin-spin relaxation ( $T_2$ ) measurements were conducted by Bryce E. Kidd at 35 °C using a 400 MHz Bruker Avance III WB NMR spectrometer, equipped with an MIC probe. The Carr-Purcell-Meiboom-Gill (CPMG) sequence ( $90^\circ_x - [\tau - 180^\circ_y - \tau]_n$ ) with an echo delay  $\tau = 5 \mu\text{s}$  afforded an exponential attenuation of signal intensity as a function of  $2\tau$  in 32-steps and fit with **Equation 4**,

$$I = I_0 e^{-\frac{2\tau}{T_2}}, \quad (4)$$

wherein  $I_0$  is the signal amplitude at  $\tau = 0$ ,  $\tau$  is the echo delay, and  $T_2$  is the spin-spin relaxation time constant. A bi-exponential fit was used, where appropriate, to extract two-component  $T_2$  values.

All variable temperature  $^7\text{Li}$  PFG-NMR experiments were performed using a 400 MHz Bruker Avance III WB NMR spectrometer, equipped with an MIC probe coupled to a Diff60 single-axis (z-axis) gradient system. Variable temperature  $^{35}\text{Cl}$  PFG-NMR experiments were performed using a 600 MHz Bruker Avance III NB NMR spectrometer, equipped with a DOTY DSI Model 20-40c probe single axis (z) gradient. In the PFG-NMR experiment, measured signal amplitude  $I$  as a function of gradient strength,  $g$ , was fit to the Stejskal-Tanner equation

$$I = I_0 e^{-D\gamma^2 g^2 \delta^2 (\Delta - \frac{\delta}{\epsilon})}, \quad (5)$$

where  $I_0$  is the signal amplitude at  $g = 0$ ,  $\gamma$  is the gyromagnetic ratio,  $\delta$  is the effective gradient pulse length,  $\Delta$  is the diffusion time between gradient pulses, and  $D$  is the self-diffusion coefficient.

Lithium ( $^7\text{Li}$ ) spin-spin relaxation ( $T_2$ ) measurements within PGEs not only give limits on usable gradient encoding periods for lithium PFG-NMR measurements (discussed below), but also report on lithium that may reside in more than one environment.<sup>5</sup> Relying on variations in local magnetic field,  $T_2$  is sensitive to differences in local environment (i.e., lithium interacting with ether-based PEO and liquid electrolyte).  $T_2$  relaxation probes a wide range of time-scales ( $\mu\text{s}$  to  $\text{s}$ ), making this technique very powerful in understanding ion-polymer and ion-liquid electrolyte interactions that play a large role in ion conduction.

Lithium  $T_2$  as a function of wt. % PETA yielded two-component fittings, short- and long- $T_2$  (**Figure 5.4**). For lithium within the liquid electrolyte, only one-component was seen with a  $T_2$  value of 1.6 s (not shown).

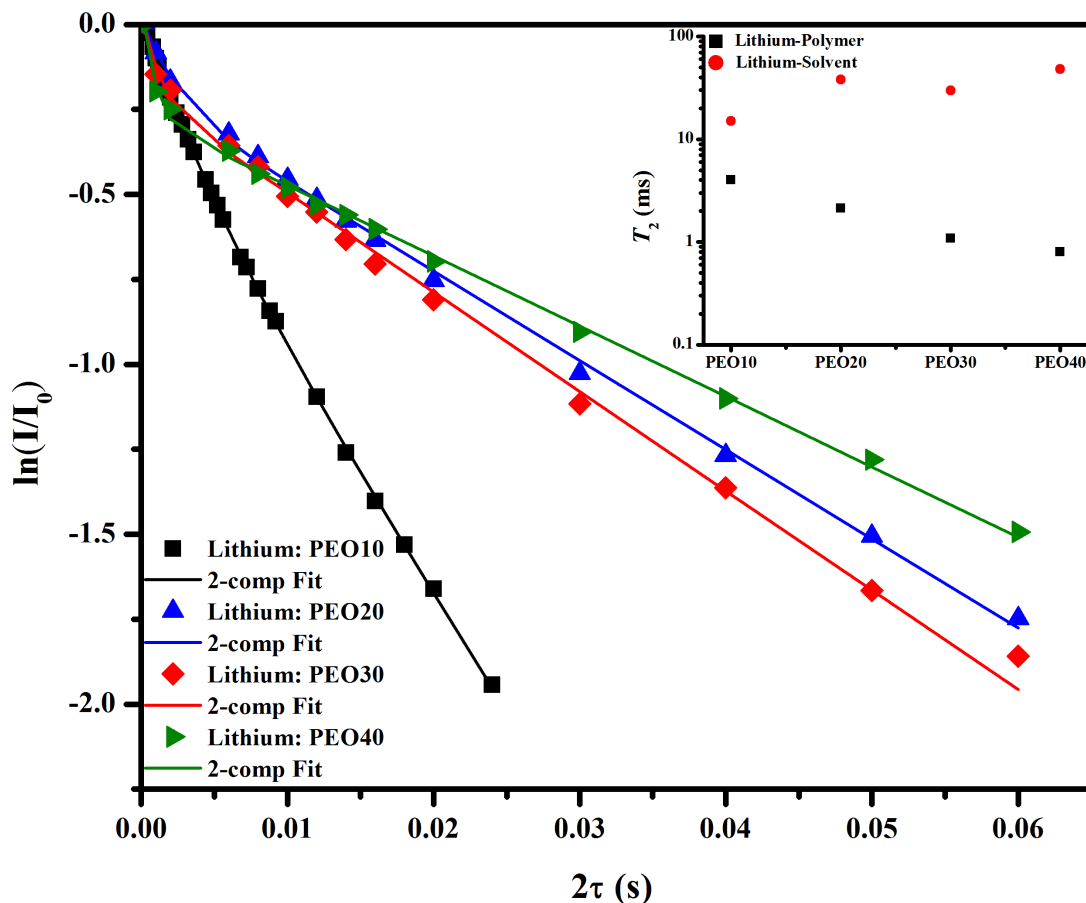


**Figure 5.4.**  $^7\text{Li}$  spin-spin lattice ( $T_2$ ) measurements (at 35 °C) yield two-component decay curves. This is suggestive of lithium within two distinct environments, where the short- $T_2$  may be lithium interacting with PEO, specifically the ether oxygens (i.e., more rigid environment), and the long- $T_2$  may be lithium interacting with the liquid electrolyte (i.e., more mobile environment). Within the figure inset, an increase and decrease in the Li-solvent (15 ms to 48 ms) and Li-polymer (4 ms to 0.8 ms), respectively, is seen as a function of wt. % PETA. Error estimated to be  $\leq 5\%$ .

We attribute the short- $T_2$  component to lithium-polymer interactions and the long- $T_2$  component to lithium-solvent interactions; lithium-polymer  $T_2$  decreases from 4 ms to 0.8 ms and lithium-solvent  $T_2$  increases from 15 ms to 48 ms as a function of wt% PETA. Adebahr *et al.* suggested lithium-polymer and lithium-solvent interactions from  $^7\text{Li}$   $T_2$

measurements of  $\text{LiPF}_6$  (in EC and gamma butyrolactone (gBL)) within uncross-linked PGE poly(methacrylate) grafted with (ethylene oxide) $_n$  as a function of PEO units.<sup>5</sup> It was shown that lithium-solvent and lithium-polymer  $T_2$  increase and decrease, respectively, as the number of PEO units increased due to a decrease in local chain segmental motion. From their two-component  $T_2$  curves and the previously reported BPP curve (i.e., variable temperature  $T_2$  measurements) for this system, it was suggested that two distinct lithium mobilities were involved as well, since the  $T_2$  values fell within the motional regime of the BPP curve. Unfortunately, no PFG-NMR measurements were reported. Ward *et al.* used PFG-NMR to study lithium and fluorine self-diffusion in PVDF samples swollen with  $\text{LiCF}_3\text{SO}_3$  and both tetraglyme and N,N-dimethylformamide.<sup>12</sup> The findings from  $T_2$  and diffusion studies were that diffusion occurs mainly in liquid-rich, polymer-poor regions of the film. With the addition of PETA to our PEO system, a decrease in PEO chain segmental motion may limit the ability of PEO to influence lithium transport (i.e., through ion-dipole interactions). Ion-dipole interactions and local polymer-chain structural relaxation (i.e., chain segmental motion) between ether-based PEO and lithium has been suggested to facilitate polymer-chain mediated charge transport within SPEs.<sup>13-15</sup> Moreover, high ionic conductivities are achieved due to shielding of lithium-anion interactions, which produces a higher concentration of charge carrying species that can contribute to conduction. At low cross-link density (PEO10), an almost uncross-linked system can be envisaged, consistent with similar  $T_2$  values. Moreover, uncross-linked PEO may strongly interact with lithium, thus shielding lithium-perchlorate and lithium-carbonate interactions. This shielding could potentially enhance diffusion, which is consistent with our ionic conductivity and lithium diffusion

measurements (discussed below). At high cross-link density (PEO20 – 40), PEO chains are more restricted and thus create a more rigid environment (reduction in short- $T_2$ ). Restricted PEO chains may increase the amount of lithium-perchlorate and lithium-carbonate interactions (increase in long- $T_2$ ) and result in a reduction in diffusion and conductivity, which is also consistent with our lithium diffusion and ionic conductivity measurements (discussed below). The present  $T_2$  data are suggestive of a decrease in lithium-polymer interactions and increase in lithium-solvent interactions as a function of wt. % PETA. As controls, electrospun PVDF and glass fibers show one-component  $T_2$  curves (not shown).

It was previously shown that impregnating  $\text{LiClO}_4$  into the cross-linked PEO fibers gives an enhancement in ionic conductivity by a factor of nearly 2 for the PEO10 samples when swollen with only 400 wt.% of a liquid electrolyte. To investigate the effect of pre-loading on lithium  $T_2$ , pre-loaded fiber mats, swollen with only EC:DMC (called “without 1M  $\text{LiClO}_4$ ”) and then with 1M  $\text{LiClO}_4$  (in EC:DMC) were also subjected to  $T_2$  measurements. **Figure 5.6** is a representative plot of lithium  $T_2$ -curves for PEO10  $\text{LiClO}_4$ -loaded (without 1M  $\text{LiClO}_4$ ), PEO10 lithium-loaded (with 1M  $\text{LiClO}_4$ ), and PEO10 (with 1M  $\text{LiClO}_4$ ), where the PEO10 (with 1M  $\text{LiClO}_4$ )  $T_2$ -curve from Figure X is used as a reference.

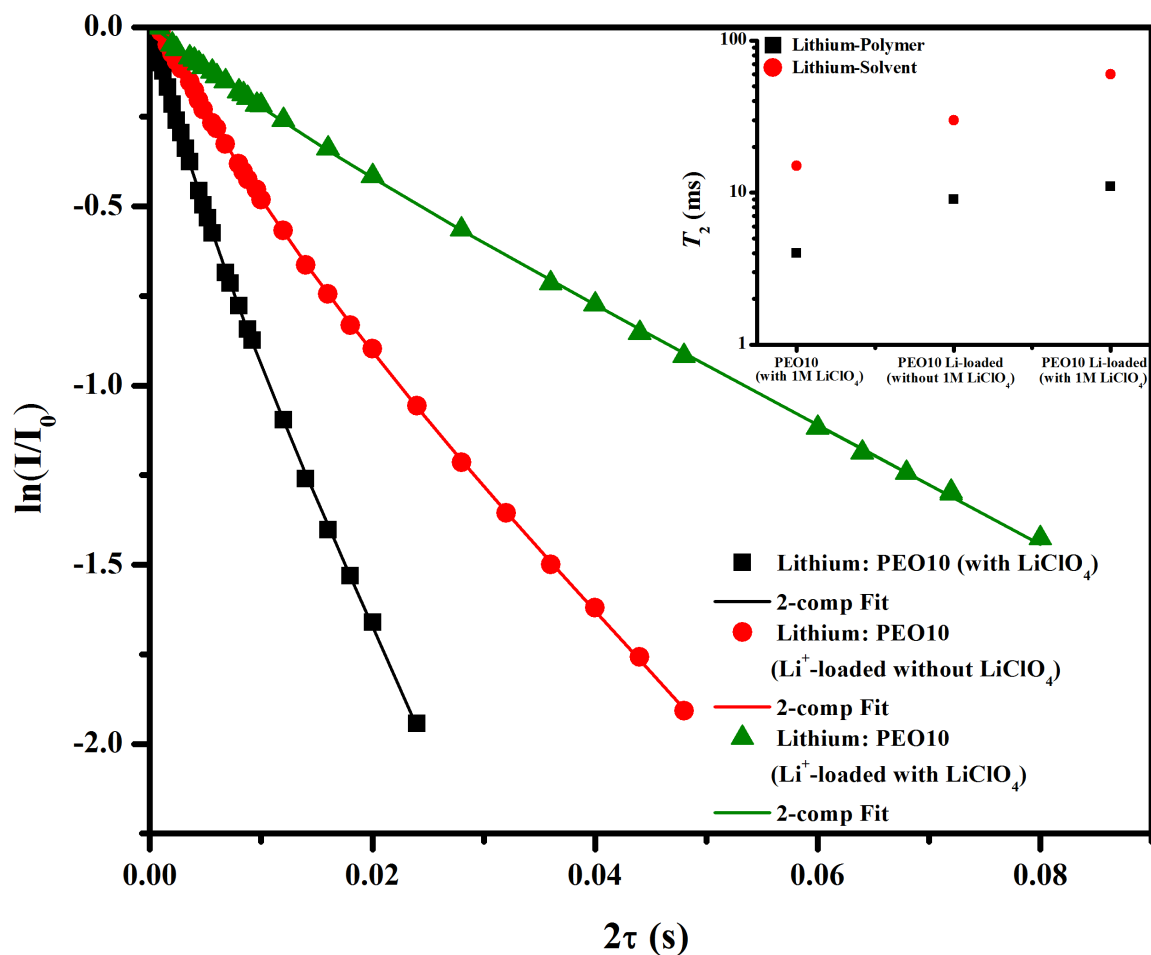


**Figure 5.6.**  $^7\text{Li}$  spin-spin lattice ( $T_2$ ) measurements (at 35 °C) for PEO10  $\text{LiClO}_4$ -loaded (with 1M  $\text{LiClO}_4$ ), PEO10  $\text{LiClO}_4$ -loaded (without 1M  $\text{LiClO}_4$ ), and PEO10 (with 1M  $\text{LiClO}_4$ ), where the previous PEO10 (with 1M  $\text{LiClO}_4$ )  $T_2$ -curve is used as a reference, yield two-component decay curves. Error estimated to be  $\leq 5\%$ .

### 5.3.2. Morphological Effects on $T_2$ Relaxation Times

From  $T_2$  as a function of wt. % PETA, two-component  $T_2$ -curves are suggestive of discrete lithium-polymer and lithium-solvent interactions. Assuming wt% PETA is not a variable for the pre-loaded PEO10 samples, one may expect no variability in the lithium-polymer  $T_2$ . However, pre-loading  $\text{LiClO}_4$  results in an increase in  $\text{Li}^+$ -polymer (4 ms to

11 ms) and  $\text{Li}^+$ -solvent (15 ms to 60 ms)  $T_2$  are seen from PEO10 (with 1M  $\text{LiClO}_4$ ) to pre-loaded PEO10 (with 1M  $\text{LiClO}_4$ ), suggestive of a change in local polymer environment post pre-loading. Essentially, an increase in  $T_2$  relates to the local environment becoming more mobile.  $\text{LiClO}_4$  pre-loading results in a more mobile polymer environment, likely caused by a reduction in crystallinity. As mentioned in chapter 1, it is well known that specific lithium-coordinated-to-PEO configurations, such as helical PEO, are formed in SPEs.<sup>16, 17</sup> Introducing a lithium salt into the PEO fibers via high swelling solvents (methanol / water) likely promotes the formation of these PEO-ion configurations. Since lithium cations strongly coordinate with PEO polymer chains to form helical structures, they inhibit PEO crystallization. It is difficult to envision  $\text{Li}^+$  penetration into a pure PEO crystalline lattice as potential coordination sites are sterically hindered. However, lithium ions have been shown to be very mobile within the PEO-salt configurations.<sup>18, 19</sup> If pure PEO crystallinity is reduced, then it follows that the polymeric matrix would become more mobile and thus an increase in the ion-polymer  $T_2$  would be observed. From DSC analysis, PEO crystallinity is disrupted within the dry fiber mat, accompanied by a higher temperature endotherm. This higher endothermic event is likely the melting / decomposition of a PEO- $\text{LiClO}_4$  complex.<sup>18-20</sup> **Figure 5.7** shows the DSC traces of Gen1 PEO/PETA fiber mats before and after pre-loading with  $\text{LiClO}_4$ . The endothermic event associated with the melting of pure PEO crystallites (60 – 65 °C) is completely absent for the pre-loaded samples. Additionally, although unobserved in the non-loaded samples, a step event in the heat capacity is observed around -60 °C, which is associated with the glass transition temperature ( $T_g$ ) of PEO. This  $T_g$  could be attributed to an increase in amorphous PEO content.

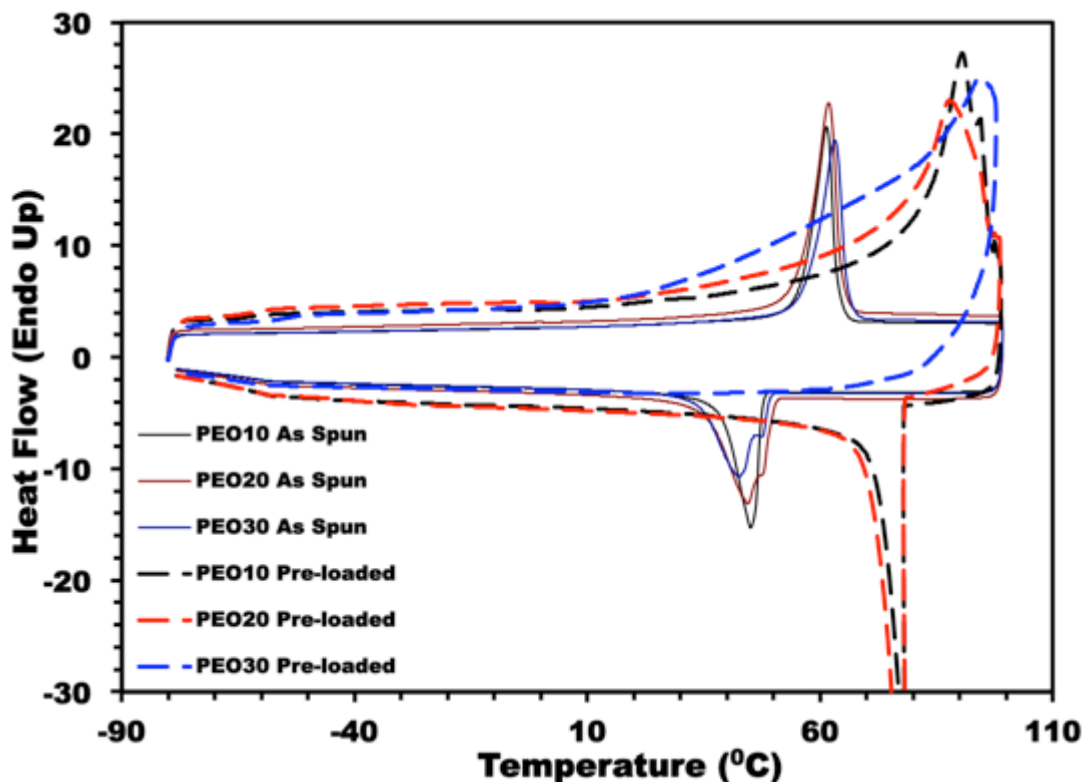


**Figure 5.7.** DSC traces of Gen1 PEO/PETA samples before (solid) and after (dashed) pre-loading with  $\text{LiClO}_4$  via ultrasonic agitation in methanol for PEO10 (black), PEO20 (red) and PEO30 (blue).

Moreover, an increase in  $\text{Li}^+$ -polymer  $T_2$  may be attributed to a decrease in the amount of free polymer interacting with the liquid electrolyte. Since PEO has a high degree of solubility in methanol, the soluble fraction of the pre-loaded samples is likely removed. Since the non-loaded samples were not washed with methanol, upon swelling with the EC:DMC liquid component, the soluble fraction (fraction of un-crosslinked PEO) exists in the liquid domains. PEO chains dissolved in the liquid domains increase viscosity and rigidity. However, removal of the soluble fraction during the pre-loading prevents free polymer chains from leaching into the liquid domains and increasing the

viscosity. The increase in ion-solvent  $T_2$  can be associated with reduced local viscosities resulting in less rigid environments. In addition to removing the soluble fraction, extra-fibrillar polymer chains (polymer chains extending out from the fibers and into the liquid matrix) may become restricted due to  $\text{Li}^+$ -polymer interactions. Basic calculations suggest that if an electrospun fiber is 1  $\mu\text{m}$  in diameter, and assuming that a PEO chain is only crosslinked close to one end, then a 300,000 molecular weight PEO chain (containing approximately 6818 repeating units each  $\sim 0.36$  nm long) would be approximately 2.4  $\mu\text{m}$  in length. That is assuming that the PEO chain is completely extended (accounting for bond angles). The end-to-end chain distance could be calculated by **Equation 6**, where  $d$  is the bond length and  $N$  is the number of bonds, resulting in a PEO chain that could extend into the liquid domain approximately 29.3 nm ( $\sim 0.03$   $\mu\text{m}$ ).

$$\langle r \rangle = d\sqrt{N} \quad (6)$$

Potentially, extended “loose-end” PEO chains could increase the average fiber diameter by 3%. PEO chains extending into the liquid domains could interact with EC, DMC and  $\text{Li}^+$ , potentially hindering ionic mobility in the liquid domains. However, if pre-loaded  $\text{Li}^+$  ions coordinate with the loose-end PEO chains, then their presence in the liquid domains may have a lesser effect on diffusing species. In the case for the non-loaded samples,  $\text{Li}^+$  ions in the liquid domains (solvated by EC:DMC) would be attracted to the PEO loose-ends, forming coordinations involving PEO,  $\text{Li}^+$  ions, EC and DMC. These large (due to the EC:DMC) coordination complexes do two things to reduce the diffusion of charge carriers in the liquid domains: 1) since the PEO chains are essentially immobile compared to the liquid components, coordination results in a loss of mobility

for  $\text{Li}^+$  ions. Additionally, the concentration of free, charge carrying  $\text{Li}^+$  ions (those not immobilized by PEO) decreases for the non-loaded samples. 2) strong coordinations between PEO loose-end chains and Li-solvated complexes become obstacles for free charge carriers to navigate. In the case of the pre-loaded PEO/PETA samples, since Li-salts are introduced prior to electrolyte swelling, PEO- $\text{Li}^+$  coordination can occur without reducing the overall concentration of free ions in the liquid domains. Furthermore, since no EC:DMC molecules are present during this coordination, the PEO- $\text{Li}^+$  complexes are likely smaller, thus having smaller footprints in the liquid domains (**Figure 5.8**).

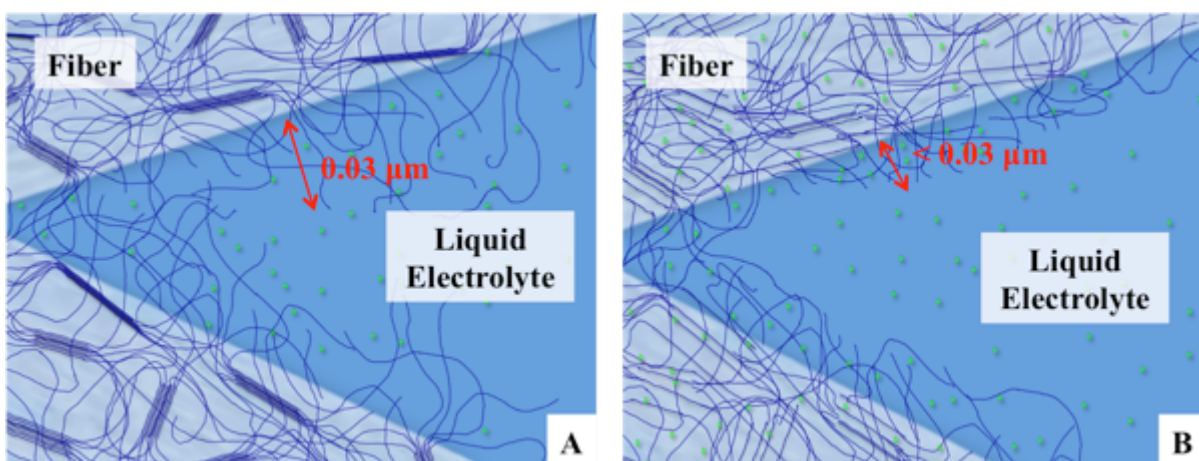


**Figure 5.8.** Cartoon schematic of electrospun fibers non-loaded (A) and pre-loaded (B) with  $\text{LiClO}_4$ . Opaque domains represent fibers, small dark blue lines represent PEO polymer chains, blue bundles represent PEO crystalline regions, light blue regions indicated liquid domains, and small green spheres represent  $\text{Li}^+$  ions.

### 5.3.3. *Liquid Electrolyte Variable Temperature Pulsed-Field Gradient NMR*

We attribute the long  $T_2$  component to  $\text{Li}^+$ -solvent interactions, thus it is imperative to understand how the liquid electrolyte influences solvent-mediated charge transport.  $^7\text{Li}$  and  $^{35}\text{Cl}$  variable temperature PFG-NMR studies allow us to probe

chemically specific transport properties, such as the diffusion coefficient  $D$  and activation energy  $E_a$  within ion dense systems. First, the pure liquid electrolyte components were examined to construct a foundation for understanding the transport properties associated with solvent, cation, and anion transport within the swollen fiber mat.

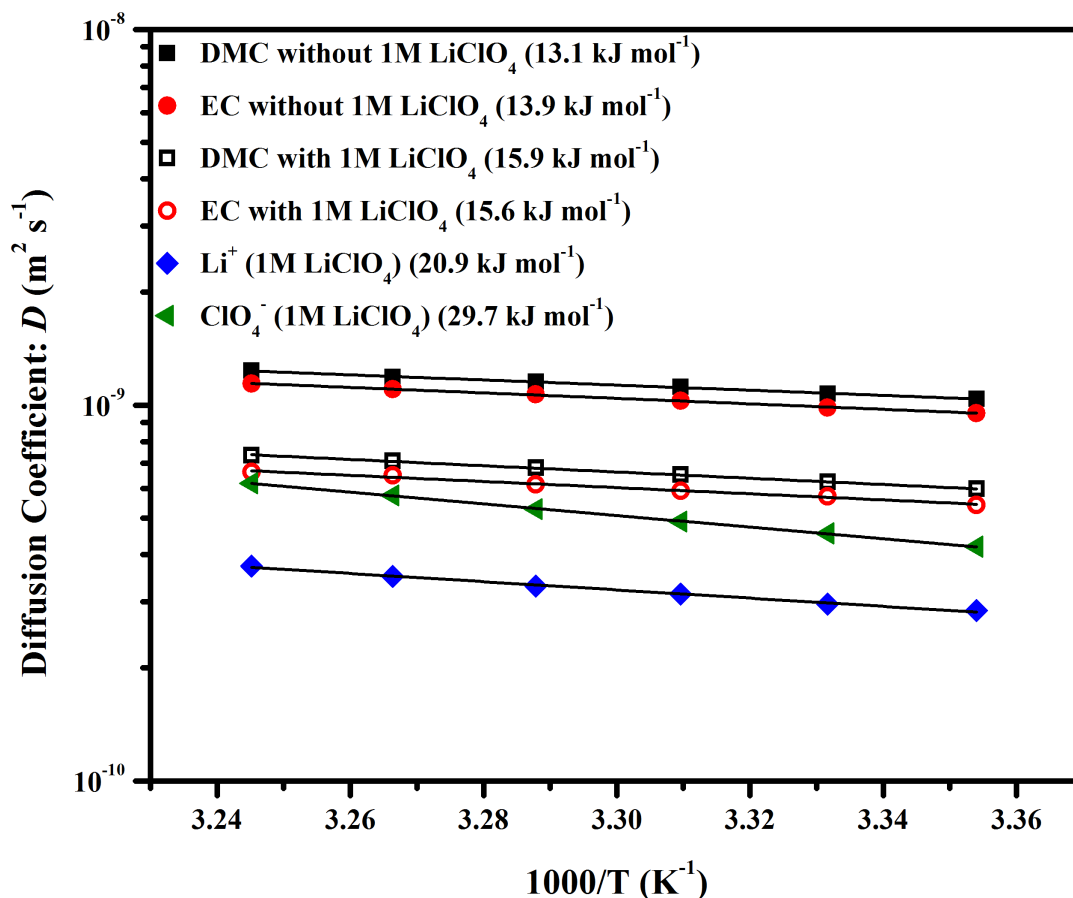


**Figure 5.9.** Arrhenius plots of lithium ( $^7\text{Li}$ ), perchlorate ( $^{35}\text{Cl}$ ), and EC ( $^1\text{H}$ ) and DMC ( $^1\text{H}$ ) (with/without  $\text{LiClO}_4$ ) give insight into pre-diffusion time-scale interactions for the liquid electrolyte. Carbonate  $D$  and  $E_a$  decrease and increase, respectively, with addition of  $\text{LiClO}_4$ . Lithium  $D$  and  $E_a$  are lower than perchlorate, suggestive of attractive and repulsive ion-dipole interactions between lithium-carbonate and perchlorate-carbonate, respectively. We estimate the error for  $E_a$  values to be  $\leq 1 \text{ kJ mol}^{-1}$ .

**Figure 5.9** is a compilation of Arrhenius plots for the individual components of the liquid electrolyte (i.e., EC, DMC, lithium, and perchlorate). The temperature range is kept small (25 – 35 °C in 2° increments) due to the volatility of DMC ( $T_b = 90$  °C). The diffusion coefficients and  $E_a$  (with an error of < 1 kJ/mol) of both EC and DMC are very similar to each other without and with LiClO<sub>4</sub>, suggestive of a homogenous mixture of both carbonates with similar local energetics. The addition of LiClO<sub>4</sub> to make a 1 M solution decreases and increases both carbonate diffusion coefficients and  $E_a$ , respectively. When compared to the carbonates, the lithium diffusion coefficient is a factor of two slower while  $E_a$  is 5 kJ mol<sup>-1</sup> larger. With dipole moments (EC,  $\epsilon = 89.6$  and DMC,  $\epsilon = 3.11$ ), ion-dipole interactions between the carbonates, lithium, and higher order positively charged ionic aggregates (if present), may influence lithium diffusion and  $E_a$ . Through molecular dynamics simulations and mass spectrometry, it has been suggested that 2 – 3 carbonate molecules, such as EC and PC, solvate and stabilize lithium ion, whereas the anion experiences repulsive ion-dipole interactions and becomes “naked.”<sup>21</sup> Moreover, for common carbonate solvents, enthalpies of solvation calculations have shown that lithium solvation (10 kcal mol<sup>-1</sup>) takes less energy than anion solvation (20 – 50 kcal mol<sup>-1</sup>), which is attributed to the high surface charge density (i.e., small  $r_i$ ) of lithium ion.<sup>22</sup> Thus, for the carbonates to have a faster  $D$  and lower  $E_a$  than Li<sup>+</sup>, there may be fast exchange of carbonates in/out of the lithium ion solvation shell. Additionally, strong Coulombic interactions between Li<sup>+</sup> and perchlorate cannot be ignored.

#### **5.3.4. Swollen Fiber Mat Variable Temperature Pulsed-Field Gradient NMR**

Our current understanding of the Arrhenius parameters to diffusion and local energetics of  $\text{Li}^+$  within the liquid electrolyte swollen PEO fiber mat to probe how varying wt. % PETA can affect lithium  $D$  and  $E_a$ . Prior to investigating crosslinked mats, however, the importance of PEO-ion interactions was investigated. **Figure 5.10** shows the Arrhenius plots of unstructured PEO gels formed by dissolving PEO in solutions of EC:DMC containing various concentrations of  $\text{LiClO}_4$ . The unstructured gels were prepared such that the EC:DMC component represented 400 wt.% of the total mass of the dry PEO. The conductivities for these unstructured gels were previously reported in chapter 3. In agreement with the conductivity results, an increase in the diffusion coefficient is observed with increasing  $\text{LiClO}_4$  concentration. The presence of PEO allows for higher concentrations of charge carrying ions due to PEOs ability to facilitate dissociation.<sup>23</sup> We see that  $\text{Li}^+$  diffusion within the uncross-linked gel increases from  $4 \times 10^{-11}$  ( $0.5 \text{ M LiClO}_4$ ) to  $7.9 \times 10^{-11} \text{ m}^2/\text{s}$  ( $2.0 \text{ M LiClO}_4$ ). Interestingly,  $E_a$  changes within error, further showing that diffusion and  $E_a$  are not coupled to each other. While the diffusion length-scale environment changes, the local environment does not change.

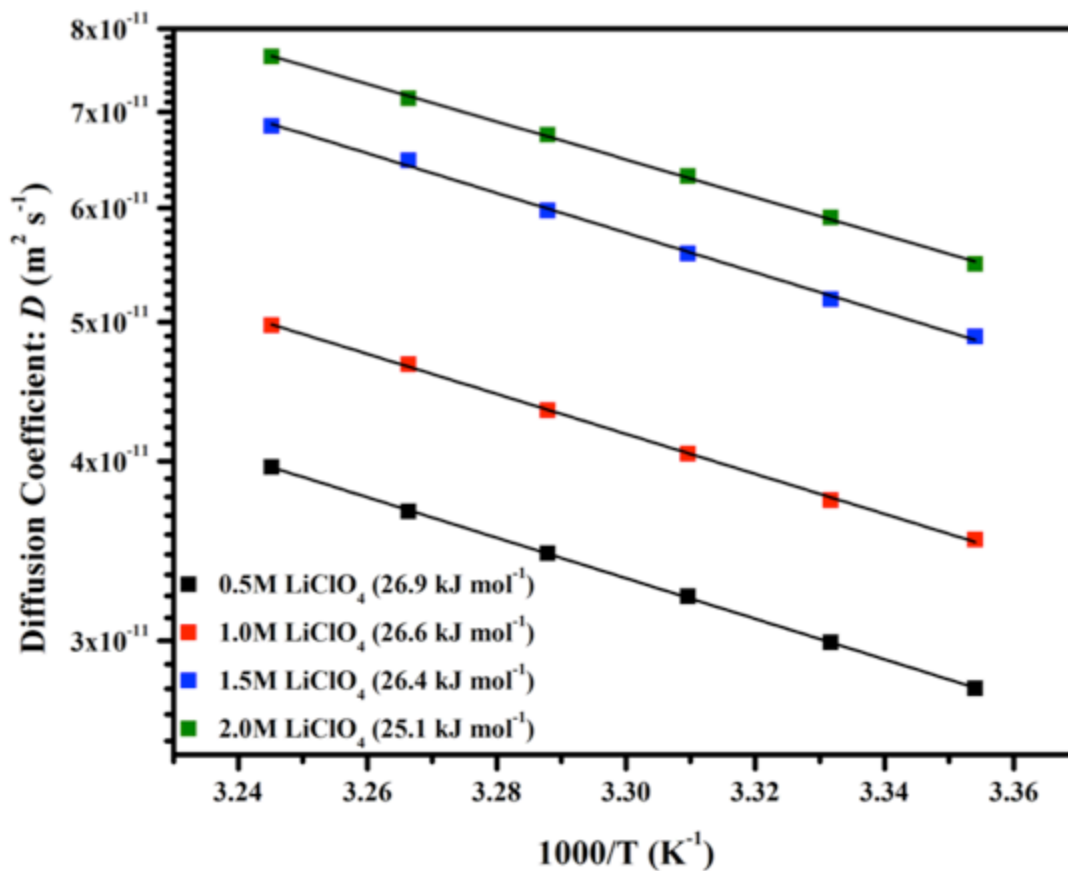


**Figure 5.10.** Arrhenius plots of unstructured PEO/EC:DMC gels containing various lithium perchlorate concentrations. Error estimated to be  $\leq 5\%$ .

Arrhenius plots of lithium ion diffusion as a function of wt.% PETA are shown in **Figure 5.11**. The mobility of PEO chains within the crosslinked polymer network has a significant role on the diffusive properties of  $\text{Li}^+$  ions. The diffusion coefficients suggest that the lithium ions in PEO10 are moving faster than in the higher wt.% PETA samples. In fact, the diffusion decreases as a function of PETA content until 40 wt.%.

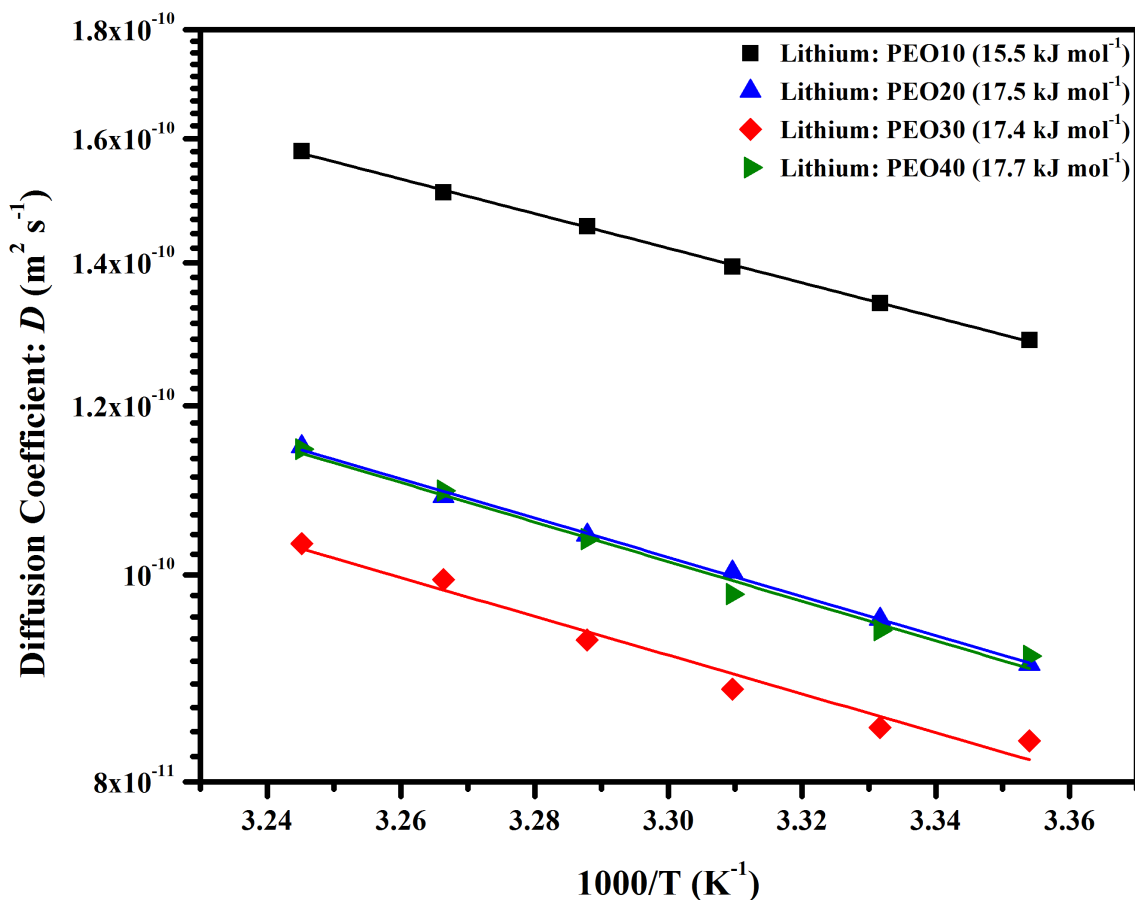


**Figure 5.11.** Arrhenius plots of PEO/PETA fibrous electrolytes as a function of wt.% PETA allows us to understand how the introduction of a cross-linker influences macro- and microscopic transport properties.  $\text{Li}^+$  diffuses fastest in PEO10 with an  $E_a$  of  $15.5 \text{ kJ mol}^{-1}$ . Error in  $D$  values is estimated to be 5% and  $E_a$  values to be  $\pm 2 \text{ kJ mol}^{-1}$ .

Ionic conductivity as a function of wt.% PETA shows that  $\sigma$  values change is within the error limits, suggestive of no ion diffusion dependence on cross-link density. However, variable temperature diffusion measurements show that  $\text{Li}^+$  diffusion and  $E_a$  are fastest ( $1.58 \times 10^{-10} \text{ m}^2 \text{ s}^{-1}$ ) and lowest ( $15.5 \text{ kJ mol}^{-1}$ ), respectively, for PEO10 with a decrease ( $1.03 \times 10^{-10} \text{ m}^2 \text{ s}^{-1}$ ) and increase ( $17.7 \text{ kJ mol}^{-1}$ ) in diffusion and  $E_a$ ,

respectively, with increasing wt. % PETA. Moreover,  $T_2$  measurements suggest that increasing wt.% PETA creates a more rigid lithium-polymer environment. Since PEO may aid in ion disassociation, a higher concentration of charge carrying species will increase bulk ionic conductivity, as described by the Nernst-Einstein equation (**Equation 1**). This implies that lithium ion diffusion and polymer chain segmental motion are intimately related in these systems. Moreover, PEO may aid in the disruption of  $\text{Li}^+$ -carbonate interactions. From the liquid electrolyte analysis, lithium  $E_a$  of  $\text{Li}^+$  diffusion represents the ensemble average of ion-dipole interactions between lithium and carbonates on the pre-diffusion time-scale ( $\leq 1$  ps). Interestingly, a reduction in  $E_a$ , by 5  $\text{kJ mol}^{-1}$ , is seen for lithium in PEO10 vs. pure liquid electrolyte.

Within this class of PGEs, an increase in ionic conductivity post-preloading was observed for PEO/PETA samples swollen with 400 wt.% liquid electrolyte. To investigate how lithium  $D$  and  $E_a$  change with pre-loading, the  $\text{Li}^+$  Arrhenius plots for diffusion are shown in **Figure 5.12**. The Arrhenius plots for the pure liquid electrolyte and PEO10 are shown as references to emphasis  $\text{Li}^+$  diffusion enhancement post pre-loading.  $\text{Li}^+$  diffusion and  $E_a$  change, respectively, within error from  $1.579 \times 10^{-10}$  and  $15.5 \text{ kJ mol}^{-1}$  (PEO10 with 1M  $\text{LiClO}_4$ ) to  $1.623 \times 10^{-10} \text{ m}^2 \text{ s}^{-1}$  and  $15.1 \text{ kJ mol}^{-1}$  (pre-loaded PEO10 swollen with only EC:DMC). It is possible similar polymeric and lithium local environments exists between non-loaded and pre-loaded PEO10 due to an equilibrium exchange of lithium ions between the polymeric and liquid domains. However, when pre-loaded PEO10 is swollen with 1 M  $\text{LiClO}_4$ ,  $\text{Li}^+$  diffusion and  $E_a$  increase to  $1.855 \times 10^{-10} \text{ m}^2 \text{ s}^{-1}$  and  $21.6 \text{ kJ mol}^{-1}$ ; the diffusion is a factor of two lower

than lithium within the pure liquid electrolyte but  $E_a$  is similar. Although PEO-Li<sup>+</sup> ion interactions promote lithium salt dissociation, they seem to hinder Li<sup>+</sup> mobility.

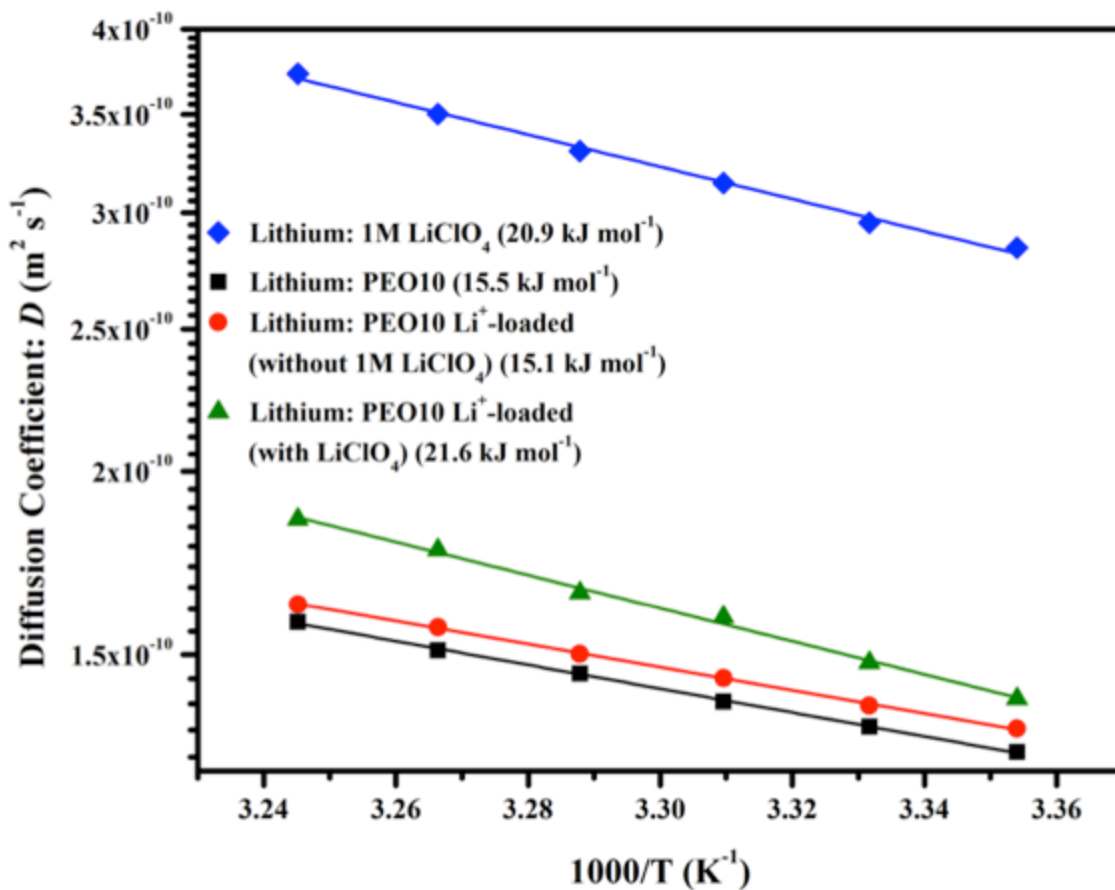


**Figure 5.12.** Arrhenius plots of lithium ion diffusion as a function of wt.% PETA. Lithium ion diffusion in pure liquid electrolyte is plotted in blue. Black data represent non-loaded PEO10 samples swollen with EC:DMC 1M LiClO<sub>4</sub>. Red data represent pre-loaded PEO10 swollen with only EC:DMC. Green data represent pre-loaded PEO10 sample swollen with EC:DMC 1M LiClO<sub>4</sub>. Error estimated to be  $\leq 5\%$ .

The Li<sup>+</sup> diffusion is of paramount importance because it is essentially the limiting factor on how fast a cell can charge or discharge. Intercalation into the anode and

cathode material is nearly an order of magnitude faster than  $\text{Li}^+$  diffusion through a polymer-gel electrolyte. For comparison, Arrhenius plots of the diffusion coefficients for  $\text{Li}^+$  ions in PEO/PETA samples are compared to those obtained from PVDF and glass fiber controls (**Figure 5.13**). Interestingly, the diffusion coefficient for  $\text{Li}^+$  ions in the glass fiber sample is the highest, which is unsurprising as glass fibers have no interaction with the liquid electrolyte solution. Thus on local length scales (probed by ionic diffusion) the mobility of  $\text{Li}^+$  ions is very high and similar to that of the pure liquid samples. However, long-range tortuosity reduces the overall diffusion as ions must navigate around impenetrable fibers. The PVDF sample exhibits the second highest lithium diffusion coefficient. Similar to the glass fibers, PVDF chains have very little interaction with  $\text{Li}^+$  ions; thus the electrolyte solvent mainly governs diffusion. Unlike the glass fibers samples, which maintain a very discrete fibrous architecture, resulting in non-viscous liquid pathways for the charge carriers to travel, PVDF gels eventually lose any structure and become homogeneous gels samples. Because of this homogeneous configuration, the local viscosities of the liquid domains are higher than the glass fiber sample. Finally, the PEO samples exhibit  $\text{Li}^+$  diffusion coefficients much lower than the glass and PVDF samples. Although the PEO/PETA network is crosslinked, which results in lower local viscosities, the PEO-ion interactions slow lithium diffusion. Since PEO chains are essentially immobile, when charge carrying  $\text{Li}^+$  ions coordinate with the ether oxygens, they are prevented from diffusing until those interactions are terminated. These results contradict the ionic conductivity data suggesting that the conductivity increase is due more to an increase in the number of charge carriers than to  $\text{Li}^+$  diffusion through polymeric domains.

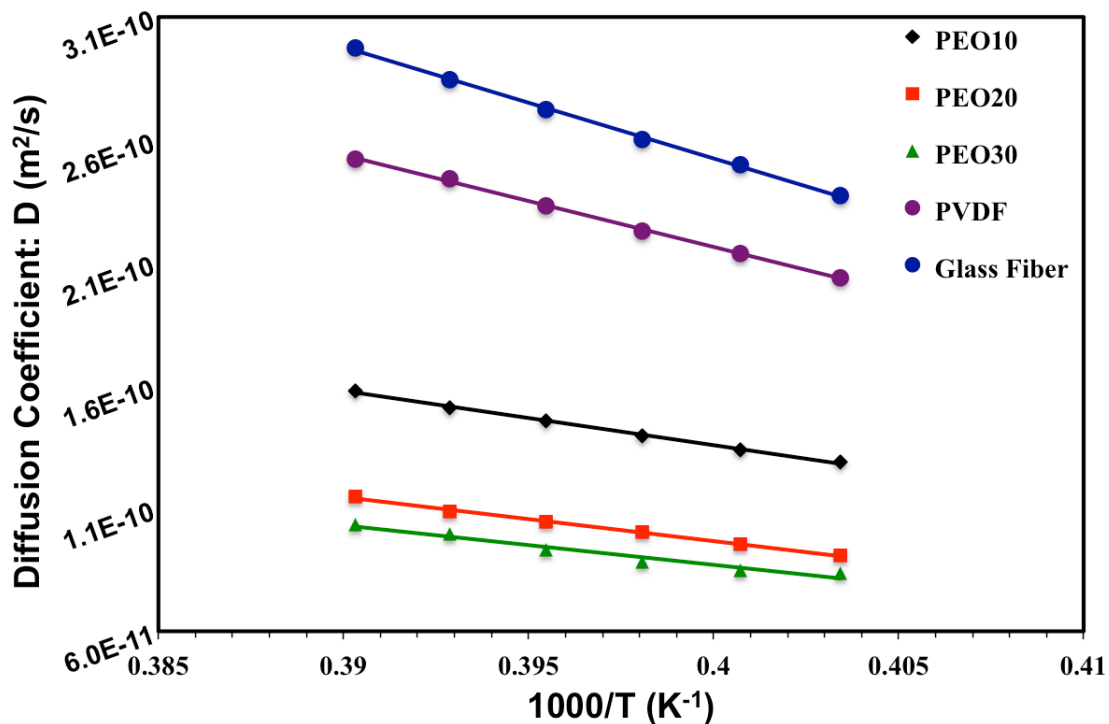


**Figure 5.13.** Arrhenius plots of  $\text{Li}^+$  diffusion coefficients in PEO/PETA samples, electrospun PVDF and glass fiber control electrolytes. Error estimated to be  $\leq 5\%$ .

#### 5.4. Conclusion

The translation of lithium ions in polymer gel electrolytes comprised of electrospun PEO/PETA crosslinked mats was investigated with PFG-NMR. The diffusion coefficients, and activation energies were compared to ionic conductivity results obtained from AC impedance spectroscopy. Solution diffusion results indicate that not only does the anion travel faster through the PGE, but also that lithium diffusion may be hindered by polymer-ion interactions. This result is unsurprising in hindsight as PEO was specifically chosen due to its ability to coordinate / interact with  $\text{Li}^+$  cations. PFG-NMR, contradict our initial rationalizations for the enhanced conductivities produced by using PEO-based electrospun PGEs involving fast  $\text{Li}^+$  ion transport through

the polymeric domains. Instead, likely polymer-ion interactions resulting in a greater number of charge carriers are responsible for the enhanced conductivity. If a PEO/PETA fiber is considered a static structure through which solvated lithium ions must travel, then the fibers impart a certain degree of tortuosity, thus resulting in a reduction in lithium diffusion. This consideration would explain why the PEO/PETA samples have much lower  $\text{Li}^+$  diffusion coefficients than the pure liquid samples. However, this does not address the nearly identical ionic conductivities obtained for fully immersed PEO/PETA samples and pure liquid electrolyte. PEO/PETA fibers may possibly act as dynamic charge separators allowing aggregates, ion pairs, and even solvated  $\text{Li}^+$  ions to become dissociated as they traverse polymer rich domains (**Figure 5.14**). Essentially, non-charge carrying species and solvated  $\text{Li}^+$  ions travel through the fiber mat. If these species come into contact with available coordination sites within the fibers, then interactions between PEO and  $\text{Li}^+$  ions may disrupt ion-ion interactions resulting in free charge carriers. Additionally, if a solvated  $\text{Li}^+$  ion interacts with a PEO active sites, if the solvation shell collapses and a lithium ion is introduced into the polymeric domain, then in order to preserve the polymer-liquid  $\text{Li}^+$  ion concentrations equilibrium, a free lithium ion may be released from another region of the fiber. Thus, instead of having to navigate around polymer chains/fibers, charge-carrying ions can travel through them instead.

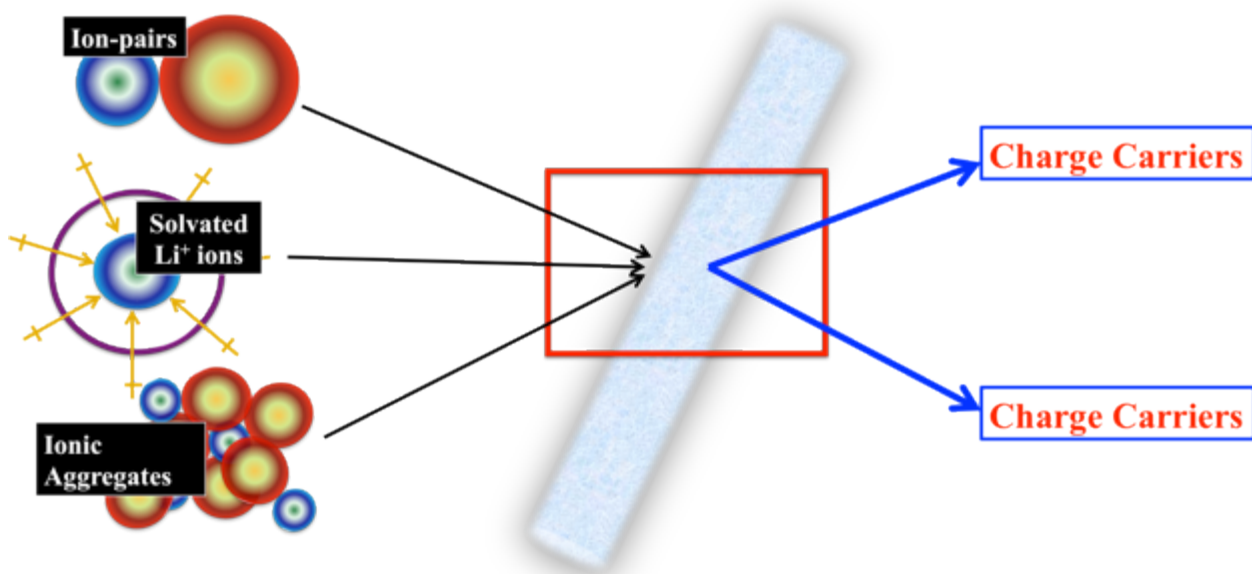


**Figure 5.14.** Cartoon depiction of possible PEO-ion interactions. Charged species traveling through the liquid domains become separated into free (naked) charge carrying species upon interaction with polymeric chains in PEO/PETA fibers.

A process such as this is consistent with both conductivity and diffusion data in terms of effects of PETA concentration. Since the PEO chains would need to be mobile to allow for efficient coordination with incoming species, the efficiency at which free charge carriers would be hindered by increasing PETA content resulting in lower conductivities. Although PEO-ion interactions are believed to hinder free  $\text{Li}^+$  ion diffusion, a shielding effect produced from these interactions may result in either an increase in free charge carriers or a reduction in diffusion pathlength. Granted, once the separated (or polymer solvated)  $\text{Li}^+$  ions leave the polymeric domains, they likely become quickly solvated, aggregated or ion-paired again. However, that brief and seemingly insubstantial increase in free charge carriers may be responsible for the conductivity improvements.

Unfortunately, lithium diffusion in electrospun PVDF samples is faster than in the PEO/PETA samples as shown by PFG-NMR. For lithium batteries, the speed at which lithium ions can travel from one electrode to the other ultimately dictates the device performance. Thus, even though the ionic conductivity data suggest that PEO/PETA samples may have better battery performance than non-interacting polymers, PFG-NMR data suggest the opposite. Thus, the battery performance (specifically the discharge characteristics) must be investigated as the ultimate indicator of how applicable these electrolyte systems are for energy storage.

## 5.5. References

1. M. D. Lingwood, Z. Zhang, B. E. Kidd, K. B. McCreary, J. Hou and L. A. Madsen, *Chemical Communications*, 2013, **49**, 4283-4285.
2. M. Videa, W. Xu, B. Geil, R. Marzke and C. A. Angell, *Journal of The Electrochemical Society*, 2001, **148**, A1352-A1356.
3. K. Xu, *Chemical Reviews*, 2004, **104**, 4303-4418.
4. K. Hayamizu, Y. Aihara, S. Arai and Garcia, *The Journal of Physical Chemistry B*, 1999, **103**, 519-524.
5. J. Adebahr, M. Forsyth, D. R. MacFarlane, P. Gavelin and P. Jacobsson, *Solid State Ionics Elsevier*, 2002.
6. C. Capiglia, Y. Saito, H. Yamamoto, H. Kageyama and P. Mustarelli, *Electrochimica Acta*, 2000, **45**, 1341-1345.
7. E. Tsuchida, H. Ohno and K. Tsunemi, *Electrochimica Acta*, 1983, **28**, 591-595.
8. G. S. Fulcher, *Journal of the American Ceramic Society*, 1925, **8**, 339-355.
9. A. Reiche, T. Steurich, B. Sandner, P. Lobitz and G. Fleischer, *Electrochimica Acta*, 1995, **40**, 2153-2157.
10. M. Watanabe, M. Kanba, K. Nagaoka and I. Shinohara, *Journal of Polymer Science: Polymer Physics Edition*, 1983, **21**, 939-948.
11. T. Miyamoto and K. Shibayama, *Journal of Applied Physics*, 1973, **44**, 5372-5376.
12. I. M. Ward, M. J. Williamson, H. V. S. A. Hubbard, J. P. Southall and G. R. Davies, *Journal of Power Sources*, 1999, **81-82**, 700-704.
13. P. G. Bruce and C. A. Vincent, *Journal of the Chemical Society, Faraday Transactions*, 1993, **89**.
14. Y. V. Baskakova, O. V. Yarmolenko and O. N. Efimov, *Russian Chemical Reviews*, 2012, **81**, 367 - 380.
15. M. S. A, *European Polymer Journal*, 2006, **42**, 21-42.
16. Y. G. Andreev, P. Lightfoot and P. G. Bruce, *Chemical Communications*, 1996, 2169-2170.
17. S. G. MacGlashan, Y. G. Andreev and P. G. Bruce, *Nature* 1999, **398**, 2.
18. C. D. Robitaille and D. Fauteux, *Journal of The Electrochemical Society*, 1986, **133**, 315-325.
19. S. K. Fullerton-Shirey and J. K. Maranas, *Macromolecules*, 2009, **42**, 2142-2156.
20. N. H. A. Nasir, C. H. Chan, H.-W. Kammer, L. H. Sim and M. Z. A. Yahya, *Macromolecular Symposia*, 2010, **290**, 46-55.
21. A. von Wald Cresce, O. Borodin and K. Xu, *The Journal of Physical Chemistry C*, 2012, **116**, 26111-26117.
22. R. J. Blint, *Journal of The Electrochemical Society*, 1997, **144**, 787-791.
23. Y. Saito, M. Okano, K. Kubota, T. Sakai, J. Fujioka and T. Kawakami, *The Journal of Physical Chemistry B*, 2012, **116**, 10089-10097.

## Chapter 6

### Battery Performance of Electrospun PEO/PETA Electrolytes

#### 6.1. Introduction

Conductivity data yield information about how charged species translate through media; however, only bulk ensemble contributions for all diffusive species are collected. Thus, in general, ionic conductivity collected from AC impedance spectroscopy only gives information on how fast charged *species* (average of both anion and cation) diffuse. PFG-NMR on the other hand has the ability to distinguish individual charged species. Although together, these two techniques can be used to get a better picture of how ions migrate through electrolyte materials, battery performance testing is necessary to ultimately determine whether or not a membrane or material will behave favorably for rechargeable lithium-ion batteries.

We focus our work in two battery performance categories for the PEO/PETA electrospun PGEs. First, the capacity and capacity retention were foci, as the PEO/PETA electrolytes should allow for easy lithium intercalation into the electrodes. The capacity retention can be represented in two ways: 1.) the capacity loss due to fast charge / discharge and 2.) the capacity loss due to degradation and or side reactions at the electrode surfaces. The main focus of this work is on the former representation. Because these electrolytes are envisioned for high power output devices, the capacity retention during rapid charge and discharge is very important. The latter of the two capacity representations is often termed the cycle life of a battery. Due to the need for liquid electrolytes, the PEO/PETA systems are subject to solid-electrolyte-interface (SEI)

formation like all other lithium-ion and lithium-polymer batteries. Thus, assuming that  $\text{Li}^+$  ions behave similarly in PEO based electrolytes as they do in other polymeric devices, the capacity retention should be similar.<sup>1,2</sup>

Secondly, we focus on the discharge characteristics, as the enhanced ionic conductivity was believed to result in faster device discharge. PEO/PETA electrospun fibers initially seemed to be likely candidates for rapid charge/discharge devices due to room temperature ionic conductivities nearly twice that of a PVDF control. Fully charged coin cell prototypes were discharged at various C rates to evaluate the specific capacity and capacity retentions.

## **6.2. PEO/PETA Electrochemical Stability**

The electrochemical stability of polymeric-gel electrolytes is very important as electrochemical reactions could lead to degradation of the electrolyte components, resulting in severe loss of battery performance. The electrochemical stability of solid PEO has been reported previously and it is anodically stable up to nearly 5V vs. Li.<sup>3,4</sup> Thus, PEO is suitable for use as a battery electrolyte. In order to ensure that no undesirable reactions occur as a result of PETA addition, the electrochemical stability of PEO/PETA samples with and without electrolyte swelling were investigated. Electrospun fibers were sandwiched between two gold electrodes (Solartron thru-plane impedance cell) and the current was monitored as the voltage was increased. **Figure 6.1** shows the stability window of PEO/PETA electrospun samples. Pure electrospun PEO samples show stability up to 4.8 V, whereas the addition of PETA reduced this stability only slightly to ~ 4.6 V. Thus crosslinking with PETA does not significantly reduce

PEO's anodic stability. Furthermore, addition of the liquid EC:DMC solution containing 1 M LiClO<sub>4</sub> only reduces the stability of PEO/PETA mats to 4.4 V. Although this reduction is significant, typical batteries only operate up to 4.2V. Electrospun fiber mats of PVDF and PVDF-HFP have been investigated previously, showing electrochemical stability up to 4.5V when swollen with various electrolyte solvents.<sup>5-10</sup> Since the no irreversible reactions occur within the operating voltage range of typical lithium polymer batteries, swollen PEO/PETA polymer-gel electrolytes were assembled into coin cell battery prototypes to investigate discharge performance.

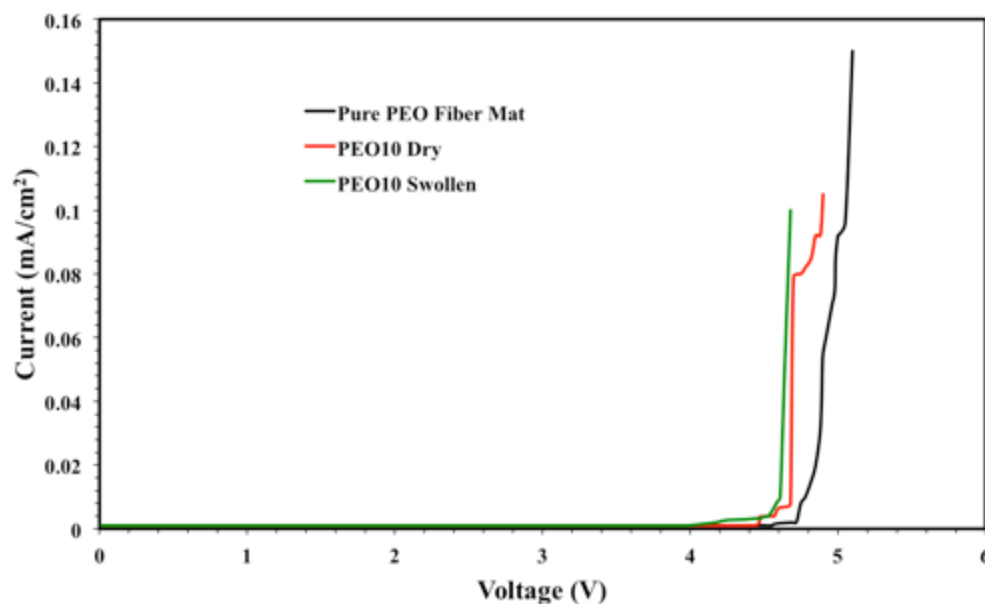


**Figure 6.1.** Electrochemical stability of electrospun PEO fiber mats: pure PEO (black), 10 wt.% PETA (red), and 10 wt.% PETA + EC:DMC (green).

### 6.3. 2032 Coin Cell Prototype Batteries

In the past decades, vast libraries of anode and cathode materials have been suggested and investigated for lithium-ion batteries. By far the most common devices

include either a carbonaceous or lithium metal anode, and a lithium – transition metal – oxide cathode.<sup>11-14</sup> Lithium-air batteries, in which O<sub>2</sub> is the cathode have also gain considerable traction in the last decade as they offer much higher theoretical capacities than the lithium metal oxide (LiMO) systems.<sup>15-17</sup> Once the stability results indicated that PEO/PETA fiber mats would be stable in a typical battery environment, 2032 coin cell prototype batteries were assembled. To ensure sufficient contact with both the top and bottom of the coin cell, a stainless steel washer spring was inserted into the bottom half of the cell followed by a stainless steel (SS) spacer, a lithium foil disk (anode), swollen PEO10 fiber mat (electrolyte), and finally a cathode consisting of LiFePO<sub>4</sub> coated onto aluminum foil. The cap was placed on the last and the cell was crimped at a pressure of approximately 800 psi. **Figure 6.2** is a diagram of a deconstructed 2030 coin cell fabricated using PEO10 as the electrolyte/separator.

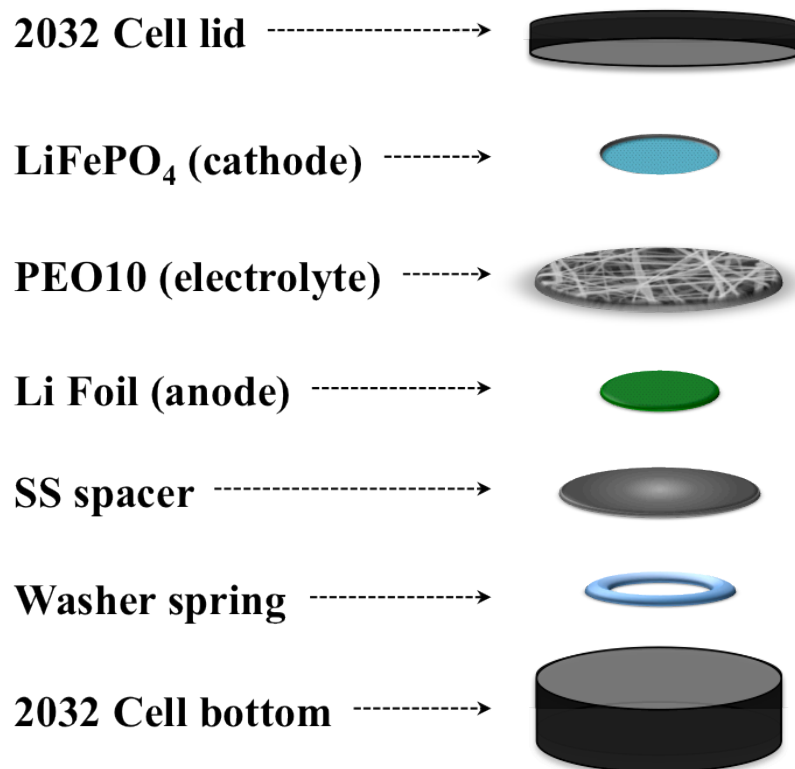


**Figure 6.2.** Diagram of a 2032 coin cell assembled using a PEO/PETA swollen fiber mat as the electrolyte/separator. Coin cells using a glass fiber separator were also assembled in the same manner.

#### **6.4. Coin Cell Battery Performance**

Coin cells were constructed with Gen1 PEO10 electrospun mats. Cells constructed with glass fiber mats were compared to the PEO samples as a performance baseline. In **Figure 6.3** SEM images of both PEO10 and glass fiber (GF) mats show that the two samples are similar. In addition to having more uniform fiber diameters, PEO10 samples are able to absorb slightly more liquid electrolyte than the GF control. Previously reported in chapter 3, PEO10 samples are able to accommodate nearly 1200 wt.% of the EC:DMC electrolyte solvent. In contrast, GF mats can only absorb ~1000 wt.% of the

liquid electrolyte. **Figure 6.4** is an image of two 2032 coin cell batteries assembled with PEO10 and glass fiber electrolytes. Both cells contained their respective electrolyte swollen with the same amount of liquid electrolyte which was determined gravimetrically to be  $\sim 1000$  wt.%.

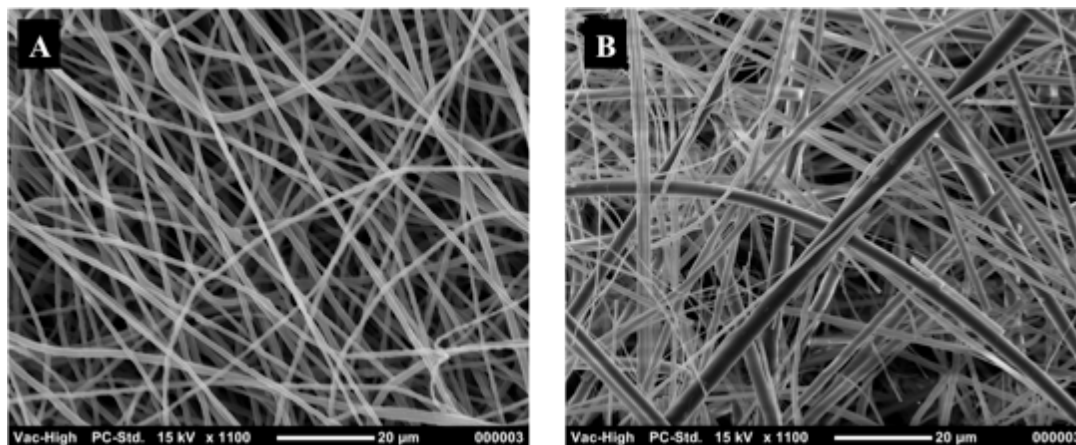


**Figure 6.3.** SEM images of fibrous electrolytes A.) Electrospun, crosslinked PEO10 fiber mats and B.) glass fiber mats.

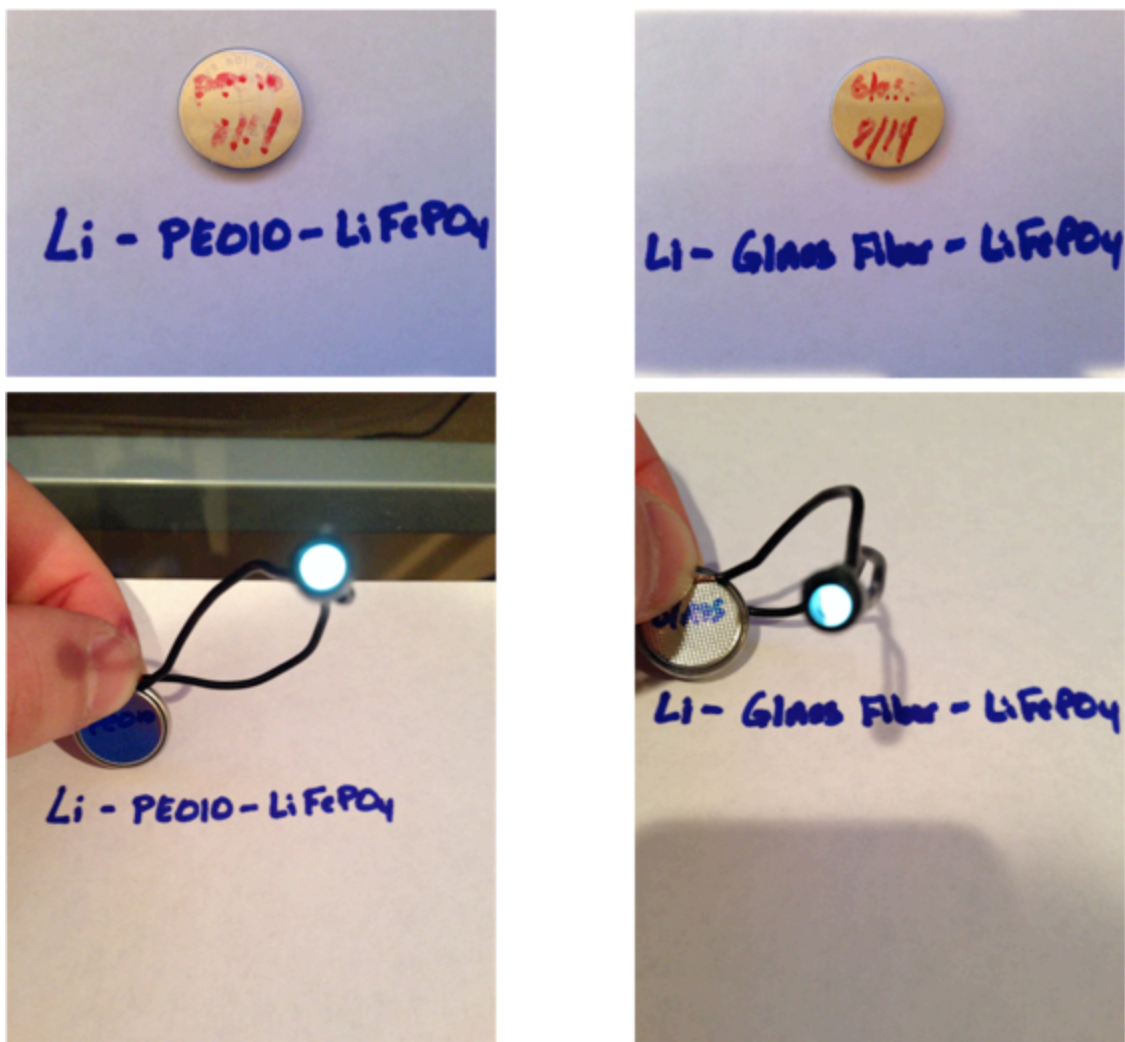


**Figure 6.4.** Images of 2032 coin cell batteries assembled with PEO10 (left) and glass fiber (right) electrolytes. Bottom images show both cells ability to light an LED.

#### **6.4.1. Initial Coin Cell Properties**

Coin cell batteries constructed using PEO10 and GF mats exhibited open circuit voltages of 2.7 and 2.5 volts respectively. Because the cathode material ( $\text{LiFePO}_4$ ) already contains lithium, it is necessary to charge these batteries potentiostatically prior to any discharge experiments. Immediately following assembly, and after every subsequent discharge, each coin cell was charged by applying a constant voltage of 4.2V

until the corresponding current dropped roughly below 5% of the theoretical 1C rate current. Since the batteries were assembled with Li foil anodes, the cathode material was deemed to be the capacity limiting component. For a  $\text{LiFePO}_4$  cathode with a reported active material density of  $160\text{g} / \text{m}^2$ , a 1.27 cm diameter disk contains approximately 0.02 grams of active material. The specific capacity of the  $\text{LiFePO}_4$  cathode material is approximately 127 mAh/g as reported from the manufacturer (MTI). Thus the capacity of each coin cell was calculated to be 2.54 mAh. A 1C rate for a 2.54 mAh device would of course be 2.45 mA. Thus once the current dropped below  $2.54 \times 10^{-5}$  A, the cell was considered charged. Allowing the cell to charge beyond this could result in metal plating of Li. **Figure 6.5** shows the current as a function of time for a typical charging experiment. It is interesting to note that the PEO10 sample displays a higher current initially than the glass fiber cell. Additionally, the PEO10 sample reaches the lower current limit faster than the glass fiber sample. This would suggest that the PEO sample charges faster than the glass fiber sample.

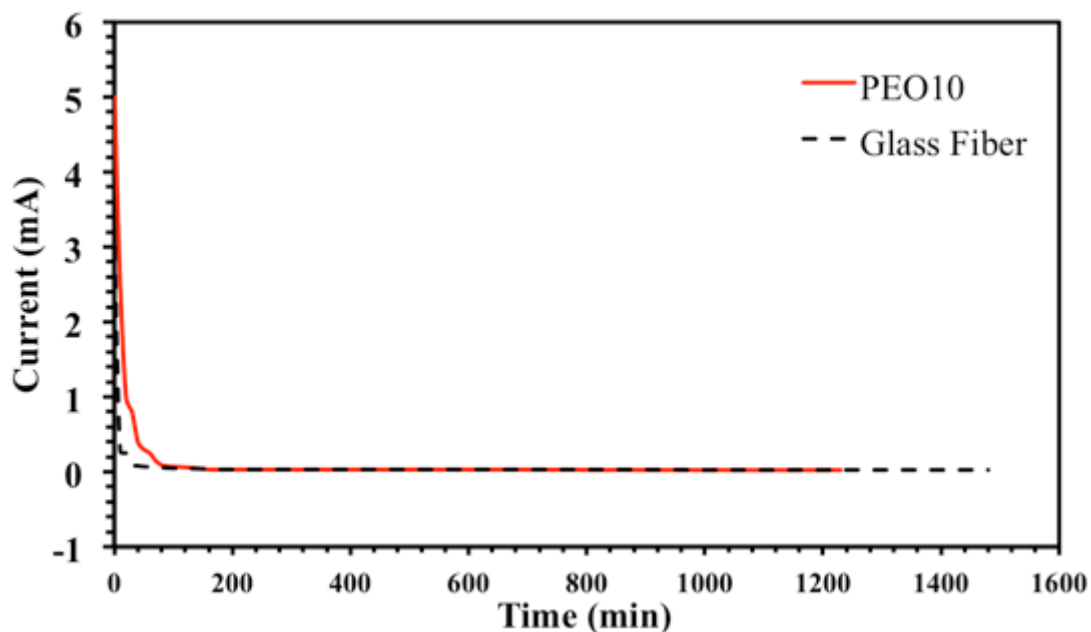


**Figure 6.5.** Charging profiles for PEO10 and glass fiber containing coin cells. Cells were charged by holding the potential at 4.2 V until the current dropped below  $2.54 \text{ e}^{-5} \text{ A}$ .

#### **6.4.2. Discharge Properties of Prototype Coin Cells**

Charged cells were then discharged at various C rates to determine how the charging speed affects the capacity efficiency. To determine the experimental capacity of the cells, each sample was discharged at a rate of C/100 (or  $-2.54 \text{ e}^{-6} \text{ A}$ ). **Figure 6.6** shows the discharge profile of both the PEO10 and GF sample cells at a C rates of 1/100, 1/30, and 1/5. The PEO10 coin cell shows an experimental capacity nearly identical to the calculated theoretical value of 2.54 mAh at a 1/100 C rate. The GF coin cell, at the same C rate only showed a capacity of  $\sim 1.65 \text{ mAh}$ . This would suggest that the PEO10 samples charge faster, completely charging during the C/100 charge. Since the polymer fibers do not hinder diffusion, and likely interact to increase the overall number of lithium charge carriers, PEO allows for faster transport. Additionally, the open circuit

voltage (OCV) of the charged PEO10 sample was measured to be 4.1 V. The GF sample has impenetrable glass fibers, which force the diffusing lithium ions through extremely tortuous paths, slowing down the overall charging time. As a result, during the C/100 charge rate, the ions do not diffuse fast enough to fully charge the cell. Another explanation for this is surface interactions. In PEO/PETA samples, since  $\text{Li}^+$  ions can interact / diffuse through the fibrous domains, essentially the entire surface of the electrodes is accessible. In the glass fiber sample, areas of the electrodes that are in contact with fibers might be blocked by the fibers impeding lithium intercalation. This phenomena is somewhat compensated by the liquid electrolyte's ability to penetrate the porous electrode material. However, in cases where liquid electrolytes are limited (as is the ideal case for safer batteries), this electrode blocking could significantly effect the overall capacity of a device.

It is important to consider the effect of  $\text{Li}^+$  impedance in the electrolyte as well as the diffusion of the ions. The conductivity data, which is directly calculated from impedance values, shows that PEO10 samples ( $\geq 12$  mS/cm) are more ionically conductive than the glass fiber samples ( $\leq 1$  mS/cm). This large difference in conductivity, largely due to the presence of more free lithium ions, could be a major reason for why PEO10 batteries have higher capacities than GF batteries. In addition to the  $[\text{Li}^+]$ , the tortuosity of the PEO10 electrolyte is much lower than for the GF electrolyte as the PEO10 polymeric domains are “phantom-like” with respect to  $\text{Li}^+$  diffusion.

One final consideration for why PEO10 PGE mats exhibit higher capacities than the GF mats could be due to how well the electrolytes retain the liquid component upon

cell assembly. These coin cells were assembled as described in **Figure 6.2**. As seen from the image, there is a space below the stainless steel spacer that is occupied by the washer spring. Since the electrolyte mats were swollen with a similar amount of liquid electrolyte and then placed in the coin cell, the pressure of crimping the cell could force loosely bound liquid out of the fiber mat and down into the void space beneath the SS spacer. The PEO10 mats likely retain the majority of the liquid electrolyte, whereas the GF mats experience a large amount of electrolyte leakage. This is due to PEO's chemical similarity to the liquid component, which is what allows it to absorb such high volumes of liquid electrolyte in the first place. If a significant amount of liquid electrolyte leaks out of the GF mat, then the accessible surface of the electrodes will be further diminished due to poor electrolyte penetration, causing a loss in capacity.

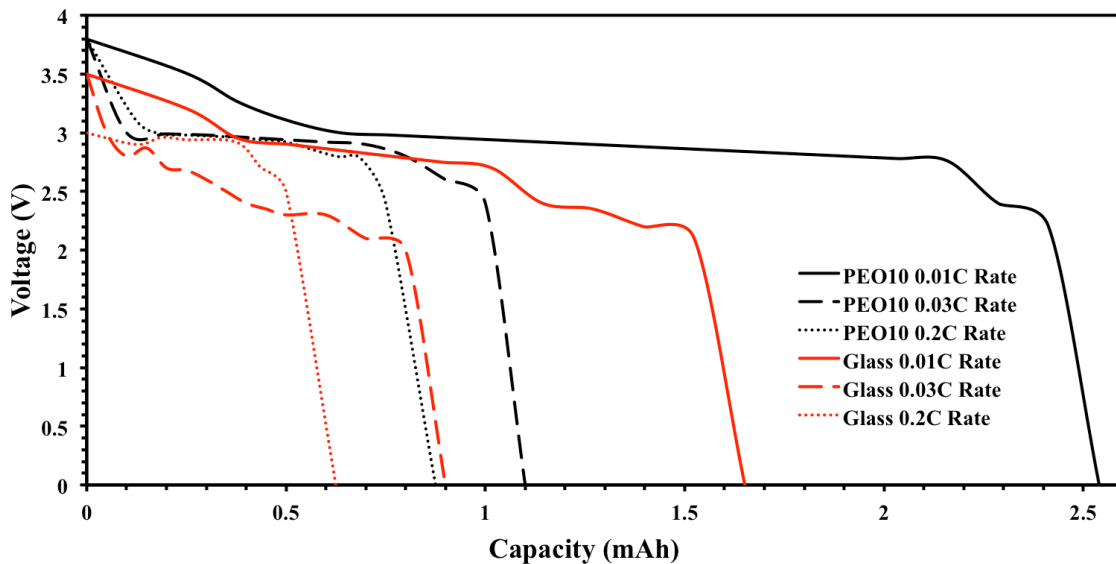


**Figure 6.6.** Discharge profile for PEO10 (black) and GF (red) at a various C rates.

PEO out performs GF coin cells at rates of C/30 and C/5 as well. **Figure 6.7** shows the specific capacities of PEO10 and GF coin cells at the three aforementioned discharge rates. It is clear that even though PEO10 out performs GF electrolytes, both samples suffer significant decreases in the overall capacity at faster discharge rates. A decrease in the overall capacity as the charge rate increases indicates insufficient  $\text{Li}^+$  mobility. If the  $\text{Li}^+$  ions cannot travel fast enough to maintain a current inside the cell equal to that of the applied current, then the cell voltage drops and the battery is considered dead, at least for that current.

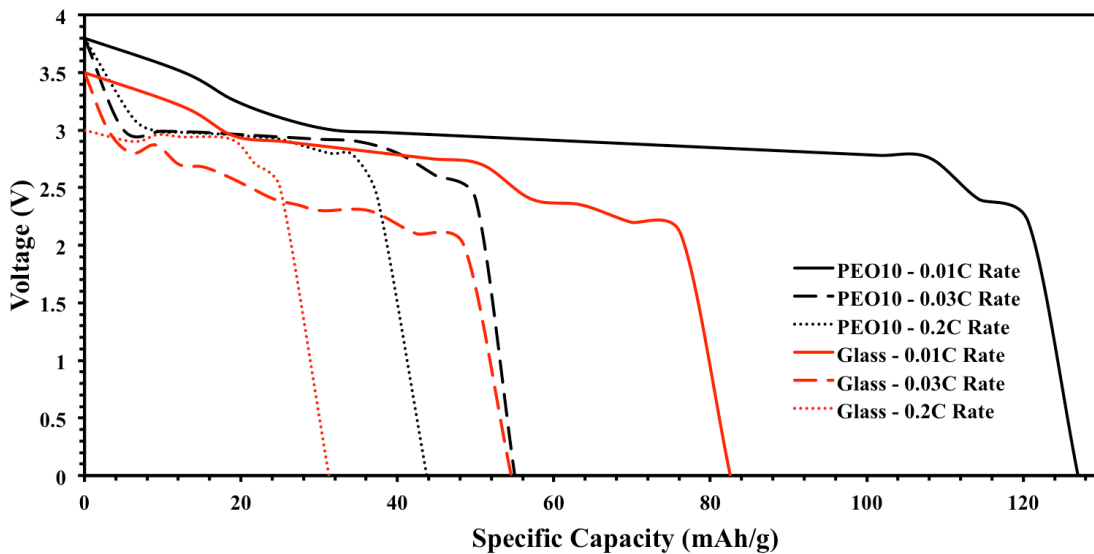


**Figure 6.7.** Specific capacity discharge profiles of PEO10 (black) and GF (red) coin cells at three C rates.

#### 6.4.3. Prototype Capacity Retention

In order to evaluate how the discharge rates affect capacity, discharge curves were constructed as a function of capacity retention. If it is assumed that the C/100 charge resulted in a 100% charge for both samples, we can then plot the capacity retention percentage vs. discharge rate (**Figure 6.8**). Interestingly, even though the PEO10 sample

displayed a higher *capacity* at all C rates, the glass fiber sample proved to have better capacity retention. Initially, PEO was chosen due to its ability to interact with lithium salts, aid in dissociation, and allow less tortuous pathways for  $\text{Li}^+$  ions to travel. This was envisioned to result in an increase in the charge/discharge performance, allowing batteries with very fast discharge capabilities. If the PEO10 polymeric domains (fibers) are considered to behave as a type of charge carrier motivator (**Figure 5.13** in chapter 5), the timescale of those polymer-species interactions could be critical. If the conversion of neutral species into charge carriers is occurring and facilitated by the PEO network, and if those interactions are slow relative to the rest of the diffusing  $\text{Li}^+$  in the liquid domains, then PEO could actually be hindering ion diffusion at high rates. In the case of fast charge/discharge, if the polymer-species interactions are slow they do not contribute to the performance. Fewer additional  $\text{Li}^+$  ions would be present since the separation of neutral species to charge carriers would be slow in addition to the added tortuosity imparted by the PEO/PETA fibers. If the exchange (or shuttling) of  $\text{Li}^+$  ions through the polymeric domains is slow compared to the  $\text{Li}^+$  ions in the solution, then charge carriers will prefer the liquid domains, resulting in a higher tortuosity. If the polymer-species interactions/conversions are quick relative to the diffusing  $\text{Li}^+$  ions (as might be the case in slow charge/discharge experiments), then the tortuosity reduction coupled with the increase in charge carriers imparted by these interactions would be expected to result in superior performance as seen in **Figure 6.6** for the C/100 data sets.

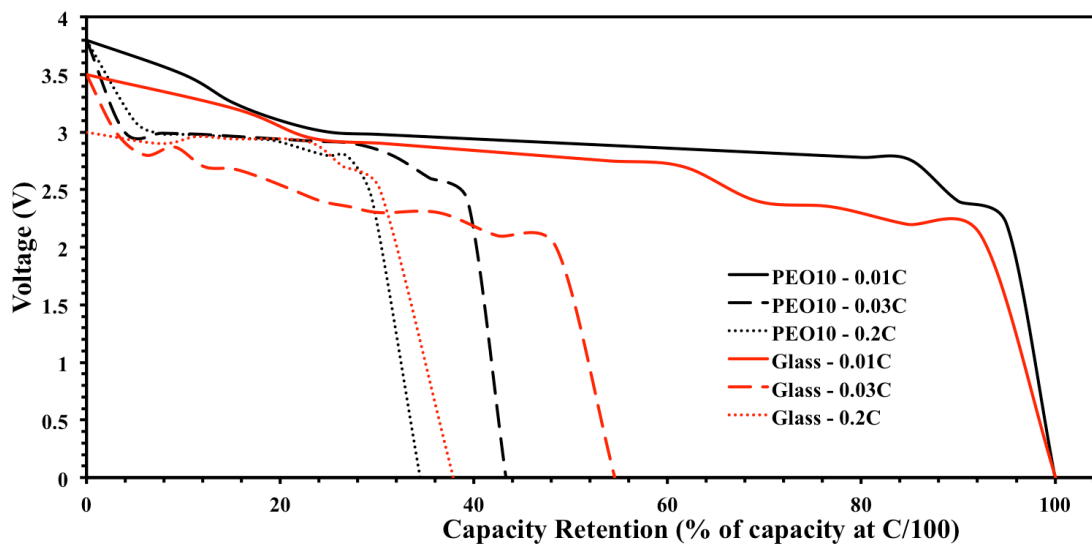


**Figure 6.8.** Capacity retention for PEO10 (black curves) and GF (red curves) at C/30 and C/5 discharge rates.

The loss in capacity at faster discharge rates for electrospun PEO/PETA samples is unfavorable for high power output devices. Ideally, for fast charge/discharge batteries to be successful, the change in capacity retention should be very small when going from low C rates to high C rates. When compared to the 0.2 C discharge capacity, a microporous film of PVDF-HFP swollen with EC:DMC and LiPF<sub>6</sub> showed a 97% capacity retention at 1C and an 85% capacity retention at 2C.<sup>18</sup> Unfortunately, the PEO10 samples were unable to discharge at any rate above C/5.

### 6.5 Conclusions

PEO/PETA polymer gel electrolytes have been demonstrated as viable electrolytes and separators in 2032 coin cell prototype lithium batteries. PEO10 demonstrates the capability to reach nearly the theoretical maximum capacity value at a

rate of  $C/100$ . In contrast, glass fiber mats swollen with a similar amount of liquid electrolyte only demonstrated discharge capabilities up to 65% of the calculated theoretical maximum at a  $C/100$  rate. The capacity retention for PEO/PETA based PGEs degraded faster with charge rate than the glass fiber control suggesting that polymer-ion interactions may promote charge/discharge performance at low  $C$  rates, but hinder the performance at higher rates. Since PEO10 samples were unable to discharge at any rate higher than  $C/5$ , they appear to be insufficient for fast charge/discharge devices. However, it should be noted that the small electrode material in coin cell prototype batteries is not ideal for evaluating fast charge and discharge performance. Large cell designs such as 18650 and pouch cell systems are able to provide more detailed information during rapid discharge experiments.

## 6.6. References

1. M. B. Pinson and M. Z. Bazant, *Journal of The Electrochemical Society*, 2013, **160**, A243-A250.
2. F. Kong, R. KostECKi, G. Nadeau, X. Song, K. Zaghieb, K. Kinoshita and F. McLarnon, *Journal of Power Sources*, 2001, **97-98**, 58-66.
3. F. Croce, R. Curini, A. Martinelli, L. Persi, F. Ronci, B. Scrosati and R. Caminiti, *The Journal of Physical Chemistry B*, 1999, **103**, 10632-10638.
4. L. Wang, X. Li and W. Yang, *Electrochimica Acta*, 2010, **55**, 1895-1899.
5. S. W. Choi, S. M. Jo, W. S. Lee and Y. R. Kim, *Advanced Materials*, 2003, **15**, 2027-2032.
6. J. R. Kim, S. W. Choi, S. M. Jo, W. S. Lee and B. C. Kim, *Electrochimica Acta*, 2004, **50**, 69-75.
7. S. W. Lee, S. W. Choi, S. M. Jo, B. D. Chin, D. Y. Kim and K. Y. Lee, *Journal of Power Sources*, 2006, **163**, 41-46.
8. G. Cheruvally, J.-K. Kim, J.-W. Choi, J.-H. Ahn, Y.-J. Shin, J. Manuel, P. Raghavan, K.-W. Kim, H.-J. Ahn, D. S. Choi and C. E. Song, *Journal of Power Sources*, 2007, **172**, 863-869.
9. A. I. Gopalan, P. Santhosh, K. M. Manesh, J. H. Nho, S. H. Kim, C.-G. Hwang and K.-P. Lee, *Journal of Membrane Science*, 2008, **325**, 683-690.
10. H.-R. Jung, D.-H. Ju, W.-J. Lee, X. Zhang and R. Kotek, *Electrochimica Acta*, 2009, **54**, 3630-3637.
11. W. Schalkwijk and B. Scrosati, eds. W. Schalkwijk and B. Scrosati, Springer US, 2002, pp. 1-5.
12. P. Arora and Z. Zhang, *Chem Rev*, 2004, 4419-4462.
13. A. S. Arico, P. G. Bruce, B. Scrosati, J.-M. Tarascon and W. van Schalkwijk, *Nature Materials*, 2005, **4**, 366-377.
14. B. Xu, D. Qian, Z. Wang and Y. S. Meng, *Materials Science and Engineering: R: Reports*, 2012, **73**, 51-65.
15. G. Girishkumar, B. McCloskey, A. C. Luntz, S. Swanson and W. Wilcke, *The Journal of Physical Chemistry Letters*, 2010, **1**, 2193-2203.
16. Y. Wang and H. Zhou, *Journal of Power Sources*, 2010, **195**, 358-361.
17. C. O. Laoire, S. Mukerjee, K. M. Abraham, E. J. Plichta and M. A. Hendrickson, *The Journal of Physical Chemistry C*, 2009, **113**, 20127-20134.
18. J. M. Song, H. R. Kang, S. W. Kim, W. M. Lee and H. T. Kim, *Electrochimica Acta*, 2003, **48**, 1339-1346.

## Chapter 7

### Conclusions and Future Work

#### *7.1. Summary of Results*

In this work, we have demonstrated that electrospinning can be used to develop multiple film morphologies including fibers, porous fibers, ribbons, and beaded or necklace type fibers. These architectures can be tailored to enhance the performance of the active layers found in energy conversion and energy storage devices. Development of bi-continuous networks with both donor and acceptor material domain sizes tailored to promote exciton dissociation will enhance the efficiency of OPV devices based on the bulk heterojunction, while incorporation of active polymers in electrolytes for energy storage results in devices with superior electrochemical performance.

#### *7.1.1 Electrospinning Unique Morphologies for Organic Photovoltaics*

This work demonstrates that electrospinning can be used to obtain several conductive polymer morphologies. The electrospinning of pure P3HT in chloroform results in polymer films consisting of platelet type morphologies with diameters on the order of 10  $\mu\text{m}$ . Electrospinning of P3HT in chloroform in a  $\text{CHCl}_3$  saturated atmosphere results in unique ribbon type morphologies. These ribbon type films contain P3HT domains on the order of 5  $\mu\text{m}$  and appear to be extremely porous, which would promote charge transfer in both the donor and acceptor domains upon addition of a fullerene. Dropping pure chloroform onto the needle tip during electrospinning resulted in P3HT fibers with porous morphologies and fiber diameters of approximately 2  $\mu\text{m}$ . These fibrous morphologies could prove to be very beneficial to exciton dissociation as the

acceptor material could potentially fill the pores, thus promoting dissociation. Electrospinning P3HT from a coaxial needle with pure  $\text{CHCl}_3$  in the sheath produced the most promising results. The coaxial technique resulted in a hybrid between ribbon and fiber type morphologies with diameters / domain sizes in the range of 5-20  $\mu\text{m}$ .

Using sacrificial polymers as either electrospinning supports or as fibrous templates resulted in the formation of unique morphologies, including necklace type fibers (P3HT & PMMA) and blended solid fibers (P3HT & PCL blends). Spin-casting P3HT solutions onto substrates containing electrospun fiber templates resulted in interesting fibrillar type structures upon removal of the PVDF domain. Electropolymerization of thiophene suggested the possibility of polymerizing a network of conductive material around a fibrous template. Although the successful electrospinning of pure P3HT and various blends of P3HT with template / sacrificial polymers has been previously reported in the literature, we were unable to get continuous fiber formation free of beads or ribbon defects. Unfortunately, none of the techniques used in this research resulted in the production of P3HT films with domain sizes on the order of 10 nm. Although unsuitable for P3HT-based OPV's, the results of this work gave way to design concepts that might be applied to other polymeric donor types. Additionally, the results from the OPV work could be applied to producing novel polymeric-gel electrolytes via electrospinning for development of lithium polymer batteries with high energy densities and superior charge-discharge properties.

### ***7.1.2. Electrospinning Hybrid Polymer-Gel Electrolytes for Lithium Polymer Batteries***

Electrospun poly(ethylene oxide) fiber mats have been crosslinked by UV curing

with pentaerythritoltriacylate and utilized as insoluble, mechanically robust polymeric-gel electrolytes. SEM images indicate that the electrospinning process is an efficient method for obtaining reproducible fibrous framework structures over a range of solution compositions. Gel fraction and porosity data indicate that PETA is an effective crosslinking agent for the PEO mats, yielding gel fractions in excess of 80%.

Upon exposure to liquid electrolyte, the fibrous framework originating from the non-woven structure of the as-spun mats persists. Solvent uptake experiments show that the PEO mats are capable of absorbing large amounts of liquid electrolyte, in excess of 1000 wt.%. Equilibrium uptake swelling experiments indicate that an increase in the PETA composition results in a decrease in the amount of liquid electrolyte absorbed. As the degree to which a cross-linked network swells is inversely proportional to the cross-link density, it may be deduced that increasing the concentration of PETA also increased the cross-link density ultimately restricting chain mobility.

AC impedance measurements of electrolyte swollen fiber mats show that the PEO samples have higher ionic conductivities than the PVDF control at all PETA concentrations. The conductivities of PEO fiber mats decrease with increasing PETA content due to limited chain mobility upon increasing cross-link density. The PEO fibers appear to be effective at enhancing the overall fraction of free lithium ions, leading to improved conductivity. Furthermore, to the best of our knowledge, the room temperature conductivities for the PEO10 sample are the highest reported for electrospun PGEs.

Since the PEO fibrous frameworks appear to exhibit ionic mobilities similar to the liquid electrolyte components, the PEO structured gel exist as a phantom-like network with respect to ion diffusion, allowing ionic transport with little or no diffusive barrier

from the PEO fibers. An increase in PETA content corresponds to an increase in the amount of crosslinks and ultimately in restriction in the polymer chain mobility, which results in reduction of ionic mobility. If the mobile polymer chains are essential to ion diffusion, then restricting chain mobility would result in a loss of conductivity. Furthermore, because restricted polymeric chain mobility limits ionic diffusion,  $\text{Li}^+$  ions will become biased towards diffusion through the liquid components, resulting in increased diffusion length and an overall reduction in conductivity. The preferential diffusion of  $\text{Li}^+$  ions through the liquid component re-establishes a significant tortuosity contribution approaching that of the PVDF control with respect to PETA content.

It is reasonable to expect that prolonged exposure to the liquid electrolyte solution containing a lithium salt will reach an exchange equilibrium of  $\text{Li}^+$  ions between the liquid domains and the fibrous polymeric domains. This exchange is likely expedited by the pre-loading procedure. Additionally, the crosslinking reaction is subject to atmospheric purity and thus, optimization of the crosslinking procedure should lead to even better mechanical performance of the PEO-based PGE's.

Although the ultraviolet initiated crosslinking of electrospun PEO fiber mats is possible with the use of a pentaerythritol triacrylate initiator, other photo- and thermo-initiators proved to be unsuccessful at producing insoluble mats. IR spectroscopy suggests that the reactivity of vinyl substituents on the PETA initiator likely provides a non-degrading means of coupling PEO radicals to form a crosslinked, insoluble network. Furthermore, reactive vinyl monomers such as vinylpropylene carbonate may be introduced into the network during UV curing. It is currently unclear whether or not the VPC monomers polymerize after reacting with PEO radicals. However, production of a

freestanding fibrous mat of PEO using 5 wt.% PETA is only produced in the presence of VPC indicating that VPC might be involved in the crosslinking mechanism. Additionally, PEO fiber mats electrospun and crosslinked in the presence of VPC exhibited smaller melting endotherms than Gen1 PEO/PETA samples, suggesting a reduction in crystallinity. These PEO/PETA/VPC mats also demonstrated higher ionic conductivities than their PEO/PETA counterparts. Unlike Gen1 PEO/PETA, the ionic conductivities of the PEO/PETA/VPC mats increased from PEO5/5 to PEO10/10. This increase in conductivity means that VPC somehow overcomes the loss of chain mobility imparted by additional crosslink density. It is unclear whether the reduction in crystallinity or the increase in coordination sites is responsible for the increasing direct relationship between conductivity and VPC content.

The translation of lithium ions in polymeric-gel electrolytes comprised of electrospun PEO/PETA crosslinked mats was investigated with PFG-NMR. The diffusion coefficients, and activation energies were compared to ionic conductivity results obtained from AC impedance spectroscopy. Solution diffusion results indicate that not only does the anion travel faster through the PGE, but also that lithium diffusion may be hindered by polymer-ion interactions. This result is unsurprising in hindsight as PEO was specifically chosen due to its ability to coordinate / interact with  $\text{Li}^+$  cations. PFG-NMR contradicts our initial rationalizations for the enhanced conductivities produced by using PEO-based electrospun PGEs involving fast  $\text{Li}^+$  ion transport through the polymeric domains. Instead, likely polymer-ion interactions resulting in a greater number of charge carriers are responsible for the enhanced conductivity. If a PEO/PETA fiber is considered a static structure through which solvated lithium ions must travel, then

the fibers impart a certain degree of tortuosity, thus resulting in a reduction in lithium diffusion. This consideration would explain why the PEO/PETA samples have much lower  $\text{Li}^+$  diffusion coefficients than the pure liquid samples. However, this does not address the nearly identical ionic conductivities obtained for fully immersed PEO/PETA samples and pure liquid electrolyte. The possibility PEO/PETA fibers act as dynamic charge separators, as aggregates, ion pairs, and even solvated  $\text{Li}^+$  ions traversing polymer rich domains, suggests a process such as that depicted in **Figure 5.13**. Essentially, non-charge carrying species and solvated  $\text{Li}^+$  ions travel through the fiber mat. If these species come into contact with available coordination sites within the fibers, then interactions between PEO and  $\text{Li}^+$  ions may disrupt ion-ion interactions resulting in free charge carriers. Additionally, if a solvated  $\text{Li}^+$  ion interacts with a PEO active site, if the solvation shell collapses and a lithium ion is introduced into the polymeric domain, then in order to preserve the polymer-liquid  $\text{Li}^+$  ion concentrations equilibrium, a free lithium ion may be released from another region of the fiber. Thus, instead of having to navigate around polymer chains/fibers, charge-carrying ions may travel through them instead.

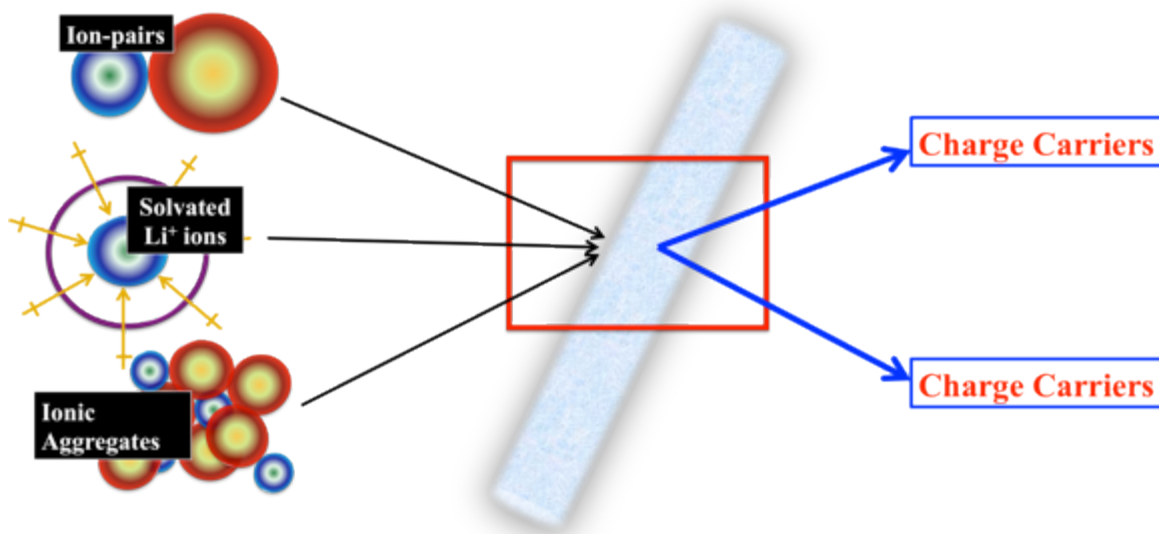


**Figure 5.13.** Cartoon depiction of possible PEO-ion interactions. Charged species traveling through the liquid domains become separated into free (naked) charge carrying species upon interaction with polymeric chains in PEO/PETA fibers.

A process such as this is consistent with both conductivity and diffusion data in terms of effects of PETA concentration. Since the PEO chains would need to be mobile to allow for efficient coordination with incoming species, the efficiency of forming free charge carriers would be hindered by increasing PETA content, resulting in lower conductivities. Although PEO-ion interactions are believed to hinder free  $\text{Li}^+$  ion diffusion, a shielding effect produced from these interactions may result in either an increase in free charge carriers or a reduction in diffusion pathlength. Granted, once the separated (or polymer solvated)  $\text{Li}^+$  ions leave the polymeric domains, they likely become quickly solvated, aggregated or ion-paired again. However, that brief and seemingly insubstantial increase in free charge carriers may be responsible for the conductivity improvements.

Unfortunately, lithium diffusion in electrospun PVDF samples is faster than in the PEO/PETA samples as shown by PFG-NMR. For lithium batteries, the speed at which lithium ions can travel from one electrode to the other ultimately dictates the device performance. Thus, even though the ionic conductivity data suggest that PEO/PETA samples may have better battery performance than non-interacting polymers, the battery performance (specifically the discharge characteristics) is the ultimate indicator of how applicable these electrolyte systems are for energy storage.

PEO/PETA polymeric-gel electrolytes have been demonstrated as viable electrolytes and separators in 2032 coin cell prototype lithium batteries. PEO10 demonstrates the capability to reach nearly the theoretical maximum capacity under a rate of C/100. In contrast, glass fiber mats swollen with a similar amount of liquid electrolyte only demonstrated discharge capabilities up to 65% of the calculated theoretical maximum under a C/100 rate. The capacity retention for PEO/PETA based PGEs degraded faster with charge rate than the glass fiber control, suggesting that polymer-ion interactions may promote charge/discharge performance at low C rates, but hinder the performance at higher rates. Since PEO10 samples were unable to discharge at any rate higher than C/5, they appear to be inadequate for fast charge/discharge devices.

## ***7.2. Future Polymer-Gel Electrolyte Work***

PFG-NMR diffusion studies suggest that PEO may actually be hindering the overall mobility of charge carrying  $\text{Li}^+$  ions. Further investigation into how the  $\text{Li}^+$  are behaving in the individual domains (polymeric and liquid) would help to shed light on why conductivity and diffusion studies contradict each other. Specifically, quantifying

the differences in  $[\text{Li}^+]$  for the PVDF, non-, and pre-loaded samples.

The effects of the Gen 2 crosslinking procedure need to be further investigated. It is unclear why the Gen 2 fiber mats display similar conductivity values as the Gen 1 even though the crosslink densities appear to be much different. PFG-NMR on the Gen 2 could shed some light on the differences in ionic mobilities. Additionally, transference numbers calculated from DC polarization techniques could provide useful information on what the conductivity data is representing, allowing for the decoupling of anionic and cationic contributions.

Mentioned in chapter 6, the coin cells produced in this work were merely prototype cells developed to act as proof of concept for the validity of PEO/PETA hybrid polymeric-gel electrolytes for use in rechargeable batteries. Thus, it is imperative that the PEO/PETA fiber mat be optimized for performance in a battery environment. A thorough investigation of the effects of fiber size, fiber density, PETA content, electrolyte solvent, electrolyte salt, and electrode materials is necessary to achieve maximum performance for fast charge and discharge applications.

Since PEO was specifically chosen due to its ability to coordinate with  $\text{Li}^+$  ions, it follows that similarly choosing a polymeric matrix that would prefer to interact with anions should display similar behaviour with the opposite effect on ion mobilities. For example, instead of choosing a polymer that has the ability to donate electron density to  $\text{Li}^+$  cations, if a polymer with substituents that can accept electron density from the counter anion might result in polymer-anion interactions. These interactions could well discourage the diffusion of anionic species during charge and discharge of a cell. Not only would this be advantageous to lithium diffusion and charge carrier concentration,

but the polarization of battery cells resulting from fast anion diffusion would be limited, further promoting  $\text{Li}^+$  diffusion.

### ***7.3. Potential Wound Healing / Artificial Skin Application of Gen2 PEO/PETA***

PEO/PETA electrospun fiber mats crosslinked under Gen2 conditions displayed unique mechanical properties, especially when wet. Unlike the Gen 1 and PVDF sample, the Gen 2 samples were easily handled and manipulated even after swelling with water. **Figure 7.1** is a photograph of a PEO10 sample swollen with water. It is clear in the image that the fiber mat stretches and has elastic qualities at low strain values. The mechanical properties of swollen PEO10 Gen 2 samples (**Figure 7.2**) show that these samples maintain some mechanical integrity when swollen. The potential application for tissue scaffolding or wound dressing is encouraging as the PEO10 Gen2 samples are porous by nature, allowing for  $\text{O}_2$  permeation; they retain water, providing moisture to trauma sites and they can be electrospun with therapeutic compounds to facilitate recovery.

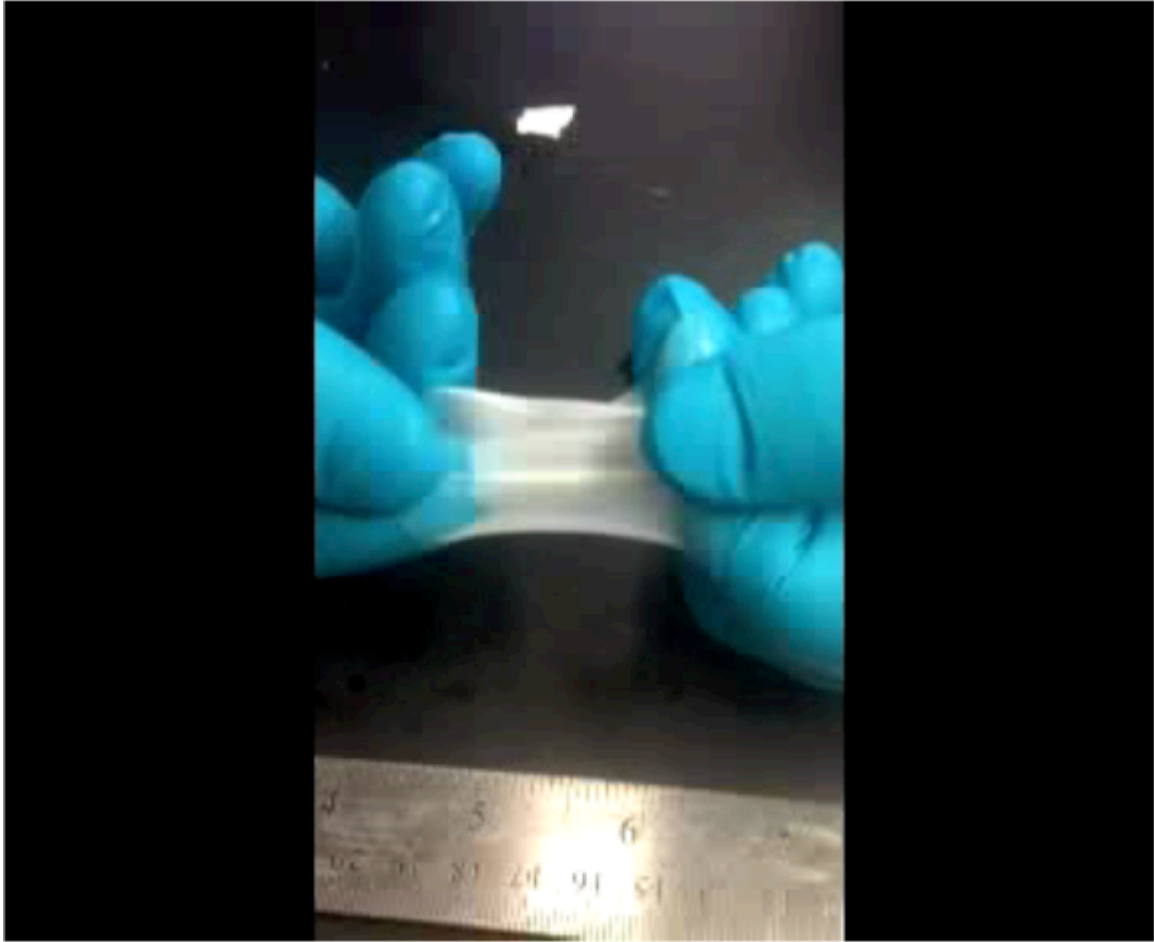


**Figure 7.1.** Image of electrospun PEO10 crosslinked under Gen2 conditions and swollen with DI water.

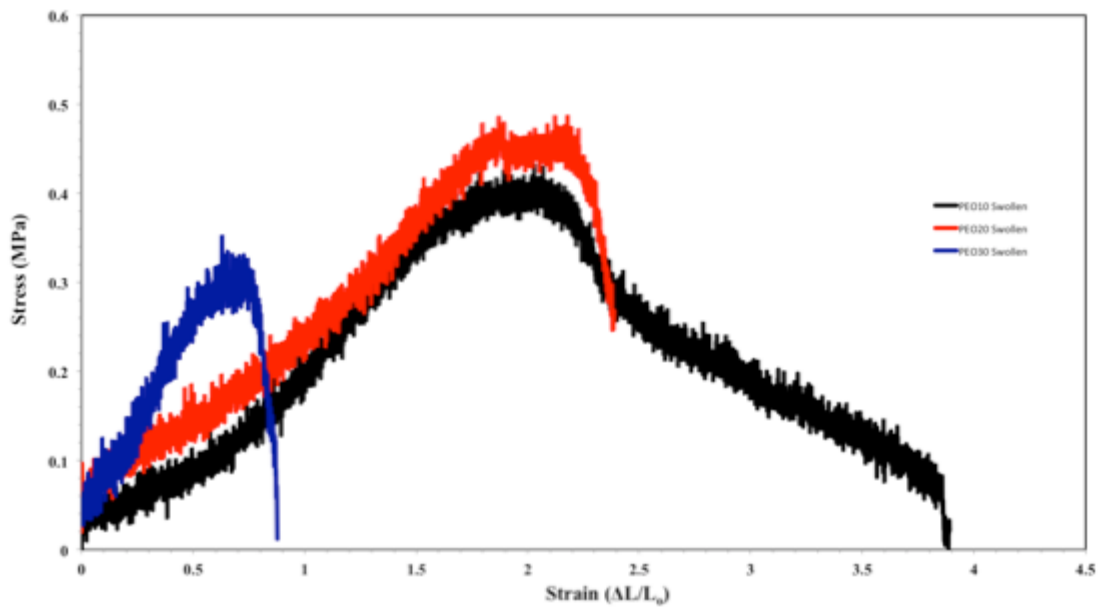


**Figure 7.2.** Stress-strain plot of PEO10 Gen2 samples swollen with DI water.